Estimating methane sources and sinks in the Arctic using atmospheric data assimilation

Sophie Wittig

université PARIS-SACLAY

Estimating methane sources and sinks in the Arctic using atmospheric data assimilation

Estimation des sources et puits de méthane en Arctique par assimilation de données atmosphériques

Thèse de doctorat de l'université Paris-Saclay

École doctorale n° 129, Sciences de l'environnement d'Île-de-France (SEIF)
Spécialité de doctorat : Instrumentation, télédétection, observation et techniques spatiales pour l'océan, l'atmosphère et le climat
Graduate School : Géosciences, climat, environnement et planètes.
Référent : Université de Versailles -Saint-Quentin-en-Yvelines

Thèse préparée dans l'unité de recherche **LSCE** (Université Paris-Saclay, CNRS, CEA, UVSQ), sous la direction de **Isabelle PISON**, Professeure, et le co-encadrement de **Antoine BERCHET**, Ingénieur-chercheur.

Thèse soutenue à Paris-Saclay, le 13 Janvier 2023, par

Sophie Luise WITTIG

Composition du jury

Membres du jury avec voix délibérative

Hélène BROGNIEZ	Présidente
Professeure des universités, UVSQ/OVSQ	
Tuula AALTO	Rapporteur & Examinatrice
Chercheuse, FMI (Finlande)	
Andreas STOHL	Rapporteur & Examinateur
Professeur des universités, Université de Vienne (Autriche)	
Line JOURDAIN	Examinatrice
Enseignante-Chercheuse, LPC2E/CNRS	

THESE DE DOCTORAT

NNT : 2023UPASJ002

université PARIS-SACLAY

ÉCOLE DOCTORALE
Sciences de l'Environnement d'Île-de-France (SEIF)

Titre: Estimation des sources et puits de méthane en Arctique par assimilation de données atmosphériques

Mots clés: méthane, Arctique, inversions, émissions

Résumé: L'Arctique est une région critique en terme de réchauffement climatique. Les changements environnementaux progressent déjà régulièrement aux hautes latitudes, ce qui accroît les émissions de méthane (CH_4). Le CH_4 étant un puissant gaz à effet de serre, des émissions supplémentaires provenant des régions arctiques pourraient intensifier e réchauffement climatique par une boucle de rétro-action positive. Diverses sources naturelles et anthropiques contribuent au bilan de CH_4 de l'Arctique, mais la quantification de ces émissions reste difficile. Dans ce travail, une approche de modélisation inverse est utilisée pour estimer les sources et puits de CH_4 dans l'Arctique. L'objectif est de mieux comprendre et quantifier les émissions de CH_4 en étudiant leurs cycles saisonniers et leurs tendances au cours des dernières années. Le réseau d'observation actuel est analysé quant à sa capacité à contraindre correctement les sources de CH_4 et identifier les tendances émergentes de ces émissions.

Title: Estimating methane sources and sinks in the Arctic using atmospheric data assimilation

Keywords: methane, Arctic, inversion, emissions

Abstract: The Arctic is a critical region in terms of global warming. Environmental changes are already progressing steadily in high northern latitudes whereby, among other effects, a high potential of enhanced methane (CH_4) emissions is induced. With CH_4 being a potent greenhouse gas, additional emissions from Arctic regions may intensify global warming in the future by positive feedback. Various natural and anthropogenic sources are currently contributing to the Arctic's CH_4 budget, however the quantification of those emissions remains challenging. Therefore, in this work, an inverse modeling approach is applied to estimate CH_4 sources and sinks in the Arctic. The objectives are to better understand and quantify CH_4 emissions from various sources by studying their seasonal patterns and trends during recent years. Additionally, the current observation network is analyzed regarding its capability to constrain CH_4 sources properly and identify emerging trends in CH_4 emissions.

Acknowledgements

"Nothing of me is original. I am the combined effort of everyone I've ever known."

Chuck Palahniuk, Invisible Monsters

First and foremost, I would like to express my gratitude to Isabelle and Antoine for supervising my thesis, supporting me along the way, giving me advice when required, and also space to be independent when needed. As supervisors, you complement each other very well, for which I am thankful because this has created a very pleasant working atmosphere for me as your student. Isabelle, thank you for your lightheartedness and enthusiasm, which is catchy and helped me to stay motivated throughout the entire time. You were always very quick to respond with great advice and constructive comments. Antoine, thank you for your enormous support, for always taking the time to answer my questions and helping me improve my skills. I am very grateful for all your encouragement during the least pleasant times, your patience with me and for your dedication to help me progress. I would also like to thank Marielle and Jean-Daniel for your advice and contribution to my work.

Many thanks to Tuula Aalto, for accepting to review my thesis and to Andreas Stohl, for reviewing my manuscript and giving me a very warm welcome in Vienna. I would also like to sincerely thank Hélène Brogniez and Line Jourdain for being part of my PhD jury. A special thank you to Patrick Crill and Andrey Skorokhod for participating in my thesis committee throughout the years and encouraging me to view ideas from a different perspective. I would also like to thank my tutor Christophe Rabouille for offering valuable advice and showing interest in my progress.

I would like to acknowledge the NUMERICS project for making this PhD thesis possible by financially supporting this work and giving me the opportunity to participate in informative schools, workshops and conferences.

I am grateful to my colleagues at LSCE for creating an inviting and pleasant working atmosphere and offering assistance but also distraction when needed. Special thanks to my two former interns, Louis and Clément, for committed work and your contribution to this thesis.

Many thanks to all the MAGIC people, especially Cyril, Claire, Julio, Julien and of course Axel, for the many beautiful moments we have experienced together and those still to come.

I am also very grateful to all my friends who have made the past three years an unforgettable experience. Barbara and Sara, thank you for being there for me from the start and

bringing even more glitter, sparkles and unicorns into my life. Many thanks to my Darling Maureen, surely one day we will make it to Achouffe! Thanks also to Jaime, Olga, Cyril and Clément for all the adventures we've had together. A great thank you to the CBB, where I could forget all my worries for many evenings. I would like to thank all my friends from Germany, especially Lea, Nina, Menti, Jessi, Loulu, Marco, Ida, Krissi, Fábi, Fred and Flori. I am thankful for all the virtual dates with you which brightened my days and cheered me up immensely throughout the many lock-downs in Paris.

A warm thanks to my whole family, for their constant support and encouragement during my thesis and long before. Many thanks to my parents, for your acceptance whatever path I chose. Thanks a lot to my nephew and sister, for all the fun times we have together, even though now I'm mostly in ganz weit weg. Special thanks to my big little cousin Dörte for the numerous Michel-times and sharing your ice cream with me.

Finally, I am enormously grateful to my fiancée Zoé, for your endless support and encouragement, your kindness and tolerance, and above all for showing me a future worth looking forward to.

Contents

List of Figures

List of Tables

Introduction

Methane is a gaseous organic compound and the simplest of all hydrocarbon molecules, consisting of one carbon and four hydrogen atoms. In the atmosphere, methane is namely the most abundant hydrocarbon, but still the total amount of methane only accounts for around 0.0002 % of all molecules in the atmosphere: methane is a so-called "trace gas". However, despite this low proportion, methane has a significant impact on the Earth's climate, on ecosystems and on air quality. Especially due to human activities, the global average concentration of methane in the atmosphere is currently around two-and-a-half times greater than its pre-industrial levels. Because of this sharp increase in atmospheric methane concentration, combined with the molecules' ability to absorb infrared radiation, methane is responsible for about 30 % of the rise in global temperatures since the Industrial Revolution.

The rising temperatures as a result of global warming are particularly prominent in the high northern latitude regions. On average, temperatures in the Arctic have already risen by 3.1 °C over the last 50 years. Predictions assume that the Arctic will have warmed by up to 10 °C by the end of this century if global warming continues to progress at such a rapid pace. The elevated temperatures in high northern latitudes trigger multiple changes in Arctic environments and ecosystems. The most noticeable impacts include the decline of sea ice in the Arctic Ocean and the thawing of terrestrial and sub-sea permafrost. These environmental changes not only put a strain on Arctic wildlife and native societies, they also initiate climate feedback loops which potentially elevate regional and global temperatures even further. One of the most important feedbacks is hereby the potential risk of increasing methane emissions from Arctic regions.

Especially, the destabilization of permafrost soils and the resulting exposure of biodegradable soil organic matter is often considered to potentially cause large amounts of additional methane emissions in the future. Some estimates even predict an Arctic "methane bomb", releasing enormous amounts of methane into the atmosphere from large carbon reservoirs that have previously been shielded by ice and frozen ground. However, not only the production but also the reduction of methane is influenced by temperature. For example, the activity of particular methane-consuming bacteria is increased under warmer climatic conditions. These processes combined with other compensating factors could possibly prevent a "methane bomb" from the Arctic in the future.

Nevertheless, at the present time, a variety of methane sources in the Arctic are already contributing to the increasing atmospheric methane concentrations. The largest natural source

are hereby high northern latitude wetlands which are widespread in the Arctic and Sub-Arctic. Additional natural methane emissions are caused by oceanic sources, especially from shallow water regions in the Arctic Ocean as well as forest fires and geological fluxes. Even though the population in the Arctic is comparatively low, anthropogenic activities additionally contribute to the Arctic's methane budget, predominantly due to the fossil fuel industry. With an estimated amount of 30 % of global undiscovered natural gas and 13 % of undiscovered mineral oil in the Arctic Circle, the region is hereby especially attractive for future drilling campaigns.

Estimating the precise amount of methane released in high northern latitudes is however challenging, and the resulting estimates are often subject to unavoidably high uncertainties. Currently, two methods are used for the estimation of methane sources and sinks: the bottom-up and the top-down approaches. The bottom-up approach gathers several methods aiming at estimating the different methane sources independently by trying to represent or observe the emission process and aggregating it to the desired scale. The top-down approach, based on the inverse problem theory, minimises the differences between simulations and observations (e.g. of atmospheric methane concentrations) by adjusting the input parameters of a model (e.g. surface fluxes). This approach thus makes it possible to deduce estimates of these input parameters that are best able to explain the observations at our disposal, given the present uncertainties. However, especially in the Arctic, top-down approaches are limited by the sparse availability of observations due to the difficulties of carrying out measurements in such remote areas.

Nonetheless, obtaining reliable quantifications of methane emissions from high northern latitudes is a key factor to assess their sensitivity to changes in environmental conditions, and thus improving future climate projections. Therefore, the main objective of this work is to better quantify methane sources and sinks in the Arctic for the most recent years by reducing uncertainties on existing estimates using an inverse modelling approach. This includes detecting eventual trends in any of the present methane sources or sinks and analyzing any occurring seasonal patterns of the different sectors as well as identifying limitations due to the available network of surface observation sites. The manuscript of this work is thereby divided into three main parts.

The first part, consisting of three chapters, explains the essential background for understanding the issues surrounding elevated methane emissions in the Arctic and demonstrates the relevance of studying this particular topic. The first chapter focuses on the Arctic region in relation to global warming and describes the different environmental conditions that respond to rising temperatures with positive feedbacks. In the second chapter, the effects of increased methane concentrations in the atmosphere are explained, the different methane sources and sinks present in the Arctic are introduced and their sensitivity to Arctic warming is demonstrated. Finally, in the third chapter, the different methods for estimating methane sources and sinks are presented, with special reference to high northern latitude regions.

The second part, consisting of two chapters, presents the material and methods that were used to carry out the studies included in this thesis. Hereby, the first chapter explains the the theory of atmospheric inverse modelling regarding the main mathematical concepts, assumptions and implementations. In the second chapter, the different ways of carrying out atmospheric measurements of methane are described, especially highlighting the available observation networks in the Arctic. Additionally, the function of the atmospheric transport model used in this work is outlined and the datasets of prior estimates on methane sources and sinks are introduced in this chapter.

The third part, consisting of three chapters, presents the scientific applications implemented within the framework of this thesis. The first chapter presents several preliminary

studies that have been carried out before or in addition to the main efforts of this work. This includes an analysis of recent atmospheric observations of methane concentrations from different measurement sites located in the Arctic in order to obtain preliminary conclusions on methane sources. Additional studies in the first chapter include an analysis of the capability of the observation network to detect oceanic methane fluxes as well as providing contributions to the evaluation and implementation of mobile measurement campaigns. The second chapter describes the study of methane sources and sinks in the Arctic nations by implementing an analytical inversion focusing on the years 2008 to 2019 using the available network of surface observation sites. The technical description of the implementation of this framework is hereby outlined, the performance of the inversion is evaluated and the obtained conclusions on Arctic methane emissions are presented. The third chapter consists of a study that aims at evaluating the detectability of a potential methane bomb in the Arctic using an inverse modelling framework with synthetic observations derived from generated emission scenarios. The potential scenarios used in this study are hereby explained and, subsequently, the performance of two different observation networks regarding adequate detection of emission trends is interpreted.

The main conclusions of the thesis are finally summarized, including potential perspectives for future works aiming at estimating methane sources and sinks in the Arctic.

Part I

General Introduction

CHAPTER

I

Global climate change and the feedback on Arctic and Sub-Arctic environments

Contents

CURRENTLY, THE ARCTIC IS CONSIDERED to be one of the most vulnerable regions in the world in terms of global warming. As temperatures in the high northern latitudes rise around three times faster than the global average, changes in environmental characteristics are proceeding rapidly, triggering positive climatic feedbacks that may further accelerate global warming in the near future.

In the following chapter, the impacts of a warming Arctic are illustrated in detail. In Section 1, the different geographical boundaries of the Arctic are defined and the environmental and climatic conditions are briefly outlined. Subsequently, global climate change and Arctic warming are explained in Section 2. Finally, the environmental changes induced by increasing temperatures in the Arctic as well as their potential climatic feedbacks are described in Section 3.

1 Presentation of the Arctic and Sub-Arctic regions

The northern polar region of the Earth is known as the Arctic. This term is derived from the Ancient Greek word *Arktikós* ($\alpha\rho\kappa\tau\iota\kappa\omega\varsigma$), which refers to the star constellation surrounding the Polar Star, known as "Ursa Major" or "the Great Bear". Unlike the southern polar region Antarctica, a continent covered by ice and surrounded by an ocean, the northern polar region consists of an ocean, known as the Arctic Ocean, in between the two land masses of Eurasia and North America. Both water and land in the Arctic are characteristically vastly covered by ice shields with seasonal variations throughout the year.

There are numerous definitions of which areas are part of the Arctic region. It is often described as the region north of the Arctic Circle at 66 °34 'N which marks the southernmost latitude at which the sun does not set on summer solstice and does not rise on winter solstice. The Arctic Circle is also the boundary which defines the eight Arctic nations whose territories are either completely or partly within the Arctic Circle. The Arctic nations include Canada, Greenland and the USA on the North American side, Russia, Finland, Sweden, and Norway on the Eurasian side and Iceland in between them.

Another common definition describes the Arctic as the area in the Northern Hemisphere, where the average temperature in July, the warmest month of the year, does not exceed 10 °C. This boundary is roughly identical to the northernmost tree line. Other characterizations of the Arctic are for instance based on the extent of land and sea ice or the extent of the permafrost region (further described in Section 3.2). The precipitation rate is generally low in high northern latitudes with less then less than 25 cm of precipitation annually. However, the whole Arctic and Sub-Arctic region is vastly covered by wetlands and small freshwater ponds and lakes.

Concerning the biomes, the Arctic can be divided into two regions: the high Arctic and the low Arctic. The high Arctic is characterized by polar desert, barren environments covered by a permanent layer of ice, where the low temperatures and poor soil conditions are mostly insufficient for plant growth. The low Arctic is known as the Arctic Tundra. Short growing seasons and low temperatures only allow for a low biotic diversity and the landscape consists of treeless plains covered with grasses and shrubs. Adjacent to the low Arctic lies the Sub-Arctic. This environment is known as the Taiga, more commonly referred to as boreal forest in North America. The longer growing seasons enable the growth of certain conifer tree species (e.g. spruce, pine, and fir) as well as a limited number of deciduous trees such as larch or tamarack.

All the various definitions of the regions belonging to the Arctic are shown in Figure I.1, page 9. Within the framework of this work, the focus lies predominantly on the combined high, low and Sub-Arctic region.

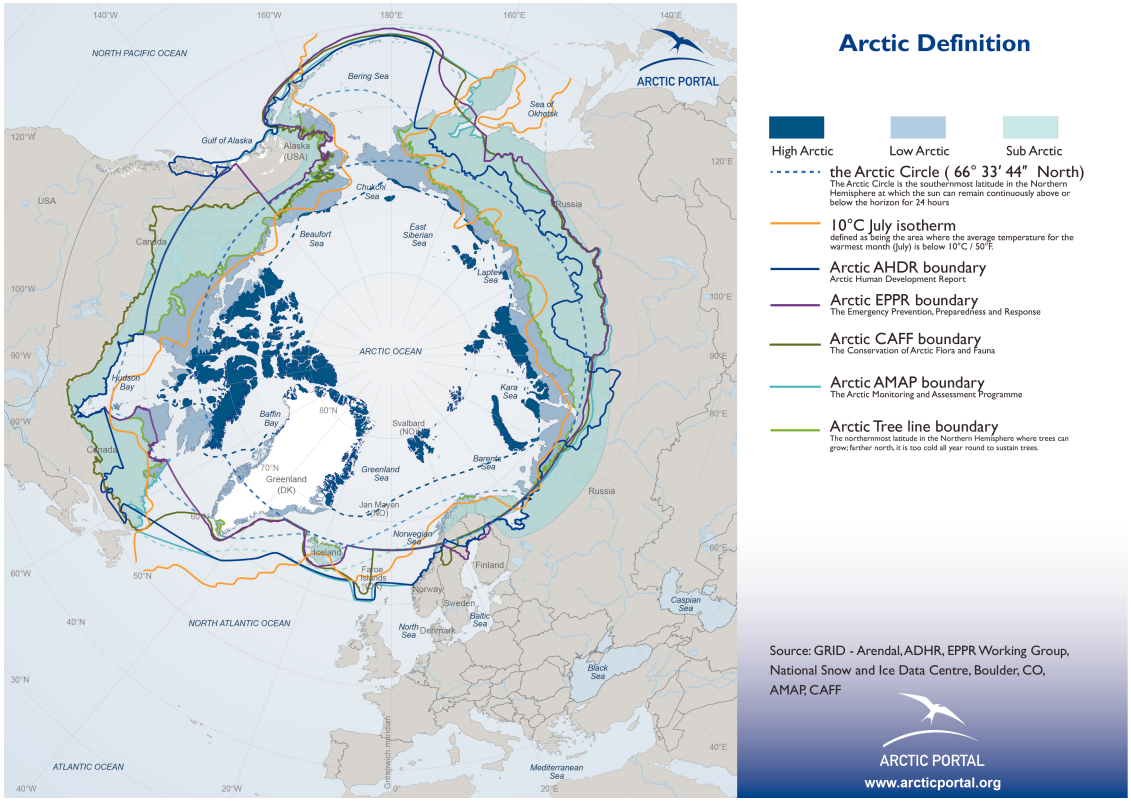

Figure I.1: Different boundaries of the Arctic. The colored regions define the high, low and Sub-Arctic. The dashed blue line shows the Arctic Circle, the orange line the 10 °C July isotherm and the light green line defines the northernmost treeline. The remaining lines show definitions of the Arctic used for different studies concerning the Arctic. Source: GRID - Arendal, ADHR, EPPR Working Group, National Snow and Ice Data Centre, Boulder, CO, AMAP, CAFF, ©Arctic Portal 2006-2022.

Living organisms which got adapted to the extreme climatic conditions in high northern latitudes have historically been very resilient. On the other hand, life in the Arctic is also vulnerable to sudden environmental changes and stresses induced by human activities endanger the adaptive capacity of many species as well as entire ecosystems. The greatest threat is hereby the rapid progress of the global climate change which is likely to have major physical, ecological, sociological, and economical impacts in the Arctic nations.

2 Global climate change

The climate of the Earth is principally controlled by the radiation budget which describes the balance between incoming and outgoing radiation. Incoming solar radiation is composed of ultraviolet, visible, as well as a limited portion of infrared energy, together called short-wave radiation, with an average irradiance of 343 Wm -2 at the top of the stratosphere. Around 31 % of the incoming solar radiation is reflected (by the Earth's surface, clouds and the atmosphere), 24 % are absorbed within the atmosphere (e.g. by ozone, dust or clouds) and the remaining 45 % are absorbed by the surface, either directly or by diffuse reflection from the atmosphere. The majority of the absorbed energy from incoming shortwave radiation is re-emitted as long-wave, or infrared, radiation. Hereby, a small fraction is directly re-emitted to space. Most of the energy from long-wave radiation is however absorbed by so called greenhouse gases (GHGs) such as water vapour (H_2O), carbon dioxide(CO_2), nitrous oxide(N_2O) and methane (CH_4). This energy is then re-emitted as long-wave radiation in all directions,

however only a small part escapes into space whereas the majority is re-emitted back towards the Earth. This process is known as the natural greenhouse effect which is essential for the maintenance of temperatures suitable for life on Earth. Without the greenhouse effect, the temperature on Earth would be around -15 °C on average. The global annual mean energy balance of the Earth is schematically illustrated in Figure I.2.

Temperature changes on the Earth are hereby linked to the greenhouse effect, which is predominantly influences by three factors: the incoming solar radiation, the surface albedo and the concentrations of GHGs in the atmosphere. If any of those climate factors undergoes a change with regard to their magnitude, the Earth's temperature adapts to keep the equilibrium and either decreases or increases. Temperature changes are additionally influenced by several orbital parameters of the Earth, such as eccentricity, tilt and time of perihelion. However, these factors will not be discussed further here, as changes in the cycles of the orbital parameters occur on a much larger time scale (several thousand years).

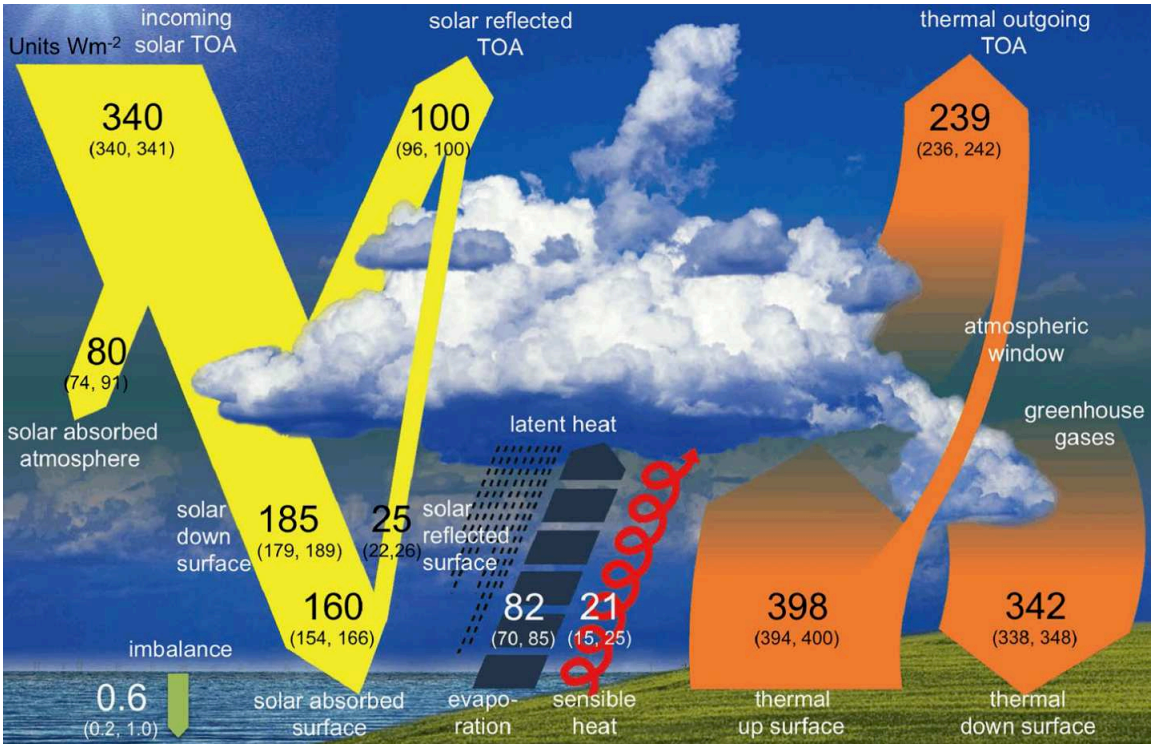

Figure I.2: Schematic diagram of the global annual mean energy balance of the Earth. The numbers refer to the energy flow in W m^{-2}. Source: Wild et al. (2015)

The incoming solar radiation is subject to natural fluctuations due to the solar cycle. Approximately every 11 years, the sun undergoes a period of increased magnetic and sunspot activity known as the "solar maximum", followed by a quiet period, the "solar minimum". Willson and Mordvinov (2003) indicated a correlation between elevated solar activity and increasing temperatures between the years 1978 and 2002, which was however not sufficient to explain the temperature increase during this period.

The second factor, the albedo, is a measure of the reflectivity of diffusely reflecting surfaces, including surface characteristics of the planet, cloud texture as well as aerosols, which are small solid or liquid particles in the atmosphere (e.g. Stephens et al., 2015). The albedo is measured on a scale from 0 to 1, with lower values indicating higher absorption of solar radiation. Fresh snow and ice have therefore the highest albedo (up to 0.8) (Hall, 2004) whereas open ocean waters have the lowest natural albedo (0.07) (Henderson-Sellers and

Wilson, 1983). Changes in albedo on the Earth's surface are predominantly caused by human activities, e.g. by the agricultural sector, the concreting of the soil through the expansion of cities and infrastructure or tropical deforestation (Berbet and Costa, 2003). The only process that has a major impact on global warming through the change of surface albedo is, however, the decline of ice and snow in the Arctic (Colman, 2013) as a consequence of elevated temperatures. This will further be explained in Section 3.1. Additionally, the accumulation of atmospheric aerosols from natural and anthropogenic sources can both have direct and indirect impacts on Earth's radiative balance. In general, aerosols are considered to exert a direct cooling effect at the Earth's surface since the majority of aerosols scatter solar radiation and thus increase the total reflected short-wave radiation. (e.g. Andreae et al., 2005; Myhre et al., 2013) However, certain aerosols strongly absorb radiation and therefore induce a warming effect. (Myhre et al., 2013). Aerosols additionally indirectly impact the cloud albedo, which is a main contributor to the total reflection of solar radiation back to space. Thereby, aerosols change the properties of clouds, which on the one hand leads to an increase in cloud albedo, but on the other hand to reduced precipitation efficiency. (Spracklen et al., 2008)

Since neither the incoming short wave radiation nor changes in albedo are the main reason for the observed temperature increase on Earth, the only remaining cause are accumulated greenhouse gases in the atmosphere to which human activities have greatly contributed since the start of the Industrial Revolution in the mid of the 18th century (IPCC, 2018)). The main drivers are hereby increased anthropogenic emissions of CO_2 and CH_4 and other less dominant anthropogenic GHGs. Increased temperatures as a consequence of elevated levels of anthropogenic greenhouse gases in the atmosphere thereby also amplify the emissions of natural GHGs, such as water vapour, inducing a positive feedback and further magnifying global warming (Manabe, 2019). The Intergovernmental Panel on Climate Change (IPCC) estimates the current average temperature rise to be 1°C higher in comparison to the pre-industrial era (IPCC, 2018). Therefore, in the course of the legally binding Paris Agreement of 2015, 193 parties agreed to aim for a a maximum average global temperature increase of 2°C by 2100 by substantially reducing greenhouse gas emissions.

According to a survey conducted in 2021 among 92 scientists who serve as experts for the IPCC (Tollefson, 2021), only about 20% of participating scientists still considered this temperature increase to be a realistic target. The majority of participants (almost 50%) estimated that the Earth's temperature will have increased by 3°C by the year 2100. The requirement of the Paris Agreement would thus be failed.

3 Arctic changes and global feedbacks

In the Arctic, the temperature rise is even more pronounced than in the rest of the world. Here, the air surface temperature has already increased by approximately 3.1 °C since the 1970s, around three times as fast as the global average. Predictions assume that by 2100, the near-surface air temperature in the Arctic will have increased between 3.3 and 10 °C.

Figure I.3, page 12 shows the forecasted increase in Arctic temperatures by the year 2090 under the SRES (Special Report on Emissions Scenarios, Nakicenovic et al., 2000) A2 scenario by the IPCC using the National Center for Atmospheric Research Community Climate Model (NCAR-CCM3, Kiehl et al., 1996).

As a result of the rising temperatures, environmental changes in high northern latitude regions are advancing steadily. The various environmental processes that have so far been observed in the Arctic and whose origin is global climate change are schematically illustrated in Figure I.4, page 12.

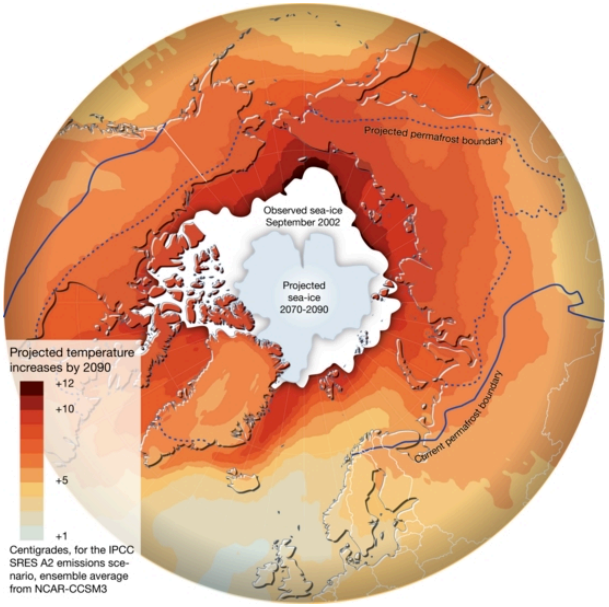

Figure I.3: Predicted temperature increase and sea ice decline in the Arctic by 2090 (NCAR-CCM3, SRES A2 experiment, Kiehl et al., 1996; Nakicenovic et al., 2000). Source: `www.grida.no/resources/7159`

Apart from the threats that rising temperatures in the Arctic pose to local ecosystems and indigenous societies, the effects of the rapid Arctic warming is also likely to have global consequences since the impacts of the progressing environmental changes lead to positives feedback loops on global warming.

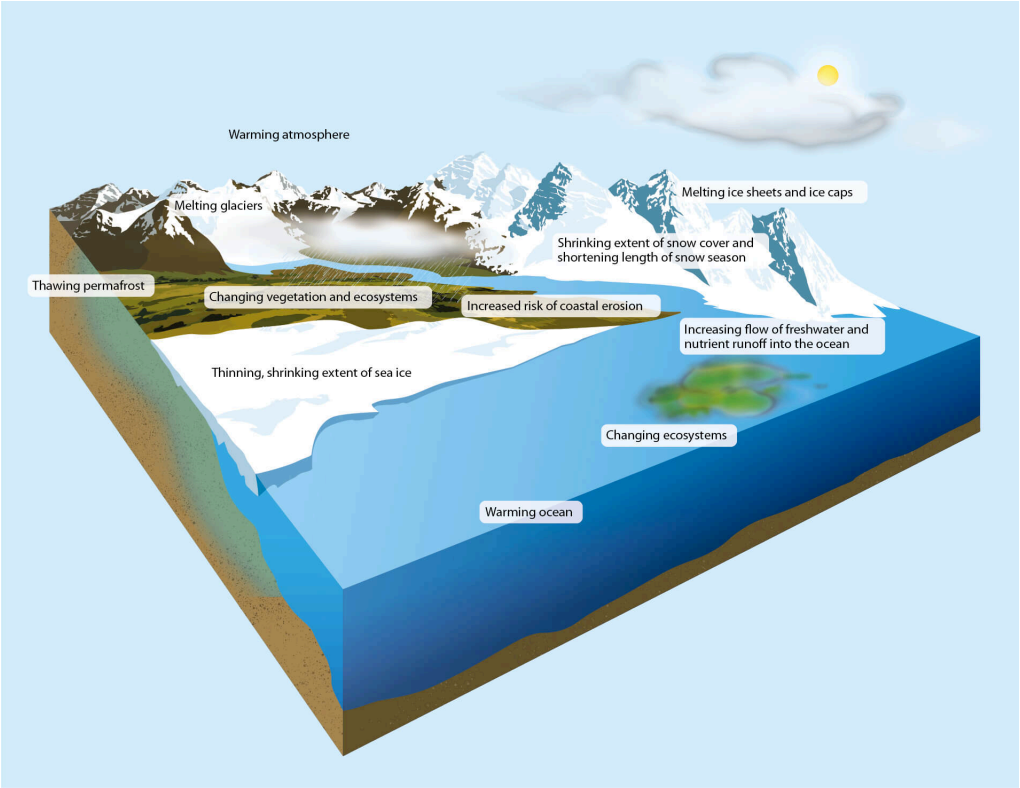

Figure I.4: Major environmental changes observed in the Arctic due to global warming. The figure is adapted from an image created by the U.S. National Center for Atmospheric Research and taken from AMAP (2017)

Out of these numerous environmental changes taking place in the Arctic region, only those which potentially provoke such a positive feedback on Arctic warming will be highlighted in the following. This includes the retreat of ice on land and at sea, permafrost degradation, increase in precipitation and changes in the Arctic's hydrologic system, shifts of vegetation zones and increasing wildfire events.

3.1 Decline of sea- and land-ice

Between 1979 and 2019, the Arctic sea-ice has declined by 43 % due to higher temperatures and increased precipitation (AMAP, 2021). With earlier melt onset and later freeze-up of the sea-ice, the summer open-water period is constantly increasing (Meredith et al., 2019; Perovich et al., 2020). The ice has also become younger and thinner over the past decades. Sea-Ice older than four years used to represent one third of the ice sheet in winter during the 1980s. Today, the share of old sea-ice is only about 1 % (Perovich et al., 2020; Tschudi et al., 2020).

The decline of the ice sheet in the Arctic Ocean is largely responsible for the accelerated rising temperatures in the Arctic because of the albedo effect. Snow-covered sea-ice reflects a relatively large share (as stated in Section 2) of the incoming solar radiation back to the atmosphere which leads to a cooling effect on the ocean surface. The albedo of open ocean waters on the other hand is one of the lowest of all natural surfaces and the high share of absorbed solar radiation is contributing to the progressive Arctic warming (IPCC, 2019).

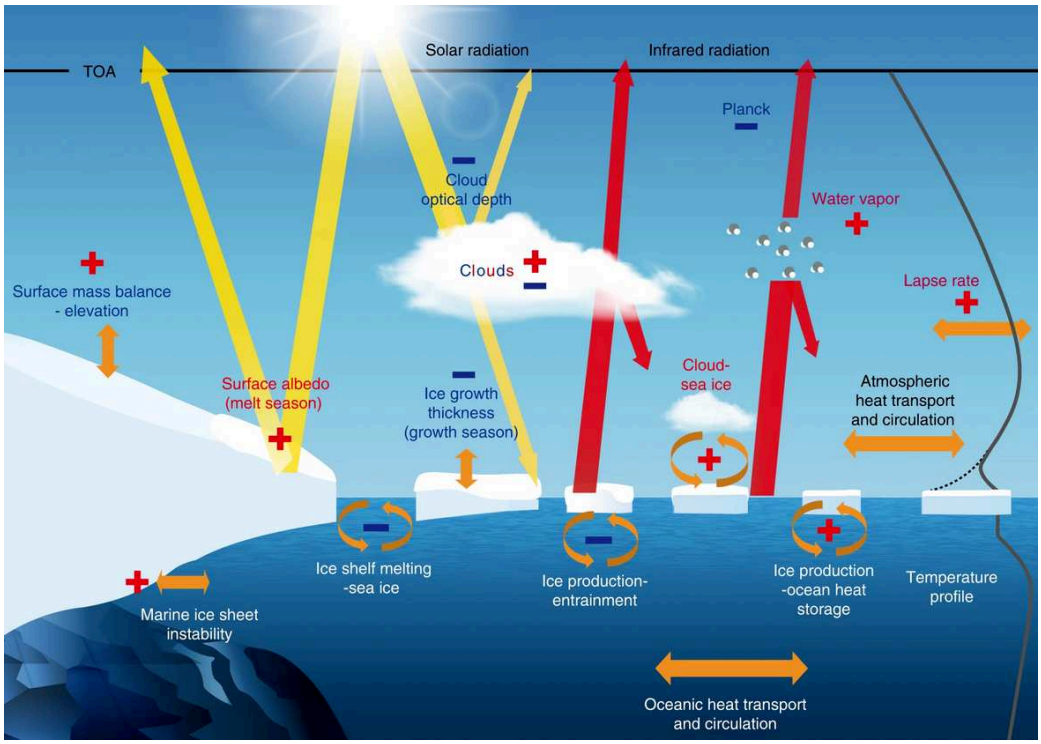

Figure I.5: Schematic radiative and non-radiative feedbacks in the Arctic involving the atmosphere, the ocean, sea ice and ice sheets. Solar radiation is presented with yellow, infrared radiation with red arrows. A red plus sign means that the feedback is positive, a negative blue sign corresponds to a negative feedback. TOA stands for top of the atmosphere. Image taken from Goosse et al. (2018)

As a consequence, the largest rise in air temperature in the Arctic is occurring over the Arctic Ocean with an estimated increase by 4 to 6 °C on average between the years 1971 and 2019 (ERA5, Copernicus, 2020). Moreover, an increasing trend in sea-surface temperatures has

been observed between the years 1982 and 2018 (Carvalho and Wang, 2020) resulting from elevated air temperatures and water vapor concentrations, declining sea-ice and, regionally, advection from neighboring seas.

Apart from the albedo effect, other factors related to the warming of the Arctic Ocean and the decline of sea-ice contribute to a positive feedback on Arctic warming. For instance, as the surface of the ocean warms, additional water vapor amplifies the greenhouse effect and induces further warming (e.g Gordon et al., 2013). A warmer climate also enhances the amount of cloud water in mixed phase clouds, which increases the amount of reflected solar radiation acting as a negative feedback on Arctic warming (Mitchell et al., 1989). However, melting sea-ice exposes additional open water resulting in surface turbulent heat fluxes which can increase humidity in the lower atmosphere and thereby increase low-level clouds. During the polar night in the Arctic, increasing low cloud cover increases downward longwave radiation which leads to further sea ice loss and thus to a positive feedback (Morrison et al., 2018; Goosse et al., 2018).

Due to the complexity of the underlying processes, these are not yet fully understood and quantified. Figure I.5 (page 13) schematically shows the main processes leading to positive and negative feedbacks related to changes in the Arctic Ocean as a consequence of global warming.

Just like the sea-ice, the land-ice in the Arctic is also diminishing (Moon et al., 2018). This is particularly pronounced in Greenland, whose ice sheet is declining by around 247 Gt per year, which accounts for about 37 % of the global loss of land ice (Bamber et al., 2018). The cumulative mass balance of land-ice for different Arctic nations is shown in Figure I.6.

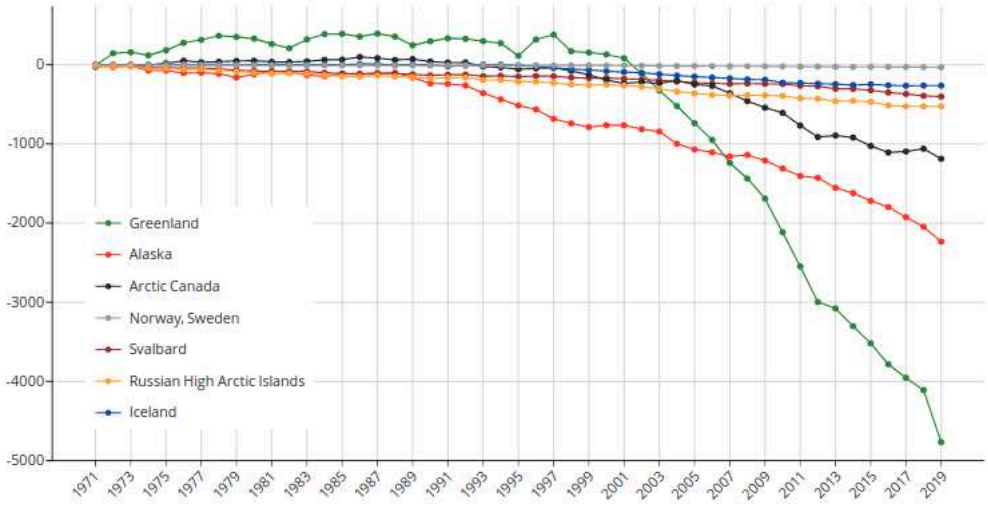

Figure I.6: Cumulative mass balance [Gt] of land-ice from 1971 to 2019 by country (AMAP, 2021)

Apart from the effects that this additional melt-water has on the sea-level, biogeochemical cycling as well as ecosystem structure and function in the coastal ocean, the decline of snow and land-ice also reduces the albedo of the ground surface, leading to increased absorption of solar radiation and thus providing a positive feedback on global warming.

3.2 Permafrost thaw

Permafrost is defined as frozen ground whose temperature is below 0 °C for at least two consecutive years. The so-called *active layer* above permafrost soils, which can be up to 20 cm

deep, is hereby defined as the soil layer that thaws during the summer and freezes again during the autumn (Dobiński, 2020). Permafrost can be found on land or beneath the seabed and consists of ice holding different types of soil such as sand and gravel. In the Northern Hemisphere, around 25 % of the ground is underlain by permafrost (Brown et al., 2014). It is assumed, that the northern permafrost regions contain up to 1.600 petagrams (Pg; 1 Pg equals 1 billion tons) of organic carbon which is estimated to make up around 50% of the global below ground organic carbon pool (Tarnocai et al., 2009; Schuur, 2019). This organic carbon hereby consists of the accumulated remains of animals, plants and microbes over a period of hundreds or even thousands of years.

Since the 1970s, the Arctic permafrost has warmed between 2 and 3 °C, causing it to thaw and destabilise (AMAP, 2021). The top layer (up to 3 m depth) is, naturally, most vulnerable to surface temperature changes. The thaw usually occurs gradually starting from the surface and proceeding downwards. Abrupt permafrost thaw on the other hand can effect tens of meters of permafrost over a short period of time (Schuur, 2019). These events are, for instance, induced by wildfires and lead to the destabilization and melting of ground ice which can cause erosion processes and soil subsidence (Brown et al., 2016; Potter and Hugny, 2020). Thereby, large pools of soil organic matter from deeper layers can be exposed to decomposition; lake and pond formation from ground subsidence (thermokarst) can also take place (Turetsky et al., 2020) as illustrated in Figure I.7.

(a) **(b)**

Figure I.7: Thermokarst collapse along the Sagavanirktok River (left, photo: D. A. Walker) and thermokarst lakes in Yamal, Russia (right, photo: M. O. Leibman). Images taken from AMAP (2017)

The resulting exposure of permafrost carbon triggers a potentially positive climate feedback since microbial decomposition of soil organic matter promotes greenhouse gas emissions. Hereby, decomposition under aerobic conditions results in carbon dioxide emissions whereas anaerobic decomposition predominantly produces methane and, to a lower extent, CO_2 as well. The ratio between the anaerobic CO_2:CH_4 production can hereby vary greatly in different regions (Treat et al., 2015). For instance, the methane production can be more than four times higher in shrub and grasslands than in forest dominated soils (Ström et al., 2005; Turetsky et al., 2007). The possible soil carbon losses related to permafrost thaw are schematically shown in Figure I.8, page 16.

How and to which extent the soil carbon can be decomposed is also dependant on multiple factors such as the burial depth, the degree of conservation and how easily the organic

matter can be disintegrated. The amount of the permafrost carbon which could possibly be released to the atmosphere by microbial conversion to greenhouse gases is therefore highly uncertain.

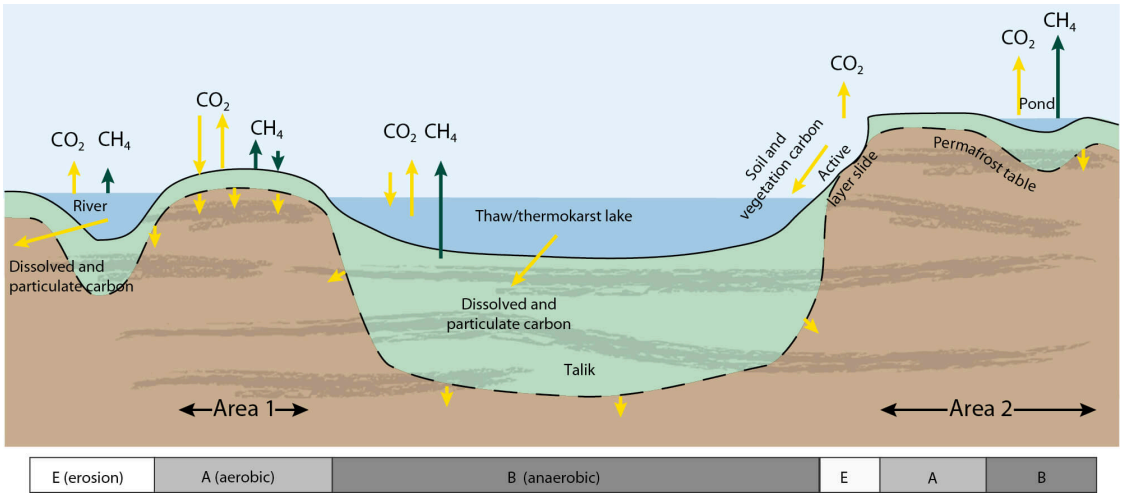

Figure I.8: Mechanisms of carbon loss from Arctic permafrost soils (excluding fire events). Area 1 has a spatially homogeneous increase in active layer thickness and Area 2 has spatially heterogeneous permafrost thaw driven by differences in soil ice content (after Van Huissteden and Dolman (2012)

Another potential positive climate feedback related to permafrost thaw are gas hydrates in the Arctic Ocean where subsea-permafrost is present (e.g. Kretschmer et al., 2015). Gas hydrates are a crystalline solid with an ice-like structure that are composed of rigid cages of water molecules with enclosed molecules of gas, predominantly methane. Since gas hydrates are only stable under specific conditions of pressure and temperature, permafrost-associated gas hydrates in the Arctic Ocean are vulnerable to elevated temperatures and are assumed to be a potential source of increased methane emissions. It is however not certain, if methane hydrated from subsea-permafrost can have a major impact on the CH_4 concentrations in the atmosphere (further described in Section 2.2).

3.3 Precipitations and changes in surface hydrology

Between the years 1971 and 2019, precipitation in the Arctic has increased by 9 % (AMAP, 2021). By the end of this century, it is predicted that precipitation will have increased between 40 and 60 % (Bintanja and Selten, 2014; Vihma et al., 2016; Bintanja and Andry, 2017). This is mainly due to three factors: increased evaporation as a result of more open water due to sea-ice loss (e.g. Bintanja and Selten, 2014; Vihma et al., 2016) as described in Section 3.1, a higher ability of the atmosphere to carry moisture as a result of higher air temperatures (Screen and Simmonds, 2010; Bintanja, 2018) as well as increased poleward moisture transport (Hao et al., 2019; Zhang et al., 2013). Additionally, the Arctic is also expected to change from a mostly snow- dominated to a rain-dominated precipitation regime (Bintanja and Andry, 2017), which has already been observed in the Atlantic sector (Łupikasza and Cielecka-Nowak, 2020). This transition is predicted to take place even if the 1.5 degree target of the Paris Agreement is achieved, especially in Greenland and the Norwegian Seas, as shown by McCrystall et al. (2021).

Changes in the Arctic's hydrologic system include various feedbacks, both positive and negative (Francis et al., 2009). For instance, increased precipitation as well as runoff from precipitation that enters rivers directly can lead to a freshening of the upper ocean layers

(Holland et al., 2007). This is because the vertical stratification is strengthened, which leads to reduced upward mixing of heat and thus cooling the surface of the Arctic Ocean. Bintanja et al. (2018) showed that a 50 % increase in precipitation in the Arctic by 2100 can slow down the projected Arctic warming by up to 2 °C. In the High Arctic, it is predicted that snowfall will continue to dominate precipitation (Bintanja and Andry, 2017) which would be a negative feedback on Arctic warming because of the albedo effect.

At lower latitudes however, increased precipitation in the form of rain could have exactly the opposite effect and increase surface albedo. Webb et al. (2021) highlighted the importance of increasing areas of surface water in the Arctic due to higher precipitation and permafrost thaw as an already important component of albedo change in the continuous permafrost zone. Intense precipitation can also lead to increased thermokarst erosion (observed for instance by Sæmundsson et al., 2018), triggering the positive feedbacks from permafrost degradation described in Section 3.2. Moreover, enhanced soil moisture resulting in lower oxygenation promotes the growth of anaerobic microbes, metabolizing the soil organic carbon and making it a more labile source of CO_2 and CH_4 emissions (Bragazza et al., 2013; Lee et al., 2014).

3.4 Vegetation shifts

The vegetation in the Arctic plays a key role in biogeochemical feedbacks, even though it is sparsely distributed and only includes a limited number of species. In the tundra biome, a process called Arctic greening has already been taking place (Berner et al., 2020; Myers-Smith et al., 2020). Here, the vegetation has grown denser and shrubs have become taller due to longer growing seasons (Elmendorf et al., 2012). With further rising temperatures it is anticipated that the vegetation zone will shift northward, the tundra will expand to the Arctic desert and the northernmost treeline of the taiga will shift to higher latitudes.

In a few regions however, a process called Arctic browning is taking place which means that the vegetation is declining in those areas (Phoenix and Bjerke, 2016). Arctic browning can be caused by different factors such as increased surface water, pest outbreaks and extreme weather events (Bjerke et al., 2014; Lund et al., 2017). Even though the vegetation decline is currently only taking place sporadically, it could become more drastic in the future.

A simple graphical indicator often used to assess the vegetation activity is the Normalized Difference Vegetation Index (NDVI). The NDVI is obtained by calculating the difference between near-infrared (which the vegetation strongly reflects) and red light (which the vegetation absorbs) whereby higher values refer to healthy and dense vegetation and lower NDVI values show sparse vegetation. Figure I.9 (page 18) shows the average NDVI during the growing season (June to August) in the Arctic between the years 1982 and 2012 (Guay et al., 2015).

The feedback of this vegetation shift is not yet clearly predictable. On the one hand, higher plant quality and Leaf Area Index, which characterizes the density of leaves in a given environment, lead to higher photosynthetic activity and therefore, to a greater carbon sink (López-Blanco et al., 2020). Shrubs also shade the ground from solar radiation, which contributes to temperature maintenance in permafrost soils (Blok et al., 2010), and enhance evapotranspiration which increases cloud formation (Rydsaa et al., 2017).

However, vegetation expansion reduces the surface albedo of the landscape (Loranty et al., 2018). When the highly reflective Arctic snow cover is displaced by shrubs and trees, more solar radiation is absorbed, which causes a warming effect. During winter, taller shrubs also capture more snow, which can effectively warm the soil since the insulation is increased (Jafarov et al., 2018).

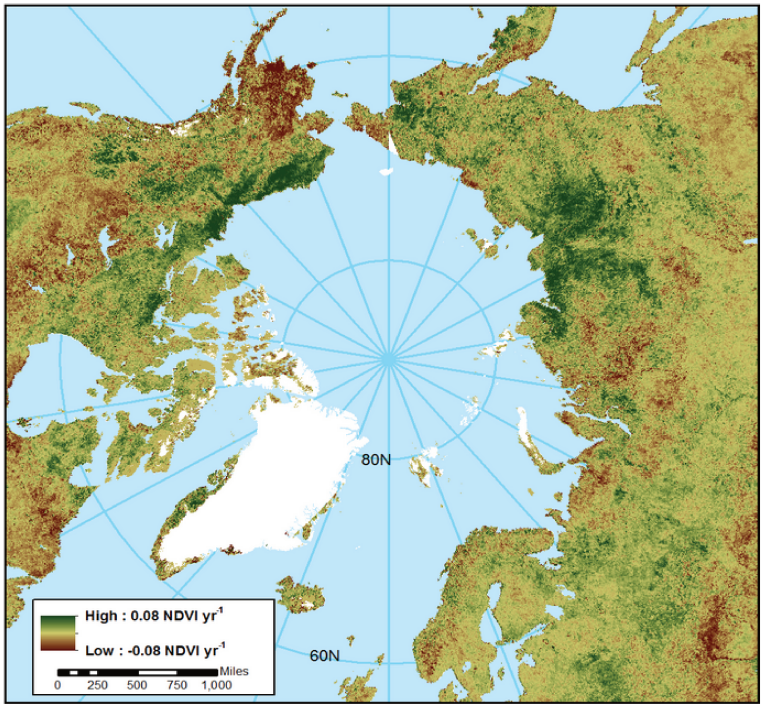

Figure I.9: NDVI for the Arctic growing season. The data is derived primarily from Advanced Very High Resolution Radiometer (AVHRR) sensors onboard several NOAA satellites between the years 1982 and 2012. Source: Guay et al. (2015)

The climate feedback of the vegetation shift is therefore dependant on multiple factors and yet to be further investigated.

3.5 Wildfire events

Earlier snowmelts and increased evapotranspiration favour the conditions for wildfire outbreaks in the Arctic tundra and taiga (Kim et al., 2020). Even though wildfires events occur so far only sporadically and without any apparent trend in high northern latitudes, the fire season length has been increasing over the last decades (Masrur et al., 2018; Jain et al., 2017).

In the Arctic, wildfires represent a positive climate feedback in different ways. First of all they can induce permafrost degradation (e.g. Brown et al., 2016; Potter and Hugny, 2020), contributing to the already progressing permafrost thaw and the thus resulting consequences described previously.

Moreover, forest fires upwind of snow and ice covers can affect the melt patterns through the deposition of light-absorbing impurities (LAI) (Conway et al., 1996; Skiles et al., 2018). Northern Hemisphere forest fires have already been shown to be linked with accelerated melt of the Greenland ice sheet (Keegan et al., 2014). As described in Section 3.1, this can lead to a lower albedo of the surface, which allows for a higher absorption of incident solar radiation. In addition to that, forest fire LAI deposition promotes microbial growths by providing nutrients for pigmented surface ice algae (Ryan et al., 2018; Cook et al., 2020) triggering a feedback loop that further decreases the surface albedo. Soot deposition can also have a negative effect on the albedo. Aubry-Wake et al. (2022) have shown that ice-melt can increase by up to 10 % in the years after extreme wildfire events.

On the other hand, wildfire smoke reduces incoming shortwave radiation (e.g. Stone et al., 2008) which can have a cooling effect on the surface (Kochanski et al., 2019). Even though it

has been anticipated that these processes balance out each other (Stone et al., 2008) this has yet to be quantified.

Fire events are also a significant source of carbon emissions (e.g. Rein and Huang, 2021), both from the vegetation layer but also from ancient soil carbon stocks, in the form of CO_2, CO and CH_4. In 2020, wildfire events in the Arctic increased by around 35 % in comparison to the previous year, causing carbon emissions between 66 and 143 Mt (McCarty et al., 2020; Lin et al., 2021; Witze, 2020).

Conclusion of the chapter

The Arctic warming is progressing at a much higher rate than the global average. Compared to pre-industrial times, the average temperature in the Arctic has already risen by 3.1 °C and it is predicted that by the end of this century, the temperature will have increased by up to 10 °C. As a consequence, various environmental changes can be observed in high northern latitude regions which, on the one hand, endanger the adaptability of local ecosystem and societies but also trigger climate feedbacks that potentially accelerate the Arctic warming. Those processes are mainly connected with changes in surface albedo, predominantly due to the decline of snow and ice. Another important feedback is the increasing exposure and biodegradability of organic matter resulting in enhanced greenhouse gas emissions, for instance in the form of CH_4.

The environmental changes progressing in Arctic and Sub-Arctic regions are very interconnected and the underlying processes not yet fully understood. Therefore, it is crucial to further study and quantify these various factors in order to obtain reliable predictions about future environmental conditions in the Arctic and their potential contribution to positive climate feedbacks.

CHAPTER

II

The role of methane with special consideration of the Arctic

Contents

AMONGST THE VARIOUS POSITIVE CLIMATE FEEDBACKS induced by global warming in the Arctic and Sub-Arctic introduced in the previous chapter, methane emissions are especially likely to gain importance in the future due to the variety of natural sources that are sensitive to changes in temperature. Especially the thawing of terrestrial and subsea permafrost is often associated with increasing CH_4 emissions (e.g. Van Huissteden and Dolman, 2012; Shakhova et al., 2019). However, various climate and environmental changes in the Arctic contribute to methane emissions either directly, such as forest fires, or indirectly, for example by promoting permafrost destabilisation or creating favourable conditions for methane production or uptake.

In the following chapter, firstly the impacts of elevated methane concentrations in the atmosphere are highlighted (Section 1). Subsequently, the various sources that contribute to CH_4 emission in the Arctic are described in Section 2 and the influence of thawing permafrost on methane emissions in high northern latitude is elaborated (Section 3). Finally, the processes that consume CH_4 from the atmosphere or otherwise restrict the emissions of methane are specified more precisely in Section 4.

1 The importance of methane in the atmosphere

Globally, the average atmospheric CH_4 concentration has increased by around 163 % since pre-industrial times and reached a current value of around 1909 ppb (NOAA, May 2022, Lan et al., 2022). This rise is presumably caused by elevated anthropogenic methane emissions, increased natural methane emissions in consequence of feedback effects, reduced oxidative capacity of the atmosphere or a combination of all these factors (Nisbet et al., 2019).

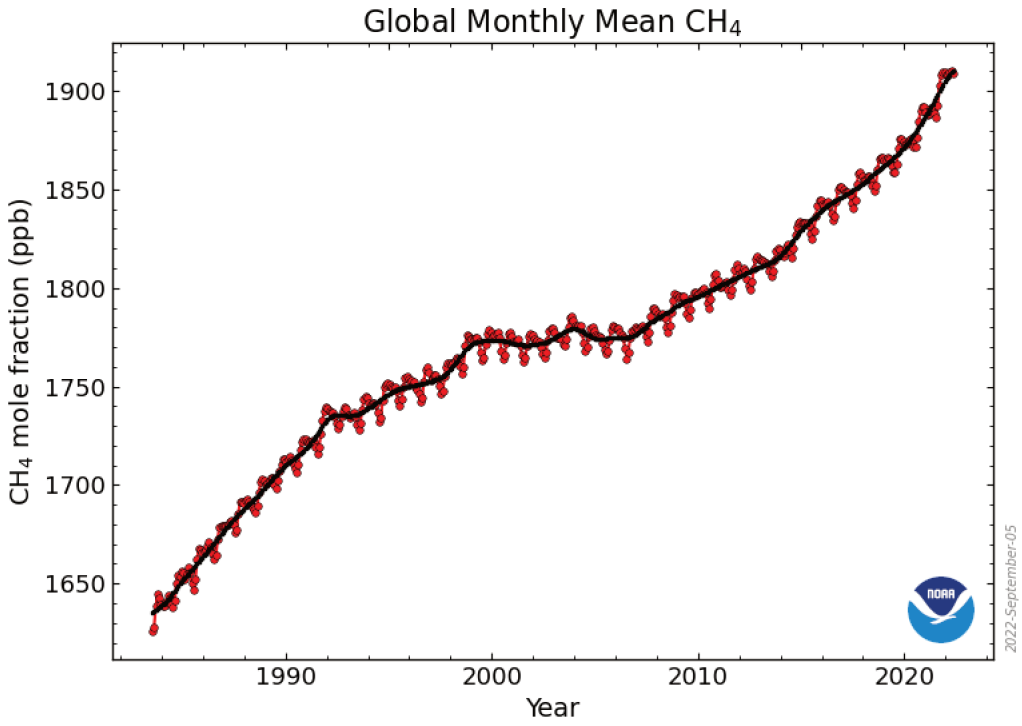

Figure II.1: Global monthly average atmospheric methane mixing ratios [ppb] from 1983 to 2021. The average mixing ratio is derived from marine surface sites of the Global Monitoring Division of NOAA-ESRL (National Oceanic and Atmospheric-Earth System Research Laboratory). Source: (Lan et al., 2022), `www.gml.noaa.gov/ccgg/trends_ch4`

The increase of measured CH_4 mixing ratios between the years 1983 and 2021 is shown in Figure II.1, page 22. If methane concentrations keep following this trajectory of rapid increase, the global average of the atmospheric concentration is expected to reach approximately 2400 ppb by the year 2100 (Nisbet et al., 2019). This global trend is overall also mirrored by the atmospheric CH_4 concentrations in Arctic regions (AMAP, 2015).

1.1 Impact on global warming

By mole fraction, dry air contains approximately 78 % nitrogen (N_2), 21% oxygen (O_2) and 0.9 % argon (Ar). Thus, greenhouse gases only account for around 0.1 % of the atmospheric gases. As mentioned before, GHGs are gases that can absorb infrared radiation, which is a property that in fact all gases whose molecules are composed of three or more atoms have.

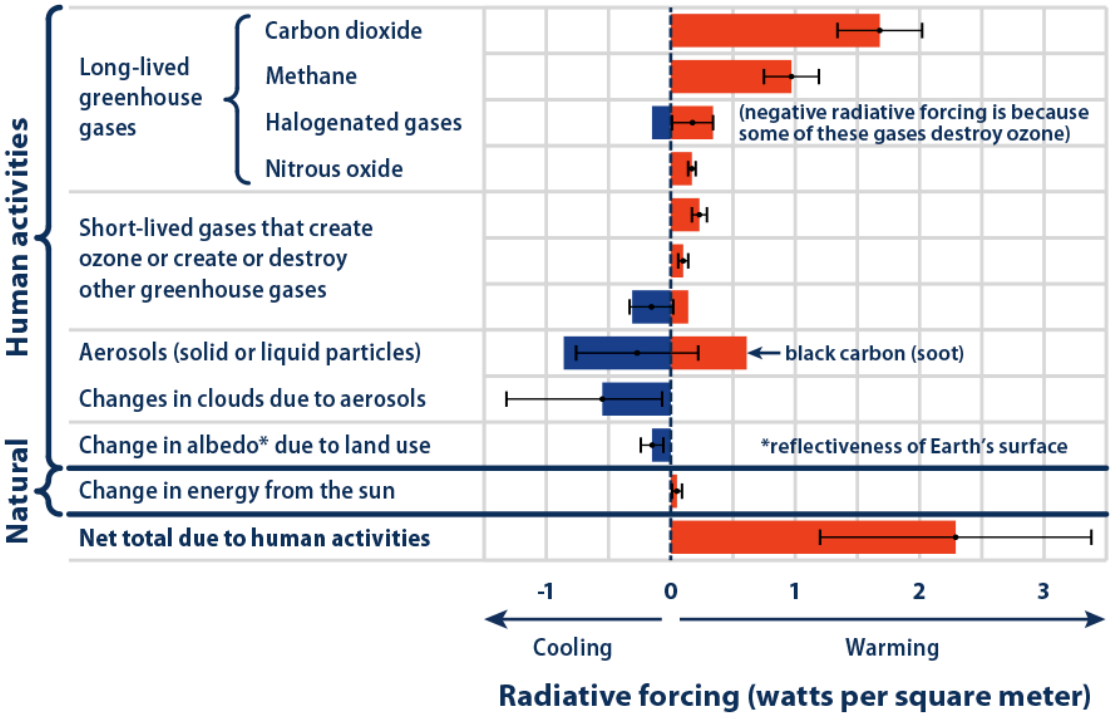

Figure II.2: Total amount of radiative forcing caused by human activities including indirect effects between 1750 and 2011 of different climate factors (IPCC, 2013)

The various GHGs are, however, associated with different impacts on global warming and there are different metrics to compare their potential contributions. The IPCC introduced the term radiative forcing (RF), also called climate forcing, which is a measure of the effect that a specific climatic factor provokes on the amount of downward-directed energy impinging upon the surface of the Earth. Climatic factors include hereby, in addition to GHGs, solar radiation, surface albedo and aerosols. Figure II.2 shows exemplary radiative forcing values for different anthropogenic climatic factors.

The RF of methane (for the year 2019) was estimated to lie between 0.43 and 0.65 $W.m^{-2}$ which accounts for around 16 % of the total radiative forcing by all anthropogenic GHGs combined (Szopa et al., 2021). However, CH_4 also has an indirect influence on other climatic factors, for instance through the production of ozone (O_3, further described in Section 1.2) and water vapour, since the oxidation of methane is an important in situ source of water vapour in the middle and upper stratosphere. (e.g. Brasseur and Solomon, 2005; Revell et al., 2016). Those indirect effects are estimated to have a RF between 0.90-1.51 $W.m^{-2}$.

Another measure to estimate the possible climate feedback of each gas is the global warming potential (GWP). The GWP of a gas hereby depends on three factors:

- the wavelengths where the molecule absorbs
- the strength of the energy absorption
- the atmospheric lifetime of the molecule.

More specifically, the GWP is a measure of how much energy the emissions of 1 ton of a certain greenhouse gas absorbs over a given time in relation to the emissions of 1 ton of CO_2.

The global warming potential of methane is estimated at around 28 over a 100-year period (e.g. IPCC, 2014). Over a period of 20 years, the GWP of CH_4 is almost three times higher, around 84, which is due to its relatively short atmospheric lifetime of around 9 years (Prather et al., 2012). The GWP of methane as a function over time is hereby illustrated in Figure II.3.

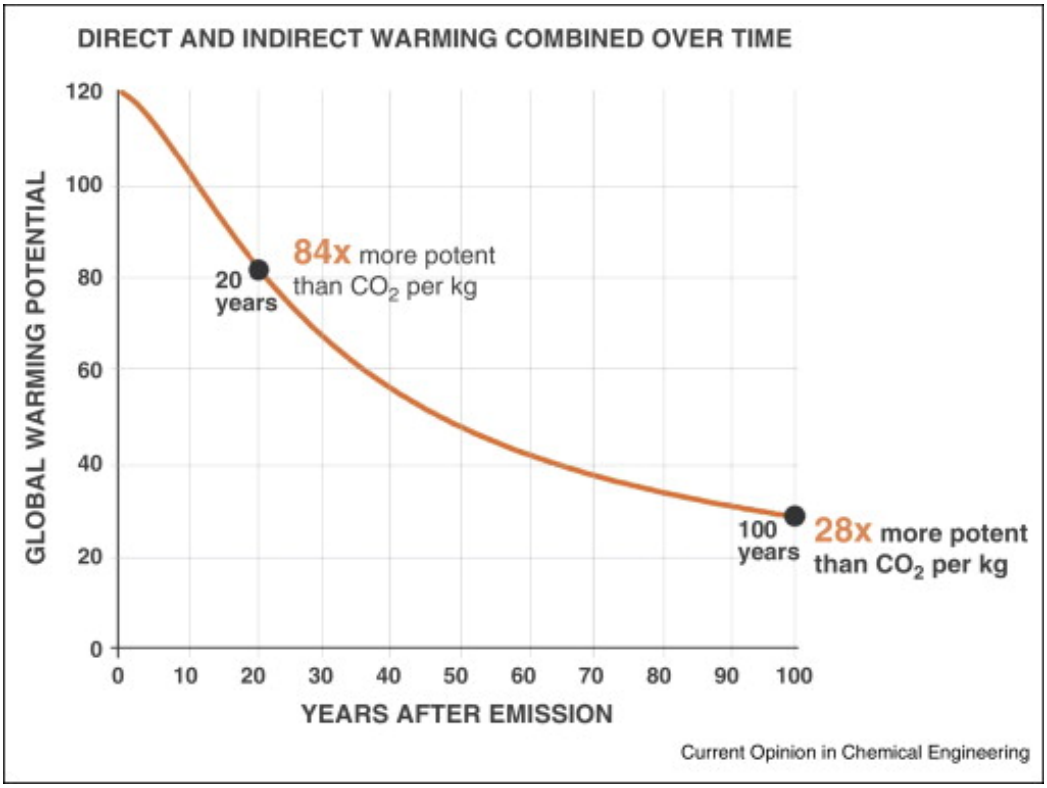

Figure II.3: Global warming for methane as a function of the time horizon. Image taken from Allen (2014).

However, high methane concentrations in the atmosphere also increase their own lifetime (e.g. Myhre et al., 2011) which is why the GWP of CH_4 is not a constant value and must be adjusted over time. Still, due to the short atmospheric lifetime of methane in comparison to other GHGs, reducing anthropogenic CH_4 emissions is a potentially effective way to limit increased radiative forcing in the near future (discussed for instance by Nisbet et al., 2019).

1.2 Impact on air quality

High methane concentrations can also have a detrimental effect on air quality and thereby jeopardise the health of living beings. The reason for this are chemical reactions with other substances, which increase the production of O_3.

Ozone is a secondary air pollutant that is formed in the troposphere by catalytic photo-

chemical reactions with nitrogen oxides (NO_x) and volatile organic compounds (VOCs) such as CH_4. As far as human health is concerned, elevated ozone levels can impair lung function and cause inflammatory reactions in the respiratory tract, which can sometimes lead to premature death, especially with long-term exposure to high ozone concentrations (Ebi and McGregor, 2008; Zhang et al., 2019). In plants, ozone is absorbed through the stomata of the leaves which can lead to reduced photosynthetic activity and destruction of the plant cells (e.g. Saxena et al., 2019). In agriculture, for example, this can lead to losses in crop yields (Emberson, 2020).

Besides, methane also has an indirect effect on O_3 production by reducing concentrations of the hydroxyl radical OH (further described in Section 4.1). OH is the most important oxidant in the troposphere and reduced concentrations can lead to the accumulation of various VOCs which are an issue in themselves and the prerequisite for ozone-generating chemical reactions.

2 Methane sources

Methane emissions are caused by both anthropogenic activities and natural processes. Anthropogenic CH_4 emission sources include livestock farming, exploitation and distribution of fossil fuels, waste management, biomass burning linked to agricultural practices and burning of agricultural waste, rice farming, the use of biofuels from agricultural residues and landfills. Natural sources of methane are wetlands and inland freshwater systems, oceanic sources (e.g. methane hydrates at the seabed of shallow ocean waters), biomass burning linked to wildfires, permafrost soils, termites, onshore geological sources (e.g. gas and oils seeps) and wild ruminants.

The primary sources of methane emissions at the global scale are shown schematically in Figure II.4.

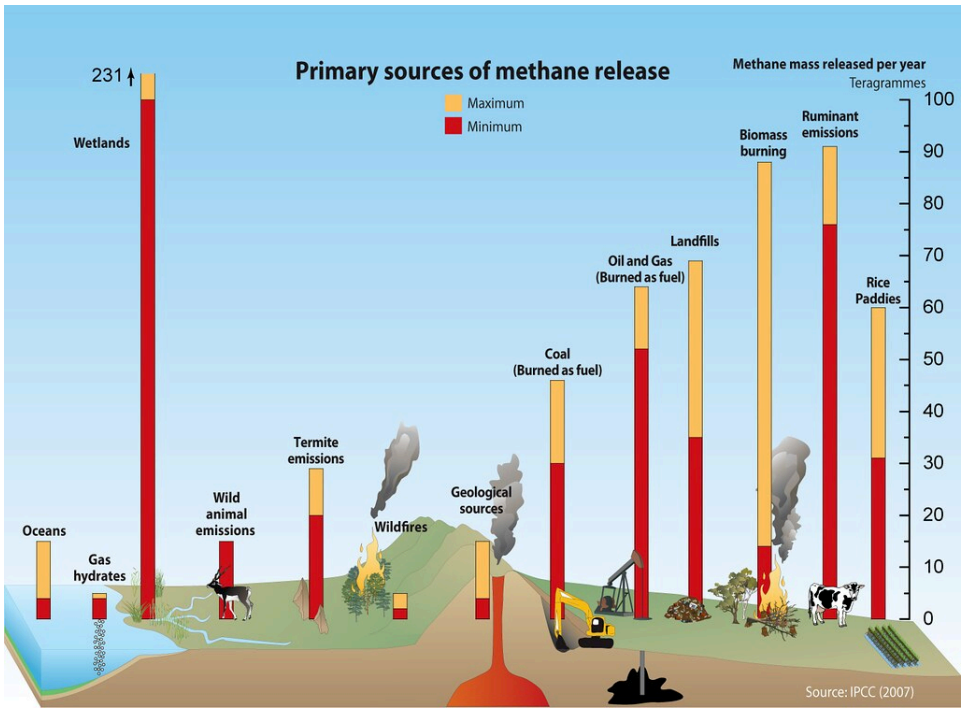

Figure II.4: Primary global sources of methane release. The estimations of the emissions are based on IPCC (2007). Cartographer: GRID-Arendal, `www.grida.no/resources/`

On a global scale, the total methane emissions were estimated to be around 576 $TgCH_4$ yr^{-1} within a range of 550 to 594 $TgCH_4$ yr^{-1} by Saunois et al. (2020) for the period 2008-2017. Hereby, the combined anthropogenic emissions were estimated at 359 $TgCH_4$ yr^{-1} which accounts for 62 % of the total CH_4 emissions. The largest natural methane source are wetlands which make up 31 % of the global CH_4 emissions with around 181 $TgCH_4$ yr^{-1}.

Methane emissions can be of three different origins: microbial, thermogenic and pyrogenic. These different origins of CH_4 can hereby be distinguished on the basis of their isotopic contents (Sherwood et al., 2017). Microbial CH_4 production is a form of anaerobic respiration and takes place through decomposition of organic matter by microbes in anoxic environments. Organisms capable of producing methane belong to the domain Archea and occur in wet, anaerobic environments. The main natural source of microbial CH_4 are therefore wetlands and freshwater systems whereas anthropogenic sources include farming activities (e.g. by manure application, enteric fermentation of farmed animals) as well as rice cultivation and wastewater treatment.

Thermogenic CH_4 is generated from thermocatalytic breakdown of complex organic molecules under high temperatures and pressures. The main natural sources are hereby geological sources such as gas and oil seeps. Thermogenic methane emissions caused by anthropogenic activities are associated with the fossil fuel industry and include the extraction, production and distribution of coal, mineral oil and natural gas (e.g. through venting or leaks).

Pyrogenic CH_4 is produced by the incomplete combustion of organic matter, which includes natural wildfire events as well as anthropogenic activities such as biofuel burning, agricultural fires and domestic wood burning.

The methane sources which are currently present in the Arctic as well as how these sources are effected by rising temperatures are subsequently briefly described.

2.1 Wetland and freshwater emissions

Wetland environments have long been known to be significant sources of methane emissions through microbial decomposition of organic matter in saturated soils (Ehhalt, 1974; Fung et al., 1991; Bartlett and Harriss, 1993). Wetlands are characterised by waterlogged soils with this high degree of water saturation creating conditions that favour methane production.

Around half of the global wetland area is located above 50°N (Matthews and Fung, 1987). Estimations of the methane emissions from high northern latitudes vary by a factor of four (between 38 and 157 $TgCH_4$ yr^{-1}) and assessments on the wetland area (between 2.2 and 4.4 million km^2) by a factor of two (Petrescu et al., 2010). The large discrepancies between the CH_4 flux estimations are, for instance, due the many environmental parameters influencing methane production from microbial decomposition which complicates accurate assessments. Another cause is possibly due to double-counting, since the extent of wetlands and small ponds and lakes are poorly constrained (Thornton et al., 2016). Figure II.5 (page 27) shows the total wetland extent above 60 °N estimated by Hugelius et al. (2021).

The underlying process leading to the production of methane is hereby called methanogenesis; this defines the final step in the anaerobic degradation of organic carbon that generates methane as the final product. Methane is hereby produces either by fermentation (acetoclastic methanogenesis) or hydrogenotrophic methanogenesis, which is formally a type of respiration (e.g. Fenchel et al., 2012).

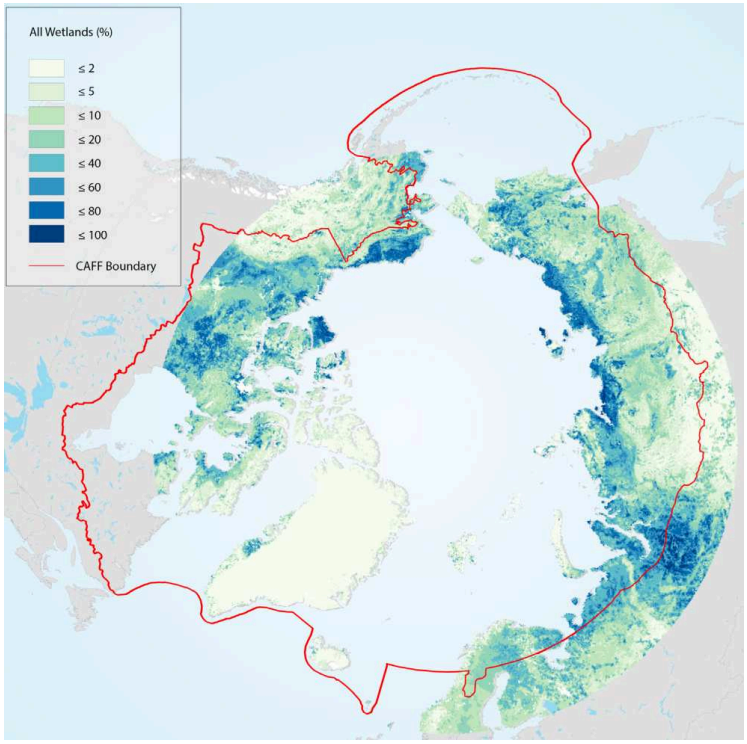

Figure II.5: Extent of Arctic wetlands, including peatlands, mineral wetlands and small open water surfaces (larger lakes are excluded). The red line shows the boundary used by CAFF (Conservation of Arctic Flora and Fauna) to define the Arctic region. Source: Hugelius et al. (2021)

Acetoclastic methanogens dismutate acetate to CH_4 and CO_2 according to:

$$CH_3COOH \longrightarrow CO_2 + CH_4.$$

Hydrogenotrophic methanogens on the other hand use hydrogen (H_2) for the reduction of CO_2 (or CO or formate) according to:

$$4\,H_2 + CO_2 \longrightarrow CH_4 + 2\,H_2O.$$

These processes are hereby complex, include different preliminary steps and depend on various environmental factors such as the temperature, the quality of organic matter, the water table, the vegetation type and the persistence of anaerobic conditions. Therefore, quantifying CH_4 emissions from wetlands is challenging, even though the understanding of the most important processes controlling methane fluxes has already improved. The various parameters on which methanogenesis depends are shown in Figure II.6 on page 28.

Once CH_4 is produced in wetlands it can reach the atmosphere via three main pathways: diffusion through the water column, gas bubble release (ebullition), and plant-mediated transport (e.g. Vroom et al., 2022).

Other freshwater sources of CH_4 include lakes, ponds, streams and rivers and the processes leading to the production of methane are similar to the microbial decomposition in wetlands. Methane emissions from those freshwater systems are often neglected in the Arctic, even though high northern latitudes contain a high abundance of lakes and ponds (Lehner and Döll, 2004). Indeed, methane emissions from Arctic freshwater systems (above 54 °N) are estimated to be as high as 13 $TgCH_4\ yr^{-1}$ (Bastviken et al., 2011).

However, as mentioned before, estimating CH_4 emissions from wetlands and shallow

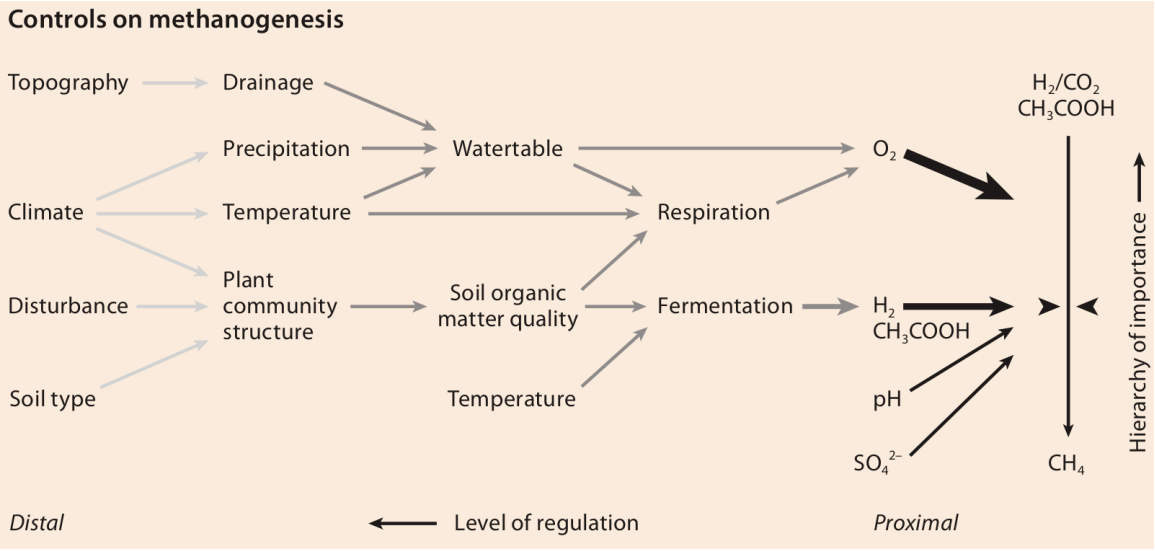

Figure II.6: Key control parameters for methanogenesis. Controlling parameters are divided into distal (climate and environmental) and proximal (chemical) and a hierarchy of importance in a complex ecosystem context is indicated. Based on Schimel (2004). Source: AMAP (2015).

lakes separately is challenging. This is for instance due to the definition commonly used for wetlands, which includes standing water up to between 2 and 2.5 m depth (e.g. Tiner et al., 2015; Cowardin, 1979). This definition includes high-latitude lakes and ponds, which tend to be shallow (less than 1 m deep), especially ponds in permafrost peatlands and thermokarst lakes (West and Plug, 2008).

Rising temperatures in the Arctic potentially influence local CH_4 emissions in different ways. For instance, soil warming is associated with increased CH_4 emissions since anaerobic decomposition is responsive to changes in temperature (e.g. Christensen et al., 2003). Changes in vegetation in high latitude peatlands caused by rising temperatures can either increase or decrease methane emissions, depending on the plant species (Treat et al., 2015). Enhanced evapotranspiration on the other hand could potentially reduce the water storage in northern wetlands which would limit the activity of anaerobic microbes and thereby reduce the CH_4 fluxes (AMAP, 2021).

The impact of global warming on future methane emissions from high latitude wetlands and freshwater systems is therefore difficult to predict and a better understanding of the various influences is needed to obtain meaningful predictions.

2.2 Oceanic methane sources

Oceanic CH_4 emissions are caused by several different sources. Methane is hereby predominantly produced throughout the subsurface of the ocean through either microbial, thermogenic or abiotic processes which occur at different depths and conditions within the sediment column.

Abiotic methane is formed by chemical reactions which do not directly involve organic matter. Those processes only occur on Earth in several specific geologic environments. In the Ocean, abiotic CH_4 is formed by via water-rock and gas-rock reactions such as serpentinization (Etiope and Sherwood Lollar, 2013), where the hydration of minerals leads to the formation of H_2. The produced hydrogen can afterwards react with carbon-containing gases, leading to the formation of CH_4. In the Arctic Ocean, serpentinization is known to occur and

the produced methane potentially accumulates in gas hydrates (Rajan et al., 2012).

In higher layers of the sediment column, CH_4 is formed by thermogenic processes. The organic matter occurring in those in depths (up to 4 to 5 km, Judd, 2004), for instance in the form of coal beds, can be degraded when temperatures increases over 110 °C (Milkov, 2005). The produced methane can subsequently be released through gas seeps which are geographically widespread across the sea floor (Judd, 2004).

At the top of the ocean sediments (up to 2 km) in anoxic and sulfate-depleted zones, microbial decomposition of organic matter takes place. Thereby around 10 % of the total organic carbon is typically converted to CH_4 (Judd, 2004). Methane is hereby produced by methanogenic archaea, similar to the processes taking place in terrestrial freshwater systems (see Section 2.1).

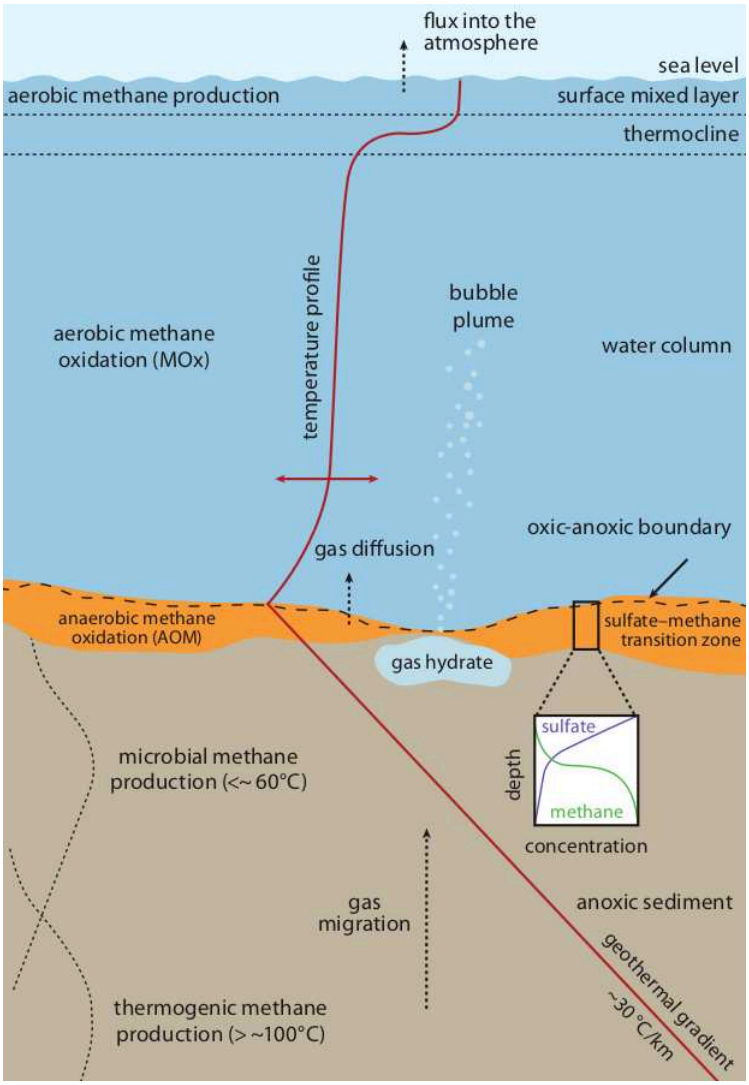

Figure II.7: Typical areas of oceanic methane production, oxidation and migration within the sediments and water column. Abiotic methane production is not included in the graphic. Oxidation and migration are further described in Section 4.3, page 37. Source: AMAP (2015).

Apart from the methane production within the sediment columns, CH_4 can be generated in the water column as well, for instance as a by-product of the decomposition of phosphonates (e.g. Carini et al., 2014). The relative contribution of these processes to the methane budget of the Arctic Ocean is hereby unclear. However, since many of these processes take

place with close proximity to the surface, they have been connected with observed methane fluxes above the Arctic Ocean (Kort et al., 2012).

The most important reservoir of oceanic CH_4 are assumed to be gas hydrates, which have already been described in Chapter I (Section 3.2, page 14). Methane hydrates can be found at depth along the continental margin and may occur at shallower depths in subsea permafrost-associated areas. Analyses of the isotopic composition indicate that the majority of the gas hydrate deposits contain biogenic methane (Archer, 2007), hydrate formation can theoretically bind methane of various origins (Rajan et al., 2013).

All the different areas of methane production, oxidation and migration are schematically shown in Figure II.7, page 29.

Marine CH_4 emissions are generally assumed to have a small influence in comparison to other methane sources (e.g. Kirschke et al., 2013; Saunois et al., 2020). Emissions from the Arctic Ocean are assumed to gain more importance in the future due to the declining sea ice cover, which allows increased exchanges between the sea surface and the atmosphere, and also because of the destabilization of sub-sea permafrost, which will be further described in Section 3.2, page 35.

2.3 Wildfires

Wildfire events are a pyrogenic CH_4 source. Currently, fire events are only a minor source of methane emissions but their importance may increase in the future, both globally and in the Arctic (Jenkins et al., 2014).

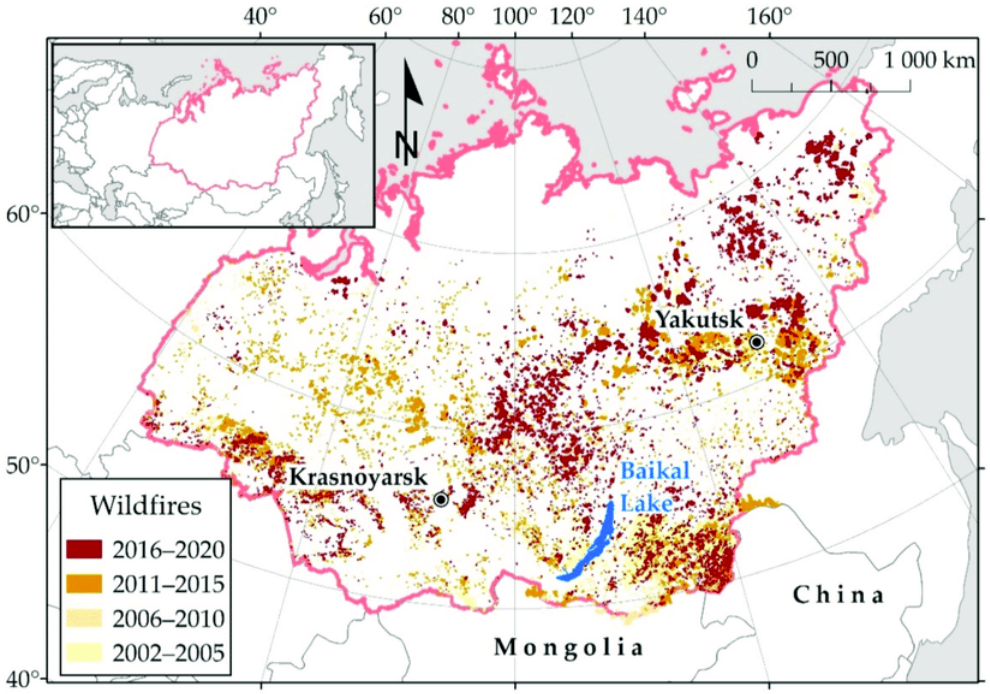

Figure II.8: Spatial distribution of wildfire events in Siberia during different periods of time. Only areas where more than 2500 ha were burnt are mapped here. Source: Ponomarev et al. (2021)

The trigger for growing risks of wildfires in Arctic regions are higher air temperatures, increased surface dryness, shrinking snow covers and extended fire seasons whereby these events also partially influence each other. For instance, earlier snowmelt due to rising tem-

peratures exposes the ground to elevated evapotranspiration which effectively dries the surface and promotes the spread of wildfires (Kim et al., 2020).

The wildfires occurring in Siberia in 2019 caused the government to declare a state of emergency (Anon, 2019) and similar events in the following year have led to the highest temperatures ever recorded in the Arctic Circle: 38 °C were measured in the Russian city of Verkhoyansk on June 20, 2020 (Farge and Soldatkin, 2020; Overland and Wang, 2021). Even though the number of wildfires in Siberia doesn't show any increase between 2001 and 2020, the burned area has more than doubled during this period, from 6.32 to 16.06 MHa (Ponomarev et al., 2021). A map of the wildfires in Siberia between 2002 and 2020 is shown in Figure II.8 on page 30. Statistics on forest fires in Siberia after 2020 have not yet been published, however it has been reported, that wildfires were difficult to control due to the use of manpower and resources in the war (e.g. Patel, 2022).

Besides the CH_4 that is directly emitted by wildfires, those events can also indirectly influence methane emissions in the Arctic. Fire events occurring in permafrost regions lead to abrupt permafrost degradation (e.g. Brown et al., 2016; Potter and Hugny, 2020) and thereby promote the formation of thermokarst lakes as well as increased exposure of degradable carbon.

2.4 Anthropogenic sources

Around one fifth of the global anthropogenic methane emissions comes from the eight Arctic nations.

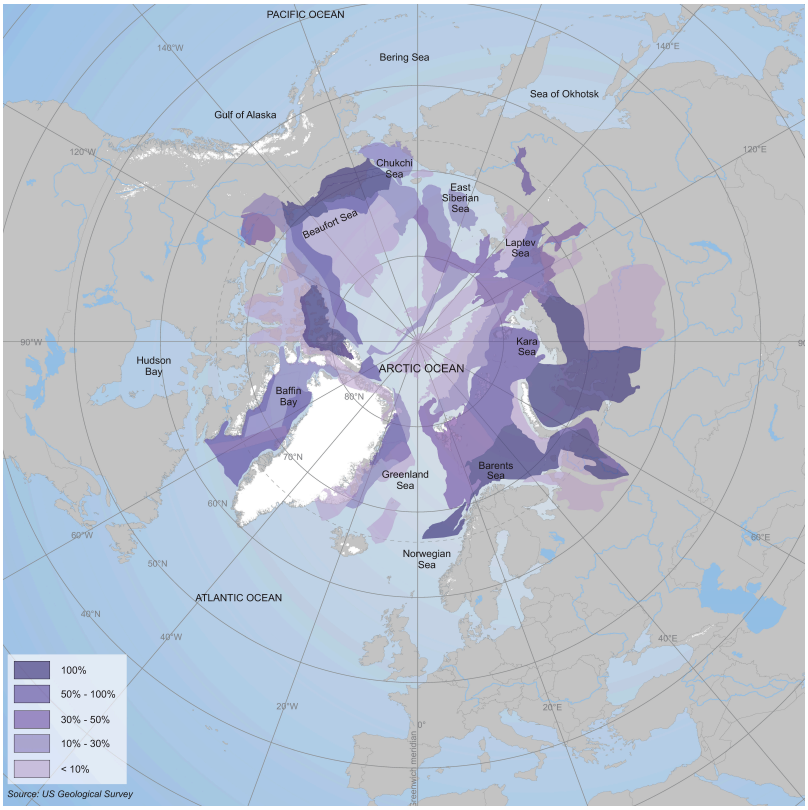

Figure II.9: Distribution of anticipated oil and gas resources in the Arctic. The different shades of purple refer to the probability of potential oil and gas fields. The map is built on information from the US Geological Survey (USGS). Source: Arctic Portal Library, www.library.arcticportal.org.

Approximately 90 % of those emissions are contributed by Russia and the USA, 6 % by Canada and 4 % by the remaining Arctic nations (Norway, Sweden, Finland, Iceland and Greenland). Since anthropogenic activities related to GHG emissions are often reported by country however, the CH_4 emissions don't necessarily take place in Arctic regions. In fact, anthropogenic methane sources only make up approximately 28 % of the total CH_4 emissions in high northern latitudes (Saunois et al., 2020), since the Arctic represents one of the least populated areas in the world, with only sparse settlements and few large cities. The highest contribution of methane emissions is hereby caused by the fossil fuel industry (around 4 $TgCH_4\ yr^{-1}$) whereas the combined emissions from wastewater management, farming activities and biomass burning are estimated to be around 2 $TgCH_4\ yr^{-1}$.

Several policies, both legally binding regulations as well as voluntary agreements, that are designed to directly or indirectly limit CH_4 emissions have already been established by all Arctic nations. The largest potential for decreasing methane emissions in the USA and Canada are hereby limiting CH_4 fluxes from unconventional gas extraction as well as extending existing separation, recycling and treatment schemes for biodegradable waste. Russia could potentially reduce emissions by limiting leakages from gas pipelines and networks as well as extending recovery and utilization of associated gas from oil extraction (AMAP, 2015).

It is however suspected that the Arctic is a large source of unexplored fossil fuel resources, as shown in Figure II.9 (page 31). Estimates assume that around 30 % of the global undiscovered natural gas and 13 % of undiscovered mineral oil can be found in the Arctic Circle (Gautier et al., 2009). Moreover, the increasing accessibility by declining sea ice in the Arctic Ocean makes this region attractive for the fossil fuel industry regarding future offshore drilling campaigns.

3 The influence of permafrost thaw on future methane emissions

Thawing permafrost, both on land and on the seabed, as a result of rising temperatures in the Arctic can have various impacts on methane emissions.

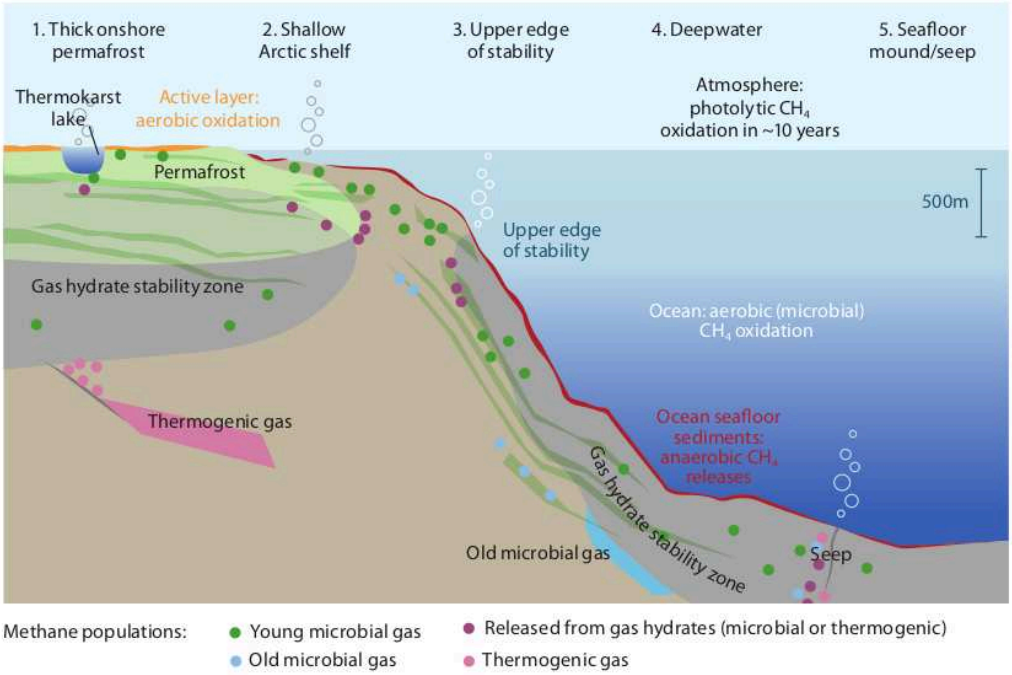

Figure II.10: Schematic illustration of permafrost related methane emissions with specification of their origin. Source: AMAP (2015), redrawn from Ruppel (2011)

CH_4 fluxes associated with destabilisation of permafrost soils are schematically shown in Figure II.10 (page 32) and the corresponding processes leading to those direct and indirect methane emissions will subsequently be described.

3.1 Terrestrial permafrost

Several studies identify terrestrial permafrost as an stand-alone emission source of methane (e.g. Saunois et al., 2020). Permafrost thaw can however both have a direct and an indirect influence on CH_4 emissions in the Arctic, which makes permafrost related methane fluxes hard to quantify. Direct fluxes of methane are of thermogenic origin and are estimated to have a small impact (around 1 Tg per year, USEPA, 2010).

Permafrost destabilization additionally impacts microbial CH_4 emissions in three different ways. As described before in Section 3.2, permafrost regions contain large pools of soil organic matter whose exposure can lead to increasing anaerobic respiration and therefore, increasing methane emissions. The estimated distribution of carbon contained in high northern latitude permafrost soils is shown in Figure II.11.

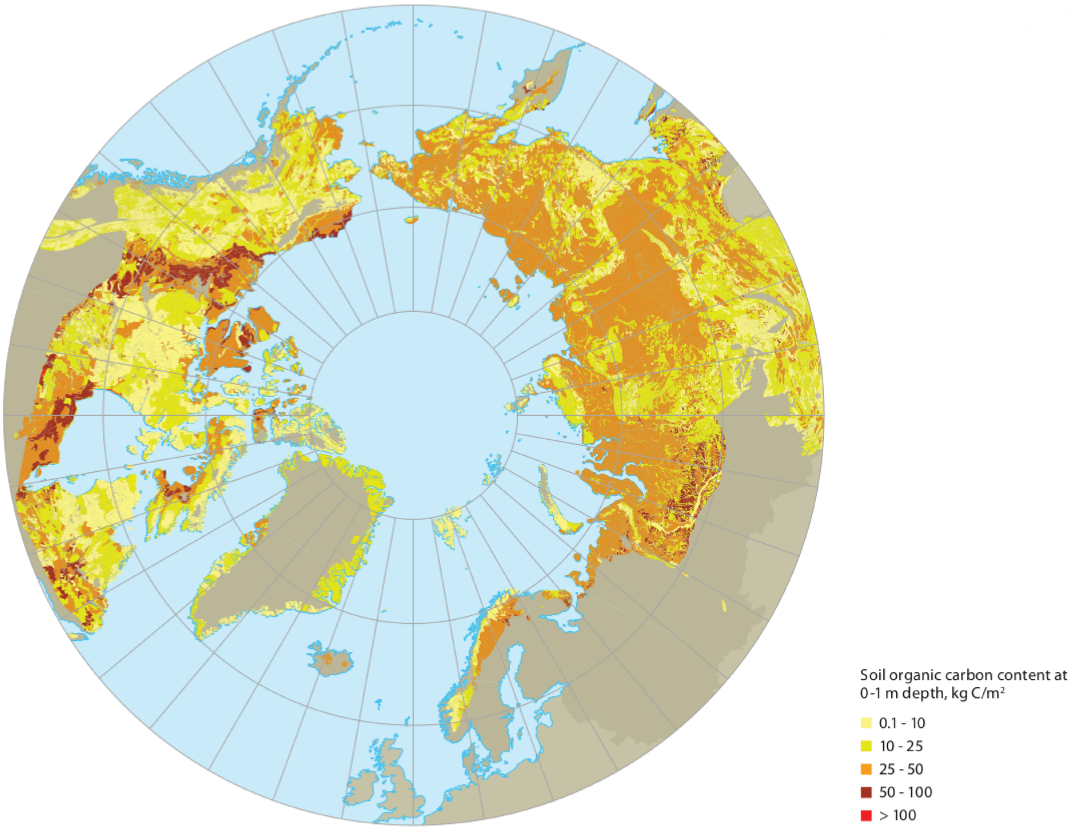

Figure II.11: Soil carbon distribution in upper soil layers (up to 1 m depth). Map derived from Northern Circumpolar Soils Database (Hugelius et al., 2013, 2014), Source: AMAP (2015).

Even though around 87 % of permafrost soils are estimated to be comprised of carbon-poor mineral cryosols (Hugelius et al., 2014), it is assumed, that 45 Pg of carbon from northern permafrost regions could be released to the atmosphere by 2040 and by 2100, up to 288 Pg. Thereby, it is assumed that only 2.3 % of the carbon will be released in the form of CH_4. Due to the increased RF of methane (Section 1.1), those emissions could however make up between a third and a half of the expected climate forcing connected with the elevated carbon emissions AMAP (2015).

A potential limitation could hereby be provided by increased microbial activity of methane-consuming archaea (described more detailed in Section 4.2). Oh et al. (2020) concluded, that the majority of the methane assumed to be produced from accessible permafrost carbon in future scenarios would be consumed by methane-oxidizing bacteria whose activity increases at elevated temperatures. The actual extent of CH_4 emissions associated with exposed carbon pools from permafrost soils remains therefore difficult to assess.

Another indirect influence of permafrost thaw are hydrological changes such as wetland formation and elevated groundwater levels which favour anaerobic decomposition of organic material. Finally, sudden permafrost thaw (e.g. by wildfire events) can cause erosion and soil collapse and promote the formation of thermokarst lakes which are, as mentioned before, a source of CH_4 emissions.

An additional phenomenon that has been occurring during recent years are so called methane craters (see Figure II.12), also known as gas emission craters (GEC). GECs have so far only been detected on the West Siberian peninsulas Yamal and Gydan (Kizyakov et al., 2020; Zolkos et al., 2021). They generally start with the mitigation and build-up of biogenic and thermogenic methane in the permafrost soils, causing a mount to form as the pressure rises. As soon as the pressure exceeds a critical point defined by the density of the upper soil layer, an explosion hurls debris hundreds of metres away (e.g. Dvornikov et al., 2019). GECs could potentially gain more importance in the future in terms of methane emissions (Schuur et al., 2022). The amount of CH_4 released from these craters has however not yet been estimated.

Figure II.12: Gas emission crater discovered in 2014 on the Yamal Peninsula in northern Siberia. Photo: Vladimir Pushkarev.

Even though the impact of those indirect emissions linked to permafrost thaw can currently not be accurately quantified, they are assumed to be able to trigger a positive climate feedback and gain importance in the future with progressing global warming (Schuur et al., 2015).

Recently, Schuur et al. (2022) concluded, that an abrupt “methane bomb” as a consequence of permafrost thaw, releasing exorbitant amounts of CH_4 to the atmosphere over the course of only a few years is currently not supported by either observations or projections. It should however always be expected that unforeseen phenomena related to thawing permafrost (such as the recent occurrence of methane craters) may change the current assess-

ment of indirect or direct methane emissions.

3.2 Sub-sea permafrost

Sub-sea permafrost thaw can influence marine CH_4 emissions in two different ways. On the one hand, similar to the terrestrial effects, declining sub-sea permafrost can expose organic material and thereby increase microbial methane production in the upper layers of the seabed. Additionally, the emissions from gas hydrates in permafrost regions could potentially increase if the overlying permafrost shielding them is destabilised.

In the Arctic Ocean, sub-sea permafrost thaw has for instance been observed in the East Siberian Arctic Shelf (ESAS) and several studies indicate the importance of this region with regards to future methane emissions (e.g. Shakhova et al., 2015, 2019; Wild et al., 2018).

However, it is debatable whether these processes will have a major impact in the near future. The reasons for this are, on the one hand, that sub-sea permafrost responds slowly to global warming since it can take centuries, or even millennia, until the elevated temperatures reach the ocean floor (e.g. Kretschmer et al., 2015; Archer, 2015). Moreover, large quantities of released oceanic CH_4 can either be oxidized in the overlying sediment or in the oxic water column, which was for instance observed in the by Overduin et al. (2015) Laptev Sea. The oxidation processes limiting oceanic methane emissions are further elaborated in Section 4.3 (page 37).

4 Atmospheric methane sinks and marine oxidation

Methane sinks describe processes in which the atmospheric CH_4 molecules are broken down into their individual components, resulting in the formation of other substances such as CO_2 or CO. The methane molecules are hereby either oxidized by free radicals in the atmosphere or by methanotrophic bacteria in the soil. Globally the methane sinks are estimated at around 571 $TgCH_4\ yr^{-1}$, whereby the chemical loss account for approximately 93 % (Saunois et al., 2020).

In marine environments, CH_4 is reduced by anaerobic or aerobic bacteria and also in the oxic water column. These processes are not defined as methane sinks however, since they do not remove CH_4 from the atmosphere, but rather as a restriction on oceanic methane sources.

4.1 Oxidation by free radicals

Free radicals are atoms, molecules or ions with at least one unpaired valence electron and an open electron shell. The availability of unpaired electrons makes free radicals highly chemically reactive with other substances or themselves. Regarding the atmosphere, free radicals mediate oxidation reactions with toxic gases (e.g. CO), tropospheric ozone precursors (e.g. VOCs) and greenhouse gases (e.g. CH_4).

The hydroxyl radical OH is hereby the primary oxidant in the troposphere and lower stratosphere since it is highly reactive with a variety of substances (Levy, 1971; Prather and Spivakovsky, 1990; Crutzen and Zimmermann, 1991; Singh et al., 1995). Its atmospheric lifetime is therefore just around 1 ns. OH is also the dominant removal mechanism for methane and accounts for around 90 % of the total CH_4 sinks (Saunois et al., 2020; Kirschke et al., 2013). The concentration of the hydroxyl radial is therefore the main factor for the atmospheric lifetime of CH_4 (9 ± 0.9 years, Prather et al. (2012)).

The primary source of OH in the troposphere results from the photolysis of ozone. Photolysis represents the absorption of a photon of solar radiation ($h\nu$) with sufficient energy to

break the O_3 molecule. Thereby, electronically excited atomic oxygen is produced:

$$O_3 + h\nu \longrightarrow O_2 + O(^1D).$$

The majority of the excited atomic oxygen subsequently reacts with molecular oxygen (O_2) or nitrogen (N_2) to relinquish the extra energy it carries. However, a small fraction reacts with water vapor to produce hydroxyl:

$$O(^1D) + H_2O \longrightarrow 2\,OH.$$

Since only the excited form of atomic oxygen can react with H_2O to produce OH, the production of hydroxyl is favored by high levels of incident solar radiation and high concentrations of water vapor. In high northern latitudes, the conditions are therefore not optimal for the OH production, especially during the winter months.

In addition to the primary production of OH from water vapour, it can also be recycled by chemical chain reactions including nitrogen monoxide (NO), the hydroperoxyl radical (HO_2) and the methyl peroxy radical (CH_3O_2) which will not be described in detailed here.

The oxidation of methane with the hydroxyl radical begins with the production of the methyl radical CH_3:

$$OH + CH_4 \longrightarrow H_2O + CH_3.$$

The methyl radical then reacts very rapidly with an oxygen molecule to produce a CH_3O_2:

$$CH_3 + O_2 \longrightarrow CH_3O_2.$$

The methyl peroxy radical and all following reaction products undergo additional chemical reactions resulting either in the complete oxidation to CO_2 or the deposition of intermediate products to the Earth's surface.

In addition to the hydroxyl radical, methane is also oxidized by atomic chlorine (Cl) and atomic oxygen ($O(^1D)$). The reaction with tropospheric chlorine results in the formation of hydrogen chloride (HCl) and CH_3:

$$CH_4 + Cl \longrightarrow CH_3 + HCl.$$

HCl is thereby rapidly removed from the atmosphere by wet deposition or acts as a chemical precursor for the chlorine radicals if it reacts with OH. Atomic chlorine represents around 20 to 35 % of stratospheric methane sinks (McCarthy et al., 2003; Rice et al., 2003) and between 0.8 and 2.5 % of tropospheric sinks (Hossaini et al., 2016; Sherwen et al., 2016; Wang et al., 2019, 2021).

Atomic oxygen is predominantly produced by ozone photolysis as described before. Since $O(^1D)$ quickly reacts with N_2, O_2 and Ar it only occurs in very small quantities in the atmosphere. With CH_4, atomic oxygen reacts as following:

$$CH_4 + O(^1D) \xrightarrow{O_2} CH_3 + OH.$$

In the stratosphere, $O(^1D)$ accounts for around 20-40 % of CH_4 sinks (McCarthy et al., 2003; Rice et al., 2003). The total stratospheric loss is estimated by Saunois et al. (2020) at around 31 $TgCH_4\ yr^{-1}$ which would result in 6.2 to 12.4 $TgCH_4\ yr^{-1}$ from atomic oxygen.

4.2 Soil uptake

Methanotrophic organisms in the soil consume methane as a source of energy. In anaerobic environments where methane is produced, certain species of bacteria consume CH_4 before it gets emitted. Other methanotrophic organisms occur in oxic soils and reduce atmo-

spheric CH_4. Under aerobic conditions, CH_4 and oxygen are combined to both CO_2, which is released to the atmosphere and formaldehyde (CH_2O), which is subsequently incorporated into organic compounds. Anaerobic conditions require electron acceptors (e.g. nitrate or sulfate) to oxidize methane.

Certain studies highlight the importance of methane oxidation taking place in mineral cryosols in high northern latitudes as a counterbalance to the existing CH_4 sources in the Arctic, especially in permafrost areas with low soil organic carbon availability, low vegetation cover and low soil moisture (Emmerton et al., 2014; Lau et al., 2015). According to Lau et al. (2015), the active atmospheric methane oxidation in permafrost-affected cryosols increases with rising temperatures due to higher microbial activity. However, the oxidation of methane is hereby strongly dependant on the soil conditions, and increased soil moisture reduces the activity of methanotrophic organisms. It is therefore uncertain whether the microbial methane oxidation in northern tundra landscapes can act as a significant limitation on increasing atmospheric CH_4 concentrations.

Globally, soil oxidation accounts for around 7 % of the total CH_4 sinks (Saunois et al., 2020). Altogether, the total estimated soil sink of Arctic landscapes remains small (up to 1.8 $mgCH_4m^{-2}d^{-1}$ in polar desert soils, Emmerton et al. (2014)) in comparison to the importance of the oxidation by OH in the atmosphere (AMAP, 2015).

4.3 Marine oxidation

Approximately 90 % of the total methane produced in marine sediments, either of biotic or abiotic origin, is consumed by anaerobic oxidation (Reeburgh, 2007). Anaerobic oxidation of CH_4 occurs by a microbial consortium of archaea and sulfate-reducing bacteria between more than 200 m below the seafloor up to the topmost layers of the sediments (Knittel and Boetius, 2009). This consumption of CH_4 produces high concentrations of bicarbonate (HCO_3^-) and hydrogen sulfide (HS^-) and contributes to the dynamic biogeochemistry found at the very top of the sediment column. The general process can be described as by the following reaction:

$$CH_4 + SO_4^{2-} \longrightarrow HCO_3^- + HS^- + H_2O.$$

Since this process both requires methane and sulfate (SO_4^{2-}), the highest anaerobic oxidation of methane rates are found in the sulfate-methane transition zone below the sediment surface (Iversen and Jorgensen, 1985).

The marine sediment therefore acts as a microbial filter for CH_4. Once methane bypasses this anaerobic filter it can subsequently be reduced through the oxidation of aerobic bacteria at the surface of the seabed (Boetius and Wenzhöfer, 2013) or in the oxic water column (Hanson and Hanson, 1996; Murrell, 2010). These processes are described in the following reaction:

$$CH_4 + 2\,O_2 \longrightarrow CO_2 + H_2O.$$

Hereby, aerobic CH_4 oxidation may lower potential methane emissions from marine sources to the atmosphere. However, it leads to other possibly harmful changes in marine environments such as reduced oxygen concentration, enhanced partial pressure of CO_2 as well as lower pH values (Biastoch et al., 2011).

Oxidation processes are however only relevant for dissolved methane. Since the solubility of CH_4 in water is low, this can lead to the formation of bubbles, shown in Figure II.13 on page 38, in areas where the marine sources of methane are very concentrated. These gas bubbles, whose CH_4 concentration account for around 90 % of the gas mixture within the bubble, (Leifer and Patro, 2002), rise quickly through the water column and can therefore be

an important pathway for possible emissions to the atmosphere. The methane concentration inside the gas bubbles can however be reduced by dissolution (McGinnis et al., 2006; Rehder et al., 2009) which is dependant on different factors e.g. the water depth and density and viscosity.

(a) **(b)**

Figure II.13: Left: Rising gas bubbles in the East Siberian Sea. Photo: Tomsk Polytechnic University, Source: The Siberian Times, www.siberiantimes.com. Right: Frozen methane bubbles in Lake Baikal. Photo: Kristina Makeeva, Source: NASA Science, www.science.nasa.gov.

Even though the Arctic Ocean is the world's smallest ocean, its surface accounts for around 85 % of the total Arctic region. As mentioned before (e.g. Chapter I, Section 3.1 and Section 3.2), thawing subsea permafrost as well as diminishing sea-ice promote both the production of oceanic CH_4 and the exchange between sea-surface and atmosphere. The various processes contributing to the oxidation of methane are therefore important limitations of marine CH_4 emissions, especially regarding the progressing Arctic warming.

Conclusion of the chapter

Methane is a powerful greenhouse gas and a primary contributor to the formation of ground-level ozone. The average global concentration of CH_4 in the atmosphere has increased by around 163 % since record keeping began in the early 1980s. This trend of increasing atmospheric CH_4 concentrations is also mirrored in the Arctic.

There are currently a variety of methane sources present in the high northern latitude regions: both natural and anthropogenic, terrestrial and oceanic. Natural emissions are hereby dependant on a variety of environmental conditions and it is anticipated that rising temperatures in the Arctic will cause future increases in regional methane emissions. This is, for instance, due to the thawing of terrestrial and sub-sea permafrost. Different processes reduce CH_4 concentrations in the atmosphere or limit fluxes of methane by oxidizing it before it gets emitted. Some processes, such as oxidation in the high northern latitude soils, could potentially gain more importance with rising temperatures and therefore, compensate increasing emissions in the Arctic.

CHAPTER

III

Estimation of methane sources and sinks

Contents

THE PRODUCTION AND REDUCTION OF METHANE in high northern latitude regions involve numerous different processes which are sensitive to a variety of climatic and environmental conditions, as described in the previous chapter. However, precisely quantifying methane sources and sinks is a key factor to gain an accurate picture of the concentrations of CH_4 in the atmosphere and thus, their impact on global warming. Moreover, it is also critical to accurately estimate present sources and sinks in order to assess their sensitivity to changes in environmental conditions, and thus improving future climate projections.

In this chapter, the two common approaches of estimating CH_4 fluxes and uptake are introduced (Section 1) and, in connection to that, the main objectives of this work are outlined (Section 2).

1 Approaches to estimate methane emissions

Precise estimations of CH_4 emissions are challenging to obtain and are often still connected with high uncertainties. Modelling estimates quantifying methane sources and sinks generally follow two approaches: bottom-up and top-down estimates. Both approaches will be briefly outlined in the following sections.

1.1 Bottom-up approach

Bottom-up approaches are based on a large number of statistical information for source sectors and processes which are subsequently extrapolated to larger spatial scales. Those estimates generally include three different methods to estimate the various emission sources.

A first approach to obtain bottom-up estimates is using process-based land surface models which simulate physical, chemical and biological processes. Those models are often improved by integrating measurement data (e.g. from satellites) and/or data from laboratory experiments and are often used to assess methane emissions from wetlands (e.g., Tang et al., 2010; Poulter et al., 2017) or biomass burning (e.g., van der Werf et al., 2017).

Process-based land surface models require a large number of input variables to represent fundamental biogeochemical processes, which are often based on simplified assumptions. The uncertainty hereby increases with the spatial extent of the models and while they provide useful information on local scales, their use for regional to global scales is rather uncertain. Another source of uncertainty is the sparsity of direct measurements of CH_4 emissions to initialise and parameterise the models.

Another method, usually used to assess and report methane emissions from anthropogenic sources, are emission inventories based on demography and statistics. Hereby, so called activity data, which describes emission-related socio-economic activities, is combined with an emission factor, which quantifies the sources or sinks per unit of activity for a certain region. Inventories provide emissions using different classifications of anthropogenic source categories (e.g. fossil fuel exploitation or livestock farming) and are usually available at the global, regional and national scales (e.g., Janssens-Maenhout et al., 2019; Hoesly et al., 2018).

Uncertainties on this approach are for instance caused by missing, incomplete or unclear information on the reported CH_4 emissions or missing data which does not allow the characterization of individual emissions. Similar to the process-based models, the numerical models used to generate inventories are based on simplifications that do not entirely represent realistic conditions and are therefore another source of uncertainties.

The third method to implement bottom-up approaches is the extrapolation of direct measurements of regional CH_4 fluxes to the regional or global scales. This approach is for instance

used for natural sources such as geological CH_4 emissions (e.g., Etiope et al., 2019).

The measurements made at the local scale may however not be representative for larger scales, which is a source of uncertainties for up-scaling models. Since CH_4 emissions follow complex, non-linear processes and are often dependant on local conditions (e.g. the soil conditions and vegetation), they have a high spatial and temporal variability which can not be fully captured by the models.

Many bottom-up estimates on methane sources and sinks are generated at global scale (e.g. Ridgwell et al., 1999; Riley et al., 2011; Ringeval et al., 2012; Poulter et al., 2017; Etiope et al., 2019). However, several studies have been implemented exclusively for high northern latitude regions. Those include, for instance, estimates on CH_4 fluxes from northern peatlands (Wania et al., 2010), Arctic lakes (Tan et al., 2015) and from boreal and arctic ecosystems (Kuhn et al., 2021). The various data sets from bottom-up estimates on methane sources and sinks are presented in Part II, Chapter V, Section 3 (page 67).

1.2 Top-down approach

As described in the previous section, the uncertainties on bottom-up approaches are various and inevitable. The goal of top-down methods is therefore to improve such estimates, in this case on CH_4 emissions, and decrease their uncertainties. The basis of the top-down approach is called atmospheric inverse modelling. Atmospheric inversion methods are statistical approaches that minimise the differences between simulations and observations (e.g. of atmospheric CH_4 mixing ratios) by adjusting the input variables of numerical atmospheric transport model (e.g. CH_4 fluxes). The hereby assessed optimal values of the input variables are therefore best able to explain the given observations. The approach is schematically shown in Figure III.1, page 42.

The observations which are generally used for those approaches are measurements of atmospheric mixing ratios of methane, which is also the case in this work. It is however possible to include other types of observation in inverse modelling set-ups like for instance satellite measurements of the CH_4 column as well as measurements of co-emitted gases such as ethane (C_2H_6) or of the isotopic composition of methane (e.g. Rice et al., 2016; Thompson et al., 2018; Thanwerdas et al., 2021).

Top-down approaches may provide estimates that are more consistent with available atmospheric observations but sometimes insufficiently differentiate between the different emission sectors. The results obtained by inverse modelling studies are also not independent from the bottom-up approaches that they are based on and which are usually referred to as *prior* estimates. Therefore, sources that are not well constrained by the atmospheric observations will tend to be close to its prior value in the top-down (*posterior*) result.

The first global study using an inverse modelling approach to estimate the spatial distribution of methane emissions was implemented by Houweling et al. (1999). One of the key findings in this study was that the top-down distributions of emissions tended to be reduced in high northern latitudes in comparison to the bottom-up estimates that they were based on. Since then a variety of inverse modelling studies on global CH_4 emissions has been implemented (e.g. Bergamaschi et al., 2009; Kirschke et al., 2013; Houweling et al., 2014; Bruhwiler et al., 2014; Saunois et al., 2016, 2020).

While the top-down studies show relatively good agreement with each other, global posterior estimates all tend to reduce CH_4 emissions in high northern latitudes in comparison to the prior information, implying that the emissions in the bottom-up approaches are too large and inconsistent with observed CH_4 concentration in the atmosphere. Other possible reasons for the decreased posterior methane emissions in high northern latitudes are due

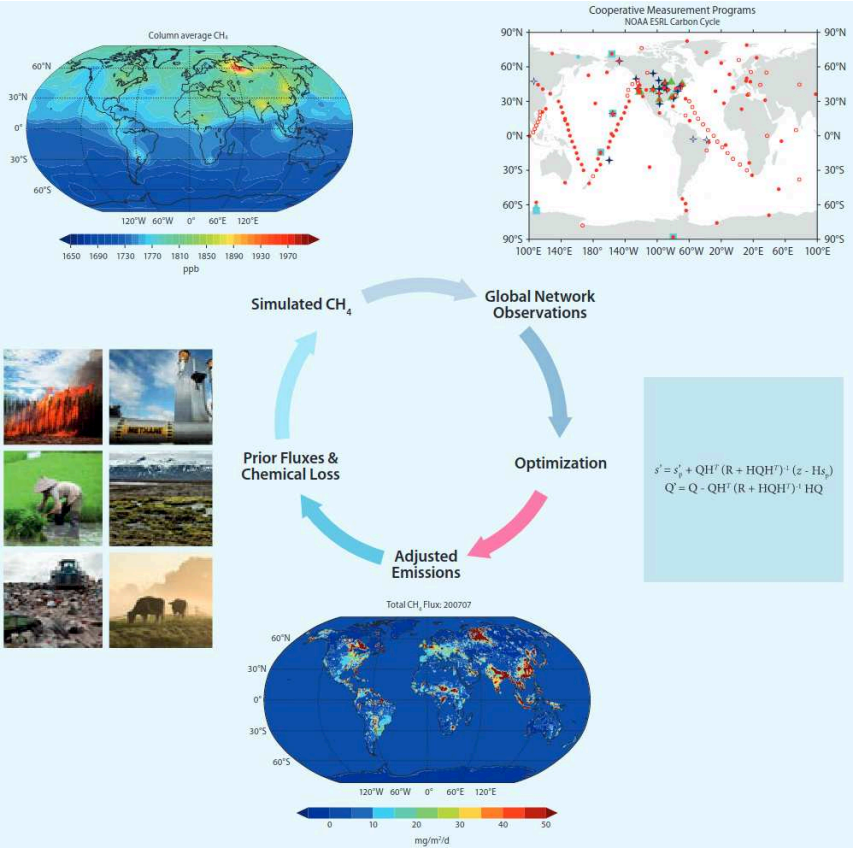

Figure III.1: Schematic illustration of atmospheric inverse modelling approaches. Source: AMAP (2015).

to the lack of observation sites in the Arctic and Sub-Arctic, fewer data points for satellite measurements (further explained in Part II, Chapter V, Section 1), the unequally large cells in models based on Cartesian grids and the low resolution of global models which don't reproduce the Arctic atmosphere properly (Saunois et al., 2017). Moreover, none of the global top-down studies demonstrated an upward trend of CH_4 emissions in the Arctic so far with the longest period (1980 to 2010) being covered by Kirschke et al. (2013).

1.3 Discrepancies of methane emission estimates

Although efforts on the different approaches aiming at quantifying CH_4 sources and sinks are continuously improving, accurate estimates are challenging to obtain. Bottom-up estimates of methane emissions are restrained by inevitable uncertainties, that can only reduced to a certain extent by top-down approaches due to insufficient constraints (e.g. lack of suitable observations). Therefore, different estimates on the various CH_4 sectors show partially large discrepancies.

Globally, bottom-up estimates on the total CH_4 emissions differ from each other by 287 Tg (594 to 881 $TgCH_4$ yr^{-1}) and top-down estimates by 44 Tg (550 to 594 $TgCH_4$ yr^{-1}) for the period between 2008 and 2017 (Saunois et al., 2020). The discrepancies are thereby generally smaller for anthropogenic sources (bottom-up: 349 to 393 $TgCH_4$ yr^{-1}, top-down 336 to 376 $TgCH_4$ yr^{-1}) in comparison to natural sources (bottom up: 245 to 488 $TgCH_4$ yr^{-1}, top-down: 183 to 248 $TgCH_4$ yr^{-1}) and CH_4 sinks (bottom-up: 500 to 798 $TgCH_4$ yr^{-1}, top-down: 501 to 574 $TgCH_4$ yr^{-1}).

Regarding high northern latitudes (between 60 and 90 °N), the total CH_4 emissions be-

tween 2008 and 2017 are hereby estimated almost twice as high by bottom-up models and inventories (around 43 $TgCH_4$ yr^{-1}, ranging between 26 and 72 Tg) than by global top-down approaches (around 22 $TgCH_4$ yr^{-1}, ranging between 17 and 29 Tg).

The discrepancies between the estimated magnitudes of methane emissions from different sources in high northern latitudes obtained by both bottom-up and top-down estimates are illustrated in Figure III.2.

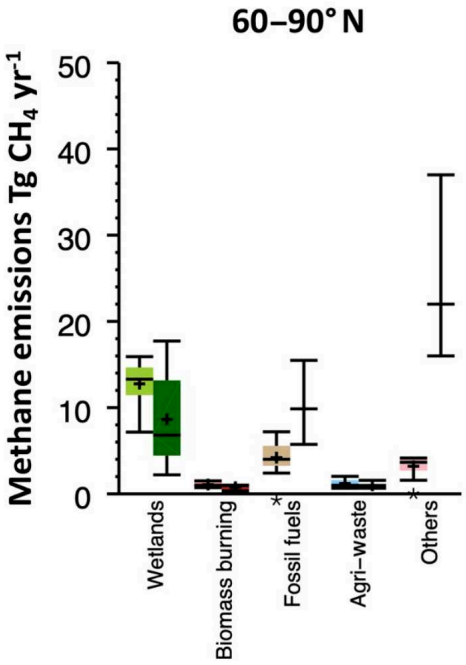

Figure III.2: Methane emissions [$TgCH_4$ yr^{-1}] between 60 and 90 °N from five broad CH_4 sectors for the 2008–2017 decade. Top-down estimates are shown on the left (light-coloured box plots) and bottom-up estimates on the right (dark-coloured box plots). Median value and first and third quartiles are presented in the boxes. The whiskers represent the minimum and maximum values when suspected outliers (shown as stars) are removed. Bottom-up quartiles are not available for bottom-up estimates, except for wetland emissions. Mean values are represented with a "+" symbols. Figure derived from Saunois et al. (2020).

2 Main objective of this work: Estimating CH_4 sources and sinks in the Arctic

In order to obtain precise estimates on CH_4 sources and sinks in high northern latitudes, in this work an inverse modelling approach is used to quantify CH_4 emissions as well as soil uptake in the Arctic during the most recent years. This also includes studying temporal and spatial differences as well as analysing the current limitations in obtaining definite conclusions.

2.1 Relevance of studying methane in the Arctic

Various inverse modelling studies have already been carried out at different regional scales in Arctic regions and with regard to different CH_4 emission sectors and time scales. In the Canadian Arctic, such studies have for instance been implemented by Ishizawa et al. (2018) for the years 2012 to 2015, in which methane emissions from various sources are estimated. A similar study was carried out by Baray et al. (2021) for the years 2010 to 2015. The work by Miller et al. (2016) assesses wetland emissions in North America for the years 2005 and 2006

and Chan et al. (2020) analyzed oil and gas emissions in Western Canada between the years 2010 and 2017. In Finland, Tsuruta et al. (2019) estimated anthropogenic and biospheric methane emissions between the years 2004 to 2014. Natural and anthropogenic methane emissions in high latitude Eurasian regions were estimated by Berchet et al. (2015) for the year 2010 and for Siberian lowlands by Winderlich (2012) for the year 2009. In the pan-Arctic (over 60 °N), Tan et al. (2016) assessed methane fluxes from wetlands and lakes for the year 2005 and Thompson et al. (2017) implemented an inverse modelling study on anthropogenic and natural CH_4 sources between 2005 and 2013 for high northern latitudes above 50 °N.

These works provide useful information on different local scales and emission sectors; it remains however difficult to obtain a complete picture of the CH_4 emissions for the whole Arctic and Sub-Arctic. The Arctic is generally an understudied region and accurate estimates are challenging to acquire, for instance due to the limited availability of observations (Part II, Chapter V, Section 1).

Especially regarding the observed temperature increase during the most recent years and the associated evident environmental consequences, studying the anticipated response of induced methane emissions is essential. This could hereby, on the one hand, be beneficial to better assess the current impact of Arctic methane sources on the global atmospheric CH_4 concentrations but also, to detect trends in either sources or sinks that may continue in the future.

2.2 Outline of the thesis

The main objective of this thesis was to implement top-down approach to estimate different sectors of CH_4 emissions and uptake for the whole Arctic and Sub-Arctic in order to analyze their development during the most recent years. This includes identifying eventual trends in any of the present methane sources or sinks as well as analyzing any occurring seasonal patterns of the different sectors. Additionally, this thesis also aimed to study the capability of the current observations network in the Arctic in detecting anticipated future trends of different CH_4 emission sources.

The theoretical framework to achieve this is presented in Part II. Chapter IV thereby thematises the mathematical concepts and assumptions of atmospheric inverse modelling. In Chapter V, the numerical tools, such as the applied atmospheric transport model, as well as the provided datasets of observations and prior information used in this work are described.

The scientific applications are specified in the Part III. In Chapter VI first of all the provided measurements of atmospheric CH_4 mixing ratios are analyzed. The objective hereby was, on the one hand, to investigate regional differences in the atmospheric CH_4 concentrations and also to determine whether the observations alone allow conclusions to be drawn about regional methane sources. Following this analysis were three main questions:

Question 1: *Is the current observation network of stationary measurement sites in the Arctic nations able to adequately constrain different sectors of CH_4 sources and sinks?*

Question 2: *What information can be derived about seasonal patterns and trends of CH_4 sources and sinks between the years 2008 and 2019 in different parts of the Arctic?*

Since these two questions are interrelated, they are both discussed in Chapter VII. Hereby, an inverse modelling approach is performed with the specific parameters, assumptions and general outline explained in detail in this chapter. The analysis of the obtained results led to the specification of the following question:

Question 3: *To which extent are future increases of CH_4 emissions in the form of an Arctic "methane bomb" accurately detected by the current network of observation sites, and what improvements can hereby be achieved by a hypothetically extended network?*

This will be discussed in Chapter VIII. In order to address this issue, different scenarios of possible future CH_4 emissions are simulated and their detectability is analyzed.

Part II

Material and methods

CHAPTER

IV

The inverse problem in atmospheric science

Contents

THE APPROACH OF ATMOSPHERIC INVERSE MODELLING was briefly introduced in Part I, Chapter II, Section 1.2. In atmospheric science, the term *atmospheric inverse problem* describes a statistical approach used to trace atmospheric measurements of certain trace gases back to the magnitude and patterns of fluxes (e.g. emissions and uptake) of these gases.

The main mathematical concepts leading to the solution of the atmospheric inverse problem are explained in the following chapter. In Section 1, the theoretical basis of atmospheric inverse problems is explained as well as the mathematical assumptions used for solving them. In Section 2 the different methods to solve atmospheric inverse problems are explained and Section 3 details the challenges of obtaining suitable uncertainty estimates.

1 General understanding of inverse problems

Atmospheric inverse modelling approaches are based on the notion of an inverse problem. Inverse problems, which are not only present in atmospheric science but also in many other fields, can be defined as the reverse of a forward problem.

Forward problems (also called modelization, simulation or direct problems) seek to determine the consequences of a certain cause, for instance predicting the values of a physical quantity by using an appropriate numerical model, based on a certain knowledge on the state of the system and some physical and numerical approximations and assumptions. As opposed to that, inverse problems aim at tracing the consequences back to the causes based on the notion of observable quantities. Inverse problems do therefore not necessarily have unique and stable solutions, in fact the number of solutions can be infinite. This is the case for atmospheric problems, as the atmosphere integrates the signals, as illustrated in Figure IV.1.

Because of this, when approaching inverse problems, it is necessary to regularise the problem and provide additional constraints in order to obtain a realistic solution out of the ensemble of possible solutions. Such constraints can, for instance, be provided by prior information on the subject.

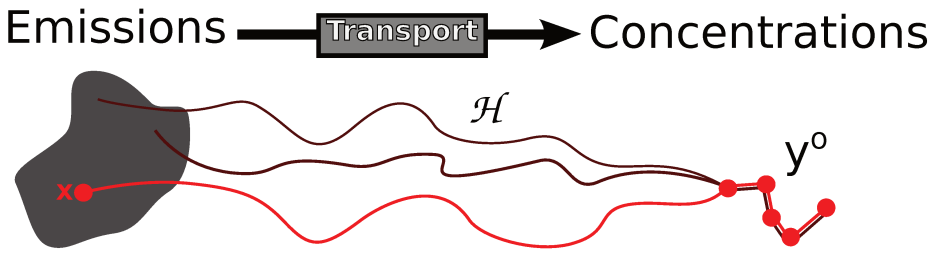

Figure IV.1: Illustration of an integrating atmosphere. The true state of emissions is x and is linked to concentrations y^0 through transport $\mathcal{H}$ by the red trajectory. Nevertheless, all the states shown in the grey area lead to the same concentrations as the truth through transport (of which two examples are shown in brown).

In this work, the specific inverse problem is the estimation of methane sources and sinks at a given regional scale so as to explain the observed atmospheric CH_4 mixing ratios in that area.

1.1 Bayes' formula

The basis for solving atmospheric inverse problems is usually provided by Bayes' theorem (Tarantola, 2005). Hereby, an unknown state x is inferred using observed data y. Since the

observations $\mathbf{y}$ are in general not direct measurements of the state variables $\mathbf{x}$, the relation between the state of the system and observations to be assimilated can be formulated as:

$$\mathbf{y} = \mathcal{H}(\mathbf{x}) + \epsilon. \tag{IV.1}$$

The observation operator $\mathcal{H}$ depicts operations needed to map the state space into the observation space. The term ϵ accounts for the errors in both the observation operator and the observation themselves.

In order to obtain the estimation of the state, the probability density function (pdf) of the variable $\mathbf{x}$ given the observation $\mathbf{y}$ is calculated using the Bayesian probability theory:

$$p(\mathbf{x}|\mathbf{y}) = \frac{p(\mathbf{y}|\mathbf{x})p(\mathbf{x})}{p(\mathbf{y})}. \tag{IV.2}$$

With regard to the atmospheric inverse problem in this work, the state $\mathbf{x}$ refers to the methane sources and sinks to be optimized whereas $\mathbf{y}$ contains observations on atmospheric CH_4 concentrations. The different components of the Bayesian formula can therefore be identified as follows:

- $p(\mathbf{x}|\mathbf{y})$ is the conditional posterior pdf. It gives the probability of a state $\mathbf{x}$ under the given observations.
- $p(\mathbf{y}|\mathbf{x})$ is the conditional pdf of the observation vector $\mathbf{y}$ under a given state, called a likelihood function.
- $p(\mathbf{x})$ is the pdf of the prior state. It is the best estimate of $\mathbf{x}$ before the observations are taken into account.
- $p(\mathbf{y})$ is the pdf of the observations. Since it is independent from the state $\mathbf{x}$ it is a constant and is discarded when solving Bayes' problem.

The main advantage of the Bayesian formalism is that it offers robust results with a relatively small number of observations compared to the number of unknowns in the system by incorporating multiple pieces of information about the system.

1.2 Gaussian assumption

In the context of atmospheric inversions, it is common to use the Gaussian assumption associated with the error estimations. This assumption is suggested by the application of the central limit theorem, which states that the sum of a large number of identical random variables follows a Gaussian (or normal) distribution. In the case of atmospheric transport and chemistry, errors are often caused by a large number of more or less unrelated phenomena which is the reason for the choice of a normal distribution. In this case, the *pdf*s $p(\mathbf{y}|\mathbf{x})$ and $p(\mathbf{x})$ can be fully described by their average and covariance matrices. Similarly, as a product of the two former Gaussian *pdf*s, the so-called posterior *pdf* $p(\mathbf{x}|\mathbf{y})$ is also Gaussian and can be described by its average, corresponding to the optimal posterior state, and its covariance matrix (see Figure IV.2, page 52 for an illustrations and Sect. 2 for details on the notations).

The Gaussian hypothesis is generally used for atmospheric inverse modelling approaches even though there are associated issues when using this assumption. For instance, the Gaussian representation can result in negative estimates for physical quantities which only allow for positive values. Past studies proposed alternative distributions to fix this limitation (e.g. Ganesan et al., 2014; Houweling et al., 2014).

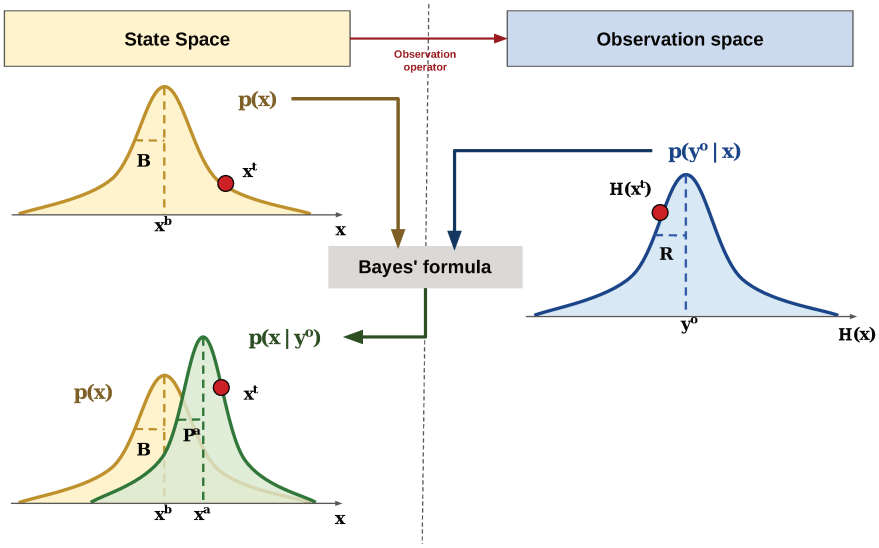

Figure IV.2: Schematic representation of the compilation of the information available through Bayes' formula in order to estimate the solution of the inverse problem. With the Gaussian assumption, the *pdf*s $p(\mathbf{y^o}|\mathbf{x})$ and $p(\mathbf{x})$ are fully described by their averages (respectively $\mathbf{y^0}$ and $\mathbf{x^b}$) and covariance matrices (respectively $\mathbf{R}$ and $\mathbf{B}$); so can $p(\mathbf{x}|\mathbf{y})$, it average being $\mathbf{x^a}$ and its covariance matrix being $\mathbf{P^a}$. From Thanwerdas (2021).

However, since this assumption facilitates finding the solution of the inverse problem, is easily applicable to Bayes' formula and also decreases the time of calculation, it is used for the majority of inverse modelling studies, including this work.

2 Methods to solve the atmospheric inverse problem

There are principally three ways to solve inverse problems in atmospheric sciences: the variational method, the ensemble method and the analytical method with the latter being used in this work. Since the other two methods represent nonetheless important approaches, they will be briefly described here for the sake of completeness.

The mathematical terms of the parameters are explained beforehand as they are common to the three approaches, which are mathematically equivalent. Thereby, $\mathbb{R}^N$ refers to the state space and $\mathbb{R}^M$ to the observation space.

- $\mathbf{x}$: is a *state vector* with $\mathbf{x} \in \mathbb{R}^N$. $\mathbf{x^b}$ refers to the prior state (*prior state vector*), $\mathbf{x^a}$ to the posterior state (*posterior state vector*).
- $\mathbf{B}$: is the *prior error covariance matrix* with $\mathbf{B} \in \mathbb{R}^{N\times N}$. The elements of this matrix describe the uncertainties on the prior state.
- $\mathbf{P}$: is the *posterior error covariance matrix* with $\mathbf{P} \in \mathbb{R}^{N\times N}$. The elements of this matrix describe the uncertainties on the posterior state.
- $\mathbf{y^o}$: is the *observation vector* with $\mathbf{y^o} \in \mathbb{R}^M$.
- $\mathbf{R}$: is the *observation error covariance matrix* with $\mathbf{R} \in \mathbb{R}^{M\times M}$. The elements of this matrix describe the uncertainties on the observations as well as modelling-related uncertainties.
- $\mathcal{H}$ is the *observation operator* which links the state to the observation space ($\mathcal{H} : \mathbb{R}^N \rightarrow \mathbb{R}^M$). It is represented by its Jacobian matrix $\mathbf{H}$ whenever linear.

2.1 Analytical method

The algebraic solution of the Gaussian Bayesian problem is called analytical inversion. When the observation operator $\mathcal{H}$ is assumed to be linear, it equals its Jacobian matrix $\mathbf{H}$ and the posterior state $\mathbf{x^a}$ and error covariance matrix $\mathbf{P}$ can explicitly be written as matrix products:

$$\begin{cases} \mathbf{x^a} &= \mathbf{x^b} + \mathbf{K}(\mathbf{y^o} - \mathbf{H}\mathbf{x^b}) \\ \mathbf{P} &= \mathbf{B} - \mathbf{K}\mathbf{H}\mathbf{B} \end{cases} \text{ or } \begin{cases} \mathbf{x^a} &= \mathbf{x^b} + (\mathbf{H}^T\mathbf{R}^{-1}\mathbf{H} + \mathbf{B}^{-1})^{-1}\mathbf{H}^T(\mathbf{y^o} - \mathbf{H}\mathbf{x^b}) \\ \mathbf{P} &= (\mathbf{H}^T\mathbf{R}^{-1}\mathbf{H} + \mathbf{B}^{-1})^{-1} \end{cases} \tag{IV.3}$$

with $\mathbf{K}$ the Kalman gain matrix: $\mathbf{K} = \mathbf{B}\mathbf{H}^T(\mathbf{R} + \mathbf{H}\mathbf{B}\mathbf{H}^T)^{-1}$

In our context, the state vector $\mathbf{x^b}$ refers to the prior state of methane emission sources and sinks as well as CH_4 background mixing ratios, whose basis are bottom-up estimates (described more detailed in Chapter V, Section 3), and the matching uncertainties on those prior estimates are given in $\mathbf{B}$. The observation vector $\mathbf{y^o}$ contains the measurements of atmospheric CH_4 mixing ratios and the error covariance matrix $\mathbf{R}$ the uncertainties on them, correspondingly. In addition to that, $\mathbf{R}$ also contains uncertainties related to the modelling of simulated CH_4 mixing ratios (explained in Section 3.1.2).

As mentioned before, the observation operator $\mathbf{H}$ maps the parameters from the state space to the observation space. Here, the elements of $\mathbf{H}$ are given by simulated CH_4 mixing ratios, which are obtained based on the prior emission and uptake estimates and an atmospheric transport model (Section 2). The assumption that the observation operator is linear is justified under condition that only CH_4 emissions and soil uptake and transport are taken into account. Chemical reactions with free radicals in the atmosphere are neglected since the air masses in the studied domain change rather quickly (up to 2 months) compared to the lifetime of CH_4 molecules (≈9 years).

The Kalman gain matrix $\mathbf{K}$ can be understood as the gain that each measurement contributes to the estimation of the state, or, in other words, how much weight is attributed to the observations. If the confidence in the observations is high relative to the confidence in the state, the Kalman gain moves towards 1 ($\mathbf{R} \to 0 : \mathbf{K} \to 1$). Conversely, $\mathbf{K}$ moves toward zero if the confidence in the state is high relative to the confidence in the observations ($\mathbf{B} \to 0 : \mathbf{K} \to 0$) and the estimated posterior state $\mathbf{x^a}$ will be closer to the prior state $\mathbf{x^b}$. Thus, the confidence in both state and observations have a large influence on the posterior results. The corresponding error covariance matrices $\mathbf{B}$ and $\mathbf{R}$ must therefore be carefully defined to avoid inaccurate estimations. Methods to define the uncertainties will be further described in Section 3.

The feasibility of the computation of the Kalman gain matrix is however one of the drawbacks of analytical inversion implementations. Depending on which set of equations in Eq. IV.3 is chosen, those matrices either have the size of the observation vector (M × M, equations on the left) or the size of the state vector (N × N, equations on the right). Therefore, if the dimensions of both the observation and the state spaces are very high, which is the case in many inversion set-ups, the explicit computation of the matrix products and inverse matrices can not be performed with reasonable computing resources.

Another computational limitation for analytical inversions is obtaining the matrix $\mathbf{H}$. This can be challenging since the observation operator must be built explicitly. This may require considerable computing time depending on the dimension of the problem. If the observation operator $\mathbf{H}$ is built beforehand, this method is simple to apply and its computational cost is

relatively low in comparison to other approaches.

One of the advantages of analytical inversions is that it allows for an easy computation of the uncertainties on the obtained optimal solution, given by the posterior error covariance matrix $\mathbf{P}$. In other words, these uncertainty estimates show how much confidence we can have in the posterior state.

2.2 Ensemble method

Ensemble methods are commonly used to address high-dimensional problems which are, for instance, computationally too complex to apply analytical approaches. Among the ensemble methods are the Ensemble Kalman Filter or smoothing methods.

Hereby, the observations are assimilated sequentially in order to reduce the dimension of the observation space and to simplify the computation of the matrix products and inverse matrices. The whole inversion time window is processed step by step with a smaller running computation window that includes a manageable number of observations. This smaller window is then gradually moved from the beginning to the end of the whole time window.

Thereby, errors are propagated from one iteration of the running window to the next one. This sequential assimilation is however only valid when assuming that the observations for each assimilation window are not correlated with each others.

Matrix products which involve the error covariance matrix $\mathbf{B}$ are approximated by reducing the space of uncertainties to a low-rank representation. This is achieved by using a Monte Carlo ensemble of possible control vectors. The matrix products $\mathbf{HBH}^{\mathrm{T}}$ and $\mathbf{BH}^{\mathrm{T}}$ can therefore be defined as:

$$\begin{cases} \mathbf{HBH}^{\mathrm{T}} & \simeq & \dfrac{1}{m-1}\left(\mathcal{H}(\mathbf{x}_1), \mathcal{H}(\mathbf{x}_2), \ldots, \mathcal{H}(\mathbf{x}_m)\right) \cdot \left(\mathcal{H}(\mathbf{x}_1), \mathcal{H}(\mathbf{x}_2), \ldots, \mathcal{H}(\mathbf{x}_m)\right)^{\mathrm{T}} \\ \mathbf{BH}^{\mathrm{T}} & \simeq & \dfrac{1}{m-1}(\mathbf{x}_1, \mathbf{x}_2, \ldots, \mathbf{x}_m) \cdot \left(\mathcal{H}(\mathbf{x}_1), \mathcal{H}(\mathbf{x}_2), \ldots, \mathcal{H}(\mathbf{x}_m)\right)^{\mathrm{T}} \end{cases} \tag{IV.4}$$

with m being the size of the ensemble.

Subsequently, the inversion can be solved with the analytical approach by the replacement of those matrix products.

The accuracy of the results from ensemble methods can however be limited by the size of the used ensemble (Bocquet, 2011).

2.3 Variational method

The probability density functions $p(\mathbf{x})$ and $p(\mathbf{y^o}|\mathbf{x})$ introduced in Section 1.1 are typically written under Gaussian assumption as, respectively:

$$p(\mathbf{x}) \propto \exp\left(-\frac{1}{2}(\mathbf{x}-\mathbf{x^b})\mathbf{B^{-1}}(\mathbf{x}-\mathbf{x^b})\right) \tag{IV.5}$$

and

$$p(\mathbf{y^o}|\mathbf{x}) \propto \exp\left(-\frac{1}{2}(\mathbf{y^o}-\mathcal{H}(\mathbf{x}))\mathbf{R^{-1}}(\mathbf{y^o}-\mathcal{H}(\mathbf{x}))\right). \tag{IV.6}$$

Following Bayes' theorem and the probability theory of joint distribution and assuming that all error terms are Gaussian, the posterior probability density function $p(\mathbf{x}|\mathbf{y^o})$ is proportional to the product of the two pdfs $p(\mathbf{x})$ and $p(\mathbf{y^o}|\mathbf{x})$:

$$p(\mathbf{x}|\mathbf{y^o}) \propto p(\mathbf{x})p(\mathbf{y^o}|\mathbf{x}) \propto \exp\left(-\frac{1}{2}\mathcal{J}(\mathbf{x})\right) \tag{IV.7}$$

with the so called cost function $\mathcal{J}(\mathbf{x})$ being defined as:

$$\mathcal{J}(\mathbf{x}) = \frac{1}{2}(\mathbf{x}-\mathbf{x^b})^{\mathrm{T}}\mathbf{B}^{-1}(\mathbf{x}-\mathbf{x^b}) + \frac{1}{2}(\mathbf{y^o}-\mathcal{H}(\mathbf{x}))^{\mathrm{T}}\mathbf{R}^{-1}(\mathbf{y^o}-\mathcal{H}(\mathbf{x})). \tag{IV.8}$$

In variational inversions, the solution $\mathbf{x}$ is defined as being the state with the maximum posterior probability $p(\mathbf{x}|\mathbf{y^o})$, which is obtained by minimizing the cost function $\mathcal{J}(\mathbf{x})$.

The variational approach becomes particularly relevant when $\mathcal{H}$ is non-linear. Since the observation operator does not need to be calculated beforehand, the computation does not require complex matrix products and is therefore not limited by the dimensions of the vectors.

However, the error covariance matrices $\mathbf{B}$ and $\mathbf{R}$ still need to be inverted, which potentially prohibits the use of complex matrices. Therefore, $\mathbf{B}$ and $\mathbf{R}$ are often reduced to manageable combinations of simple matrices, e.g. by using (block-)diagonal matrices.

In variational inversions, the minimum of the cost function is numerically estimated by using quasi-Newtonian algorithms which are based on the gradient $\nabla\mathcal{J}_{\mathbf{x}}$ of the cost function. Quasi-Newtonian methods are a group of algorithms designed to compute the minimum of a function iteratively and, in most cases, only a solution approaching the minimum can be obtained. Variational inversions can be computationally intensive, especially in high-dimension problems when a large number of iterations is necessary to reach the minimum of the cost function.

3 Error estimation

Since models are never able to perfectly represent the reality and observations are also subject to uncertainties, errors need to be taken into account when dealing with atmospheric inverse problems. As mentioned before, a poor defined set of error covariance matrices can lead to inaccuracies in the posterior estimations and therefore, the identification and quantification of these errors is an important component in atmospheric inversion implementations.

3.1 Sources of errors

In inverse modelling set-ups, the uncertainties are defined in the error covariance matrices $\mathbf{B}$ and $\mathbf{R}$, as stated previously (see Section 2.1). Subsequently, the different sources leading to errors in the state and observation spaces are described as well as methods to define the elements of these matrices and techniques to evaluate the plausibility of the error estimations.

3.1.1 Errors in the state space

The prior error ϵ^{b} defines the uncertainties on the prior information, which are in our case, uncertainties on the fluxes provided by land-surface models and inventories of CH_4

emissions and soil uptake as well as uncertainties on the atmospheric background mixing ratios. The higher the prior uncertainties are hereby defined, the less confidence there is on the information estimated before the inversion process.

With $\mathbf{x^t}$ the true state (the state of the emissions in reality), the prior error can be defined as:

$$\epsilon^{\mathbf{b}} = \mathbf{x^t} - \mathbf{x^b}. \tag{IV.9}$$

Under the assumption that the bias is zero, the prior error covariance matrix is defined as:

$$\mathbf{B} = \mathbb{E}[(\epsilon^{\mathbf{b}})(\epsilon^{\mathbf{b}})^T] \tag{IV.10}$$

whereby $\mathbb{E}[.]$ is the expectation of a random variable.

The reasons for the uncertainties on the different bottom-up estimates have already been described in section Part I, Chapter II, Section 1.1. Principally, they are due to uncertainties on spatial and temporal distributions as well as the overall magnitude of the emissions with respect to the reality.

A detailed description how the prior error covariance matrices are defined in this work follows in Part III, Chapter VII, Section 3.3.2.2.

3.1.2 Errors in the observation space

The observation error is associated with two different types of error sources: measurement errors ϵ^{μ} and modelling errors $\epsilon^{\mathbf{m}}$.

Measurement errors are generally due to uncertainties associated with the measuring instruments, the operator or the variability of the quantity measured. Those errors are, in most cases, provided by the organization who publishes the corresponding measurement data. They are estimated through rigorous calibration protocols using reference gases with known concentrations injected in the measuring instrument and other quality control procedures.

Modelling errors include a larger set of different error types generated by the discretisation of space and time and by the poor representation of some physical phenomena (e.g., Szénási et al., 2021):

- the representation error ϵ^{ρ} is due to the model having a resolution that is (much) coarser than the scales at which emissions vary and of which the observations are representative.
- the transport error ϵ^{τ} is due to discretisation with sub-grid scale parametrisations, approximations of the fundamental equations of the atmospheric transport and the meteorological fields used as input data for the transport model.
- the transported-emission ϵ^{ϕ} is due to the impact of prior errors in the emission estimates on the simulated CH_4 mixing ratios in the transport model domain.

The total observation error $\epsilon^{\mathbf{o}}$ can thus be defined as:

$$\epsilon^{\mathbf{o}} = \epsilon^{\mu} + \epsilon^{\mathbf{m}} \tag{IV.11}$$

with $\epsilon^{\mathbf{m}} = \epsilon^{\rho} + \epsilon^{\tau} + \epsilon^{\phi}$.

Thus,

$$\mathbf{R} = \mathbb{E}[(\epsilon^{\mathbf{o}})(\epsilon^{\mathbf{o}})^T]. \tag{IV.12}$$

defines the corresponding observation error covariance matrix $\mathbf{R}$

The particular definition of the observation error covariance matrices used in this work can be found in Part III, Chapter VII, Section 3.3.1.2.

3.2 Methods of error estimation

If the uncertainty matrices $\mathbf{B}$ and $\mathbf{R}$ were perfectly quantifiable, atmospheric inversion applications would only face technical problems, e.g. due to computational limits with high dimensional matrices. Defining the uncertainties is, however, a complex issue and a particular field of research within the study of atmospheric inversions.

Certain errors, such as the measurement error, can easily be quantified by calculations. Estimates on the model and prior errors rely on different approaches. Some are based on expert knowledge that includes, for example, the behaviour of atmospheric transport and surface fluxes. This expert knowledge is, for instance, obtained by intensively studying the sensitivity of the transport model to its parameterizations and forcing inputs (e.g., Denning et al., 1999; Ahmadov et al., 2007; Lauvaux et al., 2009; Locatelli et al., 2013) or by comparing prior flux estimates to measured local fluxes (e.g., Chevallier et al., 2006). Some error estimates also rely exclusively on physical considerations (e.g., Bergamaschi et al., 2005, 2010).

Apart from the actual quantification of the different errors, there are also methods designed to assess whether a plausible pair of error covariance matrices ($\mathbf{R}$,$\mathbf{B}$) has been assigned. Among them are the Desroziers scheme (Berchet et al., 2013; Desroziers and Ivanov, 2001), the observation space diagnostics (Berchet et al., 2013; Desroziers et al., 2005) and the maximum likelihood method (Berchet et al., 2013; Michalak et al., 2005). The latter method will be described in detail in Section 3.3.2. Another method is the χ^2 test (Kaminski et al., 2001), which is easy to implement and commonly used in different studies (e.g., Lauvaux et al., 2012; Winiarek et al., 2012; Peylin et al., 2002).

In this study, a Monte-Carlo approach constrained by the criteria of the maximum likelihood method is used for the definition of $\mathbf{B}$ and $\mathbf{R}$. Thereby, a large ensemble of possible posterior states is computed using first-guess tuples of uncertainty matrices with realistic error configurations. Subsequently, the pairs of $\mathbf{B}$ and $\mathbf{R}$ are evaluated given their maximum likelihood and thus, poor error configurations are excluded for the further analysis of the posterior state.

One of the drawbacks when using this method is the extensive amount of memory for the computation of such numerous inversion set-ups. However, in the context of analytical inversions, this approach is easy to implement since the computation time of each posterior state is rather quick and it allows for robust results.

3.3 Methods of evaluating the error covariance matrices

The criteria of the maximum likelihood which, as stated before, is the preferred criteria in this work, is subsequently explained. Besides, the χ^2 method will also be highlighted briefly since this approach was also considered to be used as an evaluation method for the error covariance matrices.

3.3.1 The χ^2 test

This method assumes, that the posterior state vector $\mathbf{x}^{\mathbf{a}}$ should optimally have the statistics of a χ^2 distribution with a mean equal to $d/2$, where d is equal to the number of available measurements. If the pair of error matrices is *well-defined* (in the sense that the assigned

uncertainties are plausible), the χ^2 index should be close to 1. In the context of inverse modelling approaches, χ^2 is defined as:

$$\chi^2(\mathbf{B},\mathbf{R}) = \frac{1}{d}\left[(\mathbf{y^o} - \mathbf{H}(\mathbf{x^a}))^T\mathbf{R}^{-1}(\mathbf{y^o} - \mathbf{H}(\mathbf{x^a})) + (\mathbf{x^a} - \mathbf{x^b})^T\mathbf{B}^{-1}(\mathbf{x^a} - \mathbf{x^b})\right]. \tag{IV.13}$$

While the χ^2 test is a simple method to confirm that a pair of error matrices is not ill-defined, it is not an adequate method to determine the most plausible pairs of matrices. In other words, if the χ^2 index is close to 1, the tuple of $\mathbf{B}$ and $\mathbf{R}$ is not necessarily well-defined; however, if the value is not close to 1, the tuple is certainly ill-defined. Therefore, this method is not the primary choice for the evaluation of the uncertainties in this work.

3.3.2 The maximum likelihood method

In Gaussian assumptions, the likelihood of the observations $\mathbf{y^o}$ for given $\mathbf{B}$ and $\mathbf{R}$ can be defined as (e.g. Michalak et al., 2005):

$$p(\mathbf{y^o}|\mathbf{B},\mathbf{R}) = \frac{e^{-\frac{1}{2}(\mathbf{y^o}-\mathbf{Hx^b})^T(\mathbf{R}+\mathbf{HBH}^T)^{-1}(\mathbf{y^o}-\mathbf{Hx^b})}}{\sqrt{(2\pi)^d|\mathbf{R}+\mathbf{HBH}^T|}}. \tag{IV.14}$$

A proper pair of $\mathbf{B}$ and $\mathbf{R}$ matrices is necessarily a maximum of the likelihood function for the corresponding inversion system (Dee, 1995).

For computational simplification, instead of maximizing the likelihood function, its equivalent logarithm can be maximized, which is the method used in this work. The resulting log-likelihood can be calculated as follows:

$$\ln p(\mathbf{B},\mathbf{R}|\mathbf{y^o},\mathbf{x^b},\mathbf{H}) = -\frac{1}{2}\,\mathrm{Tr}\left(\mathbf{S}_{\mathbf{R},\mathbf{B}}{}^{-1}\mathbf{S}\right) - \frac{1}{2}\ln|\mathbf{S}_{\mathbf{R},\mathbf{B}}| \tag{IV.15}$$

with $\mathbf{S} = (\mathbf{y^o} - \mathbf{Hx^b})(\mathbf{y^o} - \mathbf{Hx^b})^T$ and $\mathbf{S}_{\mathbf{B},\mathbf{R}} = \mathbf{R} + \mathbf{HBH}^T$, $|\cdot|$ is the determinant operator and $\mathrm{Tr}(\cdot)$ is the trace function.

The higher the log-likelihood of a tuple of error covariance matrices is, the more plausible are their assigned uncertainties in comparison to other tuples. The estimation of the log-likelihood provides a robust method to select the most plausible pairs of error covariance matrices with regards to the information provided by the observations and ideal statistics.

CHAPTER

V

The components of an atmospheric inversion

Contents

AFTER THE GENERAL MATHEMATICAL PRINCIPLES AND APPROACHES of atmospheric inverse modelling have elaborated in the previous chapter, the different components to implement such approaches are introduced in the following, with particular emphasis on the specific numerical tools and data sets used in this work. In Section 1, the different ways of performing atmospheric measurements of methane are presented and the stationary network of measurement sites in the Arctic is described. The atmospheric transport model used in this work and the applied methods for obtaining modelled CH_4 concentrations are presented in Section 2. Finally, the specific datasets of prior estimates on methane fluxes and oxidation as well as the computation of CH_4 background mixing ratios are described in Section 2.

1 Atmospheric observations

As stated before, one of the key components for inverse modelling implementations are atmospheric observations. In this work, this refers to measurements of CH_4 mixing ratios from fixed stations in high northern latitude regions.

The different measuring procedures as well as the observation networks used in this work are described in the following.

1.1 Surface observations of CH_4 concentrations

Surface sites allow measurements of atmospheric CH_4 concentrations to be taken on a permanent basis. To carry out the measurements, an air intake is installed at a given point, usually on a mast or tower. This air intake is either directly connected to a measuring instrument or the air is collected in a flask that is later analysed in a laboratory.

1.1.1 In situ and flask measurements

In the context of this study, the atmospheric observations predominantly consist of quasi-continuous in situ measurements of CH_4 mixing ratios and, to a lower extent, discrete flask measurements.

At quasi-continuous in situ measurement stations the air intake is directly connected to a measuring instrument, producing measurements at a high temporal frequency. Quasi-continuous observations are thereby measurements which are taken over a long period of time and provided at defined time-steps (e.g. hourly) but may include isolated gaps, for instance due to technical failures of the measuring device.

Discrete flask measurements are carried out by taking air samples in a special flask, which is subsequently sealed and transported to a location where the methane concentration is analyzed. Discrete measurements samples are obtained less frequently (e.g. several times a month) and not necessarily with equal time intervals.

There are two main technical implementation to analyze the methane concentration of air samples. The first method is based on using gas chromatography coupled to a flame ionisation detector (GC-FID). Gas chromatographs are instruments which separate gas mixtures into their individual components introducing the mixture into stationary phase (so-called columns). The individual gases can subsequently be identified by the specific time it takes them to pass these columns and quantified by using a flame ionisation detector. This method has been developed in the 1960s and, for a long time, was the only way to measure CH_4 concentrations in the air and is still widely used around the world.

The Cavity Ring-Down Spectroscopy (CRDS) method (Crosson, 2008), was likewise developed in the 1960s but not adopted to measure CH_4 concentrations until the 2000s and has since then been used increasingly. This method is based on the measurement of the absorption rate of light passing through an optical cavity filled with the given air sample. This method allows measurements to be obtained at a high frequency and does not require extensive calibrations, which simplifies handling the equipment.

1.1.2 In situ observations network in the Arctic and Sub-Arctic

Carrying out frequent measurements of atmospheric CH_4 concentrations remains challenging. The extremely low temperatures can affect the proper functioning of the measuring devices, which can lead to incorrect measurements or failures of the instruments. Additionally, missing infrastructure (or damaged infrastructure as a consequence of destabilized permafrost) in high northern latitudes can also hinder maintenance work at the measuring towers.

Nevertheless, a network of long-term observation sites has been established in the different Arctic nations. Figure V.1 shows the locations of the measurement stations used in this work, which consist of 35 observation sites providing quasi-continuous hourly measurements as well as 6 observation sites with discrete measurements of methane mixing ratios.

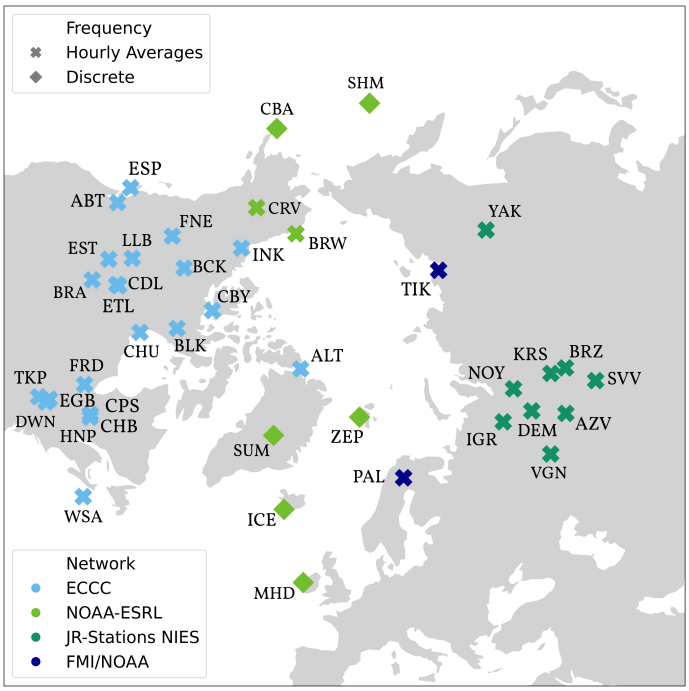

Figure V.1: Observations network used in this work. Crosses indicate quasi-continuous, diamonds discrete measurements. Different network operators are marked with different colours.

The stations are located in seven out of the eight Arctic nations: Canada, Russia, Finland, Norway, Iceland, Greenland and the USA. One additional site in Ireland is used to constrain air masses from the Atlantic Ocean.

The measurement sites are operated by Environment and Climate Change Canada (ECCC), the Japan–Russia Siberian Tall Tower Inland Observation Network (JR-STATIONS from NIES; Sasakawa et al., 2010), the National Oceanic and Atmospheric Administration Earth System

Research Laboratories (NOAA-ESRL; Dlugokencky et al., 2020) and the Finnish Meteorological Institute (FMI; Hatakka et al., 2003; Aalto et al., 2007).

In the North American Arctic, the first continuous measurement towers were established in the late 1980s: measurement data from Barrow (BRW, operated by NOAA-ESRL) in Alaska is available from 1986 and at Alert (ALT, operated by ECCC) in Nunavut, Canada from 1988. The first continuous measurement data in Eurasia is available since 2004 from Pallas (PAL, operated by FMI) in Finland and, respectively, since 2005 from three JR-stations in Siberia (IGR, NOY, KRS).

Discrete measurements of CH_4 concentrations in the Arctic were already carried out since the mid 1980s, starting in Cold Bay (CBA, 1983) and Shemya Island (SHM, 1985), both located in the USA and operated by NOAA-ESRL.

Here, we want to focus on more recent years. By the time this work was implemented, measurement data of atmospheric CH_4 concentrations from the given network was at most available until the end of 2019. A more detailed description of the measurement sites including their location, elevation, time period covered and a short description of their environmental characteristics can be found in Appendix D, Table D.1, page 184.

1.2 Additional measurements of atmospheric CH_4

One of the disadvantages of fixed observation sites is that methane mixing ratios are measured exclusively at a specific point and height. Therefore, besides the permanently installed surface observations sites, measurements of CH_4 concentrations can also be realized by satellite measurements or various types of mobile measurement campaigns. Even though those observations are not explicitly used in this work, they will briefly be described.

1.2.1 Satellite measurements

In situ and flask measurement of CH_4 mixing ratios are spatially limited. An approach to address this issue is obtaining measurements from space using satellites, which are able to cover large areas within a reasonable period of time.

Satellites measurements use remote sensing to measure CH_4 columns in the atmosphere. Remote sensing is an indirect measurement of atmospheric CH_4 columns that uses the ability of methane to absorb specific electromagnetic wavelengths. By analyzing the light spectrum emitted or reflected from the Earth's surface, it is possible to deduce the amount of CH_4 present in the path of this radiation.

The first satellite, ENVISAT (ENVIronment SATellite), used for measuring atmospheric CH_4 columns was launched in 2002 (Buchwitz et al., 2005; Frankenberg et al., 2005). Since then, several satellites have been launched by multiple operators using different instruments, e.g. GOSAT (Greenhouse gases Observing SATellite) launched in 2009 (Parker et al., 2020) and GOSAT 2 in 2018 (Suto et al., 2021).

Even though accuracy and resolution continue to increase due to improved measurement techniques, the use of satellite data in high northern latitudes remains limited. The measurement technique currently used for satellite measurements is not adequate for decreased levels of light and therefore does not provide continuous measurements under those conditions. This is a particular disadvantage in high-latitude regions during the polar nights. This is illustrated in Figure V.2 (page 63), where satellite observations of atmospheric CH_4 during the winter month from the measurement device TROPOMI (TROPOspheric Monitoring Instrument) are shown.

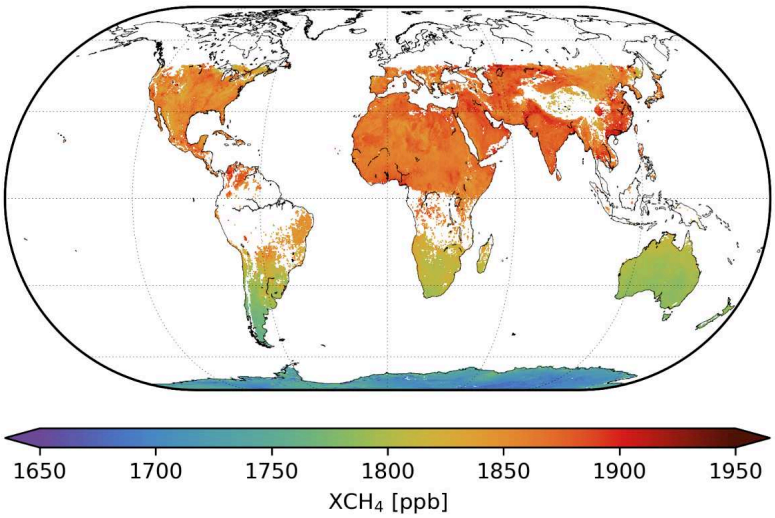

Figure V.2: Global observations of CH_4 from November 28, 2018 to January 16, 2019. The satellite (Sentinel-5P) is hereby operated by the European Space Agency (ESA) with the measurement device TROPOMI. Source: Hasekamp et al. (2022)

Another limiting factor is the solar zenith angle (SOZ). The SOZ is, amongst other factors, dependant on the latitude. In the Arctic, SOZ above 50 °are common (Pegau and Paulson, 2001), however, the SOZ may well be larger, for instance depending on the time of day and season (e.g. Shupe and Intrieri, 2004). For the use of satellite measurements, data points with solar zenith angles below 70 °are often filtered out because of measurements uncertainties from the high signal-to-noise ratio (described e.g. by Hu et al., 2016), which excludes a share of observations from high northern latitude regions. Finally, satellite observations perform best with when the surface albedo is high (e.g. Hasekamp et al., 2022). As discussed in Part I, Chapter I, Section 3.1 a large share of the Arctic is made up by the ocean with decreasing sea ice extent greatly reducing the surface albedo in that area.

Satellite measurements are therefore not suitable in the context of this work. Nevertheless, studies using measurement data from satellites for inverse modelling approaches in high northern latitudes have already successfully been implemented, either to better constrain the area or for comparing them to inverse modelling approaches with in situ measurements (e.g. Baray et al., 2021; Aalto et al., 2020).

1.2.2 Mobile measurement campaigns

Mobile measurements campaigns of CH_4 concentrations include a variety of approaches designed to tackle particular issues, using for instance different instruments for air sampling and measuring, means of transportation and covering different temporal and spatial extents. Mobile measurements are, amongst other things, useful to measure the CH_4 mixing ratios emitted from a specific source or event.

In the Arctic, those campaigns are especially interesting because of the before mentioned limitations in carrying out measurements from in situ stations as well as obtaining satellite data. Since methane emissions can have a high spatial variability at local scales in high northern latitudes, mobile campaigns are beneficial to better quantify the local differences.

Different campaigns including mobile measurements have been carried out during recent years. Those studies include ship-borne observations from expeditions in the Arctic Ocean (e.g. Pisso et al., 2016; Yu et al., 2015; Pankratova et al., 2022; Thornton et al., 2016; Berchet et al., 2020), ground-based measurements, e.g. by train (Skorokhod et al., 2017), as well as

air-borne measurements by plane, (Paris et al., 2008, 2010) and balloon measurements.

Air-borne measurements are additionally important to gain insights into the vertical profiles of CH_4 concentrations. A more recent method is hereby the AirCore technique with balloon sampling (Membrive et al., 2017; Karion et al., 2010) which allows taking samples up to approximately 30 km altitude. In the Arctic Circle those measurements were for instance carried out during the MAGIC 2021 campaign in Kiruna (see Part III, Chapter VI, Section 2.3).

Concerning this work, mobile measurements are not used for the inverse modelling implementation, mainly because they cover time periods much shorter than we intend to address in this study. Data from mobile campaigns are, however, sometimes used for verification of the obtained posterior CH_4 concentrations (e.g. Thompson et al., 2017)

2 Modelled CH_4 mixing ratios

The second component of atmospheric inverse modelling approaches to be discussed in this work are simulated quantities that are an equivalent to the observed quantities, in this case CH_4 mixing ratios. Those simulated methane concentrations are obtained by using atmospheric transport models, of which there are principally two different types: Eulerian and Lagrangian atmospheric transport models.

In this work, only the latter type of model is used to determine the modelled equivalents of the measured CH_4 concentrations, which is why the function of Eulerian models is not discussed here. The use of Lagrangian transport models in high northern latitudes for inverse modelling studies on methane emission is common and has for instance been applied by Chan et al. (2020), Thompson et al. (2017) or Ishizawa et al. (2018).

2.1 Lagrangian particle dispersion models

Lagrangian particle dispersion models (LPDMs) are used to simulate the transport and turbulent mixing of gases and aerosols in the atmosphere. Amongst them, the following are for example classically used for inversion studies: the Stochastic Time-Inverted Lagrangian Transport (STILT) model (Lin et al., 2003), the Numerical Atmospheric dispersion Modelling Environment (NAME) model (Jones et al., 2007), the Hybrid Single-Particle Lagrangian Integrated Trajectory (HYSPLIT) model (Stein et al., 2015) and the FLEXible PARTicle (FLEXPART) model (Stohl et al., 1998, 2005; Pisso et al., 2019a) which is used in this work.

LPDMs are stochastic models that simulate numerous trajectories for a large number of infinitesimally small virtual air parcels, called particles. Those particles do not represent real aerosol particles but rather minuscule points moving with the ambient flow. Each particle carries a certain mass, which can be, depending on the study the model is used for, influenced by loss and/or production processes (typically atmospheric chemistry, or physical processes such as scavenging for aerosols). The trajectories of the particles display hereby the transport by mean flow as well as turbulent, diffusive transport by unresolved parameterized subgrid-scale transport processes (for instance turbulence or deep convection) and, potentially, gravitational settling.

The criterion to formulate Lagrangian stochastic models that simulate particle trajectories under pre-defined Eulerian pdfs was established by (Thomson, 1987). Most atmospheric particle models used today are based on these theoretical principles introduced in his work.

An essential feature of LPDMs is that they can be run not only forward, but also backward in time. Those simulations should, in theory, be consistent with both the Eulerian flow field and forward calculations from LPDMs. In inversion technical words, this means that

the observation operator is "auto-adjoint", which simplifies the computations of variational inversions in particular. If the models are run forward in time, the point at which the particles are released are called *source*, whereas in backward simulations they are referred to as *receptors*.

One of the advantages of LPDMs is, that, in most applications, their computational cost does not increase substantially with the number of species transported which makes those models efficient for multispecies simulations. However, the computation time increases with the amount of particles used for simulating the trajectories while the statistical error in the model output decreases only with the square root of the particle density. It can therefore be computationally complex to decrease statistical errors. Moreover, the particle density decreases with growing distance from the point where the particles are released. Therefore, while the statistical error is typically low in close proximity to their point of release, the accuracy of the results is reduced with increasing distance. More critically, when computing receptor-based simulations, the computational cost increases linearly with the number of receptors (i.e., observation points); this limits the number of observations one can assimilate using LPDMs.

Another benefits of Lagrangian models is that the models can account for point or line sources (or receptors) at very fine spatial resolution. In combination with their ability to produce simulations backward in time, a common use of LPDMs is to trace back air parcels affecting a specific receptor. This method is used in this work, with the receptors being the observation sites where measurements of CH_4 mixing ratios are carried out (Section 1.1.2) and the backward simulations of an LPDM are used to identify the methane sources contributing to the measured concentrations. As mentioned before, the transport model used in this work is FLEXPART, which will be introduced in the following.

2.2 The Lagrangian transport and dispersion model FLEXPART

FLEXPART is one of the most widely used open-source LPDMs. It is suitable for the simulation of a large range of atmospheric transport processes from local to global scale and can be run forward or backward in time. Apart from transport and turbulent diffusion, the model can also be used for the simulations of first-order chemical reactions, deposition phenomena or radioactive decay of tracers released from point or line as well as 2 or 3 dimensional sources or even filling the whole atmosphere Stohl et al. (1998, 2005).

The first version of FLEXPART, v1, was a further development of the FLEXible TRAjectory model (FLEXTRA) Stohl et al. (1995) and has ever since been developed further with the latest available version being FLEXPART v10.4. (Pisso et al., 2019b), which is the one used in this work.

FLEXPART is an offline model that requires meteorological fields, either analyses or forecasts, as input. The version used in this work, v10.4, can be used with input data from the European Centre for Medium-Range Weather Forecasts (ECMWF) Integrated Forecast System (IFS) and data from the United States National Centers of Environmental Prediction (NCEP) Global Forecast System (GFS). Other FLEXPART model branches have been developed for input data from various limited-area models.

In this work, we use, ECMWF Reanalysis v5 (ERA5 Hittmeir et al., 2018) with 3-hourly intervals and 60 vertical layers and a $1^\circ \times 1^\circ$horizontal resolution. ECMWF data are hereby retrieved and formatted using the FLEX-extract toolbox (Tipka et al., 2020).

2.3 Footprint method

Obtaining modelled concentrations of trace gases using LPDMs is based on the source-receptor relationship, in other words, the sensitivity of a receptor element r to a source s. When dealing with linear cases, including atmospheric transport processes like advection, diffusion and convective mixing but also first-order chemical reactions, the source-receptor relationship can be reduced to the expressions r/s and can easily be calculated with any dispersion model $\mathcal{M} : s \rightarrow r$.

Since the sources and receptors usually consist of multiple elements, they can be denoted as vectors $\mathbf{r}$ and $\mathbf{s}$, with J, the number of receptors and I, the number of sources. The source-receptor relationship can therefore be expressed as a matrix, called source-receptor matrix (SRM) (Seibert and Frank, 2004; Wotawa et al., 2003).

The elements $m_{i,j}$ can be expressed as:

$$m_{i,j} = \frac{r_j}{s_i} \tag{V.1}$$

with $i \in [1,I]$ and $j \in [1,J]$ whereby, in the case of gridded data, the temporal and all spatial dimensions are combined into each of these indices.

In this work, the SRM is obtained by simulating the backward trajectories of numerous particles using FLEXPART. The corresponding method is explained in detail by Seibert and Frank (2004).

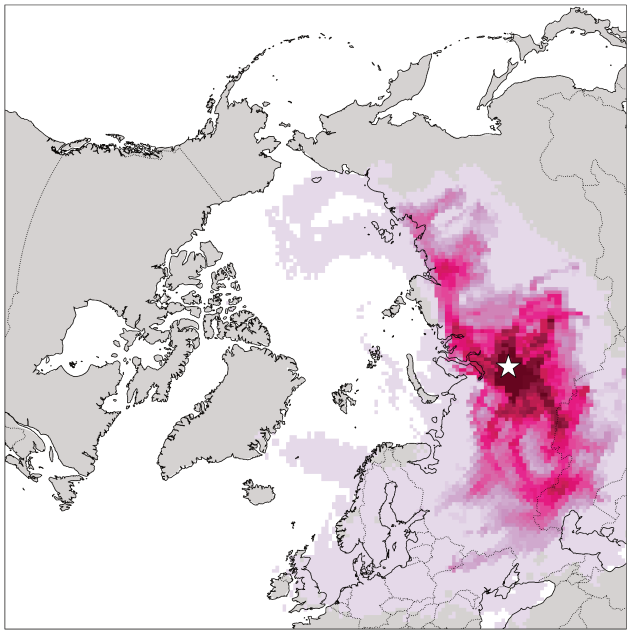

Figure V.3: Exemplary illustration of a footprint for the measurement site Noyabrsk (Russia), indicated with a white star. Darker shades indicate a longer residence time of the particles. Here, the footprint represents the monthly average of the backward trajectories simulations for January 2017.

As mentioned before in Section 2.1, the receptors hereby refer to the locations of observation sites whose measurements are used for the atmospheric inversion. In modelling space, those locations represent point sources with a certain latitude, longitude and altitude. From these receptors, particles are released and followed 10 days backwards in time as the pre-

cision decreases after 10 days due to accumulated transport errors and insufficient number of particles to represent it (Stohl et al., 1995). The number of particles per station and time stamp was hereby chosen to be 2000, to achieve satisfactory accuracy of the results with an acceptable computing time.

By sampling the near-surface residence time of the various backward trajectories of the particles, the SRM of each observation site can subsequently be determined. In atmospheric science, the SRM from backward simulations is also referred to as footprint. An exemplary image of a footprint for a specific measurement site from the surface observation network used in this work (Section 1.1.2) is shown in Figure V.3, page 66.

In the context of this work, these footprints define the connection between the CH_4 sources and soil oxidation discretised in space and time and the change in mixing ratios at the receptor. To finally obtain a time series of CH_4 mixing ratios as an equivalent to the atmospheric observations, a time series of footprints is combined with discretised methane emission estimates, which in this case are datasets of bottom-up estimates which will further be described in Section 3. Figure V.4 shows an exemplary time series of contributions from different methane sources between 2008 and 2020 for one of the observation sites.

An advantage of using this method is that the resulting concentrations at the receptor can be obtained by a simple matrix-vector multiplication. Once the footprints from an observation site are computed, its sensitivity to any emissions source or sink can quickly be obtained, avoiding any further numerical simulations.

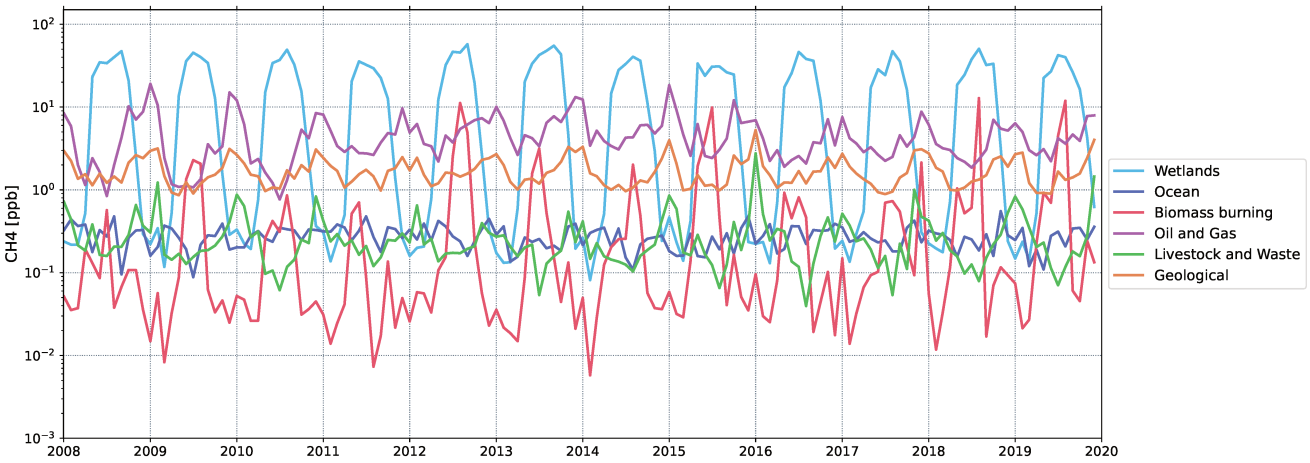

Figure V.4: Time series of monthly CH_4 mixing ratios [ppb] contributed from different sources at the measurement site Abbotsford (Canada) covering 2008 to 2020.

In addition to the simulations of CH_4 mixing ratios as a component of an inverse modelling approach on methane emissions in Arctic regions, FLEXPART has also been used for additional projects in the course of this work. Those are described in detail in Part III, Chapter VI, Section 2.

3 Prior estimates

The final component of atmospheric inverse modelling approaches are the prior information which in this case consist of a set of bottom-up estimates on CH_4 fluxes from different sources as well as the uptake of atmospheric methane by soil oxidation. The specific inventories and model estimates used in this work are introduced in the following section.

For computational costs, in this work only one dataset of prior estimates is used per CH_4 sector for the inversion. Since bottom-up estimates on the same emission source partially greatly vary from each other, using different estimates could hereby potentially be beneficial, e.g. for the verification of the posterior results or to better quantify posterior uncertainties.

3.1 Methane sources

In contrast to the estimates on anthropogenic methane emissions, which are taken from one single database, the natural CH_4 fluxes used in this work are based on a variety of different studies and databases. The emissions are thereby represented by maps of surface fluxes showing the intensity and location of the CH_4 emissions. The different emission sectors used in this study are shown in Figure V.5.

The key features of the prior estimates used in this work are summarized in Table V.1 (page 69) including the type of emissions, their reference and their temporal resolution. Subsequently, in the following sections, the individual CH_4 sectors are described in more detail.

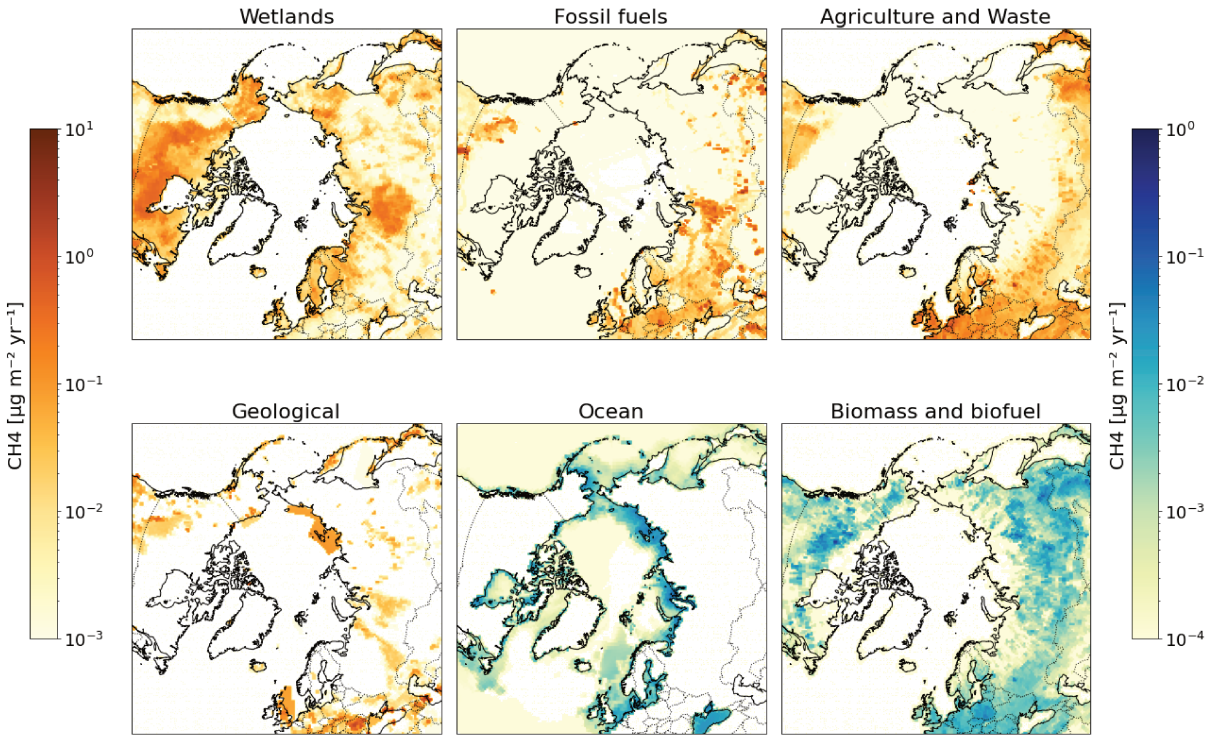

Figure V.5: CH_4 emissions of different sectors for regions above 30 °N. The maps show the average CH_4 fluxes over the period from 2008 to 2019.

3.1.1 Wetland emissions

Methane emissions associated with wetlands are inferred from a monthly climatology calculated from a set of simulations from 11 land-surface models over the period from 2000 to 2012, constrained with remote sensing surface inundation and inventory-based wetland area data (Poulter et al., 2017).

The different continental land-surface models used for obtaining this emission estimate are able to represent many biogeochemical and biophysical processes with varying degrees of complexity. The data set from Poulter et al. (2017) is available at the global scale with a 0.5 °horizontal resolution.

3.1.2 Wildfire emissions

Emissions from natural biomass burning connected with wildfire events are taken from the Global Fire Emission Database (GFED) which is described in details under this address: www.globalfiredata.org/index.html

The 4.1 version used in this work was obtained from combined satellite data on vegetation characteristics, meteorology and fire parameters (van der Werf et al., 2017). The instrument used for the satellites measurement was hereby the Moderate Resolution Imaging Spectroradiometer (MODIS), whose data was subsequently integrated in the CASA (Carnegie-Ames-Stanford Approach) biochemistry model.

The datasets are available until the year 2022 with a 0.25 °spatial and monthly temporal resolution.

Table V.1: *Methane sources and sink taken into account in the prior emissions in this work.*

Type	Source	Reference	Temporal resolution
Natural	Wetlands	Poulter et al., 2017	monthly climatology
	Ocean	Weber et al., 2019	constant
	Geological	Etiope et al., 2019	constant
	Soil Oxidation	Ridgewell et al., 1999	monthly climatology
Combined	Biomass and	GFED4.1	monthly with
	biofuel burning	EDGARv6	interannual variability
Anthropogenic	Mineral oil & gas	EDGARv6	interannual variability
	Waste & Agriculture	EDGARv6	interannual variability

3.1.3 Oceanic emissions

Estimates on oceanic methane sources are taken from the work of Weber et al. (2019). Thereby, machine learning models were used to create emission maps for the surface distribution of methane disequilibrium. Constraints on bubble-driven ebullitive fluxes were additionally used to reduced uncertainties on the total oceanic CH_4 emissions by a factor of three. The corresponding dataset is available at a 0.25 °horizontal resolution

3.1.4 Geological emissions

Geological methane sources are taken from 1 °resolution emissions estimation maps created by Etiope et al. (2019). This map includes the four main categories of natural geological CH_4 emission: onshore hydrocarbon macro-seeps (including mud volcanoes), submarine seeps, diffuse microseepage and geothermal manifestations.

For each of those categories, an inventory of point sources and area sources was developed, including coordinates and estimated CH_4 fluxes. The CH_4 fluxes are hereby determined considering several geological factors that control methane origin and seepage based on published and originally ad hoc developed datasets. In this work, the data set on geological methane sources is hereby scaled at 15 $TgCH_4\ yr^{-1}$ globally.

3.1.5 Anthropogenic methane sources

As prior estimates for the anthropogenic methane sources, the Emissions Database for Global Atmospheric Research (EDGAR) inventory developed by the Joint Research Center (JRC) for the European Commission and the PBL Netherlands Environmental Assessment Agency is used.

The EDGAR database records global anthropogenic emissions derived from international statistics and the best available emission factors. Details on the database can be found under this address: https://edgar.jrc.ec.europa.eu/.

EDGAR provides inventories at a 0.1 °× 0.1 °resolution up to the year 2021 (at the time of writing) as well as emission maps summarized at the regional and country scales. The data is hereby available for around 50 specific industrial, agricultural or economic emissions sectors.

Only some emissions sectors are taken into account in this work since only a limited number of anthropogenic activities causing CH_4 emissions take place in high northern latitudes. Those include activities related to the fossil fuel industry, agricultural activities as well as waste management and biofuel burning.

In this work, the 6.0 version of the EDGAR database is used which provides estimates from 1970 to 2018 (Crippa et al., 2021a).

3.2 Soil oxidation of methane

The soil sink of CH_4 from microbial oxidation is represented as negative emissions. The prior estimate used here is based on the work of Ridgwell et al. (1999), who provided a process-based model for the consumption of atmospheric methane. Thereby, the model incorporates the dominant factors which influence microbial diffusion and oxidation processes in the soil (such as soil temperature and moisture) to determine the spatial distribution and intensity of the soil sink on a global scale.

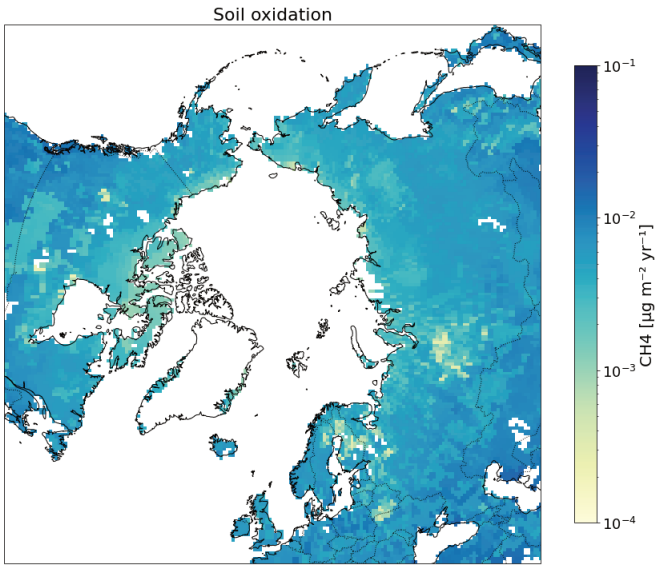

Figure V.6: Mean annual soil oxidation of CH_4 for regions above 30 °N. The uptake is hereby shown on a positive scale.

The estimate by Ridgwell et al. (1999) is provided as a monthly climatology. The corresponding map of soil uptake in high northern latitude regions averaged over one year is shown in Figure V.6.

3.3 Atmospheric background mixing ratios

As described in Section 2, the modelled CH_4 mixing ratios as an equivalent to the observations (Section 1) are obtained by simulating backward trajectories of virtual particles with FLEXPART. Those particles are hereby tracked 10 days backward in time, as outlined before. Methane on the other hand has an atmospheric lifetime considerably longer than this ($\approx$ 9 years, Prather et al. (2012)). Therefore, the simulated contributions of the different CH_4 sources introduced in Section 2.3 only display short-term fluctuations at the receptor. In order to directly compare the modelled CH_4 mixing ratios to the measured ones, the atmospheric background mixing ratios need to be taken into account.

The atmospheric background (also called baseline) is induced by processes occurring at earlier times which are smoothed out by atmospheric mixing. The background usually makes up the dominant fraction of the total atmospheric CH_4 concentrations (in this work up to 99.9 %, see Appendix D, Table D.4, with the remaining fraction being the short-term contribution from the regional CH_4 sources around the observation site.

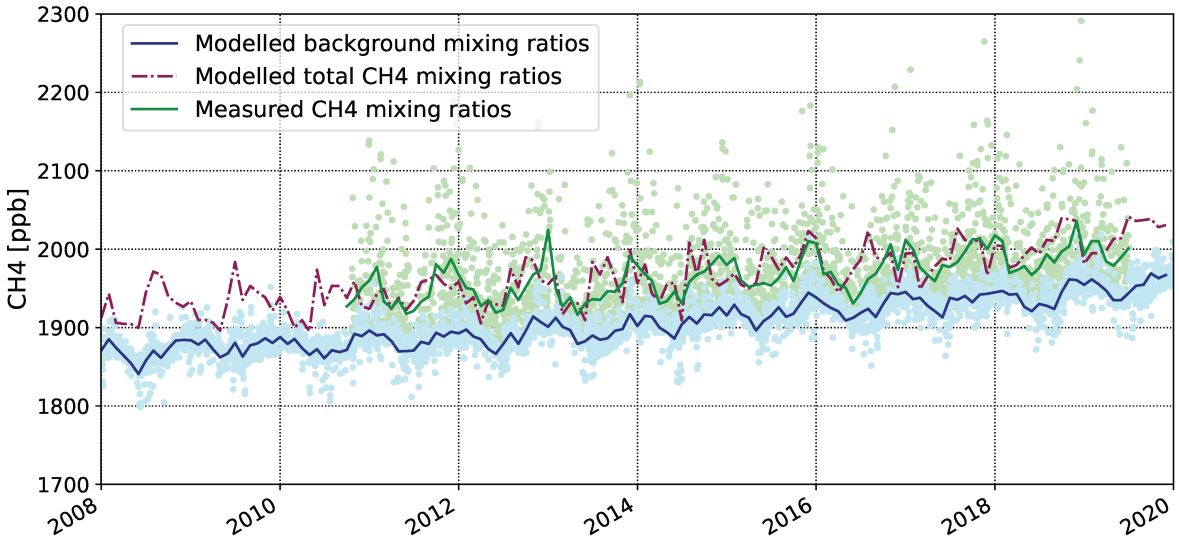

Figure V.7: Measured and modelled CH_4 concentrations [ppb] at the observation site Downsview (Canada) between 2008 and 2020. The blue line displays the background, the green line the observations and the dash-dotted purple line the total modelled CH_4 mixing ratios (monthly averages). The light blue and green dots show the daily averages of background and observations, respectively.

There are different methods for estimating the background mixing ratios. One relatively simple method is to estimate the background directly from the measurements (applied e.g. by Defratyka et al., 2021). In this work, the time series of atmospheric background mixing ratios are calculated by combining a CH_4 concentration field as initial condition with the FLEXPART backward simulations nudged to the available observations of the corresponding measurement site (e.g. Thompson and Stohl, 2014; Groot Zwaaftink et al., 2018; Pisso et al., 2019a). The thus computed background concentrations represent the average of the mixing ratios in the grid cells where each particle trajectory terminated 10 days before the corresponding observation.

The initial CH_4 mixing ratio field used in this work has 60 vertical layers, a 3-hourly temporal and a 0.75 °$\times$0.75 °spatial resolution and was provided by the Copernicus Atmospheric Monitoring Service (CAMS) global reanalysis EAC4 (ECMWF Atmospheric Composition Reanalysis 4, Inness et al., 2019). The numerical implementation for obtaining the CH_4 back-

ground mixing ratios is the Community Inversion Framework (CIF) (CIF; Berchet et al., 2021).

The total modelled CH_4 mixing ratios can finally be obtained by adding the time series of combined short-term contributions from each CH_4 emission source (including in this case also negative contributions from soil oxidation) to the time series of simulated background mixing ratios. Figure V.7 (page 71) gives an example of the computed CH_4 background mixing ratios in relation to the observations and the total modelled mixing ratios.

Part III

Scientific applications

CHAPTER

VI

Characterisation of spatio-temporal patterns in methane concentrations in the Arctic

Contents

PRECEDING THE FULL IMPLEMENTATION of atmospheric inverse modelling aimed at discussing the main scientific questions addressed in the framework of this thesis, we present preliminary studies, as well as studies carried out in parallel to the main focus of the PhD project, concerning the CH_4 spatio-temporal concentration patterns and the Arctic's methane budget in general. The thus obtained conclusions will be presented in this chapter, whereby each study is briefly outlined.

The work presented in Section 1 thereby involves the analysis of atmospheric CH_4 concentrations from selected observation sites in the Arctic in order to investigate whether conclusions about regional methane sources can be drawn from the measurements alone. Section 2 encompasses three less extensive studies on different subjects related to methane emissions in the Arctic, the results of which were obtained from contributions to completed internships as well as the participation in a mobile measurement campaign.

1 Analysis of CH_4 mixing ratios in Arctic regions using in situ observations

1.1 Motivation

In the context of this work, the fundamental aim is to obtain a better understanding about methane emission sources and uptake in Arctic regions. Before this is realized by the implementation of an atmospheric inversion with the prospect of meaningful results, the provided measurement data to be used for the assimilation is analyzed. The objective is hereby on the one hand, to gain an insight about the atmospheric CH_4 concentrations and their variations in that specific region and on the other hand to find out, whether the observations alone (i.e. without assimilation by atmospheric inversion) make it possible to obtain conclusions about the regional methane sources.

The first step of the work consisted in making a selection of measurement sites that show consistent measurements of CH_4 mixing ratios over a long period of time during recent years. The magnitude of the CH_4 concentrations of the selected sites were afterwards compared to each other in order to spot regional differences. Subsequently, the trends of the CH_4 concentrations were analyzed to detect significant increases. Finally, the seasonal cycle of concentrations was studied to discover patterns that could give information about the responsible emission sources.

1.2 Material

In Part II, Chapter V, Section 1.1.2, the whole observations network used in this work for the atmospheric inverse modelling approach is presented. By the time this preliminary analysis was carried out, the available observations were limited to quasi-continuous hourly measurements of CH_4 mixing ratios of 21 stations in Canada (ECCC), 9 stations in Russia (JR-Stations, NIES) and 2 sites in Alaska (NOAA-ESRL) shown in Figure VI.2a.

The focus of this work lies on the most recent years: 2008 to 2019. However, the periods of time covered by observations vary greatly between the different stations and the provided data is not always continuous, as shown in Figure VI.1, page 77.

Therefore, to obtain a robust comparison, a sub-set of the available measurement sites was selected. The period of time to be analysed was chosen as recent as possible to detect the eventual response to the anticipated elevated methane emissions in the Arctic due to rising temperatures. The period with the most continuous CH_4 measurement data available was identified between 2014 and 2017, which is why these years were selected.

Figure VI.1: Continuity of measurement data from the provided in situ observation sites. The percentage gives the ratio between actual and theoretically available hourly measurements.

Since in this context exclusively the CH_4 concentrations in Arctic regions were to be highlighted, observation sited located below 55 °N were discarded.

Finally, a selection of 10 observation sited was defined with relatively good data continuity between the years 2014 and 2017. The selection included 6 sites in Canada, from which 3 are located close to the Arctic Ocean and 2 are continental sites, one coastal station in Alaska and 3 sites in the Siberia. The selected sites are shown in Figure VI.2b

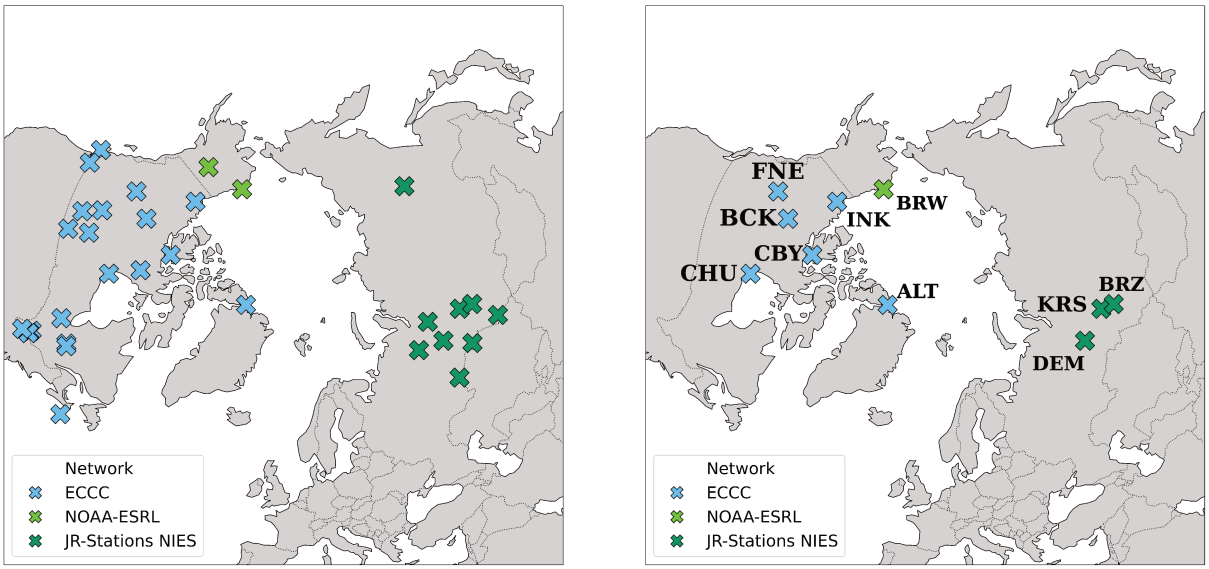

(a) Available **(b)** Selected

Figure VI.2: Provided in situ observations sites for this study. The different operators are marked with different colors.

1.3 Results

1.3.1 Regional comparison

When comparing the CH_4 mixing ratios of the selected observation sites, it is first of all striking that the measured concentrations in Siberia are during all of the four years higher than the observations in Canada and the USA. The average mixing ratios at the Siberian sites have a magnitude of 1969.6 ppb in 2014 and 2000.8 ppb in 2017. At the North American stations, the average mixing ratios over all selected stations are hereby 1918.8 ppb (2014) and 1946.8 ppb (2017), which is a difference of up to 54 ppb. This is detailed in Figure VI.3 where the mean annual mixing ratios for each station are shown. Such large scales gradients could be explained by both local to regional emissions superior in Siberia, or large scale transport patterns advecting cleaner air masses to North America than in Siberia.

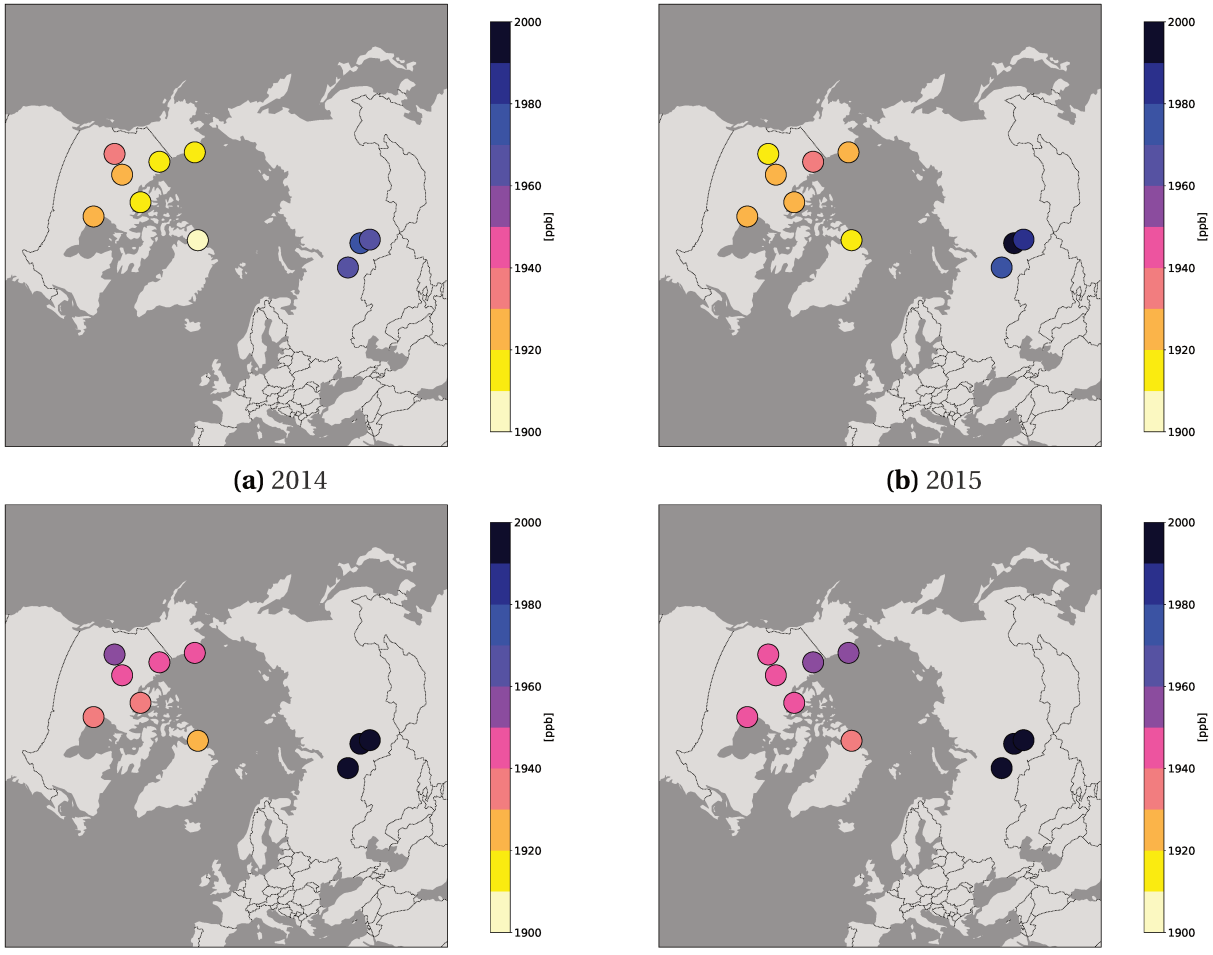

(a) 2014 **(b)** 2015

(c) 2016 **(d)** 2017

Figure VI.3: Mean annual CH_4 mixing ratios at selected observation sites between the years 2014 and 2017.

During all years, the lowest CH_4 concentrations are measured at Alert, which is located remotely from major methane emission sources and often referred to as the Arctic background site. The other stations in North America show less continuity in their mean annual magnitude and there are no significant regional patterns. Whereas in 2014 the highest CH_4 mixing ratios are found at the continental sites (FNE and BCK) as well as at the Hudson Bay (CHU), in 2017 the CH_4 mixing ratios are higher at the coastal stations in the West of the North American Continent (BRW and INK). However, the measured mixing ratios generally don't show large

variations between the different sites in North America with a maximum standard deviation of around 9 ppb.

In Siberia, the magnitudes of the CH_4 concentrations at all observation sites are essentially similar to each other during the different years. An exception is hereby the year 2016 during which exceptionally high concentrations (2061.1 ppb on average) were measured at the station DEM.

1.3.2 Trends

As indicated in the previous section, the measured mixing ratios increased over the course of the years under study. The elevated CH_4 concentrations were hereby observable at all stations included in this analysis. The majority of the stations shows hereby an unsteady increase over time, however some observation sites, such as ALT, show steadily increasing CH_4 concentrations over the course of the years under study.

The difference between the mean annual CH_4 mixing ratios between the year 2014 and 2017 is shown in Figure VI.4.

Figure VI.4: Difference of mean annual methane mixing ratios between 2014 and 2017 in ppb.

The average increase over all stations lies hereby at around 29.0 ppb. The lowest difference between the year 2014 and 2017 can be found at the North American continental site FNE, with an increase of 13.8 ppb. The increase was generally higher at the Siberian stations (37.7 ppb at DEM), however an equally high rise of CH_4 concentrations can be observed at the coastal sites BRW (35.1 ppb) and INK (37.1 ppb) in the West of North America.

During this period, the global increase of CH_4 mixing ratios in the atmosphere was estimated at around 9.2 ppb (NOAA). This is lower by around 20 ppb on average than the observed increment of atmospheric CH_4 concentrations at the studied high northern latitudes observation sites which indicates elevated methane emissions in Arctic and Sub-Arctic regions.

1.3.3 Seasonal cycles

Subsequently, the seasonal cycles of CH_4 concentrations at the different observation sites are analyzed. Similarities in the seasonal patterns could indicate the contribution from specific emissions sources for example by comparing the observed mixing ratios to estimated seasonal cycles of bottom-up CH_4 emission estimates (e.g. Belikov et al., 2019).

Due to gaps in the measurement data, analyzing the seasonal cycle of the JR-Stations is difficult during the years under study and no striking similarities between the three stations can be observed. Figure VI.5 shows the seasonal cycle of the CH_4 concentrations for the different years.

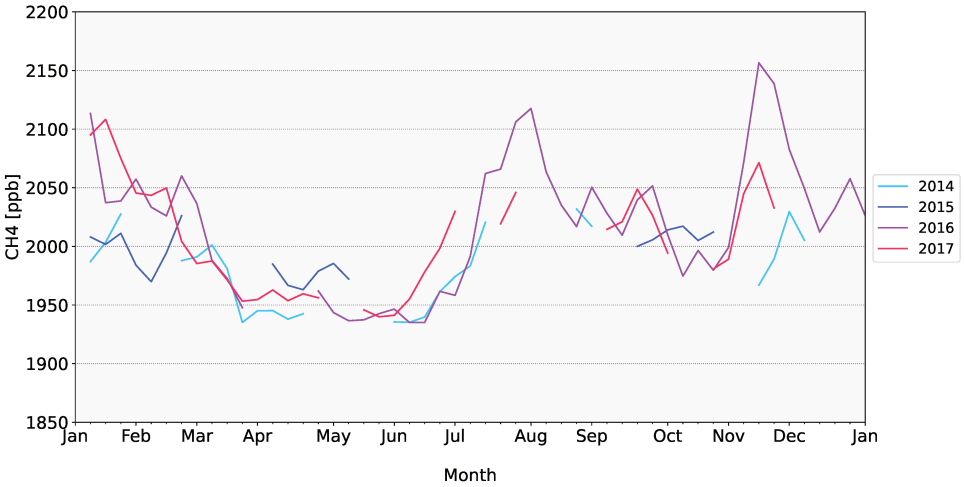

Figure VI.5: Seasonal CH_4 mixing ratios at the station KRS for the years 2014 to 2017.

Elevated concentrations of methane can hereby be observed during the winter month (November to March) and in July and August. The peaks are hereby possibly linked to elevated anthropogenic methane emissions during winter (Umezawa et al., 2012) and natural emission from wetlands during the summer months (Arshinov et al., 2009; Belikov et al., 2019).

In North America, seasonal patterns are more clearly recognisable because the data shows better continuity. Figure VI.6 shows an exemplary seasonal cycle at ALT.

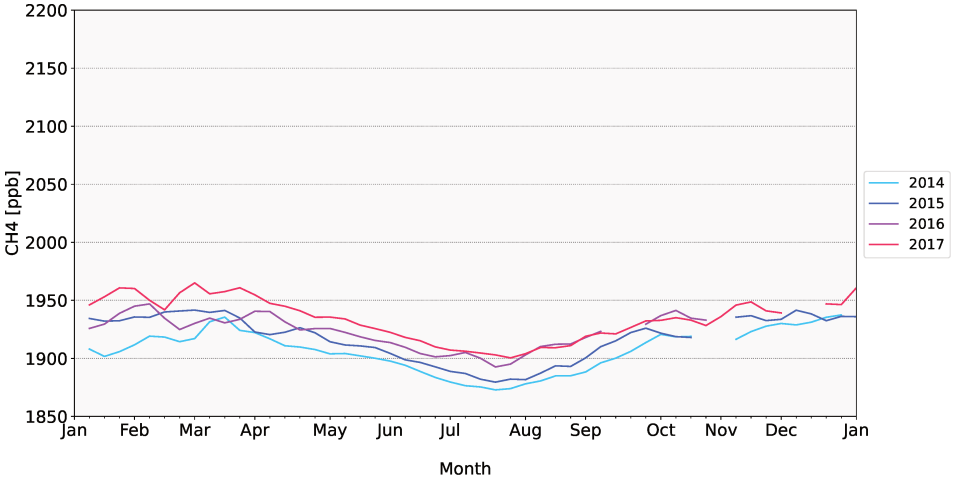

Figure VI.6: Seasonal CH_4 mixing ratios at the station ALT for the years 2014 to 2017.

Like in Siberia, the CH_4 mixing ratios are hereby elevated from November to March, whereas the minimum occurs in July and August. Since Alert site is located remotely from major methane sources, the seasonality of the CH_4 mixing ratios is indicative of the overall hemispheric variability has been linked to the concentrations of the OH radical, which is higher during the summer month and therefore provides a larger methane sink than in winter (Jones et al., 2014; AMAP, 2015). Zona et al. (2016) also highlighted the importance of methane emissions during the cold season in the Arctic due to reduced microbial processes in the soil which reduce methane oxidation.

Some stations in North America show similarities between their seasonal cycle. This can especially be observed at the five sites located on the coast of the Arctic Ocean (ALT, BRW, CBY, INK and CHU) shown in Figure VI.7a, with the corresponding measurement sites shown in Figure VI.7.

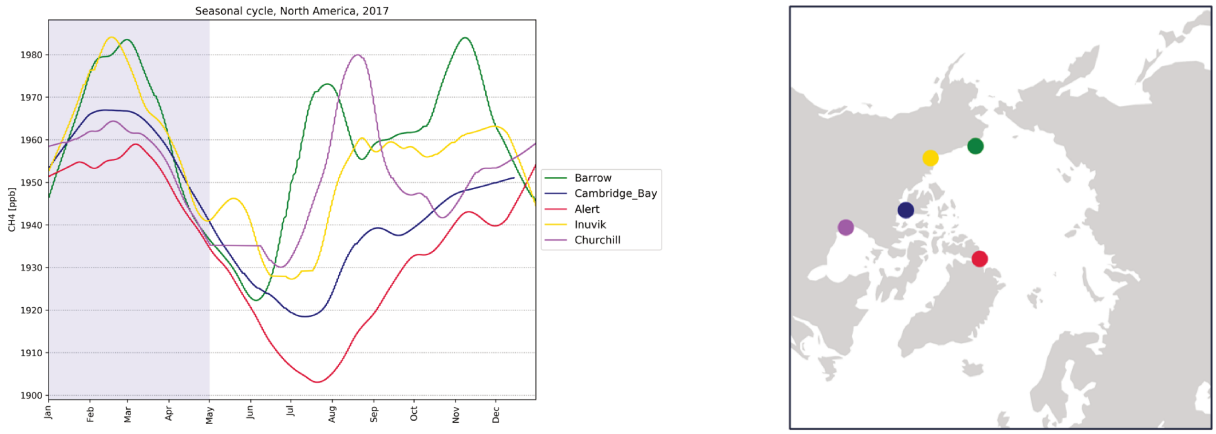

(a) Available **(b)** Selected

Figure VI.7: Comparison between the seasonal cycles of CH_4 mixing ratios of the five stations ALT, BRW, CBY, INK and CHU (left) for the year 2017. The tinted background highlights the similar pattern. The map on the right side shows the locations of the sites in the corresponding colors.

Even though the magnitude of the CH_4 concentrations varies between the different stations, all of them show elevated mixing ratios during the first months of the year. This peak is more distinct at the observation sites BRW and INK at the west coast of the Arctic Ocean which indicates the influence of regional methane sources in addition to the reduced OH concentrations. In winter months, the lower atmosphere can be extremely stratified, hence trapping local emissions close to the ground where observations are carried out, hence explaining part of the . On the opposite, in summer the mixing layer is higher, hence reducing the impact of local emissions.

During the remaining months of the year, the different observation sites show a greater variability in their seasonal patterns which points to the local contributions from different emission sources which can not be fully identified from the measurements alone.

1.4 Summary and conclusion

Observations of atmospheric CH_4 mixing ratios were analyzed from 10 in situ measurement sites above located above 55 °N providing quasi-continuous data between the years 2014 and 2017. It was shown that during those four years methane concentrations increased at all given observation sites to a higher (up to 37.7 ppb) extent in comparison to the global

average during that period (9.2 ppb), indicating probable elevated CH_4 emission in Arctic regions.

The observed CH_4 concentrations were hereby higher at the Siberian observation sites in comparison to the North American ones (up to 54 ppb) during all considered years. The Russian stations also showed a larger increase of CH_4 mixing ratios in general, however equally high increments could be observed at the two coastal stations in the West of North America, BRW and INK. Analyzing the seasonal patterns of the CH_4 mixing ratios does allow for assumptions about the influence of regional methane sources and sinks in the Arctic area such as elevated anthropogenic methane emissions during the winter month in Siberia or the reduction of CH_4.

However, the observations alone do not provide enough indicators to sufficiently identify the contribution from different local and regional methane sources and to estimate their magnitude. Therefore, to obtain an estimate of methane sources and sinks sufficient to explain the observed measurements, an inverse modelling approach was subsequently applied.

2 Additional projects to analyze methane at high northern latitudes using FLEXPART

In addition to the main effort implemented in this work, which is assessing CH_4 sources and sinks in the Arctic by using atmospheric data assimilation, several contributions were given to other studies and projects on constraining CH_4 emissions in high northern latitudes. Those included the supervision of two internships and the participation in a measurement campaign on greenhouse gases.

2.1 Arctic Ocean Methane emissions and sensitivity to upheavals in the ocean dynamic

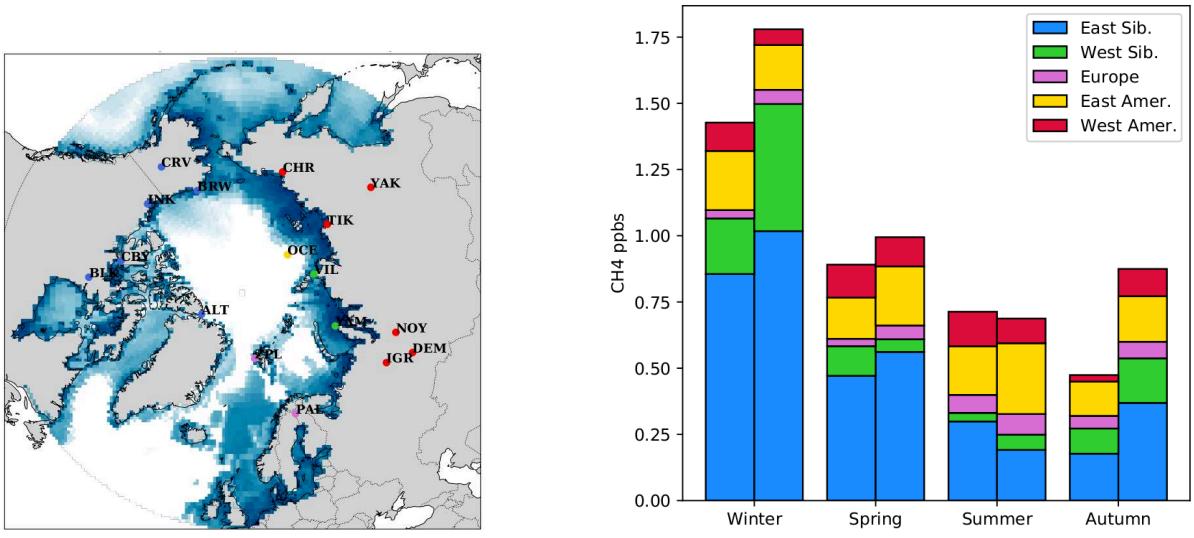

(a) **(b)**

Figure VI.8: Left: Observation network used in this study and illustrative oceanic fluxes from Weber et al. (2019). The yellow and green dots display hypothetical observation sites. Right: Detection of CH [ppb] from different areas of the Arctic Ocean at the stations Alert (Canada) during different seasons. The left bars show the year 2017, the right bars the year 2018. Figures: Netz (2021).

This work was implemented by Louis Netz as part of his Master 1 internship and was focused on CH_4 emissions from the Arctic Ocean. The aim of this study was hereby on the one hand, to find out if the current observation network in the Arctic is sufficient to detect possible changes in oceanic methane emissions and, on the other hand, to assess to which extent an expanded network could improve the detection of such emissions.

FLEXPART was thereby used to simulate footprints of observation sites with proximity to the Arctic Ocean (see Figure VI.8a, page 82) to subsequently obtain contributions of CH_4 mixing ratios under different emission scenarios based on bottom-up estimates by Weber et al. (2019) (described in Section 3.1.3). Additionally, the simulations were used to analyze the sensitivity of the measurement sites to increased Ocean fluxes from different areas of the Arctic Ocean (example shown in Figure VI.8b, page 82).

Overall, the study showed that the current network of in situ measurement sites detects increased emissions from the Arctic Ocean whereby the distribution of the fluxes did not significantly influence the detection and the expanded network (supposed in this study) potentially increases the detection by up to 30 %. The detectability of increased fluxes in the Arctic is further explored and systematically assessed in Chapter VIII.

2.2 Disentangling methane and carbon dioxide sources and transport across the Russian Arctic from aircraft measurements

This work was implemented by Clément Narbaud as part of his Master 2 internship, resulting in a publication (submitted October 2022, Narbaud et al., 2022).

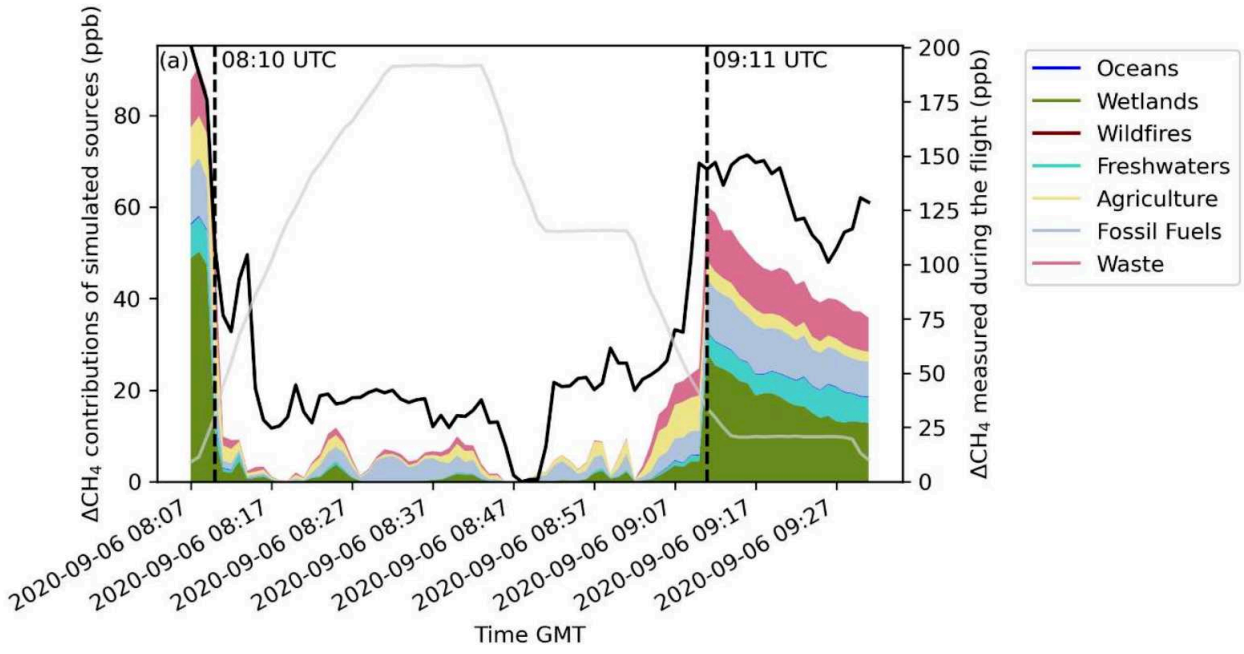

Figure VI.9: Simulated CH_4 mixing ratios from different sources (coloured stacked plot, axis on the left) and measured CH_4 (black line, axis on the right) for one of the flights during the measurement campaign northwest of Russia. Details in Narbaud et al. (2022).

In the context of this study, FLEXPART was used to identify the main emission sources influencing the measurements of CH_4 concentrations taken during a large-scale aircraft campaign (details in Belan et al., 2022) focusing on the Siberian Arctic coast which took place in September 2020. Thereby, the backward trajectories were simulated for a moving receptor including the varying longitudes, latitudes and altitudes during the flights. The thus obtained

footprints were subsequently used to calculate the contribution from natural and anthropogenic CH_4 sources and subsequently compare them with the observations obtained during the aircraft campaign to identify which emission sources were regionally dominating.

Figure VI.9 (page 83) shows the contributions from different CH_4 sources computed using the footprints simulated for a specific flight during the campaign in comparison to the measurements.

The study concluded, amongst additional results discussed in the work, that the origin of the CH_4 measurements taken in the northwest of Russia were predominantly influenced by wetlands and anthropogenic sources whereas the North East was dominated by freshwater and oceanic sources.

2.3 Measurement Campaign: MAGIC 2021

The MAGIC (Monitoring of Atmospheric composition and Greenhouse gases through multi – Instruments Campaigns) 2021 campaign took place in proximity to the Swedish town Kiruna in August 2021 (details under https://magic.aeris-data.fr/magic2021/). The campaign aimed to study the concentration and distribution of both CO_2 and CH_4 by providing a better understanding of the vertical exchanges of GHGs along the atmospheric column but also to contribute to the preparation and validation of space missions dedicated to monitoring GHGs.

The measurements were hereby taken ground-based, airborne (using both aircraft and balloons, see Figure VI.10) as well as using satellites. Around 20 different measurement instruments were thereby used to monitor the GHGs and 10 different research teams from France, Germany and the UK were participating at this campaign.

Figure VI.10: Balloon measurement during the MAGIC 2021 campaign. Photo: ©Thibaud Vergoz.

Certain measurements during this campaign were aimed at observing GHG emissions from specific emitters, whereby the trajectory of the air masses needed to be taken into account. The objective of participating in the campaign was to support the planning of the aircraft measurements by using FLEXPART. The footprints were hereby simulated for virtual

flight routes with anticipated timestamps and altitudes using ECMWF data from the Integrated Forecasting System (IFS). One of the planned flight routes as well as the corresponding footprint for a specific day during the campaign is shown in Figure VI.11. The data collected during the campaign is the subject of ongoing studies.

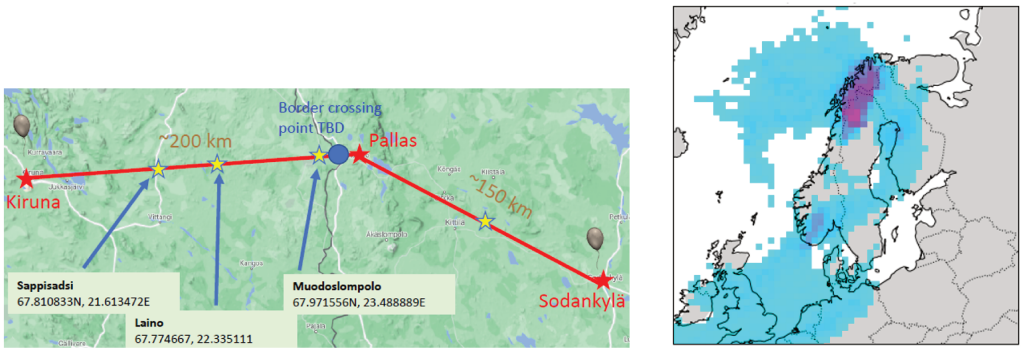

(a) (b)

Figure VI.11: Planned flight route during the MAGIC 2021 campaign (left) and corresponding footprint (right). The footprint is hereby simulated for August 17, 2021 and averaged over the whole flight route.

CHAPTER

VII

Methane emissions in the Arctic 2008-2019

Contents

THE FOLLOWING CHAPTER PRESENTS A STUDY aimed at estimating methane sources and sinks in the Arctic nations focusing on the years 2008 to 2019. Thereby, an analytical inversion is implemented using the available network of surface observation sites, various prior estimates on CH_4 fluxes and uptake as well as simulated methane concentrations acquired using the atmospheric transport model FLEXPART.

In Section 1, the underlying motivation of the study is briefly explained. Section 2 outlines the used methods and summarises the main results and conclusions. Finally, the complete article about this work is presented in Section 3.

1 Motivation

In Chapter VI, we attempted to draw a conclusion about regional methane sources in the Arctic by exclusively analyzing available observations from measurement sites in different Arctic nations. It has been shown that, even though the seasonal patterns of the observations allow for some assumptions, the measurements alone are not sufficient to identify the contribution and inter-annual changes of certain CH_4 sources. Additionally, it was also evident that within the considered period of time, the measured CH_4 concentrations were increasing at all the sites under study.

Subsequently, we attempt to trace back these atmospheric observations to the regional methane sources and sinks in the Arctic and Sub-Arctic by using an inverse modelling approach. The two underlying questions are hereby:

Question 1: *Is the current observation network of stationary measurement sites in the Arctic nations able to adequately constrain different sectors of CH_4 sources and sinks?*

Question 2: *What information can be derived about seasonal patterns and trends of CH_4 sources and sinks between the years 2008 and 2019 in different parts of the Arctic?*

2 Outline of the study

In the following study, an inverse modelling set-up is presented: it aims at constraining CH_4 surface fluxes between the years 2008 and 2019 in high northern latitudes based on surface observations in Arctic nations and an atmospheric transport model. The schematic outline of the study is shown in Figure VII.1, page 89.

The thus obtained posterior states of methane emissions and uptake are subsequently analyzed regarding their seasonal patterns as well as detectable inter-annual trends with regards to the regional constraints of each CH_4 sector.

2.1 Methodology

In this set-up, we use an analytical inversion including in situ measurements of atmospheric CH_4 concentrations from 41 observation sites in high northern latitudes, prior bottom-up estimates of various natural and anthropogenic CH_4 sources and its sink as well as simulated backward trajectories using the Lagrangian transport and dispersion model FLEXPART. For the inversion set-up, the area of study is divided into 121 individual sub-regions in order to better constrain local differences of the CH_4 sources and sink. In order to acquire reliable estimates, an ensemble of 5000 posterior states is computed using a variety of uncertainty estimates on the prior, the background and the observation errors. The plausibility of these error estimates is subsequently analyzed with the log-likelihood method to discard ill-defined configurations before analysing the results.

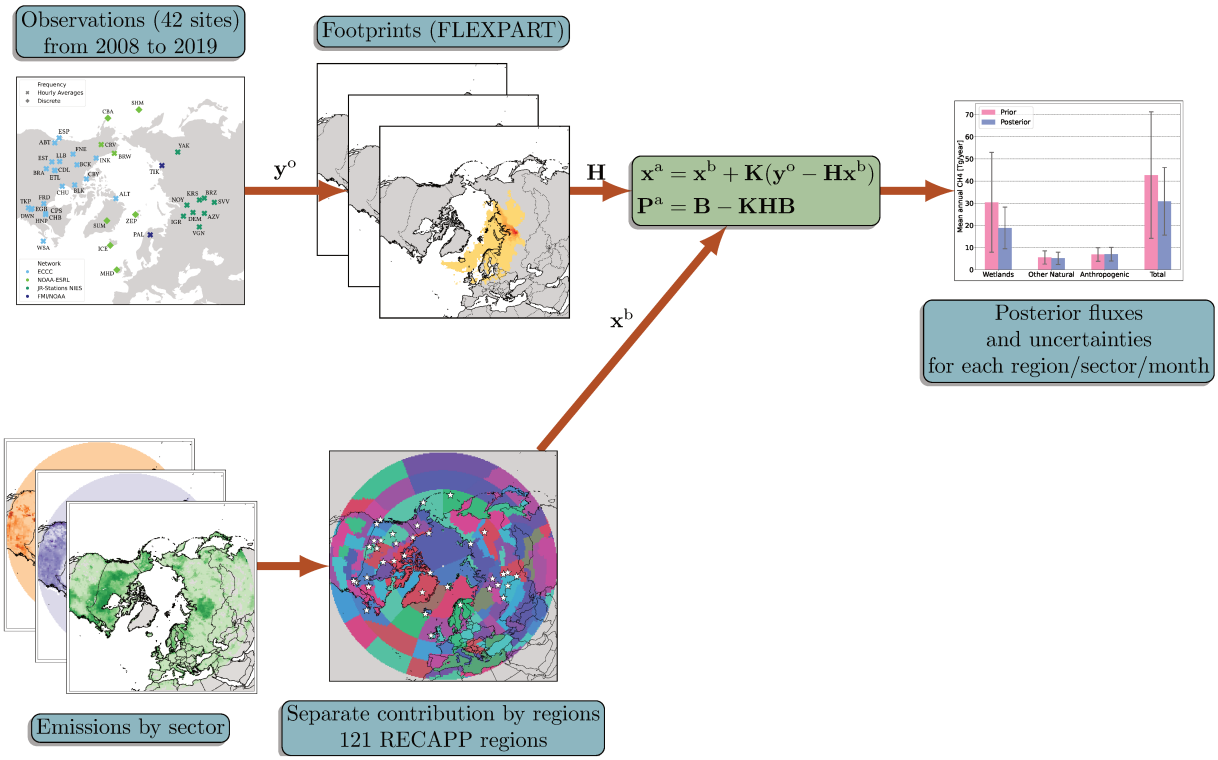

Figure VII.1: Schematic illustration of inverse modelling set-up used in this study.

2.2 Main results

The analysis of the spatial distribution of constraints on regions and CH_4 sources showed that the majority of the emission sources as well as the sink are quite poorly constrained in most of the defined sub-regions. The only exception are hereby wetland fluxes, which are well constrained in North America and certain parts of Siberia. The differences in the constraints can for instance be explained by the unevenly distributed observation network. Additionally, it was shown that a large part of the observations (up to 65 %) was used by the inversion to constrain the background mixing ratios whereas less than 10 % were used to constrain the CH_4 emissions sectors. This additionally contributes to the poor regional constraints.

Due to the low constraints, the uncertainties on the prior estimates could for most CH_4 sources not be reduced significantly and the posterior results stayed overall close to the prior ones. The CH_4 emissions from wetlands on the other hand mostly showed reduced values of posterior fluxes and uncertainties in comparison to the prior estimates. The median of the posterior emissions was hereby decreased by around 11 $TgCH_4$ yr^{-1} in North America, 2 $TgCH_4$ yr^{-1} in East Eurasia and 3 $TgCH_4$ yr^{-1} in the Arctic. In comparison to results from global inversion set-ups, the total posterior CH_4 emissions obtained in this work are consistently higher. This is most significant in the Arctic, where the results from the global inversions are up to 59 % lower.

Regarding the trends of CH_4 emissions within the period under study, the majority of the posterior results from the computed ensemble showed a slight negative trend for wetland emissions in North America with an average decrease of around -1.4 % yr^{-1}. In East Eurasia on the other hand, wetland emissions increased by around 0.08 % yr^{-1} on average. The seasonal cycles of the different emissions sectors showed minor, insignificant deviations in comparison to the prior. At the inter-annual scale the most apparent differences are obtained for the CH_4 emissions from biomass burning in North America, where the the annual peak emissions are up to 50 % (around 0.7 Tg) lower than the prior estimates during certain years

within the period under study.

2.3 Summary and conclusion

We find that the current network of observation sites is not sufficient to satisfactorily constrain most CH_4 sectors in the Arctic and Sub-Arctic regions between the years 2008 and 2020. The only source adequately constrained are wetland emissions, however almost exclusively in North America and sporadically in Russia. The constraints show hereby inter-annual variabilities and are strongly improved during the years where measurement data is sufficiently available. Therefore, it is not possible to reduce uncertainties on most methane emission sources and sinks occurring in high northern latitude regions to a satisfactory extent. Additionally, a substantial share of the observations is used to constrain the background concentrations. To better constrain the Arctic region it would therefore be necessary *(i)* to reduce uncertainties on the background mixing ratios by improved global CH_4 concentration fields and *(ii)* to expand the observation network, e.g. by adding sites to constrain transport from CH_4 hotspots such as China, India and the Middle East.

The computed posterior methane fluxes were predominantly lower in comparison to the prior estimates, however still higher than comparable results from global variational inversion set-ups. The largest reduction was hereby observed in North America, whereby the decrease was predominantly due to reduced CH_4 emissions from wetlands. Significant changes in the seasonal cycles of the methane emissions were not detectable for any source or sink. Most CH_4 sources as well as the sink from soil oxidation did not show significant trends between 2008 and 2019, since those sectors were poorly constraint by the inversion. Wetland emissions showed a slight decreasing trend in North America for the period under study whereas CH_4 emissions from wetlands in East Eurasia showed a slight increasing trend.

To get more definite results on the magnitude, trends and seasonal variability of methane emissions from various sources in high northern latitude regions, it would be beneficial to expand the observation network, to better constrain the area for future works. Complementary approaches bringing fixed and mobile measurement campaigns together could additionally be valuable to improve our understanding of the regional Arctic methane budget. Also, satellite observations (even under the given technical restrictions in high northern latitude regions) may in the future provide additional information to better constrain CH_4 emissions in the Arctic.

3 Article: Estimating Methane Emissions in the Arctic nations using surface observations from 2008 to 2019

The following manuscript was submitted to the Copernicus journal Atmospheric Chemistry and Physics on November 14th, 2022. The authors are: Sophie Wittig[1], Antoine Berchet[1], Isabelle Pison[1], Marielle Saunois[1], Joël Thanwerdas[1], Adrien Martinez[1], Jean-Daniel Paris[1], Tochinobu Machida[2], Motoki Sasakawa[2], Douglas E. J. Worthy[3], Xin Lan[4], Rona L. Thompson[5], Espen Sollum[5], and Mishail Arshinov[6].

Supplementary materials are reported in Chapter D.

[1]Laboratoire des Sciences du Climat et de l'Environnement, CEA-CNRS-UVSQ, Gif-sur-Yvette, France
[2]Center for Global Environmental Research, National Institute for Environmental Studies, Tsukuba, Japan
[3]Environment and Climate Change Canada, Climate Research Division, Toronto, Ontario, Canada.
[4]NOAA Global Monitoring Laboratory, Boulder, CO, USA
[5]Norsk Institutt for Luftforskning, NILU, Kjeller, Norway
[6]Independent researcher

3.1 Introduction

The Arctic is an especially critical area in terms of global warming. As the near-surface air temperature has increased by approximately 3.1 °C since the 1970s, three to four times as much as the global average (AMAP, 2021; Rantanen et al., 2022), environmental changes in that region are rapidly progressing (Serreze et al., 2009; Cohen et al., 2014; Jansen et al., 2020). Exceptional events like melting glaciers, reduction of sea ice, thawing permafrost, increasing occurrence of wildfires during summer and shortening of the snow season have already been observed increasingly frequently during the most recent years (Hassol, 2004; Stroeve et al., 2007; Walker et al., 2019). Predictions assume that, if the Arctic warming continues rising at this rate, by 2100 the temperature will have increased by 3.3 to 10.0 °C (AMAP, 2021).

Short-lived climate forcers such as methane (CH_4) have a significant role in this framework (AMAP, 2015). Methane is globally the second most abundant anthropogenic greenhouse trace-gas with a radiative forcing of about 0.56 W/m^2 (IPCC, 2022). The rising temperatures, at the global scale and particularly in the Arctic, influence the natural CH_4 sources in the Arctic, which may possibly intensify local emissions in the near future (IPCC, 2022). A positive feedback of the global - and regional - warming may therefore ensue.

Various CH_4 sources, both natural and anthropogenic, contribute to the Arctic methane budget. Today, the natural Arctic methane emissions are dominated by high latitude wetlands, the extent of which is still highly uncertain however. Estimations on high latitude wetland emissions show large discrepancies. Ito (2019) concluded from a process-based modelling study that the pan-Arctic (above 60°N) wetland emissions in the 2000s to be between 10.9 and 11.4 TgCH_4/year. Estimates by Petrescu et al. (2010) of northern wetland emissions (defined as wetlands in regions with a yearly average temperature lower than 5°C) varied by a factor of four (between 38 and 157 Tg per year) and the corresponding regions by a factor of two (2.2 to 4.4 million km^2). Uncertainties on the extent of high latitude wetland areas are, among other factors, a reason for the large variations. Other natural CH_4 sources occurring in this area are freshwater emissions e.g. from thermokarst lakes as well as emissions from the Arctic Ocean and biomass burning due to wildfire events in the summer months AMAP (2015). As mentioned before, natural methane emissions are anticipated to increase with rising temperatures and overall changing conditions: in the Arctic, methane net emissions could possibly be twice as high by the end of this century (Schuur et al., 2015), in part related to the high sensitivity of CH_4 emissions to the state of the permafrost (Masyagina and Menyailo, 2020), and general atmospheric conditions (Chen et al., 2015). Indeed the thawing and destabilization of permafrost lead to the exposure of large carbon pools that have so far been shielded by ice and frozen soil. Permafrost thaw is expected to influence at least four ways of carbon mobilization: i) the deliberation of CH_4 reservoirs in the upper permafrost layers, ii) retained activity from viable methanogens as well as iii) the consumption of labile organic matter by these micro-organisms and finally iv) an increased production of CH_4 in the active zone (Rivkina and Kraev, 2008). Additionally, anthropogenic activities in high northern latitudes contribute to the global methane budget with an estimated amount ranging between 2 to 18 Tg CH_4/year (Saunois et al., 2020). These emissions are mainly caused by the exploitation and distribution of fossil fuels and are especially predominant during the winter months (Thonat et al., 2017). Currently, five Arctic nations, Russia, Canada, Norway, Greenland and the United States of America (USA), perform drilling activities in their territories and exclusive economic zones in neighbouring oceans. Decreasing the emissions from anthropogenic sources is an effective way to limit the overall methane emissions in the Arctic region. However, with an estimated 13 % of undiscovered mineral oil and 30 % of undiscovered gas resources north of the Arctic Circle (Gautier et al., 2009), the Arctic is of significant interest for the petroleum industry regarding future drilling campaigns.

Even though the CH_4 observation networks in northern high latitudes have been expanded since the early 2000s, the current stationary networks remain restricted, leaving vast areas uncovered due to the difficulties in carrying out measurements in such remote areas (Pallandt et al., 2022). Thus, obtaining accurate assessments of methane emissions in northern high latitudes remains challenging since their spatial distribution at the local scale is highly variable. Current estimations are primarily based on bottom-up studies which rely on up-scaling of local flux measurements or on process-based surface models and on emission inventories which combine emission factors with socio-economic activity data. These approaches are however subject to high uncertainties at the regional scale since they imply statistical approximations as well as simplifications on chemical, biological and physical processes (e.g., Saunois et al., 2020).

Another approach is provided by top-down studies, in support of bottom-up products. Top-down studies optimally combine observations, provided either by ground based or satellite measurements of atmospheric CH_4 mixing ratios, numerical transport modelling and bottom-up emission data sets as prior emission estimates into the mathematical framework of data assimilation to retrieve emission fluxes and their uncertainties. The so-called atmospheric inversion method is therefore useful to reduce uncertainties on bottom-up estimates (used as priors) and thus gain a better understanding on the region's methane budget. Such studies have already been implemented for high latitude regions at various scales and with regard to different sources. Inverse modelling approaches for methane emissions in the Canadian Arctic have for instance been carried out by Miller et al. (2016) (for the years 2005-2006) Ishizawa et al. (2018) (for the years 2012 to 2015), Chan et al. (2020) (for the years 2010 to 2017) and Baray et al. (2021) (for the years 2010 to 2015), for Scandinavia (Tsuruta et al., 2019, for the year 2004 to 2014), in high latitude Eurasian regions (Berchet et al., 2015, for the year 2010), for Siberian lowlands (Winderlich, 2012) and also for the whole region above 50 °North latitude (Thompson et al., 2017, for the years 2005 to 2013) and above 60 °North latitude by (Tan et al., 2016, in 2005).

In this study, we estimate methane emissions during the most recent years (2008 to 2019) through atmospheric inversion based on available in-situ measurement data from observation sites located in the Arctic and Sub-Arctic. In order to obtain a reliable assessment, we compute a large ensemble of possible posterior emissions scenarios using different error estimations that are evaluated concerning their plausibility. The CH_4 emissions are subsequently analyzed with particular regards to three different questions: (i) is the available observation network sufficient to constrain all occurring CH_4 sources and sinks adequately? (ii) do the different CH_4 sources and sinks show any significant trends between the years 2008 and 2019? and (iii) do the different CH_4 sources and sinks in the posterior state show any shifts in the seasonal cycle in comparison to the prior bottom-up estimates?

3.2 Methodology

To estimate the CH_4 fluxes in the Arctic region, a Bayesian inversion framework (3.2.1) based on backward simulations of the Lagrangian particle dispersion model (LPDM) FLEXPART is used (see details in Section 3.3.3). The inversion is based on all available observation sites in the Arctic and sub-Arctic region (see details in 3.2.3). Extensive sensitivity tests are carried out to evaluate the reliability of CH_4 estimates (see details in 3.2.2)

3.2.1 Inversion framework

We apply an analytical inversion which aims at explicitly and algebraically finding the optimal posterior state of a system $\mathbf{x}^a$ and the corresponding uncertainties $\mathbf{P}^a$, which are given by:

$$\begin{cases} \mathbf{x}^{\mathrm{a}} &= \mathbf{x}^{\mathrm{b}} + \mathbf{K}(\mathbf{y}^{\mathrm{o}} - \mathbf{H}\mathbf{x}^{\mathrm{b}}) \\ \mathbf{P}^{\mathrm{a}} &= \mathbf{B} - \mathbf{K}\mathbf{H}\mathbf{B} \end{cases} \tag{VII.1}$$

with $\mathbf{K}$ the Kalman gain matrix given by:

$$\mathbf{K} = \mathbf{B}\mathbf{H}^{\mathrm{T}}(\mathbf{R} + \mathbf{H}\mathbf{B}\mathbf{H}^{\mathrm{T}})^{-1} \tag{VII.2}$$

We apply the formula on a year-by-year basis in the present work. The control vector $\mathbf{x}^{\mathrm{b}}$ refers to the prior knowledge on the system, in our case CH_4 surface fluxes from different sources (Section 3.3.2), but also background mixing ratios (Section 3.3.3.3). The observation vector $\mathbf{y}^0$ contains the available observations of atmospheric CH_4 mixing ratios (detailed in Section 3.3.1.2). The observation operator includes the transport of the emitted methane (Section 3.3.3.2) in the domain, the import from outside the domain (Section 3.3.3.3), but also, the filtering and other operations required to extract the simulated equivalents of the measurements (Section 3.3.3). Chemical oxidation of CH_4 by OH is neglected for our application (see Section 3.3.3). Thus, all operations in the observation operator are linear and we represent it by its Jacobian matrix $\mathbf{H}$. The linear assumption is required to write Eq. VII.1 and solve the Bayesian system analytically.

The error covariance matrices in the observation and control spaces, $\mathbf{R}$ and $\mathbf{B}$, define the weight of the mismatch between the modelled and the measured concentrations. $\mathbf{R}$ contains various types of errors: the error estimates of the differences between the observations and their simulated equivalents include uncertainties on the measurements, but also on the transport in the model and on the discrete representation of the continuous world by a numerical model. The dimensions of $\mathbf{R}$ are equivalent to the number of elements in the observation vector per year; it varies between 217 and 384 as observations are aggregated by station and month (see Sect. 3.3.1.2. The covariance matrix $\mathbf{B}$ is composed of two parts: $\mathbf{B}^S$ which accounts for the uncertainties on the prior methane fluxes and $\mathbf{B}^B$ for the uncertainties on the background mixing ratios. $\mathbf{B}^S$ has a constant size of 10164×10164, following the number of emission regions, emission sectors and emission periods optimized in our system (see Sect. 3.3.2); the dimensions of $\mathbf{B}^B$ are, again, equivalent to the number of observations per year.

Defining the error covariance matrices can be challenging since only the measurement uncertainties can be determined with certainty, using rigorous calibration procedures (e.g Sasakawa et al., 2010). On the other hand, unrealistic error estimations can drastically distort the results of the posterior state (Berchet et al., 2013). Therefore, in this study an ensemble of $(\mathbf{x}^{\mathrm{a}}_i)_{i=1,500}$ and $(\mathbf{P}^{\mathrm{a}}_i)_{i=1,500}$ using 500 realistic set-ups of the error matrices $(\mathbf{R},\mathbf{B})$ is computed. The ensemble of $(\mathbf{R},\mathbf{B})_{i=1,500}$ pairs of matrices is described in Section 3.3.1.2 and in Section 3.3.2.2, respectively. To account for the uncertainties in the posterior state, from each vector $\mathbf{x}^{\mathrm{a}}_i$, ten random variations are generated with the corresponding covariance matrix $\mathbf{P}^{\mathrm{a}}_i$ following a multivariate normal distribution. Thus, we obtain a total of 5000 posterior states to assess the posterior uncertainties of the inversion.

For computational reasons, the 12-year period has been split into 12 independent 1-year inversion windows computed separately. The ensemble of 500 pairs of matrices $(\mathbf{R},\mathbf{B})_{i=1,500}$ is generated based on a limited number of parameters independent from the year j (see Sect. 3.3.1.2 and 3.3.2.2). Therefore, for a given member i of the ensemble, the yearly matrices $\{(\mathbf{R}^{\mathbf{j}},\mathbf{B}^{\mathbf{j}})_i\}$ are built on the same set of underlying parameters. We then compute, for each year $j \in [2008,2019]$, 500 independent inversions.

3.2.2 Framework evaluation

3.2.2.1 Log-likelihood of samples Though realistically chosen (see Section 3.3.2.2 and Section 3.3.1.2), the members of the Monte-Carlo ensemble of ($\mathbf{R}$,$\mathbf{B}$) pairs are not equally plausible. To further compare and aggregate statistics on the ensemble, we weight each member $i \in [1,500]$ for each year $j \in [2008,2019]$ by its likelihood (see, e.g., Michalak et al., 2005). It is defined by:

$$\ln p_i^j(\mathbf{R}_i^j, \mathbf{B}_i^j \,|\, \mathbf{y}_j^{\mathrm{o}}, \mathbf{x}_j^{\mathrm{b}}, \mathbf{H}_j) = -\frac{1}{2}\,\mathrm{Tr}\left(\mathbf{S}^j_{\mathbf{R}_i^j,\mathbf{B}_i^j}{}^{-1}\mathbf{S}^j\right) - \frac{1}{2}\ln|\mathbf{S}^j_{\mathbf{R}_i^j,\mathbf{B}_i^j}| \tag{VII.3}$$

with $\mathbf{S}^j = \mathbf{y}_j^{\mathrm{o}} - \mathbf{H}_j\mathbf{x}_j^{\mathrm{b}}$ and $\mathbf{S}^j_{\mathbf{R}_i^j,\mathbf{B}_i^j} = \mathbf{R}_i^j + \mathbf{H}_j\mathbf{B}_i^j\mathbf{H}_j^T$, $|\cdot|$ is the determinant operator and $\mathrm{Tr}(\cdot)$ is the trace function.

The estimation of the log-likelihood provides a robust method to select the most reliable set-ups, with regards to the information provided by the observations and ideal statistics. For a given set-up, the higher the log-likelihood, the more plausible the pair of covariance matrices. The log-likelihood estimator in a high-dimension problem like ours is extremely sensitive to any change of configuration.

The range of the log-likelihood varies between the different years, due to the variations in the number of available sites and measurements, as well as atmospheric conditions. Then, for each member of the Monte Carlo ensemble, we define the cumulative log-likelihood as:

$$\ln p_i = \sum_{j=2008}^{2019} \ln p_i^j \tag{VII.4}$$

We use the cumulative log-likelihood to define the most plausible posterior vector over the full period of interest from 2008 to 2019, $\mathbf{x^a_{max}}$, corresponding to the member $i_{\max}$ maximizing the cumulative log-likelihood.

We also use the log-likelihood to discard the less realistic members of the Monte Carlo ensemble. To do so, the most reliable pair $i^j_{\max}$ of error matrices ($\mathbf{R^j_{max}}$, $\mathbf{B^j_{max}}$) is determined for each year j separately. Then, each optimal member $i^j_{\max}$ for year j is used on all the years of interest $j' \in [2008,2019]$, so as to obtain corresponding cumulative log-likelihood $\ln p_{i^j_{\max}}$:

Since each cumulative log-likelihood $\ln p_{i^j_{\max}}$ includes the most reliable configuration for year j, the lower threshold for the log-likelihood $\ln p_{min}$ is defined as the minimum of the 12 thus computed cumulative log-likelihood: $\min_{j\in[2008,2019]} \ln p_{i^j_{\max}}$. We define a sub-ensemble $\{\mathbf{x^a_{max}}\}$ whose elements have a cumulative log-likelihood greater or equal to this threshold: $\{\mathbf{x^a_i} \mid \sum_{j=2008}^{2019} \ln p_i^j > \ln p_{min}\}$. This sub-ensemble contains 274 configurations which corresponds to 2740 posterior states and is used in the following for a representative analysis of the posterior state.

3.2.2.2 Sensitivity and influence matrices We use two other metrics to evaluate our system and the different set-ups: the influence and the sensitivity matrices. Both are calculated using the corresponding Kalman gain matrix $\mathbf{K_{max}}$ of the previously determined $\mathbf{x^a_{max}}$. The influence matrix, $\mathbf{K_{max}H}$ (defined by Cardinali et al., 2006), also called the averaging kernel (Rodgers, 2000), contains diagonal terms between 0 and 1, which represent the sensitivity of each component of $\mathbf{x}$ to the inversion. The smaller the term $\mathbf{K_{max}H}_{r,r}$ for emissions in region r is, the less constrained region r is by the inversion. The sensitivity matrix $\mathbf{HK_{max}}$ (Cardinali et al., 2006) gives the sensitivity of the inversion to a change in one component of the observation vector. An observation with a high sensitivity brings strong constraints on the

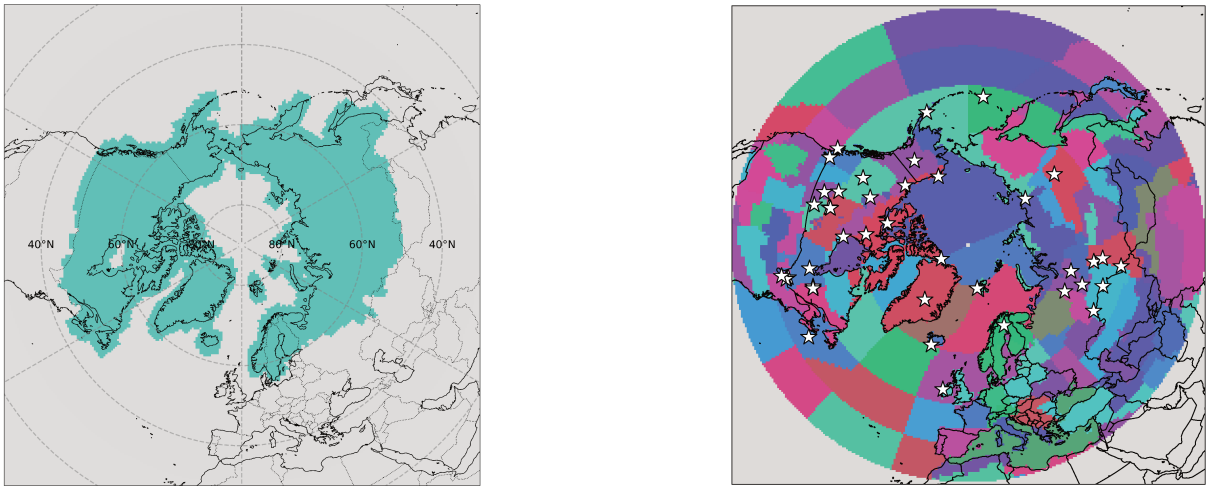

(a) Area of interest **(b)** RECCAP regions

Figure VII.2: Area of interest (left) and RECCAP regions above 30 °N (right). Measurement sites, listed in Table D.1, are indicated with white stars.

inversion. The weight of each station in the inversion can be computed by summing up the corresponding diagonal elements of $\mathbf{HK}_{\mathbf{max}}$. The trace of these two matrices also gives the "degrees of freedom for signal" (Wahba et al., 1994; Cardinali et al., 2006), while the number of observations minus this number gives the "degree of freedom for noise". This extra criterion informs on how much observations are used to constrain fluxes (and background mixing ratios).

3.2.3 Area and period of interest

The area of interest, shown in Figure VII.2a, for this study regarding the quantification of the methane fluxes includes the Arctic and Sub-Arctic, with the southern boundary being roughly the southernmost border of the taiga. For the implementation of the inversion, only observation sites within the area of interest have been included in this study. To represent concentrations at these sites as properly as possible, we simulate the influence of fluxes from the area of interest, but also from a buffer region from above 30 °N (see Sect. 3.3.3.1). Even though Arctic fluxes may influence observation sites in the buffer region, we do not include them in this study due to the increased computational costs this would induce; a future work may inquire into the impact of using as many stations as possible.

The region above 30 °N is subsequently divided into sub-regions in order to better detect local differences. However, the sub-regions should not be too small and numerous, due to the limitation of available observations for constraining those areas. A more detailed description of the selected observation sites (indicated with white stars in Figure VII.2b) can be found in Section 3.3.1.1. The sub-regions of this study are therefore selected following the proposition of the Regional Carbon Cycle Assessment and Processes (RECCAP; Ciais et al., 2022) which results in 121 regions within the area of interest (Figure VII.2b).

The time period of interest is from 2008 to 2019. For the following years, no measurements were available for the majority of the measurement sites by the time this study was implemented.

The atmospheric sites in the area and time period of interest and the available observations are described in Section 3.3.1. CH_4 emissions in this area are described in Section 3.3.2.

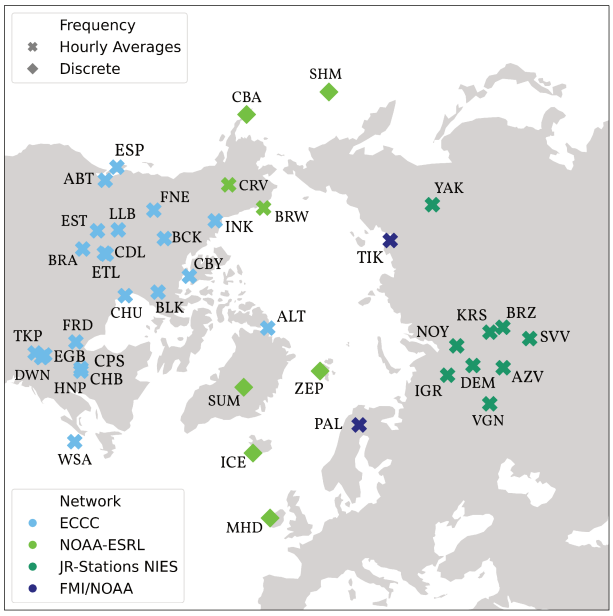

Figure VII.3: Map of the selected observation sites. Crosses indicate quasi-continuous, diamonds discrete measurements. Different network operators are marked with different colours.

3.3 Material

3.3.1 Atmospheric observations

3.3.1.1 Site description For this study, both quasi-continuous measurements (35 observation sites providing hourly measurements) and discrete measurements (6 observation sites providing task samples two to four times a month) are used. The stations are exclusively located in 7 Arctic nations (Canada, Russia, Finland, Norway, Iceland, Greenland and the USA), except for one site in Ireland, used to constrain air masses from the Atlantic Ocean. The operators of these stations are Environment and Climate Change Canada, the Japan–Russia Siberian Tall Tower Inland Observation Network (JR-STATIONS from NIES; Sasakawa et al., 2010), the U.S National Oceanic and Atmospheric Administration Global Monitory laboratory (NOAA-GML; Dlugokencky et al., 2020) and the Finnish Meteorological Institute (FMI; Hatakka et al., 2003; Aalto et al., 2007). The stations with their trigram identifications are shown in Figure VII.3.

All the measurement sites are subsequently described briefly sorted by their network operators. A summary of each station's characteristics is furthermore provided in the supplements (Table D.1).

ECCC The ECCC established its first two CH_4 measurement stations (ALT and FRD) in the end of the 1980s and has expanded its network to 22 sites to this date, 12 of them being located in the Arctic or Sub-Arctic. Alert (ALT) is often referred to as an Arctic background site since it is located remotely from any major methane emission sources on the northeastern tip of Ellesmere Island in Nunavut where the land is covered with snow for approximately ten month a year. Two additional sites are installed in Nunavut in slightly more southern latitudes: Cambridge Bay (CBY) and Baker Lake (BLK). The latter is located in the Arctic Tundra around 320 km from Hudson Bay surrounded by small lakes whereas CBY lies on the southeast coast of Viktoria Island close to the largest port of the Northwest Passage of the Arctic Ocean.

The measurement site Inuvik (INK) was established in the Arctic Tundra of the Northwest Territories in the east channel of the Mackenzie Delta. Further inland in the same Canadian province lies the station BCK, 10 km from the town Behchoko and surrounded by mixed forests, lakes and ponds.

Three of the ECCC sites are located in British Columbia. FNE, which is located close to small town Ford Nelson in the Taiga, lies at the southern fringe of the Canadian permafrost region. Estevan Point (ESP) is located on the coast of the Pacific Ocean and surrounded by woodlands. The measurement station Abbotsford (ABT) lies close to the US border 80 km from Vancouver, the largest city and main economic area in British Columbia.

The two sites in the province Alberta are LLB at the lake Lac La Biche in a region of peatlands and forest and Esther (EST) which lies in the open prairie with plenty of cattle ranches close by.

Two measurement stations are established in Saskatchewan. East Trout Lake (ETL) in the center of the province lies at the southern edge of a boreal forest region and Bratt's Lake (BRA) in the Canadian prairie.

Churchill (CHU) is located Manitoba, north of the largest continuous boreal wetland region in North America on the west coast of Hudson Bay.

Four of the sites in the province Ontario (EGB, DWN, HNP, TKP) are located relatively close to each other in the Mixedwood Plains Ecozone. Downsview (DWN) and Hanlan's Point (HNP) are urban stations in in the north of Toronto and on the Toronto Islands in Lake Ontario, respectively. Egbert (EGB) lies around 80 km from Toronto close to a rural village. The south most site Turkey Point (TKP) is located at Lake Erie in a woodland area. Further north in Ontario lies the station Fraserdale (FRD) in the boreal forest with extensive wetland coverage in the surrounding.

The two sites located in Quebec, Chapais (CPS) and Chibougamau (CHB), are likewise established close to each other in an area dominated by boreal forest with many lakes.

Finally, the observation site Sable Island (WSA) is on a remote island in the North Atlantic Ocean, 175 km from the mainland. The island is uninhabited by people and covered with grass and low-growing vegetation.

NOAA-GML The two continuous measurement stations operated by NOAA-GML are Barrow (BRW) and CARVE (CRV) in the USA (Dlugokencky et al., 2020). Methane measurements in BRW started in the late 1980s. The site is located in northern Alaska on the junction of the Chukchi and Beaufort Seas and the surrounding landscape is characterized by thermokarst lakes. The CRV tower is located in boreal Alaska with a surrounding landscape defined by evergreen forest, shrubland and some areas of woody wetlands (Karion et al., 2016).

The six discrete measurement sites operated by NOAA-GML are ZEP, SUM, ICE, MHD, CBA and SHM. The Zeppelin Observatory (ZEP) is located near the village Ny-Aalesund, which is surrounded by mountains and glaciers, on the island Spitsbergen. From 2017, ZEP observations are available as continuous data via the ICOS Carbon portal (Lund Myhre et al., 2022), but we did not include them as such to avoid perturbing the interpretation of the results for the last years. The sampling site Summit (SUM) was established on the Greenland Ice Sheet and is the highest measurement site of the Arctic Circle. Storhofdi (ICE) lies in the South of Iceland at the top of a small cape with grassy slopes and cliffs to the sea close by. The sample site Mace Head (MHD) is located at the west coast of Ireland in a wet and boggy area. The surrounding landscape is and characterized by small hills covered with grasses and sedges with many exposed rocks. At the southern tip of the Alaska Peninsula nearby the coast lies the

measurement site Cold Bay (CBA) within a wet tundra ecosystem consisting of a variety of sedges and grasses. Finally, the station SHM is located on the island Shemya, which belongs to a cluster of small islands southwest of Alaska.

JR-STATIONS The four JR-STATIONS have been installed by NIES in 2004. Three are located in the Russian taiga forest surrounded by wetlands: Demyanskoe (DEM), Karasevoe (KRS), Noyabrsk (NOY). Additionally, one station was installed in a small town close to the Ob river with around 10.000 inhabitants, likewise surrounded by wetlands.

The network has been extended by five stations in the upcoming years incorporating different biomes. Three towers have been placed in steppe regions. Azovo (AZV) and Vaganovo (VGN) are located in the immediate vicinity of highly populated cities whereas the SVV-tower (Savvushka) is installed near a small village. Additionally, one tower is located in the middle of the taiga surrounded by boreal forest (Berezorechka, BRZ) and lastly, the YAK-tower was placed close to Yakutsk in the East Siberian Taiga (Sasakawa et al., 2010; Belikov et al., 2019). However, not all of the JR-stations are currently still in operation: the dates of beginning and end of operation are indicated in Table D.1. Since the towers are provided with two to four different sampling heights up to 85 magl, only the measurements from the highest inlet are used in this study. The CH_4 measurements are reported on the NIES-94 scale and have been converted to the NOAA 2004 scale following Zhou et al. (2009).

FMI/NOAA The Finnish station Pallas (PAL) is located close to the northern edge of the Scandinavian boreal zone with a surrounding terrain of wetlands, lakes and patches of forest (Hatakka et al., 2003; Aalto et al., 2007). PAL data are available as FMI GAW CH4 data from 2004 onwards at the World Data Center for Greenhouse Gases (WDCGG). PAL data from 2017 are also available from the ICOS carbon portal Hatakka and RI (2022). Like PAL, the site Tiksi (TIK) is operated by the FMI in cooperation with NOAA-GML and is installed on the shore of the Laptev Sea on the Lena river delta (Uttal et al., 2013, 2016).

3.3.1.2 Data selection and observation uncertainties

In regional inversions, concentration peaks carry a large part of the information content on local to regional fluxes. However, transport can be erroneous and simulated peaks can be shifted in time compared to observed ones, although the magnitude can be well represented. Such errors heavily penalize Bayesian inversions, so we decided to aggregate observations at the monthly scale. This focuses the inversion on emission trends and seasonal cycles.

In the observation vector $\mathbf{y}^0$ (Section 3.2.1), we use the monthly averages of the available CH_4 atmospheric measurements at each site. When hourly quasi-continuous data was available, only measurements between 12:00 and 16:00 local time are selected, assuming a well-mixed boundary layer, which is better simulated by the model (Section 3.3.3). The discrete observations are not filtered by the time of day the measurement was taken. However, the data sets contain several measurement outliers, mostly strong concentration peaks related to local emissions, difficult to simulate with our transport model. We excluded such peaks from the observations used for the inversion if they differed more that 5 % (or 100 ppb) from the monthly average. Depending on the measurement site, between 8 and 20 % of the observations are discarded this way.

Due to the discontinuity of measurement availability, the size of $\mathbf{y}^0$ for one year varies between 217 (2008) and 384 (2018). The number of observations per year used for the inversion (and thus the size of $\mathbf{y}^0$) can be found in Table D.2. All the selected observations with the corresponding daily CH_4 concentrations are shown in Fig. VII.4.

Figure VII.4: Average daily methane concentration at each station. The observation sites are sorted by latitude.

The corresponding uncertainties on the observations are specified in the diagonal error covariance matrix $\mathbf{R}$, of which an ensemble of 500 set-ups is generated (Section 3.2.1).

To generate a large number of different error set-ups, the first step consists in obtaining an estimate of the uncertainty for each station $s \in [1,41]$ and each year $j \in [2008,2019]$ which serves as a reference point. This is done by computing the differences between the monthly mean of the measured and corresponding modelled mixing ratios (see Section 3.3.3) in absolute values:

$$\mathbf{\Delta}^{s}_{m,j} = |\mathbf{y}^{model}_{m,j} - \mathbf{y}^{obs}_{m,j}| \tag{VII.5}$$

with $\{m|0 \leq m \leq 12\}]$ one month of a given year j.

Then, the standard deviation of the ensemble of 12 monthly differences is computed for each year:

$$\sigma^{R}_{s,j} = \sqrt{\frac{1}{12}\sum_{m=1}^{12}\left(\Delta^{s}_{m,j} - \overline{\Delta^{s}_{m,j}}\right)^{2}} \tag{VII.6}$$

with $\overline{\Delta^{s}_{m,j}} = \frac{1}{12}\sum_{m=1}^{12}\Delta^{s}_{m,j}$. In the few cases when only one observation is available for a given station and a given year, no standard deviation can be computed so that the single difference between the modelled mixing ratio and measurement is used directly.

The obtained errors per station and year are subsequently varied following a log-normal distribution with $\sigma^{R}_{s,j}$ as its mode. This error distribution is chosen to include only a few very high outliers in the ensemble. To implement a log-normal distribution, a standard deviation $\sigma^{R}_{i,random}$ must be provided which is constant for each element i of the ensemble $i \in [1,500]$. Thus, the random observation error for each station s is equal for all months within one year, however varies between the different years of one element i of the ensemble. To ensure that the values of the observation errors do not vary to an unrealistic extent, a minimum of 0.5 ppb and a maximum of 150 ppb are set.

Finally, the elements of the diagonal of one error covariance matrix $\mathbf{R}_i^j(k,k)$ for $k \in \{s \in [1,41]\} \times \{m|0 \leq m \leq 12\}$ and $i \in [1,500]$ are defined as the variances $\left(\sigma_{s,j}^{R,i}\right)^2$ and the non-diagonal elements are zero.

Figure VII.5 shows an example of the frequency distribution of the observation errors at one of the selected sites, s =INK, for the year j =2012. The mode and therefore the reference point of the observation error for this year and station is around 8 ppb. To give an idea about the general magnitude of the computed uncertainties, the average of $\sigma_{s,j}^R$ over all the stations s including all years j in the period of interest is around 18 ppb.

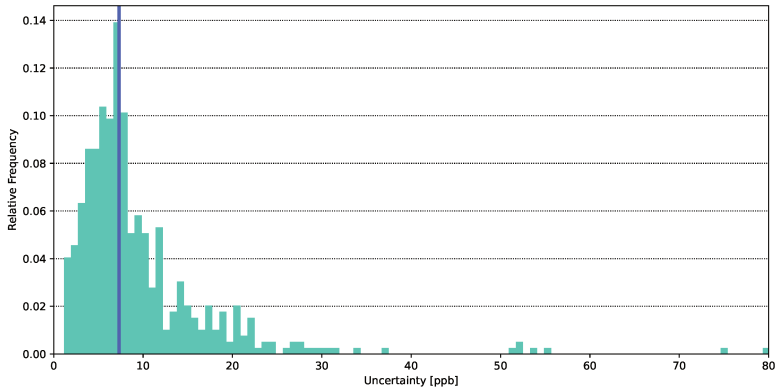

Figure VII.5: Frequency distribution of the 500 random observation errors $\left\{\sigma_{s,j}^{R,i}\right\}$ for $i \in [1,500]$ at s =INK for the year j=2012. The blue line marks the mode $\sigma_{INK,2012}^R$.

3.3.2 Prior Emissions

3.3.2.1 Emission scenarios The emissions used as prior information are based on a set of various inventories and models. The different methane sources and sinks are described in Table VII.1 with there respective temporal resolution in the prior. The natural CH_4 sources include emissions from wetlands, the Arctic Ocean and geological sources. Natural methane emissions caused by biomass burning due to wildfire events are combined with anthropogenic biofuel activities for simplification. Since emissions caused by termites are negligible in the Arctic, they are not taken into account in this study. For the CH_4 sink, soil oxidation is included as negative emissions. To reduce the number of sectors to optimize, emissions related to the exploitation and distribution of mineral oil and gas have been combined to a single data set. The same applies to the emissions from agricultural activities and waste management.

For the natural sources as well as the soil sink, monthly climatological data sets are used for the whole period so that their total fluxes do not differ between the years 2008 to 2019. The emissions from anthropogenic sources vary between the different years covered in this study, following the EDGARv6 emission trends (Crippa et al., 2021b). Emissions caused by fossil fuel activities generally increase between 2008 (15.96 Tg/year) and 2019 (17.31 Tg/year) though the highest annual emissions occur in the years 2014 and 2015. Methane emissions from agricultural activities and waste management also increase slightly throughout the period of interest however just by less then 0.18 Tg/year. The combined biomass burning scenario also shows some inter-annual variability though without any apparent tendencies. The lowest annual emissions occur in 2009 (1.87 Tg CH_4) and the highest in 2012 (3.99 Tg CH_4).

At the intra-annual scale, in contrast to the other natural CH_4 sources, the wetland scenario has a clear seasonality in the Arctic with higher emissions during the summer months. According to the data set used for this study, the highest wetland emissions occur in August

Table VII.1: *Methane sources and sink taken into account in the prior emissions. The share of the global emissions of each source is based on the average fluxes between 2008 and 2019. For data sets with inter-annual differences, the range between the lowest and highest emissions is given. EDGARv6 is described in Crippa et al. (2021b) and GFED4.1 in RANDERSON et al. (2017).*

Type	Source	Reference	Emissions globally ($Tg\ CH_4.yr^{-1}$)	Emissions area of interest ($Tg\ CH_4.yr^{-1}$ / % of global emissions)	Temporal resolution
Natural	Wetlands	Poulter et al., 2017	179.95	44.80 / 24.9	monthly climatology
	Ocean	Weber et al., 2019	11.48	3.02 / 26.3	constant
	Geological	Etiope et al., 2019	36.67	7.66 / 20.9	constant
	Soil Oxidation	Ridgewell et al., 1999	-37.88	-4.74 / 12.5	monthly climatology
Combined	Biomass and biofuel burning	GFED4.1	24.28 - 34.69	1.87 - 4.00 / 10.1	monthly with interannual variability
		EDGARv6			
Anthropogenic	Mineral oil & gas	EDGARv6	102.26 - 126.90	14.70 - 17.83 / 14.6	interannual variability
	Waste & Agriculture	EDGARv6	216.38 - 236.49	8.58 - 8.77 / 3.8	interannual variability
Total			542.80 – 587.74	75.89 – 81.28 / 17.3	

(10.72 Tg CH_4/month) and the lowest in January (0.04 Tg CH_4/month). The soil methane oxidation has a seasonal pattern symmetric to the wetland emissions with the maximum uptake taking place in August (-1.02 Tg CH_4/month) and a minimum in January (-0.01 Tg CH_4/month). The combined biomass burning scenario shows a small seasonal variability with predominantly higher emissions during the summer. Between 2010 and 2016, the highest monthly CH_4 emissions occur in July and from 2017 to 2019 the peak emissions take place in August. Hereby, the maximum of the methane emissions ranges between 0.49 Tg CH_4/month (2009) and 1.91 Tg CH_4/month (2017). The first two years within the period of interest do not fall into this seasonal pattern with increased CH_4 fluxes during the summer months. Regarding the anthropogenic methane emissions, the agricultural and waste management fluxes also show a seasonal pattern with increased emissions during the summer. According to the inventory, the emissions are highest in June (around 0.80 Tg CH_4/month) and lowest in January and December (around 0.67 Tg CH_4/month). The methane emissions from oil and gas exploitation and distribution are nearly constant over the course of each year with a maximum variation of 0.1 Tg CH_4/month.

3.3.2.2 Prior uncertainties As for the observation error, the elements of the prior error matrix $\mathbf{B}$ are obtained from a random sampling. The covariance matrix thereby contains both the uncertainties on the prior fluxes $\mathbf{B}^S$ and the uncertainties on the background mixing ratios $\mathbf{B}^B$. In the following, only the methodology of the random sampling of the prior errors is explained, the details on $\mathbf{B}^B$ are described in Section 3.3.3.3.

For each CH_4 source or sink S, the mode σ^S is set following Baray et al. (2021):

- 50 % for S =anthropogenic emissions
- 60 % for S =wetland emissions
- 100% for S =other natural sources and soil oxidation

A random sampling following a log-normal distribution with σ^S as its mode results in an ensemble of 500 prior errors per source or sink $\left\{\sigma_i^{B,S}\right\}_{i\in[1,500]}$. These random errors remain identical for each region r and month of year m per element i of the ensemble. Exemplarily, figure VII.6 shows the frequency distribution of the random prior errors for S =wetlands emissions of all the set-ups.

Finally, the elements of the diagonal of one error covariance matrix $\mathbf{B}_i^S(k,k)$ for $k \in \{S \in [1,7]\} \times \{r \in [1,121]\} \times \{m \in [1,12]\}$ are defined as the variances $\left(\sigma_i^{B,S}\right)^2$. Hereby, $\mathbf{B}_i^S$ is identical for each year.

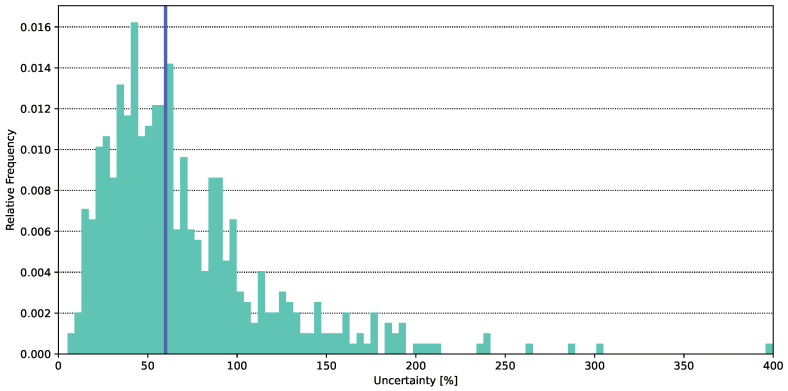

Figure VII.6: Frequency distribution of the 500 random prior errors $\left\{\sigma_i^{B,S}\right\}_{i\in[1,500]}$ for S =wetland emissions. The blue line marks the mode $\sigma^{wetlands}$

The off-diagonal elements $(\sigma_{m,n})^2$ with m the row and n the column of the corresponding matrix $\mathbf{B}_i^S$ are determined by applying spatial and temporal correlations. $\mathbf{B}_i^S$ is hereby a symmetrical matrix so that $(\sigma_{m,n})^2$ is identical to $(\sigma_{n,m})^2$.

The off-diagonal errors are computed as follows:

$$(\sigma_{m,n})^2 = (\sigma_{n,m})^2 = \left(\frac{(\sigma_{m,n=m})^2 + (\sigma_{m=n,n})^2}{2}\right) \times \exp\left(-\frac{\Delta t}{t_{corr}}\right) \times \exp\left(-\frac{\Delta d}{d_{corr}}\right) \quad \text{(VII.7)}$$

with Δt the temporal difference between the rows/columns m and n and Δd the spatial difference referring to the centres of the corresponding regions. For the spatial correlation d_{corr} a distance of 500 km is used and the temporal correlation t_{corr} has a fixed value of one week.

3.3.3 Modelled CH_4 mixing ratios

As mentioned in section 3.2.1, the simulated equivalents to the observations are included in the observation operator $\mathbf{H}$. In this case, $\mathbf{H}$ consists as well of the monthly CH_4 mixing ratios sectioned into sub-regions and sectors as of the monthly averages of the background mixing ratios by station. $\mathbf{H}$ is hereby linear since only emissions and transport of CH_4 are taken into account. The oxidation of methane by hydroxyl radicals (OH) is neglected since the life time of CH_4 is ≈9 years (Prather et al., 2012) and the air masses remain in the domain up to 2 months (Berchet et al., 2020).

3.3.3.1 Transport model set-up The modelled CH_4 mixing ratios were obtained by using the Lagrangian atmospheric transport model FLEXPART (FLEXible PARTicle) version 10.3 (Stohl et al., 2005; Pisso et al., 2019a). This model simulates numerous trajectories of infinitesimally small air parcels, called particles, and can be used either forward or backward in time. FLEXPART is an offline model that is driven by meteorological data from the European Centre for Medium-range Weather Forecast (ECMWF) ERA5 (Hittmeir et al., 2018) with 3-hourly intervals and 60 vertical layers. ECMWF data are retrieved and formatted using the FLEXextract toolbox (Tipka et al., 2020). In this study, 2000 particles are released at each observation site and time stamp (receptor) and followed 10 days backwards in time. The horizontal resolution is 1 °×1 °, which is quite commonly used for inverse modelling set-ups using Lagrangian particle dispersion models in high northern latitudes (e.g. Thompson et al., 2017; Ishizawa et al., 2018).

3.3.3.2 Source contribution By sampling the near-surface residence time of the various backward trajectories of the particles the source-receptor sensitivity matrices, also called footprints, of each observation site can subsequently be determined. These footprints define the connection between the fluxes discretised in space and time and the change in concentrations at the receptor (Seibert and Frank, 2004). To finally obtain a time series of modelled CH_4 mixing ratios, a time series of footprints is integrated with discretised methane emission estimates. Here, monthly averages of the footprints of each receptor are used to determine the mixing ratios for each sector (see Table VII.1 in Section 3.3.2.1) and sub-region (see Figure VII.2b in Section 3.2.3).

The magnitude of the thus obtained total CH_4 mixing ratios, including all methane sources and the soil sink, ranges roughly between 3 ppb and 90 ppb depending on the month of the year and location of the observation site and the average standard deviation is around 14 ppb.

3.3.3.3 Background mixing ratios and uncertainties Since CH_4 has a much longer lifetime than the released virtual particles, the previously obtained concentrations only display short-term fluctuations at the receptors. Therefore, in order to obtain a direct comparison to the measurements, the background mixing ratio needs to be taken into account.

The background mixing ratios are calculated by combining a CH_4 concentration field as initial condition with the FLEXPART backward simulations nudged to the observations of the corresponding site (e.g. Thompson and Stohl, 2014; Pisso et al., 2019a). The background thus obtained represents the average of the mixing ratios in the grid cells where each particle trajectory terminated 10 days before the observation. The initial concentration field is provided by the Copernicus Atmospheric Monitoring Service (CAMS): a CH_4 mixing ratio field from CAMS global reanalysis EAC4 (ECMWF Atmospheric Composition Reanalysis 4) with 60 vertical layers, a 3-hourly temporal and a 0.75 °×0.75 °spatial resolution has been used (Inness et al., 2019). The implementation used for the obtaining the background mixing ratios is provided by the Community Inversion Framework (CIF) (CIF; Berchet et al., 2021).

The thus computed background mixing ratios show a gradual increase over the period of interest with mean annual concentrations over all sites ranging between 1842 ppb (2008) and 1974 ppb (2019). At intra-annual scale, the monthly background mixing ratios vary from the corresponding annual average by around 8 %. Figure D.5 (supplements) shows the average background mixing ratios at each station as well as their average standard deviation.

As stated previously, the background is the major share of the total modelled mixing ratios and, in this study, makes up approximately 97.6 % at continental observations sites and 99.5 % at stations located remotely. A summary of the proportion of source contribution and background mixing ratios for each station can be found in Table D.4 in the supplements.

As mentioned before (e.g. Section 3.2.1), the uncertainties on the background mixing ratios $\mathbf{B}^B$ are included in the error covariance matrix $\mathbf{B}$. In contrast to the uncertainties on the prior emissions $\mathbf{B}^S$, which are given by region, month and CH_4 source/sink, the uncertainties on the background mixing ratios are given by observations site and month. Therefore, the size of $\mathbf{B}^B$ is equivalent to the number of available observations per year.

The elements of $\mathbf{B}^B$ are composed in a similar manner as the elements of $\mathbf{R}$ (Section 3.3.1.2), by first computing a reference error for each station and year and varying these values randomly to obtain and ensemble of 500 set-ups.

In this case, the standard deviations of the monthly background mixing ratios $\mathbf{y^{back}_{s,m,j}}$ per station $s \in [1,41]$ and year $j \in [2008,2019]$ serve as reference errors:

$$\sigma^B_{s,j} = \sqrt{\frac{1}{12}\sum_{m=1}^{12}\left(y^{back}_{s,m,j} - \overline{y^{back}_{s,m,j}}\right)^2} \tag{VII.8}$$

with $\overline{y^{back}_{s,m,j}} = \frac{1}{12}\sum_{m=1}^{12} y^{back}_{s,m,j}$ and $m \in [1,12]$.

Subsequently, the computed errors per station are varied following a log-normal distribution with a mode of $\sigma^B_{s,j}$. Again, in order to achieve a log-normal distribution, a random standard deviation $\sigma^B_{i,random}$ must be set which is consistent per element $i \in [1,500]$ of the ensemble. Similar to the observation errors, this means that each observation site s has identical values of background errors for every month m within one year but each station may have unequal errors for the different years j of one element i of the ensemble. The lower and upper limits of the background mixing ratio uncertainties are hereby 0.5 ppb and 150 ppb.

The diagonal elements of one error covariance matrix $\mathbf{B}^{B,j}_i(k,k)$ for $k \in \{s \in [1,41]\} \times$

$\{m \mid 0 \leq m \leq 12\}$ and $i \in [1{,}500]$ are finally defined as the variances $\left(\sigma_{s,j}^{B,i}\right)^2$.

Other than the observation error covariance matrix $\mathbf{R}$, $\mathbf{B}^B$ is not a diagonal matrix and the non-diagonal elements are defined by applying correlations in space and time. The computation of the non-diagonal errors $(\sigma_{m,n})^2$ with m the corresponding row and n the corresponding column of the symmetrical matrix $\mathbf{B}_i^B$ is similar to the implementation of correlations for the prior error covariance matrices $\mathbf{B}_i^S$ Section 3.3.2.2:

$$(\sigma_{m,n})^2 = (\sigma_{n,m})^2 = \left(\frac{(\sigma_{m,n=m})^2 + (\sigma_{m=n,n})^2}{2}\right) \times \exp\left(-\frac{\Delta t}{t_{corr}}\right) \times \exp\left(-\frac{\Delta d}{d_{corr}}\right) \tag{VII.9}$$

with Δt the temporal difference between the rows/columns m and n and Δd the spatial difference referring distance between the two corresponding measurement sites. The correlation lengths are d_{corr} =500 km for spatial correlations and t_{corr} =one week for temporal correlations.

3.4 Results

3.4.1 Performance of the inversions in the observation space

To evaluate the performance of the inversion, the prior and posterior CH_4 mixing ratios are compared to the observations. Figure VII.7 shows the Taylor diagrams indicating the Pearson correlation coefficient to determine similarities between the observations and simulations as well as the normalized standard deviation (SD) displaying how well the variability of the modelled mixing ratios is captured. Thus, a shorter distance to the reference point indicates a closer fit to the measured mixing ratios. In Figure VII.7, we split results for the full data set and de-trended data. The performance of the simulations for the full data set is mostly driven by the long-term trend. The de-trended data exhibits the performance in terms of seasonal cycle.

In general, and as expected, the posterior results show a better agreement with the observations compared to the prior mixing ratios of the corresponding observation site. This is more distinctive for the trended (Figure VII.7a to Figure VII.7c) than for the de-trended time series (Figure VII.7d to Figure VII.7f), although in both cases the majority of the posterior mixing ratios is closer to the measurements than the prior ones. This confirms that the climatological priors are not realistic and the inversion can realistically improve the flux trends. Both the normalized standard deviation and the correlation coefficient should ideally be close to 1. The prior trended SD range between 0.19 and 1.62 and the correlation coefficients between 0.20 and 1.09. For the posterior results the values lie between 0.19 and 1.00 (standard deviation) and 0.29 and 1.0 (correlation coefficient). Regarding the de-trended time series the normalized SD lies between 0.19 and 2.61 (prior) and 0.02 and 0.99 (posterior) and the correlation coefficient ranges between 0.20 and 1.41 (prior) and 0.10 and 1.00 (posterior).

The improvement in the posterior results is quite evident for observation sites which are remote from methane emission sources, such as ALT or ZEP (Figure VII.7a), where the posterior results are nearly equal to the observations. H ere, the standard deviations have a maximum deviation of 0.10 from the observations point whereas the difference between the correlations is ≤ 0.02. It is however noteworthy that the prior CH_4 concentrations show already a good agreement with the observations at those remote stations which are often referred to as background observation sites. This good fit can be explained by the fact that background mixing rations are computed using global mixing ratio fields generated by systems optimized using these same remote sites.

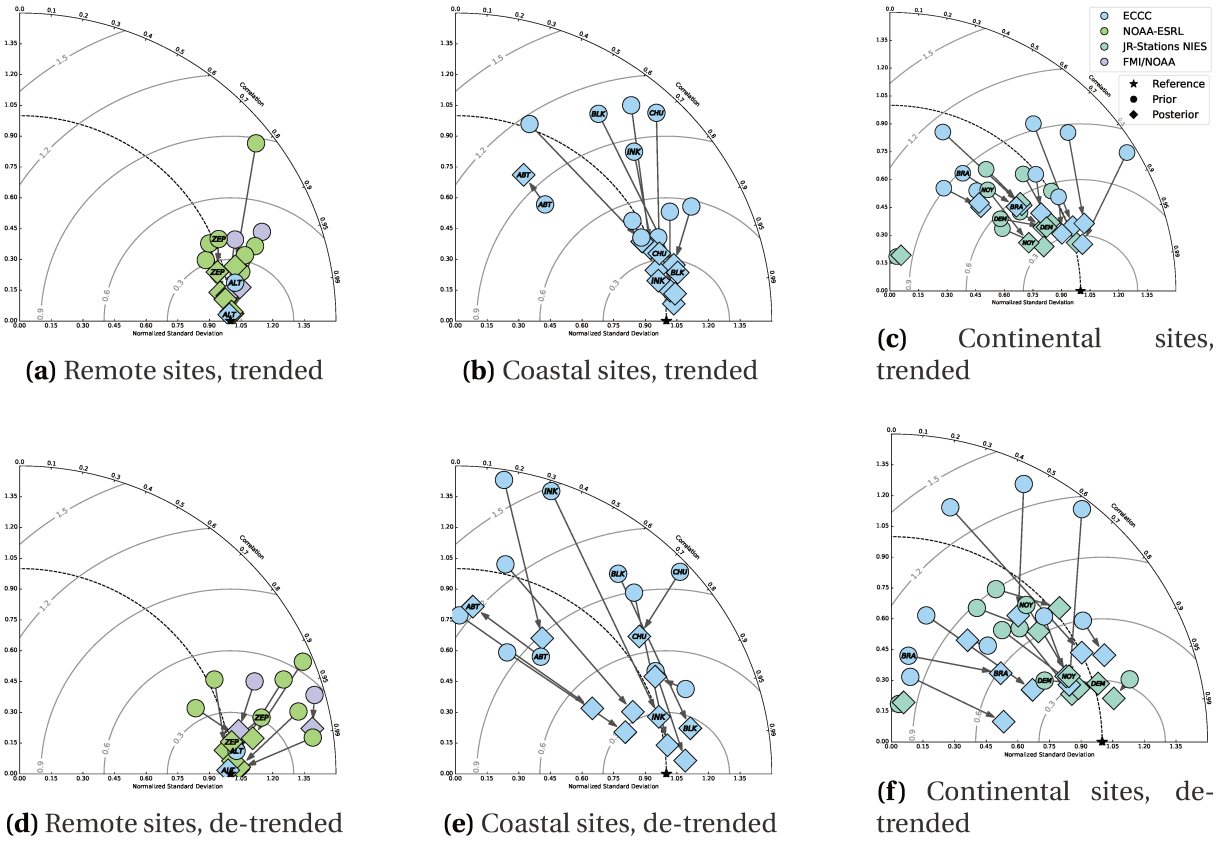

(a) Remote sites, trended

(b) Coastal sites, trended

(c) Continental sites, trended

(d) Remote sites, de-trended

(e) Coastal sites, de-trended

(f) Continental sites, de-trended

Figure VII.7: Examples of Taylor diagrams for various site categories. Raw (upper row) and de-trended (lower row) mixing ratios over the whole period of interest. Prior simulated mixing ratios are indicated with circles, posterior with diamonds.

A much larger improvement can be observed at sites close to the North American coast such as INK, BLK, and CHU (Figure VII.7c). In general, the majority (8 out of 11) of the measurements of the coastal stations has a lower standard deviation than their modelled equivalents which implies that the variability of the modelled mixing ratios is overestimated. The magnitude of the prior modelled CH_4 mixing ratios is overall higher than the measurements at North American observation sites in high northern latitudes (up to approximately 80 ppb; and on average 50 ppb).

The simulations of continental observation sites further South in North America (e.g. BRA) as well as continental sites in Russia such as NOY and IGR (Figure VII.7b) show, in general (8 out of 12 sites), a normalized standard deviation which is lower than the observations. This indicates an underestimation of the variability in the simulated CH_4 mixing ratios, both in the prior as in the posterior results. However, the correlation with the observations could still be improved by the inversion.

The only observation site where the posterior results show less agreement with the corresponding measurements is ABT (Figure VII.7b) where, in contrast to most other sites in North America, the observations are significantly higher than the simulated CH_4 mixing ratios by up to approximately 100 ppb. Local fluxes (mostly from urban environments) and complex topography (mountain range surrounding the flat area around Vancouver, Canada) are likely to influence the observations at this site and are ill represented by the model at a coarser resolution. A higher transport resolution and finer scale inversion regions could solve this issue in a future study; stations too close to urban centers and in too complex topographical configurations could also be discarded altogether to pan-Arctic studies focusing on large scale

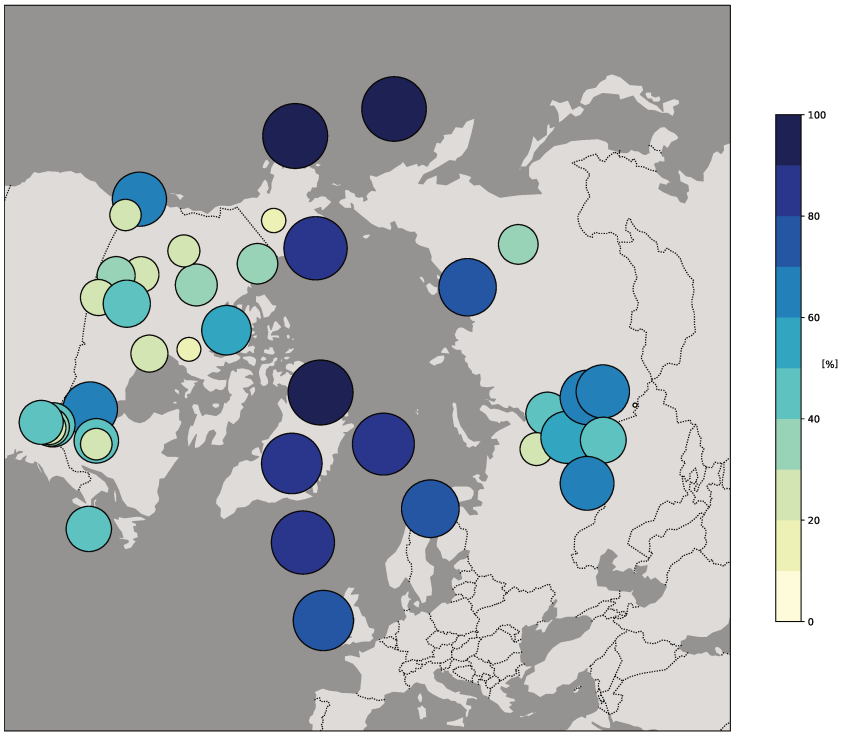

Figure VII.8: Sensitivity of the inversion to observation sites as derived from by the sensitivity matrix **HK**. Larger and darker circles indicate a higher usage of available observations [%] by the inversion. The percentage thereby shows the share of used and theoretically available measurement data.

patterns.

3.4.2 Distribution of information in the inversion system

3.4.2.1 Impact of observations on the inversion system To further analyze the network efficiency, the sensitivity matrices **HK** (see Section 3.2.2.2) are calculated for each year and averaged over the whole period of interest (Figure VII.8). The percentages indicate how much of the theoretically available observations at each site are actually used by the inversion. The observation sites which are located remotely from any other stations, mostly along the Arctic, Atlantic and Pacific oceans shores, show values of almost 100 % which means that the information provided by the measurements are almost entirely used, mostly to constrain background concentrations. This is confirmed by the amplitude of the background at these sites, as shown in Figure D.5, where the ratio between the standard deviation of the simulated signal from the background and from emissions has been computed and show similar patterns than the sensitivity to observations. In areas where the observation network is much denser (e.g. in the Southeast of Canada, and in a lesser extent in Siberian lowlands), most observation contribute for less than 50 % to the inversion. Lower constraints in dense continental areas are caused either by redundant constraints by neighbouring sites in the same emission areas and/or higher noise due to transport errors from nearby emissions. The latter has the largest impact if the site is located close to CH_4 emission sources.

3.4.2.2 Noise and information content in the inversions The trace of the influence matrix $tr(\mathbf{KH})$ (equal to the trace of the sensitivity matrix, $tr(\mathbf{HK})$) indicates how much noise is contained in the provided observations, and how the information content is used by the inversion (Section 3.2.2.2). The closer the value of $tr(\mathbf{KH})$ is to the number of available ob-

servations, the more useful is each given observation for the inversion. Furthermore, the ratio between the number of observations used to constrain the emissions and used to constrain the background mixing ratios can be determined by separately calculating $tr(\mathbf{KH_{emis}})$ and $tr(\mathbf{KH_{back}})$, using only the corresponding elements of $\mathbf{KH}$. The obtained traces for each year are given in Table D.2 (see supplements) and Figure VII.9 shows the ratio between $tr(\mathbf{KH_{emis}})$ and $tr(\mathbf{KH_{back}})$.

In total, $tr(\mathbf{KH})$ ranges between approximately 60 and 75 % of the number of available observations, with the majority constraining the background mixing ratios. Only around 10 % of the available observations are used for constraining the emissions, whereby the share remains relatively constant through the years. Moreover, it is noticeable that the trace of $\mathbf{KH}$ is closer to the number of observations during the years in which the smallest numbers of measurements are provided (e.g. 2008 and 2019).

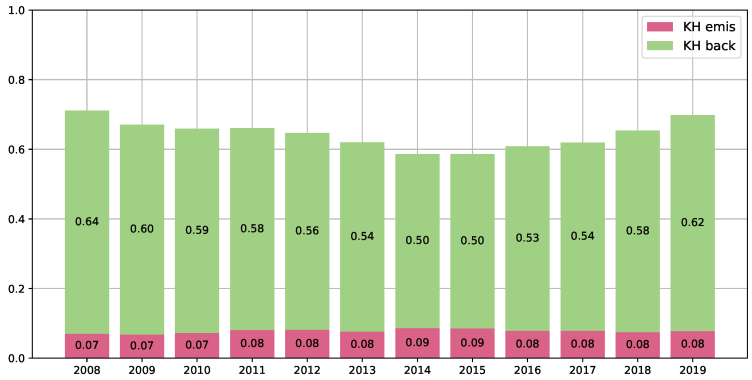

Figure VII.9: Traces of influence matrices divided by the number of available measurements of the corresponding year. See Sect. 3.2.1 for details on the computation of the influence matrix. The closer $tr(\mathbf{KH})$ is to 1, the more observations are used in the inversion.

With this limited availability of data, a higher percentage of the observations is used as information for the inversion. By contrast, in years during which more observations are available (e.g. 2015), a higher share is identified as noise and hence redundant information, similarly to spatial redundancy in regions where the observation network is denser.

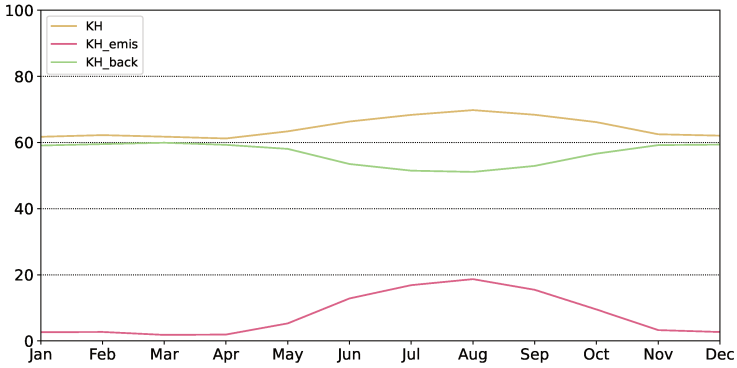

Figure VII.10: Seasonal variation of $tr(\mathbf{KH})$ averaged over the period of interest (2008-2019). The monthly traces are divided by the number of available observations for the corresponding month.

The fraction of useful information in the available observations follows a seasonal variability as shown in Figure VII.10 (see Figure D.3 in the supplements for seasonal variations of

the individual years).

The constraints on the emissions during winter are relatively small since the CH_4 emissions are comparatively smaller than during the summer months, but also because meteorological conditions (in particular a stratified cold boundary layer) make the comparison of observations with simulations more challenging. During the summer months, a higher fraction of observations (up to 20 %) is used to constrain emissions. In general, the total trace $tr(\mathbf{KH})$ is higher during the summer month which means that less of the observations are identified as noise. However, additional constraints on the emissions during summer do not ensure constant constraints on the background. Instead, a share from the constraints on the background mixing ratio is transferred to constrain the emissions during the summer months.

By construction $tr(\mathbf{KH_{back}})$ is proportional to $\mathbf{B_{back}}$ and $\mathbf{H_{back}}$. $\mathbf{H_{back}}$ cannot be reduced due to the physics of the atmospheric transport (see Table D.4). One way to reduce the share of the information constraining the background in the inversion set-up would be to decrease the uncertainties on the background mixing ratios in $\mathbf{B_{back}}$. This relies, however, also on the performances of simulations of global CH_4 concentration fields. Even though in recent years those applications have already improved, they still do not provide a sufficient level of precision that would allow to reduce the uncertainties for the implementation of our inversion set-up (Inness et al., 2019).

Moreover, the limited transport backwards in time in FLEXPART (10 days in our case) is much smaller than the average residence time of air masses in the Arctic (typically a few weeks; see, e.g., Berchet et al., 2020). Hence part of the influence of Arctic fluxes on observations is diluted in the background in our system. One way of mitigating this issue would be to dramatically increase the backward transport time of virtual particles up to a few weeks; but to limit numerical artefacts, multi-weeks backward simulations need a very large number of particles to be accurate, at the expense of much high computational costs. Another way of solving the issue would be to fully couple FLEXPART within a global circulation model, thus accounting for the influence of fluxes on observations indefinitely backwards in time; this is what is done in, e.g., Maksyutov et al. (2020) or could be done in the Community Inversion Framework with one of the available global models (LMDZ or TM5; Berchet et al., 2021).

3.4.2.3 Spatial distribution of constraints on regions and sources The influence matrix $\mathbf{KH}$ defines how well each emission sector is constrained by the inversion in each sub-region. The majority of the CH_4 sources are quite poorly constrained in the sub-regions defined in Section 3.2.3 with the elements of the influence matrix being less than 10 %. In comparison to that, the wetland emissions are relatively well constrained as shown in Figure VII.11. Hereby, the figure on the left shows the average constraints over all years, the middle and right figure show two exemplary years (2011 and 2014) to highlight inter-annual differences. The remaining years are shown in Figure D.4 in the supplements.

The average values of the annual influence matrices (Figure VII.11a) indicate that the current observation network is able to constrains wetland emissions well for most North American sub-regions. In Eurasia on the other hand, most areas are unseen by the inversion and the well constrained areas are predominantly limited to certain parts of Siberia (e.g. the West Siberian Plains). This is partly due to the distribution of the observation network (the denser the network, the better the constraints) and to the heterogeneity of data collection within the period of interest (some years have much more available observations than others, especially towards the end of the period). As shown in Figure D.4d and Figure D.4g, the extent of the constraints strongly varies between the different years due to the availability of observations in Eurasia. Those variations are can also be noticed in North America, however the well con-

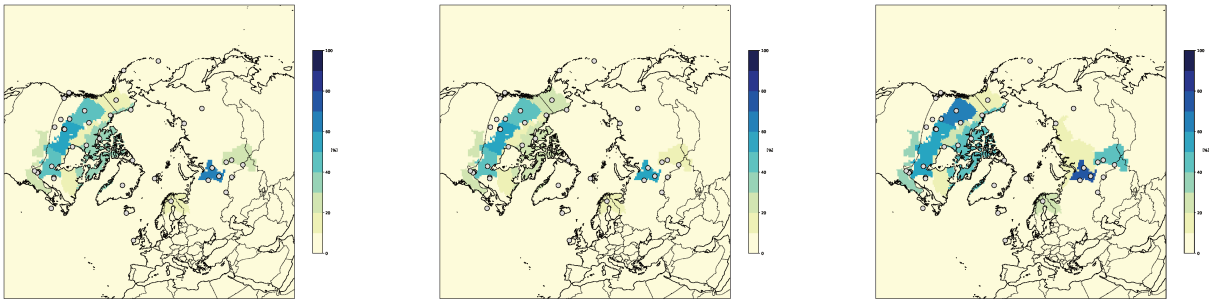

(a) Average **(b)** 2011 **(c)** 2014

Figure VII.11: Regional constraints on wetland emissions as derived from the influence matrix $\mathbf{KH}$. Darker areas thereby indicate higher constraints. The percentages of the areas refer to the corresponding summed elements of $\mathbf{KH}$. The observation sites are marked as grey circles.

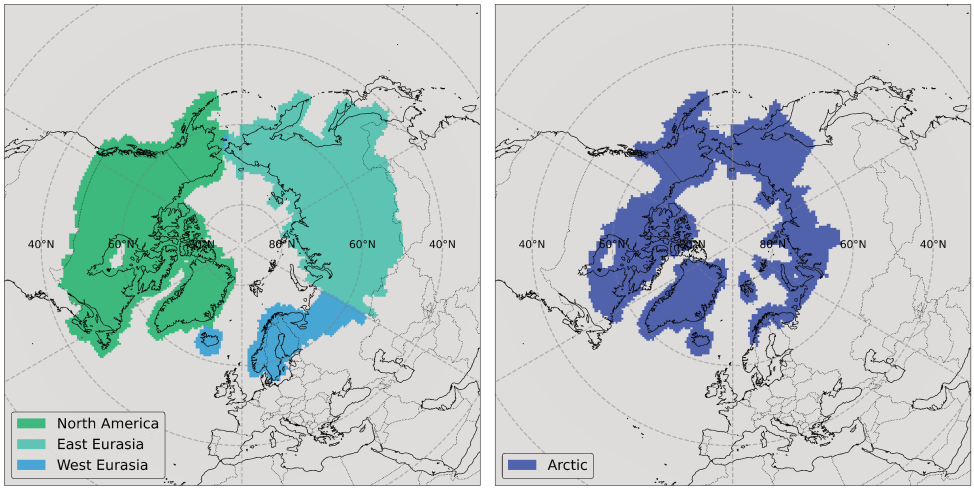

Figure VII.12: Supra-regions for analysis of posterior CH_4 fluxes.

strained areas remain relatively identical over the whole period.

Another cause of the limited constraints on the emissions is that the available observations in Russia are rather used to constrain the background mixing ratios (see Section 3.4.2.2). In North America, where a larger number of observation sites are established and more evenly distributed over the area, the observations of certain stations are used to provide the information on the background.

Installing additional observation sites in high northern latitudes in Eurasia would therefore be useful to better constrain local emissions in the future. However, measurement stations in lower latitudes at the sub-arctic boundary would also be necessary to better constrain transport from CH_4 hotspots such China, India and the Middle East.

3.4.3 Analysis of posterior fluxes

3.4.3.1 Total methane fluxes In order to compare the prior to the posterior fluxes, the area of interest is divided into to four different supra-regions: North America, East Eurasia, West Eurasia and the Arctic (including the High and Low Arctic) as shown in figure Figure VII.12.

Since most emission sources don't show large differences between the prior and the posterior state and are also poorly constrained by the inversion (Section 3.4.2.3), the sectors de-

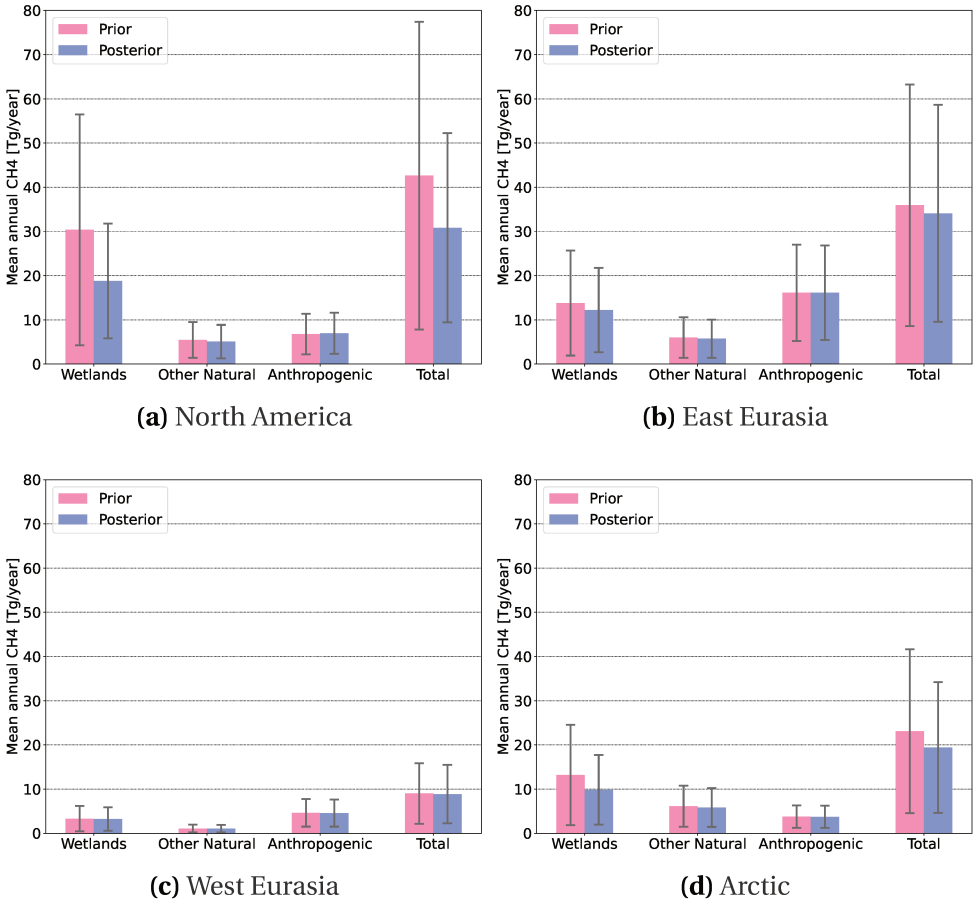

(a) North America **(b)** East Eurasia

(c) West Eurasia **(d)** Arctic

Figure VII.13: Mean annual CH_4 emissions by sector for $\mathbf{x}^{\mathbf{a}}_{\mathbf{max}}$ with corresponding uncertainties.

scribed in Section 3.3.2.1 are combined to wetlands, other natural (including the CH_4 sink from soil oxidation) and anthropogenic emissions. In particular, geological fluxes from the ocean do not deviate significantly from the prior and are not further commented here. Thereby, the combined natural and anthropogenic fluxes from biomass burning are included in the natural emission sources for simplification since the natural emissions are exceed the anthropogenic ones.

The mean annual prior and posterior CH_4 emissions in each region are shown in Figure VII.13 and, more detailed, in Table D.3 for the set-up $\mathbf{x}^{\mathbf{a}}_{\mathbf{max}}$ with the highest log-likelihood (Section 3.2.2.1) together with the corresponding uncertainties obtained from the $\mathbf{P}^{\mathbf{a}}$ matrix. As expected, the poorly constrained anthropogenic and other natural emissions don't show significant changes between the prior and posterior fluxes for either of the regions, neither in their magnitude nor in their uncertainties. The wetland emissions are decreased in the posterior state, except in West Eurasia. The largest decrease is found in North America, which is also the region best constrained by the inversion. Here, the prior wetland emissions have a magnitude of around 30±26 Tg CH_4/year whereas the posterior emissions amount to 19±13 Tg CH_4/year. Even though the uncertainties of the posterior wetland fluxes are still high with around 69 %, they are reduced by around 17 % in comparison to the prior uncertainties. In East Eurasia, the wetland emissions are decreased from approximately 14±12 to 12±10 Tg CH_4/year and in the Arctic from 13±11 to 10±8 Tg CH_4/year with an uncertainty reduction of respectively 8 and 6 %.

Comparison to global inversion set-ups In order to compare this study to other inversion set-ups, the prior and posterior emissions are set against five different posterior states obtained with variational inversion frameworks used for the Global Carbon Project (GCP). The comparative CH_4 fluxes are hereby an updated version of the results from Saunois et al. (2017, 2020). The variational inversions are performed globally with two different inversion systems, CIF-LMDz using surface observations (Thanwerdas et al., 2021) and PYVAR-LMDz using satellite observations from GOSAT (Zheng et al., 2018). The inversion set-ups 1 and 2 use the prior fluxes distributed for the Global Methane Budget and TRANSCOM chemical fields with the latter including OH inter-annual variability from Patra et al. (2021). The third set-up is a sensitivity test where freshwater fluxes are added in the prior state. The mean annual total CH_4 emissions in the different regions are shown in Figure VII.14. Since the GOSAT observations are not available for the years 2008 and 2009, the PYVAR-LMDz posterior results are averaged over the remaining period of interest.

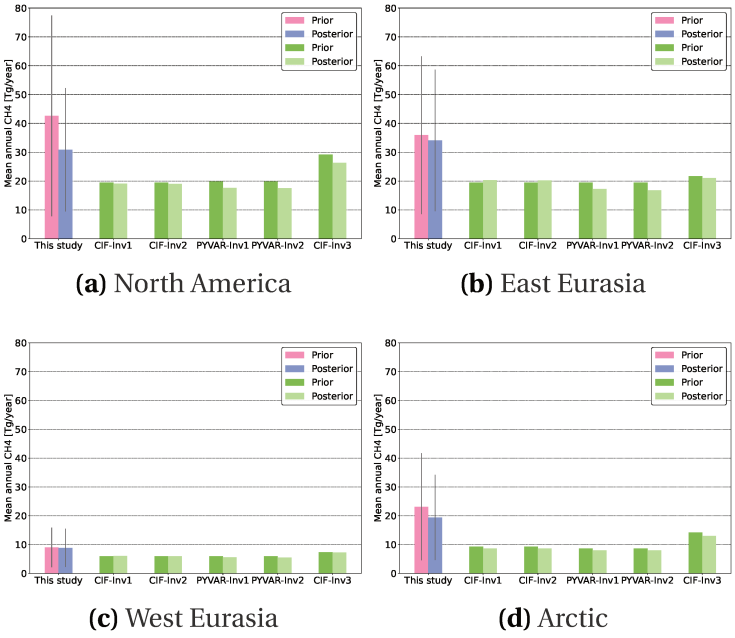

(a) North America **(b)** East Eurasia

(c) West Eurasia **(d)** Arctic

Figure VII.14: Total mean annual CH_4 emissions in comparison to different inversion set-ups from GCP.

In general, the total fluxes of the variational inversion set-ups are all lower than the posterior results of this work. The largest discrepancies are found in the Arctic, where the total posterior fluxes are up to 59 % higher than the results from GCP and only the inversion set-up number 3 lies within the posterior uncertainty range of our inversion set-up. In North America, the CH_4 fluxes of the variational inversion set-ups are between 14 and 44 % lower, in East Eurasia between 38 and 51 % and in West Eurasia between 18 and 38 % in comparison to our posterior emissions. In all of the regions, the results from the inversions using satellite data (PYVAR-LMDz) are the least consistent with the posterior CH_4 emissions obtained in this work. The smallest difference to our results is given by the inversion set-up in which the freshwater emissions are added in the prior state (set-up 3).

As our system explicitly provides posterior uncertainties, contrary to many other inversion systems, it is possible to assess the consistency of our results with other inversions. The discrepancies between the posterior methane emissions from our study and the global variational inversions could be due to the fact that global inverse systems do not perform as well in high latitudes. This has already been identified in Saunois et al. (2017) and can be tracked back to (i) global inversions use fewer observation sites in the Arctic, (ii) global inversions

constrained by satellite measurements have only very few data point above 30°N, (iii) global models with very low resolution cannot reproduce the Arctic atmosphere properly. However, the discrepancies should be further inquired into.

Comparison to previous Arctic studies In comparison to previous studies using inverse modelling to assess methane emissions in high northern latitude regions our results lie roughly in the same magnitude. Thompson et al. (2017) concluded the total CH_4 emissions between 2005 and 2013 to lie between 16.6 and 17.1 Tg/year in North America (above 50°N) and Baray et al. (2021) estimated the combined natural and anthropogenic emissions in Canada at 16.6 and 18.2 Tg/year (between 2010 and 2015). Both values are within the lower limit of the uncertainty range of our ensemble of posterior states in North America (31±15 Tg/year). Berchet et al. (2015) estimated the methane fluxes in the Siberian lowlands to be between 5 and 28 Tg/year in the year 2010 (comparable to region East Eurasia in this study at 34±18 Tg/year). In Eurasia, the total CH_4 emissions obtained by Thompson et al. (2017) are between 55.2 and 59.5 Tg/year which is at the higher limit of the uncertainty range of the results from out study for the combined areas of East and West Eurasia (43±23 Tg/year).

Due to the differences in the spatial extent of the regions covered in those studies it is however difficult to obtain reliable comparisons of the estimated methane emissions.

3.4.3.2 Trends of emission sources In a changing climate, detecting changes in trends of regional emissions in high northern latitudes is critical. Therefore, the trends of all 5000 possible posterior fluxes from the ensemble (see Section 3.2.1) have been calculated by sector and region. The results for wetland emissions, which is the only source well constrained by the inversion, are shown in Figure VII.15 for North America and East Eurasia:

- the mean annual CH_4 emissions are displayed on the horizontal axis and the corresponding trend of the annual wetland fluxes on the vertical axis.
- the associated probability density functions (PDFs) are shown next to the corresponding axes
- the darker shaded segments show the range of the ensemble $\{\mathbf{x}^{\mathbf{a}}_{\mathbf{max}}\}$ with the most plausible error configurations (Section 3.2.2.1) which make out 55 % of the total ensemble.
- the posterior result with the maximum log-likelihood $\mathbf{x}^{\mathbf{a}}_{\mathbf{max}}$ is highlighted as well as the trend and the mean annual emissions of the prior flux estimates.

Since the data set of the wetland emissions is equal for each year within the period of interest, there is no trend in the prior state. The trend of the posterior wetland emissions in North America (Figure VII.15a), including all possible uncertainty configurations, ranges approximately between -7.3 and 12.2 %/year with corresponding mean annual emission between around 15 and 30 Tg CH_4/year. The trends of the corresponding ensemble of $\{\mathbf{x}^{\mathbf{a}}_{\mathbf{max}}\}$ range between -1.4 and 1.2 %/year, with 65 % of the 2740 posterior results showing a negative trend. The most plausible of all set-ups $\mathbf{x}_{\mathbf{max}}$, according to the log-likelihood, also has a decreasing trend of -1.4 %/year. Thus, according to our system, although small (less than 20% per decade), there is a plausible negative (although uncertain) trend on wetland emissions in North America between the years 2008 and 2019.

The trend of the posterior results of the wetland emissions in East Eurasia shown in Figure VII.15b ranges between -7.5 to 11.7 %/year and mean annual amount of CH_4 emissions between 10 to 15 Tg CH_4/year. Here, the elements of $\{\mathbf{x}^{\mathbf{a}}_{\mathbf{max}}\}$ do not include any negative trends with values ranging between 0 and 2.1 %/year and $\mathbf{x}^{\mathbf{a}}_{\mathbf{max}}$ shows increasing trend of 0.8 %/year. The results point to a very small but statistically significant positive trend in East Eurasia. A positive growth rate in CH_4 mixing ratios between 2009 and 2019 in West Siberia was detected by Someya et al. (2020) and attributed to increased wetland emissions in this

area, compatible with our conclusion.

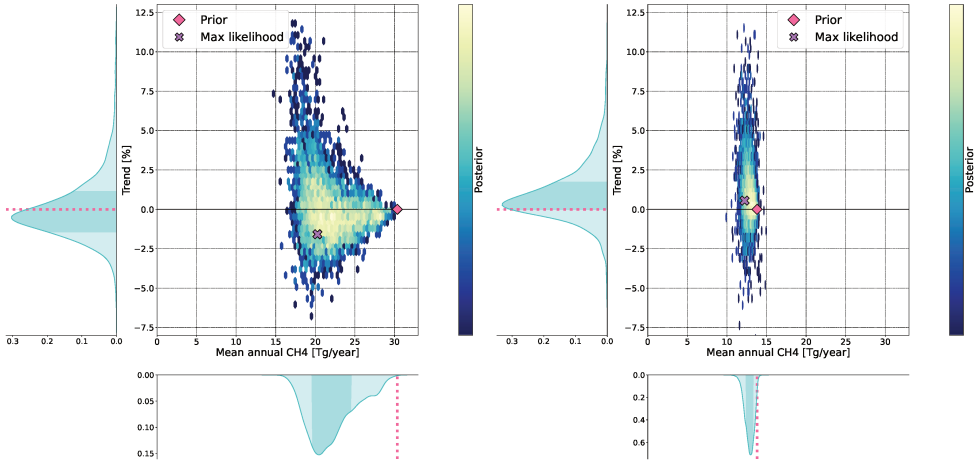

(a) North America **(b)** East Eurasia

Figure VII.15: Trend and mean annual fluxes of wetland emissions for ensemble of posterior results with corresponding density distributions. Brighter colors of scatters indicate a higher density.

To give an example of a CH_4 emission source with a trend in the prior state, Figure VII.16 shows the emissions from biomass burning of the two beforehand discussed regions. Since the uncertainties on the emissions from biomass burning have been chosen to be higher in comparison to the wetland emissions (Section 3.3.2), the posterior results contain several negative CH_4 fluxes, which are not included in the figures. In both regions, the prior state shows an increasing trend of 30 %/year in North America and 9 %/year in East Eurasia with corresponding mean annual emissions of 1.15 and 2.01 Tg CH_4/year.

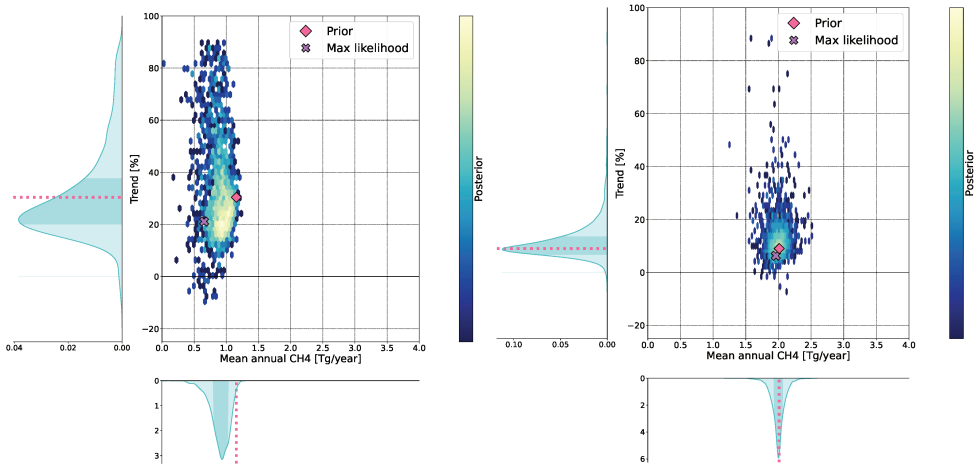

(a) North America **(b)** East Eurasia

Figure VII.16: Trend and mean annual fluxes of biomass burning emissions for ensemble of posterior results with corresponding density distributions.

In North America (Figure VII.16a), the posterior trends show a large variability with values of the total ensemble lying between -11/year and 92 %/year. The trend of the most plausible configuration $\mathbf{x}^{\mathbf{a}}_{\mathbf{max}}$ is around 21%/year which still indicated a positive trend, however lower than the prior estimate. The magnitude of the CH_4 emission from biomass burning in North America is predominantly decreased in the posterior state with $\mathbf{x}^{\mathbf{a}}_{\mathbf{max}}$ being 0.7 Tg/year lower

than the prior mean annual emissions. In East Eurasia (figure VII.16b), the mean annual emissions of the total ensemble lie between 0.35 and 3.47 Tg CH_4/year and the trends show, equally to North America, high variability in the posterior state (between -8 and 89 %/year). The ensemble $\{\mathbf{x}^{\mathbf{a}}_{\mathbf{max}}\}$ on the other hand only shows minor deviations and both the trend and the fluxes are close to the prior state.

It has to be mentioned that, even though the fluxes from biomass burning are partially well constrained in some regions and years, the emissions are poorly constrained throughout the whole period of interest and as described in section 3.4.2.3, the results are highly uncertain.

For most of the methane emissions sources and sinks, the results of the posterior ensemble do not show major deviations from the prior state at all, independent of the prior and observations error.

In addition to that, the obtained trends of the posterior fluxes could as well be influenced by the varying data availability and the the results are therefore still highly uncertain.

3.4.3.3 Seasonal variability Subsequently, the seasonal cycles of the prior and posterior CH_4 fluxes are examined. Figure VII.17 shows the seasonal cycle of the prior and posterior fluxes for the total CH_4 emissions in North America. Hereby, the displayed posterior fluxes are the median values of the ensemble $\{\mathbf{x}^{\mathbf{a}}_{\mathbf{max}}\}$. To achieve a better comparison between the different years, the monthly values are divided by the maximum methane fluxes of the prior state.

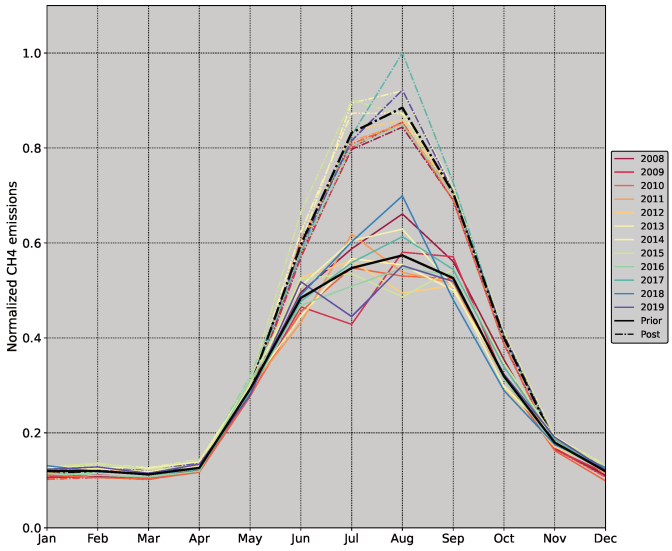

Figure VII.17: Normalized total CH_4 fluxes of prior (dash-dotted lines) and posterior (continuous lines) state per month in North America. The coloured lines display the different years, the black lines show the average over all years.

Over the course of the period of interest, the prior emissions show a greater consistency in the annual seasonal cycles. The peak of the emissions are predominantly in August, sporadically already in June. The sectors that contribute to the seasonal differences of the prior state are emissions from wetlands and biomass burning as well as the soil oxidation (section 3.3.2.1). Since the data set of the wetland emissions and the soil oxidation are consistent for each year, the differences in the seasonality of the prior fluxes is entirely driven by the CH_4 fluxes from biomass burning. In comparison to that, the average of the posterior state still reaches the maximum emissions in August, however the peak is less pronounced and the

emissions decrease more gradually during the autumn months. The annual seasonal cycles of the posterior fluxes are more divergent from each other. The majority of the years still show the highest methane emissions in August, although some years (e.g. 2012 and 2015) have a local minimum during that month. Unlike the prior state, the differences in the seasonal fluxes of the different years are not exclusively influenced by emissions from biomass burning. As shown in figure VII.18, most of the changes in the seasonal cycle of the total CH_4 emissions arise from adjustments of the monthly wetland fluxes since the local high and low points are predominantly during the same time of the year.

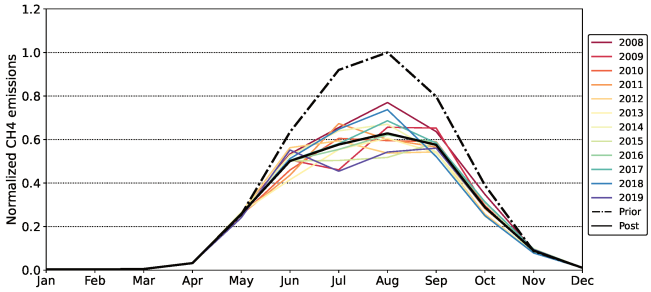

Figure VII.18: Normalized wetland CH_4 fluxes of posterior state per month in North America. The black dash-dotted line shows the average prior, the continuous line the average posterior state.

The other three regions assessed in this study show similar minor changes in the seasonal cycles which are predominantly influences by wetland emissions and don't show any clear seasonal pattern between the different years.

3.4.3.4 Inter-annual variability Finally, we inquire into the inter-annual differences of the methane emissions. Figure VII.19 shows a time series of the total CH_4 fluxes in prior and posterior state. The posterior emissions are again obtained by calculating the median of the most plausible results $\{\mathbf{x}^{\mathbf{a}}_{\mathbf{max}}\}$, with the corresponding minimum and maximum values of this ensemble marking the uncertainty range. Therefore, in the following section, the given quantification of the monthly CH_4 emissions refers to the median values.

In West Eurasia (figure VII.19c) there is effectively no inter-annual variability, neither in the prior nor the posterior state, with peak values of the 1.2 Tg CH_4/month each year; small deviation from the prior comes from very small constraints on that region. Similarly, the emissions in the Arctic (figure VII.19d) show very little deviations in the prior state, with the maximum fluxes only deviate by 0.1 Tg. The posterior fluxes on the other hand gradually decrease from a peak value of 4.0 CH_4/month in 2008 to 3.1 CH_4/month in 2015, which marks the year with the largest difference to the prior state. In the following years the emissions slightly increase again to a maximum value of 3.3 Tg/month and stay constant until the end of the period of interest. In East Eurasia, shown in figure VII.19b, the inter-annual variations are fairly low both in the prior and posterior state. According to the prior estimates, the highest methane emissions occur in 2012 with a peak value of 5.6 CH_4/month. Also, the fluxes are slightly lower in the beginning of the period of interest (around 4.9 Tg) than during the last four years (around 5.4 Tg). The posterior emissions mostly follow that pattern with a maximum reduction of 0.5 Tg in 2012. The most prominent variabilities are, unsurprisingly, found in the North America (figure VII.19a) which is best constrained by the inversion. As mentioned before, the inter-annual differences of the prior state are caused by variations in the emissions from biomass burning. The largest prior total methane emissions occur in 2017 with a maximum of 9.5 Tg CH_4/month, the year with the lowest peak emissions (7.9 Tg CH_4/month) is 2008. Like the emissions in East Eurasia, the peak values of the prior state are

generally higher during the last years of the period of interest whereas the years with the lowest CH_4 emissions can be found at the beginning. The posterior fluxes in North America vary between peak emissions of 5.0 Tg (2015) and 6.6 Tg (2018) without showing a clear pattern. In fact, the year 2008, which shows the lowest emissions in the prior state, has the second highest methane fluxes of all years whereas the emissions in the year 2019 are almost as low as in 2015.

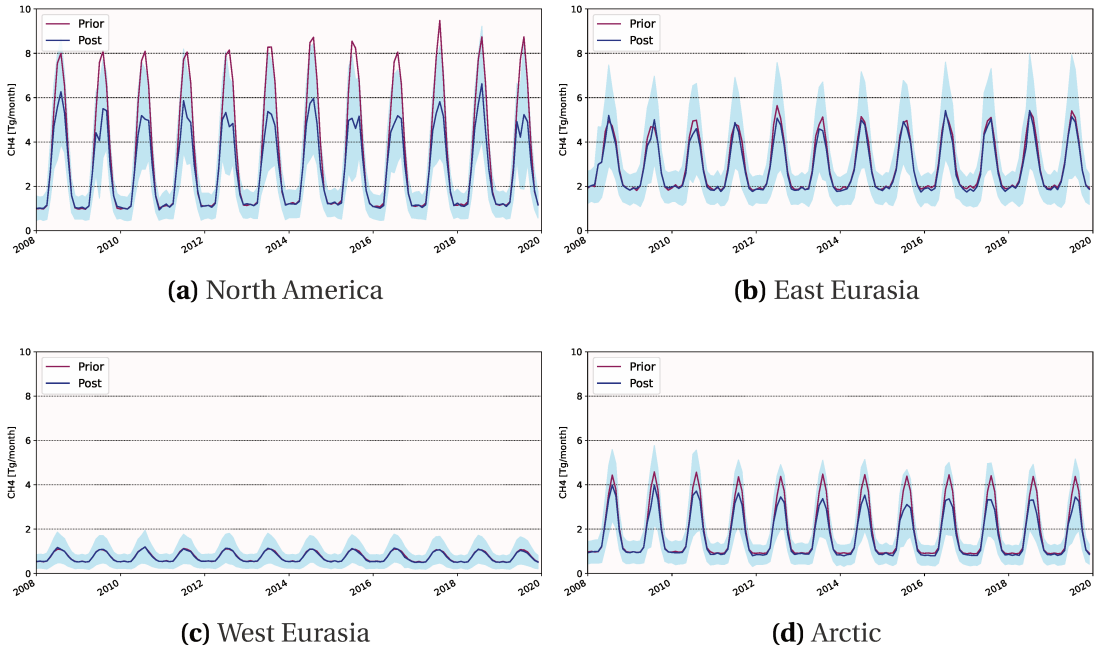

(a) North America **(b)** East Eurasia

(c) West Eurasia **(d)** Arctic

Figure VII.19: Total seasonal prior (purple) and posterior (blue) CH_4 emissions between 2008 and 2019.

An explanation for the large discrepancies in the inter-annual variabilities between the prior and the posterior state in North America is the reduction of fluxes from biomass burning in the posterior state which are shown in figure VII.20. The prior estimates show a large variability with exceptionally high emissions in the years 2013 to 2015 and, most evident, in the year 2017 with up to 1.4 Tg CH_4/month. These increased emissions during certain years do not agree with the observations though which is why the peak emissions in the posterior state are up to 50 % lower.

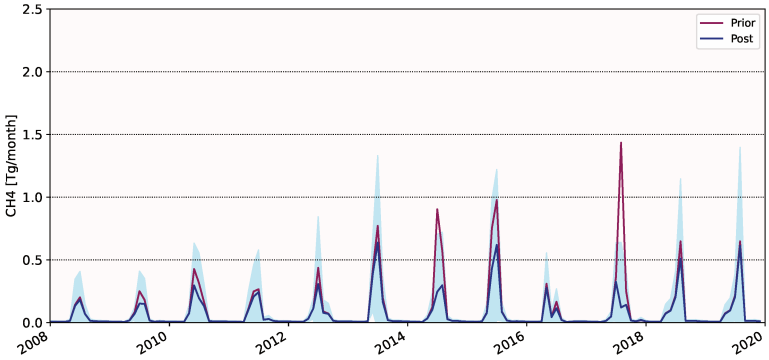

Figure VII.20: Seasonal CH_4 emissions from biomass burning between 2008 and 2019.

Another factor that has to be taken into account when analysing the posterior inter-annual variabilities is the inconsistent availability of observations throughout the different years. For

years during which only few information from the measurements are available, the posterior state is likely to be closer to the prior.

3.5 Conclusion

We designed an inversion system to constrain CH_4 surface fluxes in high northern latitudes based on surface observations in Arctic regions and an atmospheric transport model. Extensive sensitivity tests were carried out to comprehensively assess the methane emissions and uptake, respectively, from different CH_4 sources and sinks during the years 2008 to 2019. We aimed to reduce uncertainties on current bottom-up estimates and thereby gain a more accurate understanding of the the extent, seasonality and inter-annual trends of methane emissions in Arctic and Sub-Arctic regions. In order to achieve that, we computed a total of 5000 posterior states of posterior methane fluxes with varying uncertainties on the observations, background mixing ratios and prior flux estimates and evaluated their plausibility to get a reliable assessment of the methane emissions in high northern latitudes.

The atmospheric observations used for this study included both quasi-continuous and discrete measurements from 41 observation sites in different Arctic nations. We found that this observations network is not sufficient to satisfactorily constrain most CH_4 sources and sinks in high northern latitudes over the whole period of interest. Only wetland emissions are adequately constrained in North America and sporadically in Russia although with inter-annual variabilities. It is therefore not possible to reduce uncertainties on most CH_4 emissions sources and sinks occurring in high northern latitude regions to a substantial extent. Besides, a considerable share of the observations is used by the inversion to constrain the background mixing ratios. This share could be reduced by improved initial CH_4 mixing ratio fields which would allow for lower uncertainties on the background. Moreover, additional stations at the sub-arctic boundary would be necessary to better constrain transport from CH_4 hotspots such China, India and the Middle East. If adding stations in the buffer zone, which in this case included latitudes from 30 °N, would improve the constraints on high northern latitude regions should be investigated further.

The obtained posterior CH_4 fluxes were, in comparison, predominantly lower that the prior estimates though still higher than comparable posterior results from variational inversion set-ups. In North America, the average total methane fluxes were reduced by around 11 Tg/year with a corresponding uncertainty reduction of 26 %. In East Eurasia and the Arctic, fluxes were declined by 2 and 3 Tg/year, respectively, with uncertainty reductions of 13 (East Eurasia) and 12 % (Arctic).

Significant changes in the seasonal cycles of the methane emissions could not be observed in either of the regions studied. Minor shift in the seasonal cycles in certain years were exclusively influenced by CH_4 emissions from high-latitude wetlands.

Inter-annual differences were most significant in North America where the largest discrepancies between the prior and posterior state could be observed since the region is well constrained. Whereas the highest peak emissions in the prior state took place at the end of the period of interest, raised methane emissions in the posterior state were predominantly observed at the start. The CH_4 peak emissions were hereby also up to 4.3 Tg/month lower. Those differences can be explained by a reduction in emissions from biomass burning, which appear to have been overestimated for certain years (e.g. 2014 and 2017) in the prior estimate.

The wetland emissions in North America showed a small decreasing trend between 2008 and 2019 whereas the CH_4 emissions from wetlands in East Eurasia were slightly increasing within the period of interest. Since most regions in the Arctic and Sub-Arctic were poorly constrained by the inversion, most methane emissions sources as well as the soil oxidation

didn't show any significant trends in the period under study.

To get a conclusive understanding about magnitude, long-term trend and seasonal variability of methane emissions in the entire Arctic region, it would be beneficial to expand the observation network, especially in Eurasia, to better constrain the area for future works. Complementary approaches bringing fixed and mobile platforms (ships, aircrafts, trains, etc.) together should also be explored to refine our understanding of the regional Arctic budget (e.g., Pankratova et al., 2022; Berchet et al., 2020; Pisso et al., 2016; Thornton et al., 2020, etc.). New satellite platform may also in the future expand our coverage of Arctic methane emissions, even though technical difficulties (albedo, clouds, etc.) hampers our capability to use high-latitude satellite retrievals.

This is particularly important since ongoing environmental changes due to rising temperatures in high northern latitudes are affecting natural sources and sinks of CH_4, further complicating the estimation and prediction of Arctic methane emissions, their contribution to the global budget and the resulting potential climate feedback.

CHAPTER

VIII

Network detectability of the Arctic "methane bomb"

Contents

THE FINAL CHAPTER OF THIS PART IS DEDICATED to a study focusing on the detection of potential future increases in methane emissions from the Arctic region. Like the work presented in the previous chapter, this study was conducted by implementing an analytical inversion, however in this case integrating synthetic observations based on speculative scenarios of methane emissions and observation networks.

1 Motivation

In Chapter VII, we attempted, amongst other subjects, to detect trends in the present methane sources in the Arctic and Sub-Arctic during the most recent years. By analyzing the regional constraints on the different sources it has however been shown that only CH_4 emissions from high northern latitude wetlands are adequately constrained by the inverse modelling set-up for large parts of the Arctic region. The detected most plausible trends on wetland emission are thereby small with around -1.4 % yr^{-1} in North America and 0.08 % yr^{-1} in East Eurasia. Meaningful conclusions about the trends of methane sources which were not sufficiently constrained by the inversion (e.g. oceanic CH_4 fluxes) could therefore not be drawn.

The sensitivity of the various CH_4 sources and sinks present in high northern latitudes to increasing temperatures and the thereby induced environmental changes have been discussed in detail in Part I (Chapter II, Section 2). The multiplicity of the different feedbacks potentially enhancing natural CH_4 emissions in the Arctic is very drastically expressed in some studies: it is called *a sleeping giant*, (Mascarelli, 2009), *a methane time bomb* (Glikson, 2018) or even *the methane apocalypse* (Ananthaswamy, 2015). The "methane bomb" is thereby predominantly connected with the thawing of terrestrial and subsea permafrost and the resulting exposure of large pools of degradable carbon (e.g. Whiteman et al., 2013; Glikson, 2018), described more in details in Part I, Chapter II, Section 3. For instance, Shakhova et al. (2010) estimated that around 50 Gt of methane could be released from gas hydrates over the course of 50 years in the ESAS (East Siberian Arctic Shelf) alone. Regarding terrestrial permafrost, predictions assume that until 2100, up to 274 Pg of carbon could be released to the atmosphere, with CH_4 making up around 2.3 % those carbon releases, while however accounting for 40 to 70 % of the permafrost-affected radiative forcing (Schneider von Deimling et al., 2015; Walter Anthony et al., 2018).

However, other studies assessing the potential of a possible "methane bomb" in the Arctic are more optimistic. For instance, McGuire et al. (2018) concluded that substantial net losses of carbon from northern permafrost regions would not occur until after 2100 under the condition that effective climate protection policies are implemented. A similar result concerning the Siberian region was achieved by Anisimov and Zimov (2021), who demonstrated that the feedback between thawing wetlands in Siberia and the global climate have been significantly overestimated. According to them, CH_4 emission from Siberian wetlands will increase by less that 20 Tg yr^{-1} by the mid of the 21st century, which would lead to an increase in global temperatures less than 0.02 °C. A recent study by Schuur et al. (2022) on the carbon cycle feedbacks from the Arctic warming also came to the result that the idea of a sudden "methane bomb" in the Arctic, whereby overwhelming levels of CH_4 are released to the atmosphere over the course of a short period of time, is currently not supported by observations or projections. However, new phenomena associated with increased CH_4 releases (e.g. methane craters described in Part I, Chapter II, Section 3.1) should be considered as potential contributors to methane emissions from the Arctic regions in the future.

Apart from the likelihood of an Arctic "methane bomb" in the near future, the objective of this chapter is to analyze the capability of the stationary observation network to properly detect such an event, since, as discussed beforehand, the region is generally poorly constrained.

This study therefore aims at discussing the following question:

Question 3: *To which extent are future increases of CH_4 emissions in the form of an Arctic "methane bomb" accurately detected by the current network of observation sites, and what improvements can hereby be achieved by a hypothetically extended network?*

Thereby, two different network scenarios are used with the first one consisting of the currently installed in situ measurement stations (Part II, Chapter V, Section 1.1.2) and the second network including further, hypothetical measurement sites (based on network extensions planned to our knowledge as of today). In order to simulate a future methane bomb, emission scenarios involving different sources of CH_4 are anticipated to compute synthetic future observations of methane concentrations.

2 Method

To carry out this study, a framework similar to the one described in the previous chapter has been applied. The basis is hereby a Bayesian inversion framework including backward simulations from the Lagrangian particle dispersion model FLEXPART (Part II, Chapter V, Section 2) and a set of bottom-up estimates of CH_4 source and sinks used as prior information (Part II, Chapter V, Section 3).

However, in this part of our work, we want to study different future scenarios of CH_4 emissions and it is therefore not possible to use measurements of CH_4 mixing ratios as a component of the inversion. Instead, we simulate synthetic observations based on assumptions on different CH_4 sources. The approach and components of the inverse modelling method is outlined in the following sections.

2.1 Framework of the inversion

The Bayesian inversion framework is used for applying the analytical method, aiming at explicitly and algebraically finding the optimal posterior state of a system $\mathbf{x}^a$ and the corresponding uncertainties $\mathbf{P}^a$. This approach is defined by:

$$\begin{cases} \mathbf{x}^a &= \mathbf{x}^b + \mathbf{K}(\mathbf{y}^o - \mathbf{H}\mathbf{x}^b) \\ \mathbf{P}^a &= \mathbf{B} - \mathbf{K}\mathbf{H}\mathbf{B} \end{cases} \tag{VIII.1}$$

with $\mathbf{K}$ the Kalman gain matrix given by:

$$\mathbf{K} = \mathbf{B}\mathbf{H}^T(\mathbf{R} + \mathbf{H}\mathbf{B}\mathbf{H}^T)^{-1}. \tag{VIII.2}$$

In this study, a time period of 36 years is covered (Section 3.1). For computational reasons, this period has been split into 36 independent 1-year inversion windows which are computed separately.

The prior knowledge of the state, in this case surface fluxes and soil uptake of CH_4, is defined by the control vector $\mathbf{x}^b$. Here, $\mathbf{x}^b$ also contains information on the initial CH_4 background mixing ratios. The corresponding uncertainties are specified in the prior error covariance matrix $\mathbf{B}$. The uncertainties are hereby obtained from the study presented in Chapter VII whereby a Monte Carlo approach is implemented with an ensemble of plausible sets of covariance matrices. For the study described here, the error covariance matrix $\mathbf{B}$ with the maximum log-likelihood from this ensemble is chosen (described more precisely in Chapter VII, Section 3.2.2).

$\mathbf{B}$ is hereby composed of two matrices accounting for the different errors: $\mathbf{B_{prior}}$ contains the uncertainties on the prior state and $\mathbf{B_{back}}$ the uncertainties on the background mixing ratios. $\mathbf{B_{prior}}$ is directly obtained from the Monte Carlo ensemble and is therefore the matrix with the maximum log-likelihood $\mathbf{B_{prior,max}}$. $\mathbf{B_{back}}$ on the other hand is dependant on the number of available observations. Since in this work, the number of observations is not identical to the study carrying out the Monte Carlo sampling, the average uncertainties of $\mathbf{B_{back,max}}$ was used instead.

The observation operator is assumed to be linear since chemical oxidation of CH_4 by free radicals in the atmosphere is neglected for this application. It is therefore defined as its Jacobian matrix $\mathbf{H}$ and contains the simulated equivalents of the observations Section 3.3.

2.2 Synthetic future observations

In classical inverse modelling approaches, the observation vector $\mathbf{y^o}$ contains available observations, e.g. on CH_4 mixing ratios. In this work we want to study different future scenarios of CH_4 emissions and therefore, the "observations" are simulated using different assumptions. The true state of the CH_4 emissions is defined as $\mathbf{x^t}$ and changes with a given trend k, which is constant throughout all the years within the period of interest. The observations vector for a given year j can then be calculated as:

$$\mathbf{y_j^o} = \mathbf{H}(\mathbf{x_{j-1}^t} + \mathbf{x_{j-1}^t}k). \tag{VIII.3}$$

The corresponding uncertainties defined by the observations error covariance matrix $\mathbf{R}$ is also based on the Monte Carlo ensemble described before. Like the uncertainties on the background mixing ratios, the size of $\mathbf{R}$ is dependant on the number of available observations and can therefore not be directly obtained from the ensemble. Instead, the average of the matrix with the maximum log-likelihood $\mathbf{R_{max}}$ defines the uncertainties on the observations.

3 Material

The majority of the material used in this study, including the prior estimates, the applied transport model and the observation network, has already been described in detail in Part II, Chapter V as well as in the preceding chapter (Chapter VII). In order to avoid superfluous repetitions, the important characteristics of the already introduced components are just briefly recapitulated whereas the additional material is described more comprehensively.

3.1 Area and period of interest

The period of interest covers 36 years and ranges from 2020 to 2055. This period of time has been chosen to carry out a long-term study of possible future scenarios of methane emissions to the horizon of the middle of the century.

The area for this study is identical to the region used for the inverse modelling approach described in Chapter VII, Section 3.2.3. The total area includes all latitudes above 30 °N which is divided into 121 sub-regions proposed by RECCAP (Ciais et al., 2022), shown in Figure VIII.1. Hereby, the white stars show the locations of the observation sites which are described in more detail in Section 3.4.

3.2 Prior information and simulated CH_4 mixing ratios

The different methane sources and sinks used as prior information are based on a set of different emission inventories and land-surface models, which are described in Part II, Chap-

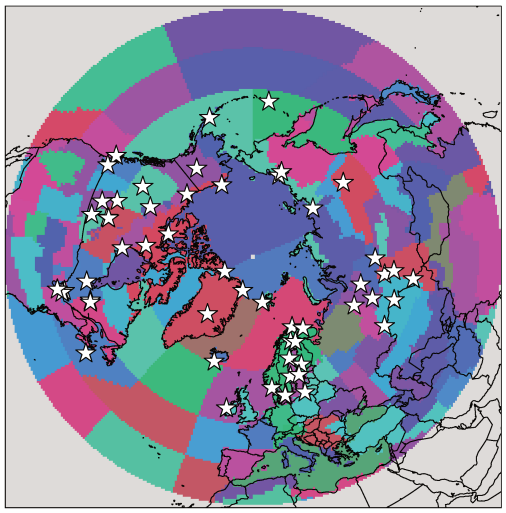

Figure VIII.1: RECCAP regions above 30 °N. The white stars indicate the observation sites used in this study.

ter V, Section 3.3.2. Natural methane sources include hereby emissions from high northern latitude wetlands, geological fluxes, CH_4 emissions from the Arctic Ocean and wildfire events. The CH_4 emissions related to anthropogenic activities include the exploitation and distribution of natural gas and mineral oil, agricultural activities as well as waste managements and biofuel burning. Soil oxidation due to microbial activities is included in the form of negative CH_4 emissions.

3.3 Simulated CH_4 mixing ratios

The simulated CH_4 concentrations are obtained by using FLEXPART simulations of backward trajectories prepared for the study presented in the previous chapter (described more in details in Chapter VII, Section 3.3.3.1). The obtained footprints were computed by releasing 2000 virtual particles at each observation site, which were followed 10 days backward in time covering the years 2008 to 2019.

As mentioned in Section 3.1, the period under study covers the years 2020 to 2055. To represent this period of time, which partly lies in the future, we take the existing FLEXPART simulations (covering 12 years) and string together this sequence of footprints three times in a row. It is hereby assumed that the climatology of atmospheric transport and fluxes does not change significantly in the 36 years following the year 2019.

3.4 Observation Network

As described in Section 2, the observations used for the inverse modelling approach are based on simulated CH_4 mixing ratios assuming different emission scenarios. We use however an existing network of measurement sites located in high northern latitudes. The corresponding stations include hereby both in situ and flask measurements. To simulate an "optimal" observation network, we assume that all of those observation sites provide continuous measurements.

Two different network scenarios are used for this study. The first one, from here on referred to as *current*, includes all observation sites whose data was provided to us for the inverse modelling study described in Part II, Chapter V, Section 1.1.2. The second network, referred to as *extended*, includes additional observation sites in high northern latitudes. The different observation networks are shown in Figure VIII.2, page 126.

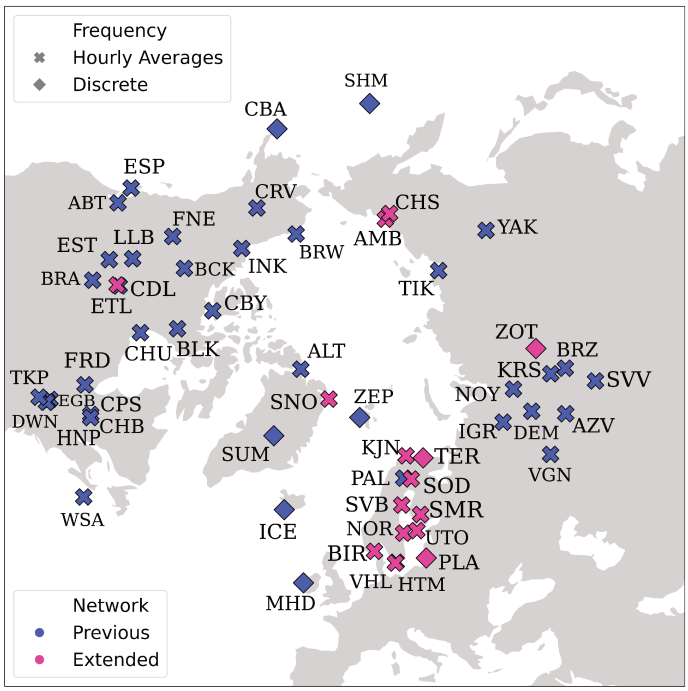

Figure VIII.2: Observation sites used for this study. The current network is shown in blue, the additional stations in pink. Crosses indicate quasi-continuous, diamonds discrete measurements. The types of measurements refer to the measurements that are currently taking place at these sites, whereas in this study we assume all measurements to be continuous.

An overview of the current observation network can be found in Appendix D, Table D.1, page 184. The additional stations of the extended network are summarized in Table VIII.1, page 127.

The extended network hereby contains observation sites where measurements of atmospheric CH_4 concentrations are (*i*) only recently available, (*ii*) not taking place anymore or where (*iii*) the measurement data is not publicly available or where (*iv*) the measurements do not consist of mixing ratios but of CH_4 columns or (*v*) CH_4 is currently not measured at all but measurements of other trace gases or air pollutants are taking place. As the observation network is limited at high northern latitudes, these additional stations were added to investigate what benefits a reasonably realistic extended network might offer for constraining methane fluxes.

3.5 Scenarios

For obtaining the potential observations used in this study, we create scenarios by varying four different parameters:

- the CH_4 emission sources
- the speculative trend on the CH_4 emission sources
- the regions in which the trends are applied
- the observation network.

The two different observation networks are described in the previous section (Section 3.4). The CH_4 sources on which an assumed trend is applied (separately) are emissions from wetlands, anthropogenic activities and the Arctic Ocean. Several studies indicate a potential increase in methane emissions from high northern latitude wetlands, for instance in connection with thawing permafrost soils due to rising temperatures (e.g. Schuur et al., 2015).

Table VIII.1: *Additional observation sites of the extended network.*

ID	Site, country	Latitude	Longitude	Elevation (masl)	Operator
SNO	Station Nord, GRL	81.6 °N	16.7 °W	8	ICOS
KJN	Kjolnes, NOR	70.9 °N	29.2 °E	30	Univ. Exeter/ICOS
AMB	Ambarchik, RUS	69.6 °N	162.3 °E	5	MPI-BGC
TER	Teriberka, RUS	69.2 °N	35.1 °E	83	MGO
CHS	Cherskii, RUS	68.6 °N	161.3 °E	23	IASOA
SOD	Sodankyla, FIN	67.4 °N	26.6 °E	227	ICOS
SVB	Svartberget, SWE	64.3 °N	19.8 °E	275	ICOS
SMR	Hyytiälä, FIN	61.9 °N	24.3 °E	181	ICOS
ZOT	Zotto, RUS	60.8 °N	89.4 °E	104	MPI-BGC
NOR	Norunda, SWE	60.1 °N	17.5 °E	46	ICOS
UTO	Utö, FIN	59.8 °N	21.4 °E	65	ICOS
BIR	Birkenes Observatory, NOR	58.4 °N	8.3 °E	219	ICOS
HTM	Hyltemossa, SWE	56.1 °N	13.4 °E	255	ICOS
VHL	Vavihill, SWE	56.0 °N	13.2 °E	175	PSI
PLA	Preila, LTU	55.4 °N	21.1 °E	5	FTMC
CDL	Candle Lake, CAN	55.4 °N	105.1 °E	600	ECCC

Wetland emissions undergo seasonal variabilities however and the estimated emissions in the dataset used in this study are nearly zero within the area of interest during the winter month. Here, we keep a seasonal cycle with no emissions during the winter months and increase only the emissions in summer; a set of scenarios for completing this study, based on more information on the potential changes in the length of the growing season or the potential of emissions in winter (which are currently not available for the whole Arctic), could easily be implemented.

In the second emission scenario, a positive trend is imposed on the anthropogenic emission sources. Methane emissions connected with human activities in the Arctic are not explicitly assumed to increase in the future; however the large estimations of unexplored fossil fuel resources make this region potentially attractive for future drilling campaigns (Gautier et al., 2009). Additionally, this scenario was chosen to take into account increased methane emissions without strong seasonal fluctuations.

In the third emission scenario, the methane emissions from oceanic sources are increased. The significance of CH_4 emissions from the Arctic Ocean has been indicated by several studies, especially in shallow water stretches which are underlain by permafrost (e.g. Damm et al., 2010; Kort et al., 2012). Sub-sea permafrost thaw has hereby for instance been observed in the

ESAS and several studies highlight the importance of this region in particular (e.g. Shakhova et al., 2015, 2019; Wild et al., 2018).

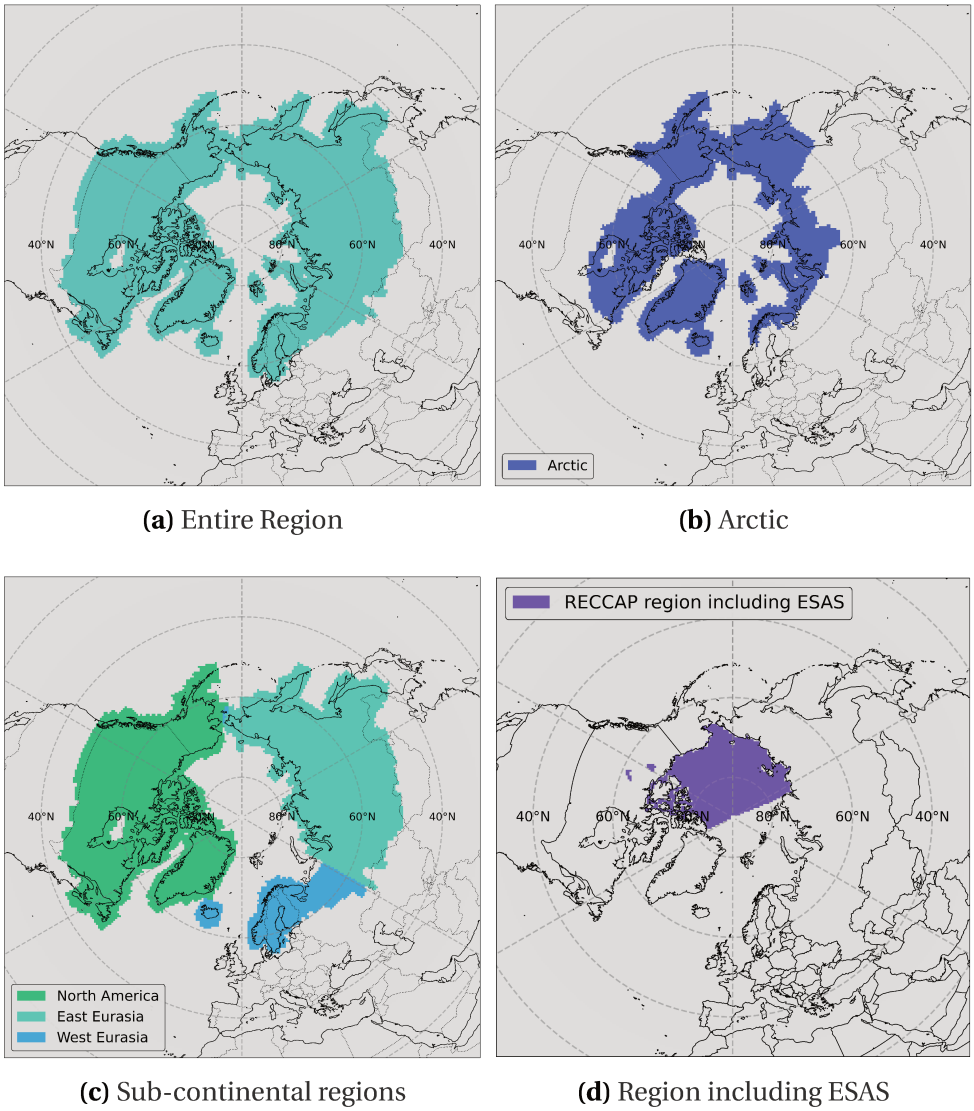

(a) Entire Region **(b)** Arctic

(c) Sub-continental regions **(d)** Region including ESAS

Figure VIII.3: Supra-regions (figures a to c) used for applying trends on wetland and anthropogenic CH_4 emissions and RECCAP region including the ESAS (figure d) used for applying trends on oceanic methane sources.

The emission scenarios are considered for different regions within the area under study. We define five supra-regions (Figure VIII.3): the Arctic, the Arctic and Sub-Arctic combined (hereafter referred to as the *entire region*), North America, East Eurasia and West Eurasia whereby the last three regions only refer to high northern latitude areas within those continents. Additionally, 121 sub-regions are defined as introduced in Section 3.1.

For each of those supra- and sub-regions, positive trends on wetland and anthropogenic emissions are applied separately. The oceanic sources on the other hand are only increased in the sub-region which contains the ESAS.

The trends applied on methane fluxes from the Arctic Ocean are also partially different from the ones selected for emissions from wetlands and anthropogenic sources. This is due to the fact that oceanic CH_4 emissions are more difficult to quantify and predict, they are associated with higher uncertainties.

Table VIII.2: *Overview of the different scenarios used to obtain the simulated observations.*

Methane Source	Region	Trend [% per year]	Network
Wetlands	All supra-regions, All sub-regions	0.1, 0.5, 1, 2, 5, 10, 20	current, extended
Anthropogenic	All supra-regions, All sub-regions	0.1, 0.5, 1, 2, 5, 10, 20	current, extended
Ocean	Only ESAS region	1, 5, 10, 20, 50, 75, 100	current, extended

An overview of all the scenarios used to simulate potential observations can be found in Table VIII.2. In total, 3542 different set-ups are created.

4 Results

4.1 Comparison of truth and posterior state over time

In order to evaluate how well the anticipated trends in the different regions are captured by the inversion over the whole period of interest, the time series of the true and posterior states are compared to each other.

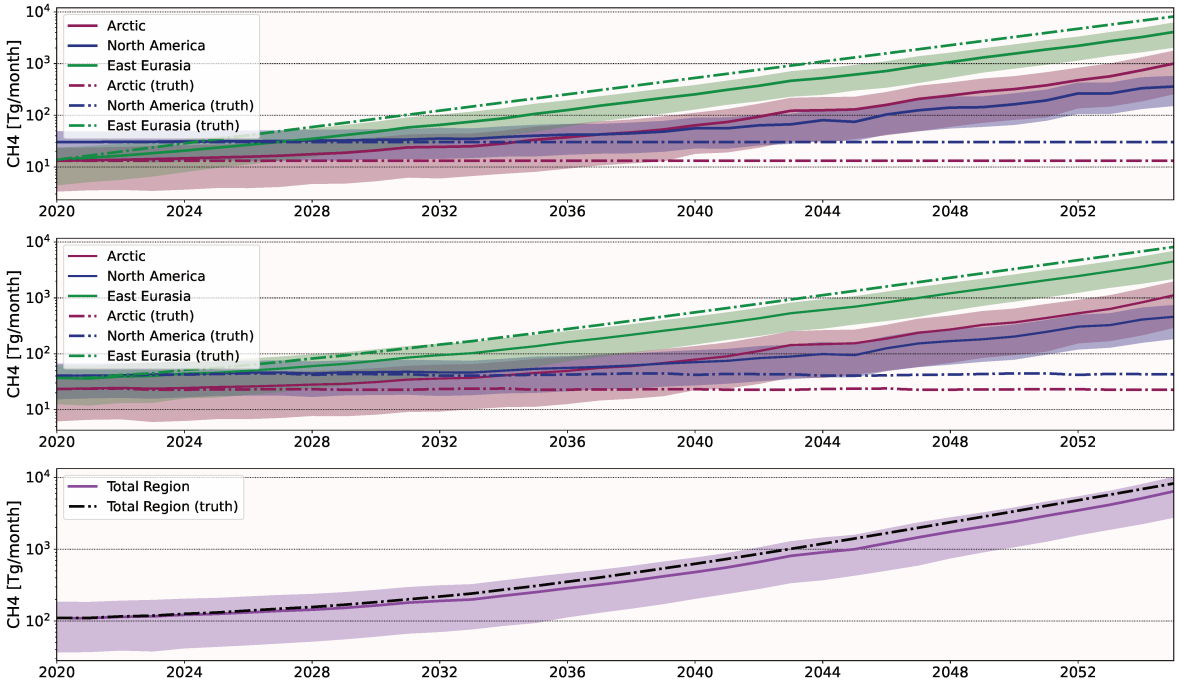

Figure VIII.4: Time series of emissions [$TgCH_4$ yr^{-1}] between 2020 and 2055 with a 20%-per-year increase in wetland emissions in East Eurasia. The continuous lines show the posterior state and the dash-dotted the true state. The Arctic is shown in pink, North America in blue, East Eurasia in green and the entire region in purple. The shaded areas refer to the posterior uncertainties obtained from the P^a matrix. Top panel: Regional wetland CH_4 emissions, middle panel: Regional total CH_4 emissions, bottom panel: Entire total CH_4 emissions.

The true state (hereafter called *truth*) refers hereby to the emission scenario (dependant of the trend, CH_4 source and region) used to compute the synthetic observations. Figure VIII.4 (page page 129) shows the time series of wetland and total CH_4 emissions between the years 2020 and 2055 in different supra-regions (North America, East Eurasia and the Arctic) as well as the total CH_4 emissions for the entire regions. The truth is hereby a 20 % increase in wetland emissions only in the supra-region East Eurasia. In this example, the extended observation network was used for the inversion.

Since the wetland emissions are only increased in East Eurasia in this scenario, only this region should be updated by the inversions and the posterior emissions in any other region should, in theory, not be changed. The wetlands emissions in East Eurasia are indeed increased following the truth, but posterior fluxes do not keep up with the increasing rate of the truth. The wetland emissions in East Eurasia are reduced in the posterior state in comparison to the truth, as soon as the year 2021. By the year 2055, the posterior emissions (around 4092 $TgCH_4\ yr^{-1}$) are approximately 50 % lower than the truth (around 8152 $TgCH_4\ yr^{-1}$). This is also found for the total emissions in the entire Arctic and Sub-Arctic region where the posterior emissions are around 28 % lower than the truth in 2055.

On the other hand, it is shown that the posterior wetland emissions are also increasing over time in other regions, where they should not. The defined Arctic region partially overlaps with East Eurasia, which is why an increase of posterior CH_4 emissions in this region is not surprising. Here, the increase in the posterior state can already be observed from around 2024. In North America, the posterior state starts deviating from the truth from around 2032. At the end of the period in 2055, the annual CH_4 emissions from wetlands are ≈330 Tg higher than the given unmodified truth (≈30 $TgCH_4\ yr^{-1}$). This means that part of the increase in the truth in East Eurasia is incorrectly distributed to other regions by the inversion. Overall, the applied increase in the simulated scenarios is underestimated in the "correct" area and partially compensated for by overestimations in the same emission sector in different regions.

Table VIII.3: *Absolute and relative discrepancies between truth and posterior state in the year 2055 for different trends on wetland emissions. The posterior values refer to total CH_4 emissions under increased wetland fluxes in the corresponding region only.*

Trend	Difference between truth and posterior state			
	North America		East Eurasia	
[%]	[$TgCH_4\ yr^{-1}$]	[%]	[$TgCH_4\ yr^{-1}$]	[%]
0.1	0.3	0.7	0.2	0.2
0.5	1.5	3.1	1.2	3.0
1	3.3	5.9	2.6	6.1
2	7.9	10.7	6.2	12.2
5	35.52	19.7	28.1	28.3
10	213.2	24.6	168.4	41.0
20	4638.6	26.0	3663.1	41.1

When the same emission scenario (20 % increase in wetland emissions) is applied to the region North America, the opposite effect is observed: whereas the posterior wetland emissions in North America are underestimated, in East Eurasia the posterior CH_4 fluxes are sig-

nificantly higher in comparison to the truth. The discrepancies are however lower in comparison to the scenario anticipating elevated wetland emissions in East Eurasia (shown in Table VIII.3, page 130). This can be explained by the denser observation network available in North America, hence computing a better posterior distribution of fluxes. Nevertheless, even when the extended observation network is used for the inversion of this scenario, the system does not assign regional increases in CH_4 emissions correctly from an early point (around 2024) in the total period of interest. Similar results are obtained under elevated anthropogenic CH_4 emissions.

For the different trend scenarios, the discrepancies between the true and the posterior states increase in percentage terms, whereby the attributed posterior trends are increasingly overestimated the larger the true trend is, as shown in Table VIII.3. However, even under the lowest emission scenario (0.1 % increase per year) elevated emissions are obtained in regions where no trend is prescribed, confirming that no matter the emission scenario, the observation network is not fit to accurately distribute changes in emissions in the Arctic.

4.2 Regional trend detection

Subsequently, we analyze how well the prescribed trends in the different regions are detected by the inversion in the posterior state. Thereby, only the highest trend scenarios (20 % for wetlands and anthropogenic emissions, 100 % for oceanic emissions) are examined in the following.

All the Figures presented in the following sections combine 121 different scenarios: in 120 of the defined sub-regions, a trend on wetland emissions is applied on each sub-region individually. The remaining region is the ESAS region (Section 3.5, Figure VIII.3d), where the trend is applied on CH_4 emissions from the Arctic Ocean. These scenarios are chosen for the exemplary Figures since similar results are obtained for applied trends on anthropogenic emissions. Moreover, the general conclusions about the regional differences are similar for the scenarios using only sub-regions (as presented in the following maps) to the results obtained from applying trends to larger regions.

4.2.1 Temporal threshold of sub-regions

Before analyzing the regional differences in the detection of the trend, we define a temporal threshold in each of the 121 sub-regions r in order to determine when the posterior state is statistically different. To define the threshold, we select every year, for which the difference between the annual posterior emissions $emis^a_{j,r}$ and the annual prior $emis^b_{j,r}$ (corresponding to the truth in the first year) is larger than the absolute error $\epsilon^a_{j,r}$ in the threshold year, such that:

$$emis^a_{j,r} - emis^t_{2020,r} < \epsilon^a_{j,r} \tag{VIII.4}$$

with $j \in [2021, 2055]$ and $r \in [1{,}121]$ is **not** fulfilled. Figure VIII.5 on page 132 shows the threshold year of each sub-region.

Due to the looping of reference footprints and fluxes from 12 reference years to generate the truth, it can happen that the criterion is matched for some years discontinuously first, then continuously until the end of the inversion in 2055. We discard the first discontinuous years to compute the threshold, which is defined as the first year after which all years are detected.

The threshold year is hereby generally higher for regions with a sparse observation network. In regions with a dense observation network, such as northern North America, the

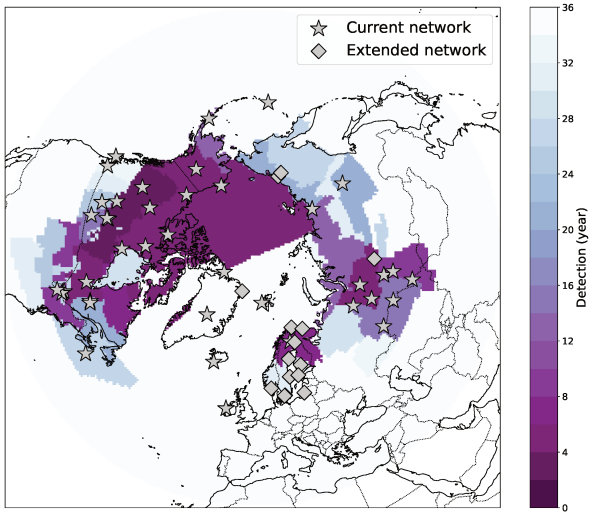

Figure VIII.5: Threshold year counted from 2020 for each sub-region for combined emissions scenarios from wetland (20 % annual increase) and oceanic emissions (100 % annual increase) applied in each sub-region separately. Here, the inversion is performed using the current observation network only (indicated with grey stars). The stations of the extended network are additionally presented in this map (indicated with grey diamonds).

threshold year is detected quite early (after ≈ 5 years) in comparison to the whole period under study (36 years long). These numbers reflect an ideal case for which uncertainties in the inversion system are minimized and for which data are assumed to be instantly available. In the real world, it could take much longer to detect a significant trend, even in regions with relatively dense networks. This anyway points at the need to develop operational inversion systems dedicated to the Arctic, with an efficient sharing of data to detect as soon as possible any climate feedback to regional fluxes.

4.2.2 Trend detection in sub-regions

Subsequently, the scenarios in which the annual trends are applied individually on each of the sub-regions are examined in order to determine where the truth is best detected by the observation network.

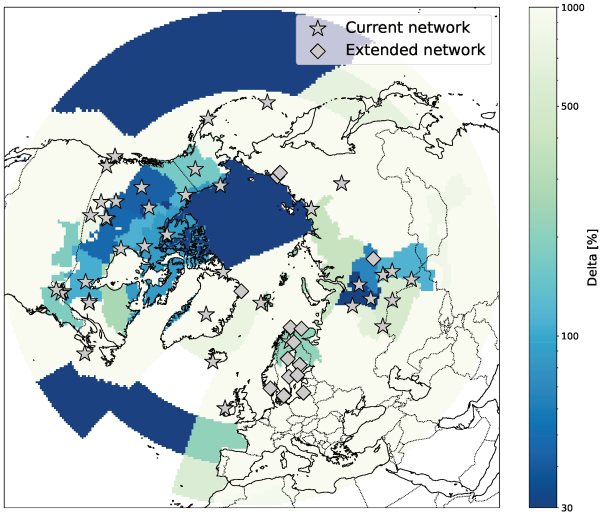

Figure VIII.6: Relative difference [%] between the threshold year and 2020 in terms of annual CH_4 emissions of the true state in each sub-region.

Figure VIII.6 (page **??**) shows the relative difference of CH_4 emissions in the true state between the threshold year and the first year of the period under study (2020). The regional CH_4 fluxes are hereby presented in relation to the spatial dimension of the corresponding region; hence we normalize total emission differences by region by their area. The difference is generally higher (more than 1000 % increase over the period until the threshold year) in regions where the observation network is sparser; this corresponds to the varying threshold years of the different regions. With shorter periods of time, the difference to the initial state of the truth is, naturally, smaller. In the corresponding regions, the increase until the threshold year is approximately between 20 and 200 %.

The deviation between the posterior state and the truth is presented in Figure VIII.7a. The relative difference $\Delta emis_{j,r}$ is hereby calculated as the difference between the posterior annual CH_4 emissions $emis^a_{j,r}$ in the threshold year and the corresponding truth $emis^t_{j,r}$ divided by the truth in the threshold year:

$$\Delta emis_{j,r} = \frac{emis^a_{j,r} - emis^t_{j,r}}{emis^t_{j,r}} \tag{VIII.5}$$

for $j \in [2021, 2055]$ and $r \in [1, 121]$. Therefore, the closer the difference $\Delta emis_{j,r}$ is to zero, the better the truth is captured in the posterior state of the corresponding sub-region.

The posterior increment between 2020 and the defined threshold year is closer to the truth in areas with a dense observation network, as expected. Those include North America, certain parts of Siberia, the RECCAP region containing ESAS as well as parts of Northern Europe. In those regions, the posterior results deviate from the truth approximately between 0 and 45 %. The exceptions are hereby certain oceanic regions outside the Arctic Ocean. Here, the small differences between the posterior emissions and the truth is unrelated to the observation network but rather because wetland emissions are not present in those regions and trends on marine fluxes are only applied in the ESAS region.

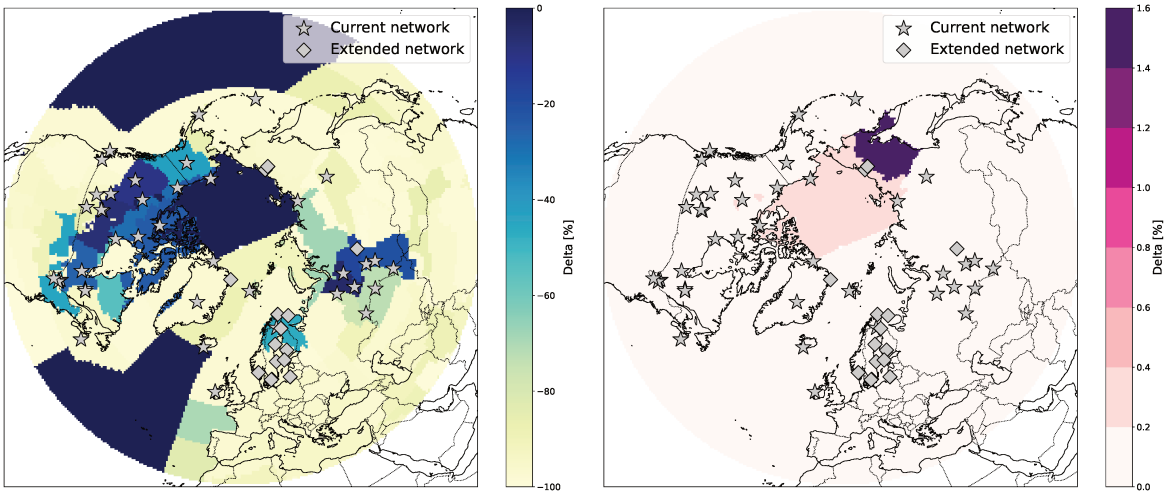

(a) **(b)**

Figure VIII.7: Left: Relative difference [%] between posterior annual CH_4 emissions [$TgCH_4$ yr^{-1}] and truth in the threshold year. Darker shades indicate regions where the increment in the posterior state is closer to the truth. The inversion is hereby performed using the extended network. Right: Difference between current and extended observation networks regarding the relative differences between the truth and the posterior state.

Regarding the differences between the two observation networks, the improvements observed with the extended network in comparison to the current network are remarkably low. Only the two additional observation sites at the coast of the East Siberian Sea (AMB and CHS) seem to provide additional constraints for the surrounding regions. Figure VIII.7b, page 133, shows the relative difference between the differences ($\Delta emis_{j,r}$) for the current and the extended observation networks. The improvements of the extended observation network are hereby however low (maximum 1.6 % larger in comparison to the current network).

In Northern Europe, where the network was extended by 10 additional observation sites, the differences between the current the extended networks are insignificantly small and additional improvements could therefore not be achieved in this inversion set-up. This particular feature is related to our particular set-up, for which background concentrations are optimized alongside fluxes. In the case of Northern Europe, despite the provision of numerous additional sites, the inversion attributes observation discrepancies between the truth and the prior to the background concentrations instead of the fluxes.

4.2.3 Redistribution of CH_4 emissions

In Section 4.1 it was shown, that the trend applied on the truth was not only detected in the intended region in the posterior state, but also in various other regions. This will further be explored in the following. Hereby, we calculate how much increase is detected in the posterior CH_4 emissions in all other regions for the given threshold year in relation to the growth detected in the region for which the increment was actually applied. In other word, which extent of the applied trend in the region examined is "redistributed" to regions outside.

For instance, for an applied trend in RECCAP region i, the increment ratio $\kappa_{j,i}$ can be defined as:

$$\kappa_{j,i} = \frac{\sum \Delta emis^a_{j,r}}{\Delta emis^a_{j,i}} \tag{VIII.6}$$

for the threshold year $j \in [2021, 2055]$ and the region $r \in [1{,}121]\ r \neq i$. $\Delta emis^a$ hereby represents difference between the posterior CH_4 emissions and the truth in the corresponding region r for the threshold year j.

The results are presented in Figure VIII.8a on page 135 for the extended observation network. Areas colored in deep green show hereby regions for which the increment outside was much larger than in the region the increment was intended to be and pink colored regions tend to decrease the CH_4 fluxes outside. The brighter a region is colored, the less the emissions are increased or decreased in regions outside.

First of all, it is shown that areas with a denser observation network generally show less redistribution of CH_4 fluxes to other regions, following the results presented in Section 4.2.2. Hereby, the increment ratio in other regions is around 0 to 40 %. For areas with a sparse network of surface observation sites, increases of CH_4 fluxes in other regions can be more than 1000 %.

The improvements achieved through the expansion of the network are more substantial regarding the redistribution of CH_4 fluxes to other regions, compared to the results presented in Section 4.2.2, as shown in Figure VIII.8b, page 135. Hereby, the difference of the computed increment ratios for both network scenarios is shown: darker shades of purple show regions where the extended network performed better in comparison to the current network regarding the redistribution. For example, the improvement by the two stations AMB and CHS described in the previous section can also be observed here. For the region those sites

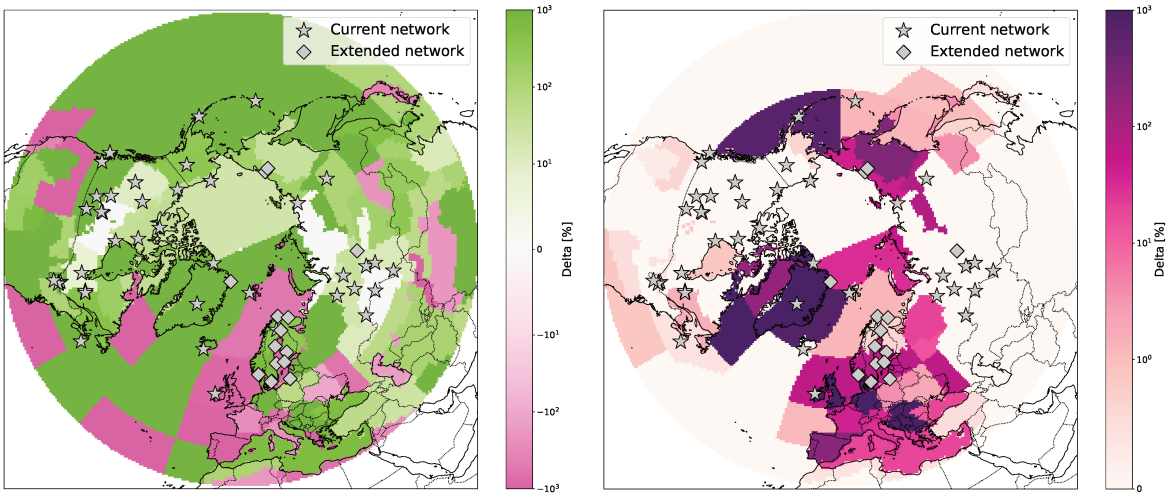

(a) (b)

Figure VIII.8: Left: Redistribution of detected CH_4 emissions to regions other than the region a trend was applied to. Deeper shades show hereby a large increase (green) or decrease (pink) in other regions. Right: Difference between increment ratio of current and extended network.

are located in, the increment ratio was 286 % in the scenario using the current network and only 34 % in the extended network. Improvements can hereby also be observed in Europe and Greenland.

5 Conclusion

Within the framework of this study, we generated numerous future scenarios simulating an assumed "methane bomb" in the Arctic and Sub-Arctic. In order to determine how well the existing as well as a possible future network of surface observation sites is able to detect future increases in CH_4 emissions, the scenarios were integrated in the form of simulated observations in an analytical inversion framework. The period under study covers the years 2020 to 2055. During this period, different annual increases are applied to three CH_4 sources including wetlands, fluxes from oceanic sources and anthropogenic emissions. Those scenarios of possible trends for the selected CH_4 sectors are subsequently applied on different sub-regions in the high northern latitudes. The two different observation networks include the current observation network in the Arctic and Sub-Arctic providing measurements of atmospheric CH_4 concentrations (consisting of 41 sites) as well as an extended network adding 16 potential sites.

It is shown that the posterior CH_4 emissions are predominantly underestimated (up to 41 % lower) in the regions a trend was assigned to. The discrepancies are hereby more pronounced in later years within the period under study and proportional to the magnitude of the true trend. Additionally, increasing posterior CH_4 fluxes are also found in regions where elevated emissions are not prescribed by the corresponding scenarios. This effect is less pronounced when the true trend is assigned to regions with a dense observation network but can however not be completely avoided even by the extended observation network. This indicates that neither of the two observation networks used in this study is able to quantify as well as locate correctly increases in methane emissions. Concerning the correct detection of the true trend in a specific area, the regional differences confirm that the trend is predominantly better detected in regions where more observation sites are located, such as in northern North America or certain parts of Siberia. However, the improvements achieved by the extended observation network are remarkably small. An obvious difference is only observed

in the North East of Russia, presumably brought about by the additional sites AMB and CHS. However the detection is hereby only up to 1.6 % better than with the current network in the corresponding regions.

A more significant advantage of the extended observation network concerns the redistribution of CH_4 fluxes. As stated before, the posterior results show that increased CH_4 emissions are not only detected in the region where the trend actually occurs, but also in various other regions. This redistribution is predominantly observed in regions where the observation network is sparse. The inversion set-ups using the extended observation network show hereby significant improvements for instance in the North East of Russia, Europe and Greenland. Therefore, even though the extended observation network only brings few advantages concerning the correct detection of the trend in a specific region, the false detection of trends in other regions is largely improved in certain areas.

Overall, this study points at our lack of capability to accurately and quickly detect any potential "climate bomb" in the Arctic, apart from specific regions with good observation coverage. Future efforts should be dedicated to increase the coverage of observations in the Arctic, as well as dissemination and sharing effort to be able to design operational inversion systems able to provide flux estimates with a delay as small as possible. Due to logistical issues, any extension of the fixed network would come at a significant cost. Therefore, mobile campaigns, especially ship-based campaigns alongside the shores of the Arctic ocean, as well as new-generation satellite platforms providing reliable high-latitude CH_4 products should be supported and integrated in inversion systems.

Part IV

Conclusions and outlook

Conclusion

THE AIM OF THIS THESIS WAS TO CONTRIBUTE TO THE GENERAL EFFORT to better quantify the methane budget in the Arctic, to understand potential developments in different methane sources during recent years and to draw conclusions about the detectability of future changes in methane emissions. The Arctic is in general considered to be an understudied region, and reliable estimates on the methane budget of high northern latitude regions are challenging to obtain. However, studying this subject is particularly important since ongoing environmental changes in the Arctic caused by the global climate change are affecting natural methane sources and sinks, further complicating the estimation and prediction of methane emissions, their contribution to the global budget and the resulting potential climate feedback(s).

Within the framework of this thesis, three scientific questions were presented, first introduced in Part I (Chapter III, Section 2.2) of this work. In order to address these questions, two main studies were carried out. The first study included the implementation of an analytical inversion to assess CH_4 sources and sinks in the Arctic during recent years. The second study involved the integration of possible future scenarios of methane emissions in high northern latitudes in an inversion framework. The discussion of the three scientific questions is summarized in the following.

Question 1: *Is the current observation network of stationary measurement sites in the Arctic nations able to adequately constrain different sectors of CH_4 sources and sinks?*

In order to discuss this question, an analytical inversion was performed using available measurements within the period 2008 to 2019 from 41 surface observation sites in different Arctic nations, prior estimates of different methane emission sources and one methane sink in the form of soil oxidation as well as modelled equivalents of CH_4 mixing ratios obtained from the atmospheric transport model FLEXPART. The analysis of the network efficiency demonstrated that, in our inverse modelling set-up, the observation network is in fact not sufficient to satisfactorily constrain most CH_4 sources as well as the soil sink in high northern latitudes over the whole period of interest. Only wetland emissions were adequately constrained in North America and sporadically in certain parts of Russia although with strong inter-annual variabilities dependent on the amount of suitable observations. Besides, it was shown that a considerable share of the provided observations was used by the inversion to constrain the background mixing ratios, which additionally contributed to the low constraints on the emissions sources.

Question 2: *What information can be derived about seasonal patterns and trends of CH_4 sources and sinks between the years 2008 and 2019 in different parts of the Arctic?*

This question was addressed within the same inverse modelling implementation used to tackle the first question, as both of them are interlinked. To obtain reliable estimates of CH_4 emissions between the years 2008 and 2019 in different parts of the Arctic, a total of 5000 posterior emission estimates were computed and evaluated according to the plausibility of their uncertainties on observations and prior information. Since we concluded from the previous question that only wetland emissions are adequately constrained by the inversion, the obtained posterior estimates of CH_4 sources and sinks are still subject to relatively high uncertainties. Nevertheless, the posterior uncertainties are hereby reduced to some extent. Taking these uncertainties into account, the following results can be considered as significant. It was shown that the posterior emissions were lower in comparison to the prior ones in all regions under study. The discrepancies were hereby especially high for wetland emissions in North America, indicating that the prior fluxes were overestimated in this region and sector. Within the 12-year period under study, the posterior CH_4 emissions from wetlands showed a slight negative annual trend in North America and a slight positive trend in East Eurasia. Interannual differences in total regional CH_4 emissions between the prior and posterior states were predominantly influenced by emissions from biomass burning, which were reduced in North America in particular. The seasonal cycles of the different emission sectors showed minor, insignificant deviations in comparison to the prior.

Question 3: *To which extent are future increases of CH_4 emissions in the form of an Arctic "methane bomb" accurately detected by the current network of observation sites, and what improvements can hereby be achieved by a hypothetically extended network?*

To address this question, we have integrated synthetic observations derived from different potential future scenarios of methane emissions in an inverse modelling set-up. Within the framework of these scenarios, various positive annual growth rates have been applied on CH_4 emissions from wetlands, anthropogenic sources and the Arctic Ocean in different sub-regions between the years 2020 to 2055. Two different observation networks have been used, the current network consisting of 41 surface measurement sites in different Arctic nations as well as an extended network with 16 additional sites. It was shown that the posterior CH_4 emissions from both the current and the extended network were underestimated in comparison to the truth in the region the increment was applied to. It was hereby found that the higher the intended trend of the scenario, the greater the discrepancies between the truth and the posterior emissions. Regionally, the growth in CH_4 emissions was generally better detected in the posterior state in areas where a denser observation network is available. However, an improvement in the detection of regional trends could only be achieved to a very small extent and was limited to a few regions by an extended observation network. Additionally, the results of the inversion revealed that methane emissions were partially redistributed to other regions where no trend was prescribed in the truth. This reinforced the conclusion that not only does the current observation network in the Arctic lead to underestimations of occurring trends in CH_4 emissions in inverse modelling approaches, the elevated fluxes are also not correctly located. However, regarding the redistribution of emissions in different regions, the extended observation network did show significant improvements in areas where additional observation sites were added, which demonstrates the importance of additional observation sites in the Arctic.

Perspectives

THIS WORK IS PART OF AN ONGOING EFFORT TO BETTER QUANTIFY methane emissions and sinks in the Arctic, a region with a variety of CH_4 emission sources likely to gain even more importance in the upcoming years. The results obtained in this work by applying an analytical inverse modelling set-up are built on many insights and developments that have been made in the past and advanced to the present day. In the following, we discuss and reflect on possibilities to further improve such approaches and applications in the future.

1 Expanding the observation coverage in the Arctic

One of the limitations often addressed in this work is the insufficient availability of suitable observations. The different options for providing additional measurements of atmospheric CH_4 concentrations are subsequently described in the following sections.

1.1 Surface observation network

The idea of an extended observation network of stationary observation sites has been suggested in the framework of the study presented in Part III, Chapter VIII and the thereby achieved improvements have been detailed. In addition to that, mobile surface observations can potentially provide complementary information.

1.1.1 Stationary observation sites

Although the inversion in this study was successfully implemented and provided promising results, further work is needed to better quantify methane emissions in the Arctic and Sub-Arctic. Especially in high northern latitude regions, atmospheric inverse modelling implementations suffer from a lack of accessible high quality, multi-decal atmospheric CH_4 observations. Indeed, our examination of the regional constraints showed that the majority of the CH_4 sources are poorly constrained by the observations in vast parts of the Arctic region. This significantly complicates achieving the reduction of uncertainties on estimates of methane emissions in the Arctic as well as reliably detecting inter-annual and regional trends of the different emission sources. Moreover, the spatial and temporal resolutions accessed to by our inversion system are still insufficient to precisely separate the emission processes and to analyse their high-frequency (e.g. seasonal or faster) temporal variabilities.

In order to obtain more reliable estimates of methane emissions in the Arctic over a long period of time, it would therefore not only be necessary to increase the spatial coverage of observations by extending the network of stationary sites, but also to maintain these surface observation sites over multiple decades in order to detect regional changes in CH_4 concentrations. Especially in the Russian Arctic and Sub-Arctic, large areas are not covered by stationary measurement sites, making it impossible to assess local methane sources. Additionally, an efficient communication of ongoing developments and access to the data need to be ensured. For instance, a new measurement site ("DIAMIS") was installed on the western coast of the Taimyr Peninsula with available measurement of CH_4 and CO_2 starting in 2018 (Panov et al., 2021). Including this new observation site in future inverse modelling studies would for instance be valuable to better constrain methane emissions from the Arctic Ocean. However, due to the currently ongoing war in Ukraine, cooperation between scientific institutions in the European Union and those located in Russia is unfortunately severely limited on both sides.

1.1.2 Mobile surface measurement campaigns

Extending the fixed surface observation network in the Arctic is costly and logistically challenging. Therefore, integrating data obtained from mobile measurement campaigns in inversion systems should be considered in future works. Those measurements are for instance useful to measure the CH_4 mixing ratios due to a specific source or caused by a particular event.

Mobile surface measurement campaigns include thereby, for instance, observations carried out by ship or by train. Train measurements in high northern latitudes have for instance been carried out by Skorokhod et al. (2017). Those observations can be useful to quantify the local differences in CH_4 emissions and to constrain terrestrial regions that are not covered by the current stationary observation network. Ship-borne observations from expeditions in the Arctic Ocean have also been carried out during recent years (e.g. Pisso et al., 2016; Yu et al., 2015; Pankratova et al., 2022; Thornton et al., 2016; Berchet et al., 2020). Integrating measurement data from such ship-borne campaigns in inversion implementations could thereby be beneficial to better address oceanic CH_4 fluxes, which are difficult to constrain with the current in situ observation network.

1.2 Including satellite and airborne observations

As stated in the previous section, in this work we have restricted ourselves to the use of near-surface observations of CH_4 concentrations as a component of the inversion. Additional space- and airborne measurements have hereby not been taken into account. However, these measurements are currently available and may contain valuable information on the state of the atmosphere in the Arctic. Due to the scarcity of in situ observations in high northern latitudes, these other types of measurements should be considered as potential additional constraints.

1.2.1 Satellite measurements

The limitations regarding satellite observations in high northern latitudes have been already discussed in Part II, Chapter V, Section 1.2.1. The restrictions in obtaining accurate measurements of CH_4 include hereby the solar zenith angle, the surface albedo as well as the decreased levels of light during the Polar night. Nevertheless, the broad coverage of satellite observations could be used to derive an indicator of large-scale gradients in methane concentrations over the Arctic. These gradients would be easily implemented in inversion set-ups and would add information on the boundary conditions of the domain as well as on

total regional emissions. Several studies using inverse modelling approaches were already successfully carried out in high northern latitudes (such as by Aalto et al., 2020; Baray et al., 2021). Furthermore, in the medium term, new satellite missions (e.g. the Franco-German MERLIN project) will possibly provide large, accurate and high-spatial-resolution data sets, which could for instance be used to characterise the plumes from regional sources.

1.2.2 Airborne measurement campaigns

Unlike satellite data, airborne measurements of atmospheric methane are accurate and provide a fine vertical resolution. However, these measurements only cover relatively short periods of time (and limited areas), which makes it difficult to include them into an inverse modelling study aimed at covering several years, as presented in this work. Additionally, the vertical structure of CH_4 concentrations is more sensitive to the distribution of surface fluxes and to the quality of the simulation of transport and mixing than the variability of methane concentrations measured at surface observation sites. Therefore, the separation of errors in the transport simulation and in the prior fluxes by the inversion system is difficult for such observations. Furthermore, the limited availability of these observations restricts their applicability in constraining regional fluxes. For these reasons, data from airborne campaigns are generally used to evaluate the posterior results of inversions rather than being included in inverse modelling implementations.

Nevertheless, airborne measurements carried out for instance within the YAK-AEROSIB project (on board planes) accurately document the three-dimensional distribution of methane concentrations. Using balloons, the quality and number of vertical CH_4 profiles obtained by AirCore measurement have been increasing over the last decade and provide new information to potentially better constrain the inverse modelling studies in the future. In high northern latitudes, AirCore measurements have for instance been carried out during the MAGIC 2021 campaign (`https://magic.aeris-data.fr/magic2021/` and Part III, Chapter VI, Section 2.3). However, using AirCore measurements for inversions would require accurately modelled CH_4 concentrations in the stratosphere. Since the differences between models and observation are hereby still relatively high and the vertical resolution of the models is very coarse in comparison to the AirCore measurements, these observations are currently not relevant for atmospheric data assimilations. However, as soon as a better representation of stratospheric transport is possible, AirCore measurements could provide useful additional constraints.

2 Components of the inversion set-up

The different components of the inversion set-up could be modified in order to improve the reliability of the results.

2.1 Prior emissions and uncertainties

Regarding the estimates used as prior information in the inverse modelling implementation, it could be beneficial to consider different bottom-up estimates for each methane emission source. Many studies focusing on the quantification of CH_4 sources and sinks by applying inversion approaches use the same databases to build their prior estimates of CH_4 emissions (e.g. EDGAR for anthropogenic emissions or GFED for fire events). Using different estimates of the same CH_4 sector could hereby be beneficial either to better quantify posterior uncertainties or else to evaluate the posterior results. Even though such an implementation would be relatively simple to carry out in our inversion set-up, computing inversions with several prior estimates can be time consuming. This is especially the case in our approach,

since a large set of posterior states needs to be computed. This process does not just take a relatively long time but also requires a lot of storage space.

An additional issue is hereby that a large variety of prior estimates on CH_4 emission sources is, so far, not available for the Arctic. Therefore, further development and evaluation of ecosystem process-based models for different methane sources would ensure more accurate estimations. Ongoing efforts are already applied to better calibrate process-based models (e.g. Kaminski et al., 2013; Salmon et al., 2021); however, complete systems able to simulate and separate various high latitude ecosystems are still not mature. For instance, in our study CH_4 emission from freshwater systems other than wetlands were not explicitly taken into account. This is, on the one hand, due to the lack of available prior estimates covering the whole Arctic and Sub-Arctic region, but also because of the likelihood of double-counting, since small lakes are partially included in bottom-up estimates of wetland emissions. However, CH_4 emissions from freshwater sources are assumed to be an important source of methane in high northern latitudes and may gain more importance in the future (for instance due to the formation of thermokarst lakes). Appropriate estimates that separate freshwater from wetland emissions would be beneficial to disentangle the contributions of these two emission sources on the Arctic methane budget.

Another limitation regarding the prior information is the estimation of the methane sink from soil oxidation. Whereas estimates of the different CH_4 sources in the Arctic are relatively recent, the available bottom-up data set by Ridgwell et al. (1999) estimating CH_4 reduction in the soil has been created several decades ago. However, since the soil oxidation has been shown to increase with rising temperatures in the Arctic (Emmerton et al., 2014; Lau et al., 2015), inverse modelling studies focusing on high northern latitudes would benefit from updated estimates to account for a correct magnitude of the sink oxidation.

The estimates on the prior uncertainties could also be defined more precisely. Even though in this set-up we take a large variety of different uncertainties on the prior estimates into account, the reference values obtained from Baray et al. (2021) hereby rely on estimates concerning certain parts of North America only. For simplification, these reference values are used for the whole region of interest in our work. Estimating regional uncertainties could hereby improve the reliability of the results; however, this task remains complex due to the lack of information.

2.2 Definition of the sub-regions

Another suggestion to improve the implementation of the inversion concerns the definitions of the supra- and sub-regions. Using the division suggested by RECCAP (Ciais et al., 2022) was a valuable tool to assess regional differences in CH_4 emissions. However, it cannot be ruled out that local emissions have not been adequately captured. For instance, the ESAS region, which is an anticipated hot spot of oceanic CH_4 emissions, can not be separately evaluated with the regional division used in this work. Improving the definition of the subregions to adapt them to methane emissioms could thereby potentially lead to more accurate local estimates.

To define the supra-regions, accessible masks (internally available at LSCE) were used to assess the prior and posterior methane emissions in different regions of the Arctic. However, it is difficult to classify the results in relation to other studies that aim at quantifying methane emissions in the Arctic. A consistent definition of Arctic and Sub-Arctic regions and matching available masks for numerical applications would simplify the comparison between studies.

2.3 Improving the background mixing ratios

It has been shown that a considerable share of the observations is used by the inversion to constrain the background mixing ratios instead of the different Arctic CH_4 sources. One way to reduce the share of the information constraining the background in the inversion set-up would hereby be to substantially decrease the uncertainties on the background mixing ratios. This relies, however, on the performances of simulations of global methane concentration fields. Even though they have already become much more precise in recent years, they still do not provide a sufficient level of accuracy that would allow us to reduce the uncertainties on the background in our inversion set-up (Inness et al., 2019).

Moreover, the backward transport in FLEXPART is limited in time (10 days in this case) and is much shorter than the average residence time of air masses (approximately 2 months, Berchet et al., 2020) in high northern latitudes. Therefore, part of the influence of the Arctic fluxes on the observations is diluted in the background in our system. One way of dealing with this problem would be to dramatically increase the backward transport time of the virtual particles in the FLEXPART simulations: up to several weeks. However, to ensure accurate results, a very large number of particles would be necessary, which is computationally complex. Another approach could be to fully couple FLEXPART within a global circulation model, thus accounting for the influence of fluxes on observations indefinitely backwards in time. This has for instance been applied by Maksyutov et al. (2020) and could be done by the Community Inversion Framework with one of the available global models (LMDZ or TM5; Berchet et al., 2021).

3 Improving atmospheric inversion systems dedicated to the Arctic

In addition to the components of inversion discussed in the previous section, several parameters could be adjusted or added to improve atmospheric inversion systems developed for estimating methane emissions in the Arctic.

3.1 Refinement of atmospheric transport modelling

In our inversion frameworks, the modelled CH_4 mixing ratios were obtained from simulated backward trajectories using the atmospheric transport model FLEXPART. The horizontal resolution of those simulations was thereby $1\,^\circ \times 1\,^\circ$, which is the one quite commonly used for inverse modelling set-ups using Lagrangian particle dispersion models in high northern latitudes (e.g. Thompson et al., 2017; Ishizawa et al., 2018). However, using a finer resolution would increase the accuracy of the results, especially regarding observation sites located close to emission hot spots. The finest recommended spatial resolution that can be achieved with FLEXPART v10.4, used in this work, is $0.1\,^\circ \times 0.1\,^\circ$using current ECMWF operational data (e.g., Pisso et al., 2019a). Moreover, increasing the vertical resolution could lead to more accurate simulation outputs since it potentially improves the representation of vertical gradients and decreases misrepresentations of the vertical mixing of CH_4 concentrations. Finer horizontal and vertical resolutions would therefore benefit the accurate representation of the atmosphere, especially in stratified conditions in winter. Finally, extending the backward simulation periods beyond the 10 days commonly used in Lagrangian transport models has been shown to improve the overall performance of the model and potentially increase constraints on emission sources in regions poorly covered by observation sites (Vojta et al., 2022).

3.2 Using additional constraints

In addition to measurements of CH_4 concentrations, observations on methane isotopes as well as trace gases known to be co-emitted with CH_4 can provide additional constraints for inversion applications.

One of the co-emitted species of CH_4 is ethane (C_2H_6). C_2H_6 emissions are hereby connected with the extraction and distribution of oil and gas production (e.g. Kort et al., 2016) as well as continental geological sources (Etiope and Ciccioli, 2009), making the CH_4 to C_2H_6 ratio a strong constraint on thermogenic emissions. Observations of ethane have already been used as a constraint for CH_4 emissions in inverse modelling approaches (e.g. Thompson et al., 2018; Rice et al., 2016). Another known co-emitted trace gas is carbon monoxide (Turner et al., 2019). CO is hereby co-emitted with methane during biomass combustion and, additionally, the oxidation of CH_4 by the OH radical in the atmosphere can lead to the formation of CO. The two species are therefore related to each other and their emissions can be optimised within the same inversion (Fortems-Cheiney et al., 2011). Stationary surface observations of co-emitted specie are for instance carried out in Thule (Greenland, measurements of ethane, Hannigan et al., 2009) or in Eureka (Canada, measurements of ethane and carbon monoxide, Batchelor et al., 2009). However, measurements of those trace gases are, until now, even more sparsely distributed in high northern latitudes than measurements of atmospheric CH_4 mixing ratios. Therefore, these observations can currently only provide limited additional information about methane sources in the Arctic.

Additional constraints can also be achieved by including observations of methane isotopic signatures as has already been demonstrated in several implementations of atmospheric inversions (e.g. Rice et al., 2016; Thompson et al., 2018; Thanwerdas et al., 2021). Most commonly integrated are thereby measurements of $\delta^{13}C_{CH4}$. Deviations from the $\delta^{13}C_{CH4}$ background values in ambient air help distinguishing the contributions of specific source types to atmospheric methane concentrations. For instance, biogenic sources are relatively depleted in ^{13}C (in comparison to background air) whereas thermogenic sources are relatively enriched in ^{13}C. However, similar to the measurements of co-emitted species, measurements of isotopic composition are sparse in high northern latitudes. Whereas a few observation sites in North America (Alert, Barrow and Cold Bay) and Europe (Ny Ålesund, Pallas and Kjolnes) provide measurements of $\delta^{13}C_{CH4}$, such observation sites are so far not available in the Russian Arctic. Additionally, the detectability of methane sources in the Arctic using $\delta^{13}C_{CH4}$ observations has been found challenging and only observation sites which are significantly influenced by emission sources were able to differentiate regional emissions with a reasonable level of confidence (Thonat et al., 2019). Nevertheless, observations on methane isotopes could provide regional improvements in inverse modelling frameworks aiming at studying CH_4 emissions in the Arctic.

3.3 Coupling the atmosphere to continental and ocean surfaces

Despite their capability to constrain surface fluxes to and from the atmosphere, complex data analysis work is needed to translate the conclusions derived from atmospheric inversions into valuable knowledge for the land-surface or ocean model communities or for inventory agencies. Indeed, atmospheric inversions simply rescale prior fluxes, without providing extra knowledge for interpreting the posterior scaling with regards to environmental variables. Moreover, the atmospheric inversion is agnostic of physical, socio-economical and environmental processes related to the spatial distribution and temporal variability of prior and posterior fluxes. Thus, unrealistic posterior corrections can be applied, because they provide an optimal solution as seen by the atmosphere, even though it is incompatible with external constraints.

One way to overcome these limitations is to move towards so-called CCDAS (Carbon Cycle Data Assimilation Systems; e.g. Kaminski et al., 2013; MacBean et al., 2022) and FFDAS (Fossil-fuel Data Assimilation System; Kaminski et al., 2022). Such systems couple several models together in order to complement the data assimilation pipeline as used in atmospheric inversions. For instance, a land-surface model is used to generate surface fluxes, which are then transported in the atmosphere using a transport model. Such a modelling pipeline allows to assimilate observations from various data streams (eddy covariance, atmospheric concentrations, satellite imagery, etc.) constraining various variables (local fluxes, concentrations, auxiliary parameters such as soil moisture, etc.). With such constraints and modelling pipeline, it is possible to optimize underlying parameters in land-surface models, instead of flux maps, hence directly calibrating the model (e.g. Bacour et al., 2019a,b).

3.4 Towards operational systems

Currently, the sharing and distribution of data used for atmospheric inversions could be improved in terms of efficiency. For instance, observations of atmospheric CH_4 mixing ratios are often published several years after the data was collected, whereby only retroactive conclusions can be drawn by inverse modelling implementations. An approach to tackle this issue would be the development of an inversion system that process data on a day-to-day basis in order to operationally monitor CH_4 sources and sinks in the Arctic. Such implementations have for instance been introduced by Kaiser-Weiss et al. (2019) or Deng et al. (2022).

Developing operational systems would require *(i)* observational data streams from traceable and quality-controlled measurements of atmospheric CH_4 concentrations and surface-atmosphere fluxes, *(ii)* prior estimates of spatially and temporally resolved CH_4 fluxes from natural and anthropogenic sources as well as *(iii)* a data assimilation system that combines the information using atmospheric transport modelling in a quantitative way to estimate CH_4 sources and sinks.

Such operational systems are planned in the long term in at least two Arctic nations, Finland and Canada. However, for the entire Arctic, the implementation of an adequate operational system would not be feasible at this stage since the observation network is not sufficiently developed, especially in Russia. Therefore, in order to realize such a project, it would be necessary to establish a denser monitoring network, improve collaboration and data sharing and finally, receive funding to develop dedicated data assimilation systems for the entire Arctic.

Bibliography

Aalto, T., Hatakka, J., and Lallo, M.: Tropospheric methane in northern Finland: seasonal variations, transport patterns and correlations with other trace gases, Tellus B, 59, 251–259, https://doi.org/10.1111/j.1600-0889.2007.00248.x, 2007.

Aalto, T., Lindqvist, H., Tsuruta, A., Tenkanen, M., Karppinen, T., Kivimäki, E., Smolander, T., Kangasaho, V., and Rautiainen, K.: Final report: Solving METHane fluxes at northern latitudes using atmospheric and soil EO data (MethEO), 2020.

Ahmadov, R., Gerbig, C., Kretschmer, R., Koerner, S., Neininger, B., Dolman, A., and Sarrat, C.: Mesoscale covariance of transport and CO2 fluxes: Evidence from observations and simulations using the WRF-VPRM coupled atmosphere-biosphere model, Journal of Geophysical Research: Atmospheres, 112, 2007.

Allen, D. T.: Methane emissions from natural gas production and use: reconciling bottom-up and top-down measurements, Current Opinion in Chemical Engineering, 5, 78–83, 2014.

AMAP: Assessment 2015: Methane as an Arctic climate forcer. Arctic Monitoring and Assessment Programme (AMAP), Oslo, Norway. vii + 139 pp., URL https://www.amap.no/documents/doc/amap-assessment-2015-methane-as-an-arctic-climate-forcer/1285, 2015.

AMAP: AMAP, 2017. Snow, Water, Ice and Permafrost in the Arctic (SWIPA) 2017. Arctic Monitoring and Assessment Programme (AMAP), Oslo, Norway. xiv + 269 pp, URL https://www.amap.no/documents/download/2987/inline, 2017.

AMAP: Arctic Climate Change Update 2021: Key Trends and Impacts. Arctic Monitoring and Assessment Programme (AMAP), Tromsø, Norway. viii+148pp, URL https://www.amap.no/documents/download/6836/inline, 2021.

Ananthaswamy, A.: The methane apocalypse, New Scientist, 226, 38–41, 2015.

Andreae, M. O., Jones, C. D., and Cox, P. M.: Strong present-day aerosol cooling implies a hot future, Nature, 435, 1187–1190, 2005.

Anisimov, O. and Zimov, S.: Thawing permafrost and methane emission in Siberia: Synthesis of observations, reanalysis, and predictive modeling, Ambio, 50, 2050–2059, 2021.

Anon: Russia declares emergency over huge wildfires. Deutsche Welle, 30th July. www.dw.com/en/russia-declares-emergency-over-huge-wildfires-in-siberia/a-49817454., 2019.

Archer, D.: Methane hydrate stability and anthropogenic climate change, Biogeosciences, 4, 521–544, 2007.

Archer, D.: A model of the methane cycle, permafrost, and hydrology of the Siberian continental margin, Biogeosciences, 12, 2953–2974, 2015.

Arshinov, M. Y., Belan, B., Davydov, D., Inoue, G., et al.: Spatio-temporal variability of CO2 and CH4 concentration in the surface atmospheric layer over West Siberia., Optika Atmosfery i Okeana, 22, 183–192, 2009.

Aubry-Wake, C., Bertoncini, A., and Pomeroy, J. W.: Fire and Ice: The Impact of Wildfire-Affected Albedo and Irradiance on Glacier Melt, Earth's Future, 10, e2022EF002 685, 2022.

Bacour, C., Maignan, F., MacBean, N., Porcar-Castell, A., Flexas, J., Frankenberg, C., Peylin, P., Chevallier, F., Vuichard, N., and Bastrikov, V.: Improving estimates of gross primary productivity by assimilating solar-induced fluorescence satellite retrievals in a terrestrial biosphere model using a process-based SIF model, Journal of Geophysical Research: Biogeosciences, 124, 3281–3306, 2019a.

Bacour, C., Maignan, F., Peylin, P., Macbean, N., Bastrikov, V., Joiner, J., Köhler, P., Guanter, L., and Frankenberg, C.: Differences between OCO-2 and GOME-2 SIF products from a model-data fusion perspective, Journal of Geophysical Research: Biogeosciences, 124, 3143–3157, 2019b.

Bamber, J. L., Westaway, R. M., Marzeion, B., and Wouters, B.: The land ice contribution to sea level during the satellite era, Environmental Research Letters, 13, 063 008, 2018.

Baray, S., Jacob, D. J., Maasakkers, J. D., Sheng, J.-X., Sulprizio, M. P., Jones, D. B. A., Bloom, A. A., and McLaren, R.: Estimating 2010–2015 anthropogenic and natural methane emissions in Canada using ECCC surface and GOSAT satellite observations, Atmospheric Chemistry and Physics, 21, 18 101–18 121, https://doi.org/10.5194/acp-21-18101-2021, 2021.

Bartlett, K. B. and Harriss, R. C.: Review and assessment of methane emissions from wetlands, Chemosphere, 26, 261–320, 1993.

Bastviken, D., Tranvik, L. J., Downing, J. A., Crill, P. M., and Enrich-Prast, A.: Freshwater methane emissions offset the continental carbon sink, Science, 331, 50–50, 2011.

Batchelor, R. L., Strong, K., Lindenmaier, R., Mittermeier, R. L., Fast, H., Drummond, J. R., and Fogal, P. F.: A new Bruker IFS 125HR FTIR spectrometer for the polar environment atmospheric research laboratory at Eureka, Nunavut, Canada: measurements and comparison with the existing Bomem DA8 spectrometer, Journal of Atmospheric and Oceanic Technology, 26, 1328–1340, 2009.

Belan, B. D., Ancellet, G., Andreeva, I. S., Antokhin, P. N., Arshinova, V. G., Arshinov, M. Y., Balin, Y. S., Barsuk, V. E., Belan, S. B., Chernov, D. G., et al.: Integrated airborne investigation of the air composition over the Russian sector of the Arctic, Atmospheric Measurement Techniques, 15, 3941–3967, 2022.

Belikov, D., Arshinov, M., Belan, B., Davydov, D., Fofonov, A., Sasakawa, M., and Machida, T.: Analysis of the Diurnal, Weekly, and Seasonal Cycles and Annual Trends in Atmospheric CO2 and CH4 at Tower Network in Siberia from 2005 to 2016, Atmosphere, 10, 689, https://doi.org/10.3390/atmos10110689, 2019.

Berbet, M. L. and Costa, M. H.: Climate change after tropical deforestation: seasonal variability of surface albedo and its effects on precipitation change, Journal of Climate, 16, 2099–2104, 2003.

Berchet, A., Pison, I., Chevallier, F., Bousquet, P., Conil, S., Geever, M., Laurila, T., Lavrič, J., Lopez, M., Moncrieff, J., et al.: Towards better error statistics for atmospheric inversions of methane surface fluxes, Atmospheric Chemistry and Physics, 13, 7115–7132, 2013.

Berchet, A., Pison, I., Chevallier, F., Paris, J.-D., Bousquet, P., Bonne, J.-L., Arshinov, M. Y., Belan, B., Cressot, C., Davydov, D., et al.: Natural and anthropogenic methane fluxes in Eurasia: a mesoscale quantification by generalized atmospheric inversion, Biogeosciences, 12, 5393–5414, 2015.

Berchet, A., Pison, I., Crill, P. M., Thornton, B., Bousquet, P., Thonat, T., Hocking, T., Thanwerdas, J., Paris, J.-D., and Saunois, M.: Using ship-borne observations of methane isotopic ratio in the Arctic Ocean to understand methane sources in the Arctic, Atmospheric Chemistry and Physics, 20, 3987–3998, https://doi.org/10.5194/acp-20-3987-2020, 2020.

Berchet, A., Sollum, E., Thompson, R. L., Pison, I., Thanwerdas, J., Broquet, G., Chevallier, F., Aalto, T., Berchet, A., Bergamaschi, P., Brunner, D., Engelen, R., Fortems-Cheiney, A., Gerbig, C., Zwaaftink, C. D. G., Haussaire, J.-M., Henne, S., Houweling, S., Karstens, U., Kutsch, W. L., Luijkx, I. T., Monteil, G., Palmer, P. I., Saunois, M., Scholze, M., Tsuruta, A., and Zhao, Y.: The Community Inversion Framework v1.0: a unified system for atmospheric inversion studies, Geosci. Model Dev., p. 24, 2021.

Bergamaschi, P., Krol, M., Dentener, F., Vermeulen, A., Meinhardt, F., Graul, R., Ramonet, M., Peters, W., and Dlugokencky, E.: Inverse modelling of national and European CH 4 emissions using the atmospheric zoom model TM5, Atmospheric Chemistry and Physics, 5, 2431–2460, 2005.

Bergamaschi, P., Frankenberg, C., Meirink, J. F., Krol, M., Villani, M. G., Houweling, S., Dentener, F., Dlugokencky, E. J., Miller, J. B., Gatti, L. V., Engel, A., and Levin, I.: Inverse modeling of global and regional CH4 emissions using SCIAMACHY satellite retrievals, Journal of Geophysical Research: Atmospheres, 114, https://doi.org/10.1029/2009JD012287, 2009.

Bergamaschi, P., Krol, M., Meirink, J. F., Dentener, F., Segers, A., van Aardenne, J., Monni, S., Vermeulen, A., Schmidt, M., Ramonet, M., et al.: Inverse modeling of European CH4 emissions 2001–2006, Journal of Geophysical Research: Atmospheres, 115, 2010.

Berner, L. T., Massey, R., Jantz, P., Forbes, B. C., Macias-Fauria, M., Myers-Smith, I., Kumpula, T., Gauthier, G., Andreu-Hayles, L., Gaglioti, B. V., et al.: Summer warming explains widespread but not uniform greening in the Arctic tundra biome, Nature Communications, 11, 1–12, 2020.

Biastoch, A., Treude, T., Rüpke, L. H., Riebesell, U., Roth, C., Burwicz, E. B., Park, W., Latif, M., Böning, C. W., Madec, G., et al.: Rising Arctic Ocean temperatures cause gas hydrate destabilization and ocean acidification, Geophysical Research Letters, 38, 2011.

Bintanja, R.: The impact of Arctic warming on increased rainfall, Scientific reports, 8, 1–6, 2018.

Bintanja, R. and Andry, O.: Towards a rain-dominated Arctic, Nature Climate Change, 7, 263–267, 2017.

Bintanja, R. and Selten, F.: Future increases in Arctic precipitation linked to local evaporation and sea-ice retreat, Nature, 509, 479–482, 2014.

Bintanja, R., Katsman, C. A., and Selten, F. M.: Increased Arctic precipitation slows down sea ice melt and surface warming, Oceanography, 31, 118–125, 2018.

Bjerke, J. W., Karlsen, S. R., Høgda, K. A., Malnes, E., Jepsen, J. U., Lovibond, S., Vikhamar-Schuler, D., and Tømmervik, H.: Record-low primary productivity and high plant damage in the Nordic Arctic Region in 2012 caused by multiple weather events and pest outbreaks, Environmental Research Letters, 9, 084 006, 2014.

Blok, D., Heijmans, M. M., SCHAEPMAN-STRUB, G., Kononov, A., Maximov, T., and Berendse, F.: Shrub expansion may reduce summer permafrost thaw in Siberian tundra, Global Change Biology, 16, 1296–1305, 2010.

Bocquet, M.: Ensemble Kalman filtering without the intrinsic need for inflation, Nonlinear Processes in Geophysics, 18, 735–750, 2011.

Boetius, A. and Wenzhöfer, F.: Seafloor oxygen consumption fuelled by methane from cold seeps, Nature Geoscience, 6, 725–734, 2013.

Bragazza, L., Parisod, J., Buttler, A., and Bardgett, R. D.: Biogeochemical plant–soil microbe feedback in response to climate warming in peatlands, Nature Climate Change, 3, 273–277, 2013.

Brasseur, G. P. and Solomon, S.: Composition and chemistry, Aeronomy of the Middle Atmosphere: Chemistry and Physics of the Stratosphere and Mesosphere, pp. 265–442, 2005.

Brown, D. R., Jorgenson, M. T., Kielland, K., Verbyla, D. L., Prakash, A., and Koch, J. C.: Landscape Effects of Wildfire on Permafrost Distribution in Interior Alaska Derived from Remote Sensing, Remote Sensing, 8, https://doi.org/10.3390/rs8080654, 2016.

Brown, J., Ferrians, O., Heginbottom, J., and Melnikov, E.: Circum-Arctic Map of Permafrost and Ground-Ice Conditions., National Snow and Ice Data Center, Boulder, Colorado USA., 2014.

Bruhwiler, L., Dlugokencky, E., Masarie, K., Ishizawa, M., Andrews, A., Miller, J., Sweeney, C., Tans, P., and Worthy, D.: CarbonTracker-CH4: an assimilation system for estimating emissions of atmospheric methane., Atmospheric Chemistry, 14:8269-8293, 2014.

Buchwitz, M., De Beek, R., Noël, S., Burrows, J., Bovensmann, H., Bremer, H., Bergamaschi, P., Körner, S., and Heimann, M.: Carbon monoxide, methane and carbon dioxide columns retrieved from SCIAMACHY by WFM-DOAS: year 2003 initial data set, Atmospheric Chemistry and Physics, 5, 3313–3329, 2005.

Cardinali, C., Pezzulli, S., and Andersson, E.: Influence-matrix diagnostic of a data assimilation system, Quarterly Journal of the Royal Meteorological Society, 130, 2767 – 2786, https://doi.org/10.1256/qj.03.205, 2006.

Carini, P., White, A. E., Campbell, E. O., and Giovannoni, S. J.: Methane production by phosphate-starved SAR11 chemoheterotrophic marine bacteria, Nature communications, 5, 1–7, 2014.

Carvalho, K. and Wang, S.: Sea surface temperature variability in the Arctic Ocean and its marginal seas in a changing climate: Patterns and mechanisms, Global and Planetary Change, 193, 103 265, 2020.

Chan, E., Worthy, D. E. J., Chan, D., Ishizawa, M., Moran, M. D., Delcloo, A., and Vogel, F.: Eight-Year Estimates of Methane Emissions from Oil and Gas Operations in Western Canada Are Nearly Twice Those Reported in Inventories, Environmental Science & Technology, 54, 14 899–14 909, https://doi.org/10.1021/acs.est.0c04117, 2020.

Chen, X., Bohn, T. J., and Lettenmaier, D. P.: Model estimates of climate controls on pan-Arctic wetland methane emissions, p. 19, 2015.

Chevallier, F., Viovy, N., Reichstein, M., and Ciais, P.: On the assignment of prior errors in Bayesian inversions of CO2 surface fluxes, Geophysical Research Letters, 33, 2006.

Christensen, T. R., Ekberg, A., Ström, L., Mastepanov, M., Panikov, N., Öquist, M., Svensson, B. H., Nykänen, H., Martikainen, P. J., and Oskarsson, H.: Factors controlling large scale variations in methane emissions from wetlands, Geophysical Research Letters, 30, 2003.

Ciais, P., Bastos, A., Chevallier, F., Lauerwald, R., Poulter, B., Canadell, J. G., Hugelius, G., Jackson, R. B., Jain, A., Jones, M., Kondo, M., Luijkx, I. T., Patra, P. K., Peters, W., Pongratz, J., Petrescu, A. M. R., Piao, S., Qiu, C., Von Randow, C., Regnier, P., Saunois, M., Scholes, R., Shvidenko, A., Tian, H., Yang, H., Wang, X., and Zheng, B.: Definitions and methods to estimate regional land carbon fluxes for the second phase of the REgional Carbon Cycle Assessment and Processes Project (RECCAP-2), Geoscientific Model Development, 15, 1289–1316, https://doi.org/10.5194/gmd-15-1289-2022, 2022.

Cohen, J., Screen, J. A., Furtado, J. C., Barlow, M., Whittleston, D., Coumou, D., Francis, J., Dethloff, K., Entekhabi, D., Overland, J., and Jones, J.: Recent Arctic amplification and extreme mid-latitude weather, Nature Geoscience, 7, 627–637, https://doi.org/10.1038/ngeo2234, 2014.

Colman, R.: Surface albedo feedbacks from climate variability and change, Journal of Geophysical Research: Atmospheres, 118, 2827–2834, 2013.

Conway, H., Gades, A., and Raymond, C.: Albedo of dirty snow during conditions of melt, Water resources research, 32, 1713–1718, 1996.

Cook, J. M., Tedstone, A. J., Williamson, C., McCutcheon, J., Hodson, A. J., Dayal, A., Skiles, M., Hofer, S., Bryant, R., McAree, O., et al.: Glacier algae accelerate melt rates on the south-western Greenland Ice Sheet, The Cryosphere, 14, 309–330, 2020.

Copernicus: Copernicus, 2020. Copernicus Climate Change Service (C3S): ERA5: Fifth generation of ECMWF atmospheric reanalyses of the global climate., URL https://cds.climate.copernicus.eu, 2020.

Cowardin, L. M.: Classification of wetlands and deepwater habitats of the United States, Fish and Wildlife Service, US Department of the Interior, 1979.

Crippa, M., Guizzardi, D., Muntean, M., Schaaf, E., Lo Vullo, E., and Solazzo, E.: EDGAR v6.0 Greenhouse Gas Emissions, European Commission, Joint Research Centre (JRC) [data set], 2021a.

Crippa, M., Guizzardi, D., Muntean, M., Schaaf, E., Vullo, E. L., Solazzo, E., Monforti-Ferrario, F., Olivier, J., and Vignati, E.: EDGAR v6.0 Greenhouse Gas Emissions, URL http://data.europa.eu/89h/97a67d67-c62e-4826-b873-9d972c4f670b, publisher: European Commission, Joint Research Centre (JRC), 2021b.

Crosson, E.: A cavity ring-down analyzer for measuring atmospheric levels of methane, carbon dioxide, and water vapor, Applied Physics B, 92, 403–408, 2008.

Crutzen, P. J. and Zimmermann, P. H.: The changing photochemistry of the troposphere, Tellus A: Dynamic Meteorology and Oceanography, 43, 136–151, 1991.

Damm, E., Helmke, E., Thoms, S., Schauer, U., Nöthig, E., Bakker, K., and Kiene, R.: Methane production in aerobic oligotrophic surface water in the central Arctic Ocean, Biogeosciences, 7, 1099–1108, 2010.

Dee, D. P.: On-line estimation of error covariance parameters for atmospheric data assimilation, Monthly weather review, 123, 1128–1145, 1995.

Defratyka, S. M., Paris, J.-D., Yver-Kwok, C., Fernandez, J. M., Korben, P., and Bousquet, P.: Mapping urban methane sources in Paris, France, Environmental Science & Technology, 55, 8583–8591, 2021.

Deng, Z., Ciais, P., Tzompa-Sosa, Z. A., Saunois, M., Qiu, C., Tan, C., Sun, T., Ke, P., Cui, Y., Tanaka, K., et al.: Comparing national greenhouse gas budgets reported in UNFCCC inventories against atmospheric inversions, Earth System Science Data, 14, 1639–1675, 2022.

Denning, A. S., Holzer, M., Gurney, K. R., Heimann, M., Law, R. M., Rayner, P. J., Fung, I. Y., Fan, S.-M., Taguchi, S., Friedlingstein, P., et al.: Three-dimensional transport and concentration of SF6 A model intercomparison study (TransCom 2), Tellus B: Chemical and Physical Meteorology, 51, 266–297, 1999.

Desroziers, G. and Ivanov, S.: Diagnosis and adaptive tuning of observation-error parameters in a variational assimilation, Quarterly Journal of the Royal Meteorological Society, 127, 1433–1452, 2001.

Desroziers, G., Berre, L., Chapnik, B., and Poli, P.: Diagnosis of observation, background and analysis-error statistics in observation space, Quarterly Journal of the Royal Meteorological Society: A journal of the atmospheric sciences, applied meteorology and physical oceanography, 131, 3385–3396, 2005.

Dlugokencky, E., Crotwell, A., Mund, J., Crotwell, M., and Thoning, K.: Atmospheric Methane Dry Air Mole Fractions from the NOAA GML Carbon Cycle Cooperative Global Air Sampling Network, Version 2020-07, 2020.

Dobiński, W.: Permafrost active layer, Earth-Science Reviews, 208, 103 301, 2020.

Dvornikov, Y. A., Leibman, M. O., Khomutov, A. V., Kizyakov, A. I., Semenov, P., Bussmann, I., Babkin, E. M., Heim, B., Portnov, A., Babkina, E. A., et al.: Gas-emission craters of the Yamal and Gydan peninsulas: A proposed mechanism for lake genesis and development of permafrost landscapes, Permafrost and Periglacial Processes, 30, 146–162, 2019.

Ebi, K. L. and McGregor, G.: Climate change, tropospheric ozone and particulate matter, and health impacts, Environmental health perspectives, 116, 1449–1455, 2008.

Ehhalt, D.: The atmospheric cycle of methane, Tellus, 26, 58–70, 1974.

Elmendorf, S. C., Henry, G. H., Hollister, R. D., Björk, R. G., Boulanger-Lapointe, N., Cooper, E. J., Cornelissen, J. H., Day, T. A., Dorrepaal, E., Elumeeva, T. G., et al.: Plot-scale evidence of tundra vegetation change and links to recent summer warming, Nature climate change, 2, 453–457, 2012.

Emberson, L.: Effects of ozone on agriculture, forests and grasslands, Philosophical Transactions of the Royal Society A, 378, 20190 327, 2020.

Emmerton, C., St Louis, V., Lehnherr, I., Humphreys, E., Rydz, E., and Kosolofski, H.: The net exchange of methane with high Arctic landscapes during the summer growing season, Biogeosciences, 11, 3095–3106, 2014.

Etiope, G. and Ciccioli, P.: Earth's degassing: a missing ethane and propane source, Science, 323, 478–478, 2009.

Etiope, G. and Sherwood Lollar, B.: Abiotic methane on Earth, Reviews of Geophysics, 51, 276–299, 2013.

Etiope, G., Ciotoli, G., Schwietzke, S., and Schoell, M.: Gridded maps of geological methane emissions and their isotopic signature, p. 22, 2019.

Farge, E. and Soldatkin, V.: Siberian temperatures hit June record, fires spread: EU data. Reuters, 7th July. www.reuters.com/article/climate-change-arctic-idAFL8N2ED4MB., 2020.

Fenchel, T., Blackburn, H., Blackburn, T. H., and King, G. M.: Bacterial biogeochemistry: the ecophysiology of mineral cycling, Academic press, 2012.

Fortems-Cheiney, A., Chevallier, F., Pison, I., Bousquet, P., Szopa, S., Deeter, M., and Clerbaux, C.: Ten years of CO emissions as seen from Measurements of Pollution in the Troposphere (MOPITT), Journal of Geophysical Research: Atmospheres, 116, 2011.

Francis, J. A., White, D. M., Cassano, J. J., Gutowski Jr, W. J., Hinzman, L. D., Holland, M. M., Steele, M. A., and Vörösmarty, C. J.: An arctic hydrologic system in transition: Feedbacks and impacts on terrestrial, marine, and human life, Journal of Geophysical Research: Biogeosciences, 114, 2009.

Frankenberg, C., Meirink, J. F., van Weele, M., Platt, U., and Wagner, T.: Assessing methane emissions from global space-borne observations, Science, 308, 1010–1014, 2005.

Fung, I., John, J., Lerner, J., Matthews, E., Prather, M., Steele, L., and Fraser, P.: Three-dimensional model synthesis of the global methane cycle, Journal of Geophysical Research: Atmospheres, 96, 13 033–13 065, 1991.

Ganesan, A., Rigby, M., Zammit-Mangion, A., Manning, A., Prinn, R., Fraser, P., Harth, C., Kim, K.-R., Krummel, P., Li, S., et al.: Characterization of uncertainties in atmospheric trace gas inversions using hierarchical Bayesian methods, Atmospheric Chemistry and Physics, 14, 3855–3864, 2014.

Gautier, D. L., Bird, K. J., Charpentier, R. R., Grantz, A., Houseknecht, D. W., Klett, T. R., Moore, T. E., Pitman, J. K., Schenk, C. J., Schuenemeyer, J. H., Sorensen, K., Tennyson, M. E., Valin, Z. C., and Wandrey, C. J.: Assessment of undiscovered oil and gas in the arctic, Science, 324, 1175–1179, https://doi.org/10.1126/science.1169467, 2009.

Glikson, A.: The methane time bomb, Energy Procedia, 146, 23–29, 2018.

Goosse, H., Kay, J. E., Armour, K. C., Bodas-Salcedo, A., Chepfer, H., Docquier, D., Jonko, A., Kushner, P. J., Lecomte, O., Massonnet, F., et al.: Quantifying climate feedbacks in polar regions, Nature communications, 9, 1–13, 2018.

Gordon, N., Jonko, A., Forster, P., and Shell, K.: An observationally based constraint on the water-vapor feedback, Journal of Geophysical Research: Atmospheres, 118, 12–435, 2013.

Groot Zwaaftink, C. D., Henne, S., Thompson, R. L., Dlugokencky, E. J., Machida, T., Paris, J.-D., Sasakawa, M., Segers, A., Sweeney, C., and Stohl, A.: Three-dimensional methane distribution simulated with FLEXPART 8-CTM-1.1 constrained with observation data, Geoscientific Model Development, 11, 4469–4487, 2018.

Guay, K., Beck, P., and Goetz, S.: Long-Term Arctic Growing Season NDVI Trends from GIMMS 3g, 1982-2012, ORNL DAAC, 2015.

Hall, A.: The role of surface albedo feedback in climate, Journal of Climate, 17, 1550–1568, 2004.

Hannigan, J. W., Coffey, M. T., and Goldman, A.: Semiautonomous FTS observation system for remote sensing of stratospheric and tropospheric gases, Journal of Atmospheric and Oceanic Technology, 26, 1814–1828, 2009.

Hanson, R. S. and Hanson, T. E.: Methanotrophic bacteria, Microbiological reviews, 60, 439–471, 1996.

Hao, M., Luo, Y., Lin, Y., Zhao, Z., Wang, L., and Huang, J.: Contribution of atmospheric moisture transport to winter Arctic warming, International Journal of Climatology, 39, 2697–2710, 2019.

Hasekamp, O., Lorente, A., Hu, H., Butz, A., aan de Brugh, J., and Landgraf, J.: Algorithm Theoretical Baseline Document for Sentinel-5 Precursor Methane Retrieval, Netherlands Institute for Space Research, 2022.

Hassol, S. J.: Impacts of a warming Arctic: Arctic Climate Impact Assessment, Cambridge University Press, Cambridge, U.K. ; New York, N.Y, oCLC: ocm56942125, 2004.

Hatakka, J. and RI, I.: ICOS Atmosphere Level 2 data, Pallas, release 2022-1, https://doi.org/10.18160/BM0E-F42G, medium: Collection of ICOS ATC ASCII files Publisher: ICOS ERIC – Carbon Portal Version Number: 1.0, 2022.

Hatakka, J., Aalto, T., Aaltonen, V., Aurela, M., Hakola, H., Komppula, M., Laurila, T., Lihavainen, H., Paatero, J., Salminen, K., and others: Overview of the atmospheric research activities and results at Pallas GAW station, Boreal Environment Research, 8, 365–384, publisher: FINNISH ZOOLOGICAL AND BOTANICAL PUBLISHING BOARD, 2003.

Henderson-Sellers, A. and Wilson, M.: Surface albedo data for climatic modeling, Reviews of Geophysics, 21, 1743–1778, 1983.

Hittmeir, S., Philipp, A., and Seibert, P.: A conservative reconstruction scheme for the interpolation ofextensive quantities in the Lagrangian particle dispersion modelFLEXPART, preprint, Numerical Methods, https://doi.org/10.5194/gmd-2017-323, 2018.

Hoesly, R. M., Smith, S. J., Feng, L., Klimont, Z., Janssens-Maenhout, G., Pitkanen, T., Seibert, J. J., Vu, L., Andres, R. J., Bolt, R. M., Bond, T. C., Dawidowski, L., Kholod, N., Kurokawa, J.-i., Li, M., Liu, L., Lu, Z., Moura, M. C. P., O'Rourke, P. R., and Zhang, Q.: Historical (1750–2014) anthropogenic emissions of reactive gases and aerosols from the Community Emissions Data System (CEDS), Geosci. Model Dev., p. 40, 2018.

Holland, M. M., Finnis, J., Barrett, A. P., and Serreze, M. C.: Projected changes in Arctic Ocean freshwater budgets, Journal of Geophysical Research: Biogeosciences, 112, 2007.

Hossaini, R., Chipperfield, M. P., Saiz-Lopez, A., Fernandez, R., Monks, S., Feng, W., Brauer, P., and Von Glasow, R.: A global model of tropospheric chlorine chemistry: Organic versus inorganic sources and impact on methane oxidation, Journal of Geophysical Research: Atmospheres, 121, 14–271, 2016.

Houweling, S., Kaminski, T., Dentener, F., Lelieveld, J., and Heimann, M.: Inverse modeling of methane sources and sinks using the adjoint of a global transport model., Geophysical Research: Atmospheres, 104:26,137-26,160, 1999.

Houweling, S., Krol, M., Bergamaschi, P., Frankenberg, C., Dlugokencky, E. J., Morino, I., Notholt, J., Sherlock, V., Wunch, D., Beck, V., Gerbig, C., Chen, H., Kort, E. A., Röckmann, T., and Aben, I.: A multi-year methane inversion using SCIAMACHY, accounting for systematic errors using TCCON measurements, Atmospheric Chemistry and Physics, 14, 3991–4012, https://doi.org/10.5194/acp-14-3991-2014, 2014.

Hu, H., Hasekamp, O., Butz, A., Galli, A., Landgraf, J., Aan de Brugh, J., Borsdorff, T., Scheepmaker, R., and Aben, I.: The operational methane retrieval algorithm for TROPOMI, Atmospheric Measurement Techniques, 9, 5423–5440, 2016.

Hugelius, G., Tarnocai, C., Broll, G., Canadell, J., Kuhry, P., and Swanson, D.: The Northern Circumpolar Soil Carbon Database: spatially distributed datasets of soil coverage and soil carbon storage in the northern permafrost regions, Earth System Science Data, 5, 3–13, 2013.

Hugelius, G., Strauss, J., Zubrzycki, S., Harden, J. W., Schuur, E., Ping, C.-L., Schirrmeister, L., Grosse, G., Michaelson, G. J., Koven, C. D., et al.: Estimated stocks of circumpolar permafrost carbon with quantified uncertainty ranges and identified data gaps, Biogeosciences, 11, 6573–6593, 2014.

Hugelius, G., Barry, T., et al.: Arctic Peatlands and Mineral Wetlands Maps, 2021.

Inness, A., Ades, M., Agustí-Panareda, A., Barré, J., Benedictow, A., Blechschmidt, A.-M., Dominguez, J. J., Engelen, R., Eskes, H., Flemming, J., Huijnen, V., Jones, L., Kipling, Z., Massart, S., Parrington, M., Peuch, V.-H., Razinger, M., Remy, S., Schulz, M., and Suttie, M.: The CAMS reanalysis of atmospheric composition, Atmospheric Chemistry and Physics, 19, 3515–3556, https://doi.org/10.5194/acp-19-3515-2019, 2019.

IPCC: IPCC, 2007: Climate Change 2007: Synthesis Report. Contribution of Working Groups I, II and III to the Fourth Assessment Report of the Intergovernmental Panel on Climate Change [Core Writing Team, Pachauri, R.K and Reisinger, A. (eds.)]. IPCC, Geneva, Switzerland, 104 pp., URL https://www.ipcc.ch/site/assets/uploads/2018/02/ar4_syr_full_report.pdf, 2007.

IPCC: IPCC, 2013: Climate Change 2013: The Physical Science Basis. Contribution of Working Group I to the Fifth Assessment Report of the Intergovern- mental Panel on Climate Change [Stocker, T.F., D. Qin, G.-K. Plattner, M. Tignor, S.K. Allen, J. Boschung, A. Nauels, Y. Xia, V. Bex and P.M. Midgley (eds.)]. Cambridge University Press, Cambridge, United Kingdom and New York, NY, USA, 1535 pp., URL https://www.ipcc.ch/site/assets/uploads/2018/02/WG1AR5_all_final.pdf, 2013.

IPCC: IPCC, 2014: Climate Change 2014: Mitigation of Climate Change. Contribution of Working Group III to the Fifth Assessment Report of the Intergovernmental Panel on Climate Change [Edenhofer, O., R. Pichs-Madruga, Y. Sokona, E. Farahani, S. Kadner, K. Seyboth, A. Adler, I. Baum, S. Brunner, P. Eickemeier, B. Kriemann, J. Savolainen, S. Schlömer, C. von Stechow, T. Zwickel and J.C. Minx (eds.)]. Cambridge University Press, Cambridge, United Kingdom and New York, NY, USA., URL https://www.ipcc.ch/site/assets/uploads/2018/02/ipcc_wg3_ar5_full.pdf, 2014.

IPCC: IPCC, 2018: Summary for Policymakers. In: Global Warming of 1.5°C. An IPCC Special Report on the impacts of global warming of 1.5°C above pre-industrial levels and related global greenhouse gas emission pathways, in the context of strengthening the global response to the threat of climate change, sustainable development, and efforts to eradicate poverty [Masson-Delmotte, V., P. Zhai, H.-O. Pörtner, D. Roberts, J. Skea, P.R. Shukla, A. Pirani, W. Moufouma-Okia, C. Péan, R. Pidcock, S. Connors, J.B.R. Matthews, Y. Chen, X. Zhou, M.I. Gomis, E. Lonnoy, T. Maycock, M. Tignor, and T. Waterfield (eds.)]. Cambridge University Press, Cambridge, UK and New York, NY, USA, pp. 3-24, doi:10.1017/9781009157940.001., 2018.

IPCC: IPCC, 2019. IPCC Special Report on the Ocean and Cryosphere in a Changing Climate. Pörtner, H.-O., D.C. Roberts, V. Masson-Delmotte, P. Zhai, M. Tignor, E. Poloczanska, K. Mintenbeck, A. Alegría, M. Nicolai, A. Okem, J. Petzold, B. Rama and N.M. Weyer (eds.)., 2019.

IPCC: IPCC, 2022: Climate Change 2022: Impacts, Adaptation, and Vulnerability. Contribution of Working Group II to the Sixth Assessment Report of the Intergovernmental Panel on Climate Change [H.-O. Pörtner, D.C. Roberts, M. Tignor, E.S. Poloczanska, K. Mintenbeck, A. Alegría, M. Craig, S. Langsdorf, S. Löschke, V. Möller, A. Okem, B. Rama (eds.)]. Cambridge University Press. In Press., URL https://www.ipcc.ch/report/ar6/wg2/downloads/report/IPCC_AR6_WGII_FinalDraft_FullReport.pdf, 2022.

Ishizawa, M., Chan, D., Worthy, D., Chan, E., Vogel, F., and Maksyutov, S.: Analysis of atmospheric CH₄ in Canadian Arctic and estimation of the regional CH₄ fluxes, preprint, Gases/Atmospheric Modelling/Troposphere/Physics (physical properties and processes), https://doi.org/10.5194/acp-2018-907, 2018.

Ito, A.: Methane emission from pan-Arctic natural wetlands estimated using a process-based model, 1901–2016, Polar Science, 21, 26–36, https://doi.org/10.1016, 2019.

Iversen, N. and Jorgensen, B. B.: Anaerobic methane oxidation rates at the sulfate-methane transition in marine sediments from Kattegat and Skagerrak (Denmark) 1, Limnology and Oceanography, 30, 944–955, 1985.

Jafarov, E. E., Coon, E. T., Harp, D. R., Wilson, C. J., Painter, S. L., Atchley, A. L., and Romanovsky, V. E.: Modeling the role of preferential snow accumulation in through talik development and hillslope groundwater flow in a transitional permafrost landscape, Environmental Research Letters, 13, 105 006, 2018.

Jain, P., Wang, X., and Flannigan, M. D.: Trend analysis of fire season length and extreme fire weather in North America between 1979 and 2015, International Journal of Wildland Fire, 26, 1009–1020, 2017.

Jansen, E., Christensen, J., Dokken, T., Nisancioglu, K., Vinther, B., Capron, E., Guo, C., Jensen, M., Langen, P., Pedersen, R., Yang, S., Bentsen, M., Kjær, H., Sadatzki, H., Sessford, E., and Stendel, M.: Past perspectives on the present era of abrupt Arctic climate change, Nature Climate Change, 10, 1–8, https://doi.org/10.1038/s41558-020-0860-7, 2020.

Janssens-Maenhout, G., Crippa, M., Guizzardi, D., Muntean, M., Schaaf, E., Dentener, F., Bergamaschi, P., Pagliari, V., Olivier, J. G. J., Peters, J. A. H. W., van Aardenne, J. A., Monni, S., Doering, U., Petrescu, A. M. R., Solazzo, E., and Oreggioni, G. D.: EDGAR v4.3.2 Global Atlas of the three major greenhouse gas emissions for the period 1970–2012, Earth System Science Data, 11, 959–1002, https://doi.org/10.5194/essd-11-959-2019, 2019.

Jenkins, L. K., Bourgeau-Chavez, L. L., French, N. H., Loboda, T. V., and Thelen, B. J.: Development of methods for detection and monitoring of fire disturbance in the Alaskan tundra using a two-decade long record of synthetic aperture radar satellite images, Remote Sensing, 6, 6347–6364, 2014.

Jones, A., Thomson, D., Hort, M., and Devenish, B.: The UK Met Office's next-generation atmospheric dispersion model, NAME III, in: Air pollution modeling and its application XVII, pp. 580–589, Springer, 2007.

Jones, B. T., Muller, J. B., O'Shea, S. J., Bacak, A., Le Breton, M., Bannan, T. J., Leather, K. E., Booth, A. M., Illingworth, S., Bower, K., et al.: Airborne measurements of HC (O) OH in the European Arctic: A winter–summer comparison, Atmospheric Environment, 99, 556–567, 2014.

Judd, A. G.: Natural seabed gas seeps as sources of atmospheric methane, Environmental Geology, 46, 988–996, 2004.

Kaiser-Weiss, A. K., Mamtimin, B., and Plass-Dülmer, C.: Integrated greenhouse gas monitoring system for Germany., in: Geophysical Research Abstracts, vol. 21, 2019.

Kaminski, T., Rayner, P. J., Heimann, M., and Enting, I. G.: On aggregation errors in atmospheric transport inversions, Journal of Geophysical Research: Atmospheres, 106, 4703–4715, 2001.

Kaminski, T., Knorr, W., Schürmann, G., Scholze, M., Rayner, P., Zaehle, S., Blessing, S., Dorigo, W., Gayler, V., Giering, R., et al.: The BETHY/JSBACH carbon cycle data assimilation system: Experiences and challenges, Journal of Geophysical Research: Biogeosciences, 118, 1414–1426, 2013.

Kaminski, T., Scholze, M., Rayner, P., Voßbeck, M., Buchwitz, M., Reuter, M., Knorr, W., Chen, H., Agustí-Panareda, A., Löscher, A., et al.: Assimilation of atmospheric CO2 observations from space can support national CO2 emission inventories, Environmental Research Letters, 17, 014 015, 2022.

Karion, A., Sweeney, C., Tans, P., and Newberger, T.: AirCore: An innovative atmospheric sampling system, Journal of Atmospheric and Oceanic Technology, 27, 1839–1853, 2010.

Karion, A., Sweeney, C., Miller, J. B., Andrews, A. E., Commane, R., Dinardo, S., Henderson, J. M., Lindaas, J., Lin, J. C., Luus, K. A., Newberger, T., Tans, P., Wofsy, S. C., Wolter, S., and Miller, C. E.: Investigating Alaskan methane and carbon dioxide fluxes using measurements from the CARVE tower, Atmospheric Chemistry and Physics, 16, 5383–5398, https://doi.org/10.5194/acp-16-5383-2016, 2016.

Keegan, K. M., Albert, M. R., McConnell, J. R., and Baker, I.: Climate change and forest fires synergistically drive widespread melt events of the Greenland Ice Sheet, Proceedings of the National Academy of Sciences, 111, 7964–7967, 2014.

Kiehl, J., Hack, J., Bonan, G., Boville, B., and Briegleb, B.: Description of the NCAR community climate model (CCM3). Technical Note, Tech. rep., National Center for Atmospheric Research, Boulder, CO (United States . . . , 1996.

Kim, J.-S., Kug, J.-S., Jeong, S.-J., Park, H., and Schaepman-Strub, G.: Extensive fires in southeastern Siberian permafrost linked to preceding Arctic Oscillation, Science advances, 6, eaax3308, 2020.

Kirschke, S., Bousquet, P., Ciais, P., Saunois, M., Canadell, J. G., Dlugokencky, E. J., Bergamaschi, P., Bergmann, D., Blake, D. R., Bruhwiler, L., Cameron-Smith, P., Castaldi, S., Chevallier, F., Feng, L., Fraser, A., Heimann, M., Hodson, E. L., Houweling, S., Josse, B., Fraser, P. J., Krummel, P. B., Lamarque, J.-F., Langenfelds, R. L., Le Quéré, C., Naik, V., O'Doherty, S., Palmer, P. I., Pison, I., Plummer, D., Poulter, B., Prinn, R. G., Rigby, M., Ringeval, B., Santini, M., Schmidt, M., Shindell, D. T., Simpson, I. J., Spahni, R., Steele, L. P., Strode, S. A., Sudo, K., Szopa, S., van der Werf, G. R., Voulgarakis, A., van Weele, M., Weiss, R. F., Williams, J. E., and Zeng, G.: Three decades of global methane sources and sinks, Nature Geoscience, 6, 813–823, https://doi.org/10.1038/ngeo1955, 2013.

Kizyakov, A., Leibman, M., Zimin, M., Sonyushkin, A., Dvornikov, Y., Khomutov, A., Dhont, D., Cauquil, E., Pushkarev, V., and Stanilovskaya, Y.: Gas emission craters and mound-predecessors in the north of west Siberia, similarities and differences, Remote Sensing, 12, 2182, 2020.

Knittel, K. and Boetius, A.: Anaerobic oxidation of methane: progress with an unknown process, Annual review of microbiology, 63, 311–334, 2009.

Kochanski, A. K., Mallia, D. V., Fearon, M. G., Mandel, J., Souri, A. H., and Brown, T.: Modeling wildfire smoke feedback mechanisms using a coupled fire-atmosphere model with a radiatively active aerosol scheme, Journal of Geophysical Research: Atmospheres, 124, 9099–9116, 2019.

Kort, E., Wofsy, S., Daube, B., Diao, M., Elkins, J., Gao, R., Hintsa, E., Hurst, D., Jimenez, R., Moore, F., et al.: Atmospheric observations of Arctic Ocean methane emissions up to 82 north, Nature Geoscience, 5, 318–321, 2012.

Kort, E., Smith, M., Murray, L., Gvakharia, A., Brandt, A., Peischl, J., Ryerson, T., Sweeney, C., and Travis, K.: Fugitive emissions from the Bakken shale illustrate role of shale production in global ethane shift, Geophysical Research Letters, 43, 4617–4623, 2016.

Kretschmer, K., Biastoch, A., Rüpke, L., and Burwicz, E.: Modeling the fate of methane hydrates under global warming, Global Biogeochemical Cycles, 29, 610–625, 2015.

Kuhn, M. A., Varner, R. K., Bastviken, D., Crill, P., MacIntyre, S., Turetsky, M., Walter Anthony, K., McGuire, A. D., and Olefeldt, D.: BAWLD-CH 4: a comprehensive dataset of methane fluxes from boreal and arctic ecosystems, Earth System Science Data, 13, 5151–5189, 2021.

Lan, X., Thoning, K., and Dlugokencky, E.: Trends in globally-averaged CH4, N2O, and SF6 determined from NOAA Global Monitoring Laboratory measurements. Version 2022-10, https://doi.org/10.15138/P8XG-AA10, 2022.

Lau, M. C., Stackhouse, B., Layton, A. C., Chauhan, A., Vishnivetskaya, T., Chourey, K., Ronholm, J., Mykytczuk, N., Bennett, P., Lamarche-Gagnon, G., et al.: An active atmospheric methane sink in high Arctic mineral cryosols, The ISME journal, 9, 1880–1891, 2015.

Lauvaux, T., Pannekoucke, O., Sarrat, C., Chevallier, F., Ciais, P., Noilhan, J., and Rayner, P.: Structure of the transport uncertainty in mesoscale inversions of CO 2 sources and sinks using ensemble model simulations, Biogeosciences, 6, 1089–1102, 2009.

Lauvaux, T., Schuh, A., Uliasz, M., Richardson, S., Miles, N., Andrews, A., Sweeney, C., Diaz, L., Martins, D., Shepson, P., et al.: Constraining the CO 2 budget of the corn belt: exploring uncertainties from the assumptions in a mesoscale inverse system, Atmospheric Chemistry and Physics, 12, 337–354, 2012.

Lee, H., Swenson, S. C., Slater, A. G., and Lawrence, D. M.: Effects of excess ground ice on projections of permafrost in a warming climate, Environmental Research Letters, 9, 124 006, 2014.

Lehner, B. and Döll, P.: Development and validation of a global database of lakes, reservoirs and wetlands, Journal of hydrology, 296, 1–22, 2004.

Leifer, I. and Patro, R. K.: The bubble mechanism for methane transport from the shallow sea bed to the surface: A review and sensitivity study, Continental Shelf Research, 22, 2409–2428, 2002.

Levy, H.: Normal atmosphere: Large radical and formaldehyde concentrations predicted, Science, 173, 141–143, 1971.

Lin, J., Gerbig, C., Wofsy, S., Andrews, A., Daube, B., Davis, K., and Grainger, C.: A near-field tool for simulating the upstream influence of atmospheric observations: The Stochastic Time-Inverted Lagrangian Transport (STILT) model, Journal of Geophysical Research: Atmospheres, 108, 2003.

Lin, S., Liu, Y., and Huang, X.: Climate-induced Arctic-boreal peatland fire and carbon loss in the 21st century, Science of The Total Environment, 796, 148 924, 2021.

Locatelli, R., Bousquet, P., Chevallier, F., Fortems-Cheney, A., Szopa, S., Saunois, M., Agusti-Panareda, A., Bergmann, D., Bian, H., Cameron-Smith, P., et al.: Impact of transport model errors on the global and regional methane emissions estimated by inverse modelling, Atmospheric Chemistry and Physics, 13, 9917–9937, 2013.

López-Blanco, E., Jackowicz-Korczynski, M., Mastepanov, M., Skov, K., Westergaard-Nielsen, A., Williams, M., and Christensen, T. R.: Multi-year data-model evaluation reveals the importance of nutrient availability over climate in arctic ecosystem C dynamics, Environmental research letters, 15, 094 007, 2020.

Loranty, M. M., Abbott, B. W., Blok, D., Douglas, T. A., Epstein, H. E., Forbes, B. C., Jones, B. M., Kholodov, A. L., Kropp, H., Malhotra, A., et al.: Reviews and syntheses: Changing ecosystem influences on soil thermal regimes in northern high-latitude permafrost regions, Biogeosciences, 15, 5287–5313, 2018.

Lund, M., Raundrup, K., Westergaard-Nielsen, A., López-Blanco, E., Nymand, J., and Aastrup, P.: Larval outbreaks in West Greenland: Instant and subsequent effects on tundra ecosystem productivity and CO2 exchange, Ambio, 46, 26–38, 2017.

Lund Myhre, C., Platt, S. M., Hermansen, O., Lunder, C., and RI, I.: ICOS Atmosphere Level 2 data, Zeppelin, release 2022-1, https://doi.org/10.18160/DVRW-N591, medium: Collection of ICOS ATC ASCII files Publisher: ICOS ERIC – Carbon Portal Version Number: 1.0, 2022.

Łupikasza, E. and Cielecka-Nowak, K.: Changing probabilities of days with snow and rain in the atlantic sector of the arctic under the current warming trend, Journal of Climate, 33, 2509–2532, 2020.

MacBean, N., Bacour, C., Raoult, N., Bastrikov, V., Koffi, E., Kuppel, S., Maignan, F., Ottlé, C., Peaucelle, M., Santaren, D., et al.: Quantifying and Reducing Uncertainty in Global Carbon Cycle Predictions: Lessons and Perspectives From 15 Years of Data Assimilation Studies with the ORCHIDEE Terrestrial Biosphere Model, Global Biogeochemical Cycles, p. e2021GB007177, 2022.

Maksyutov, S., Oda, T., Saito, M., Janardanan, R., Belikov, D., Kaiser, J. W., Zhuravlev, R., Ganshin, A., Valsala, V. K., Andrews, A., Chmura, L., Dlugokencky, E., Haszpra, L., Langenfelds, R. L., Machida, T., Nakazawa, T., Ramonet, M., Sweeney, C., and Worthy, D.: Technical note: A high-resolution inverse modelling technique for estimating surface CO_2 fluxes based on the NIES-TM – FLEXPART coupled transport model and its adjoint, Atmospheric Chemistry and Physics Discussions, pp. 1–33, https://doi.org/https://doi.org/10.5194/acp-2020-251, publisher: Copernicus GmbH, 2020.

Manabe, S.: Role of greenhouse gas in climate change, Tellus A: Dynamic Meteorology and Oceanography, 71, 1620 078, 2019.

Mascarelli, A.: A sleeping giant?, Nature climate change, 1, 46–49, 2009.

Masrur, A., Petrov, A. N., and DeGroote, J.: Circumpolar spatio-temporal patterns and contributing climatic factors of wildfire activity in the Arctic tundra from 2001–2015, Environmental Research Letters, 13, 014 019, 2018.

Masyagina, O. V. and Menyailo, O. V.: The impact of permafrost on carbon dioxide and methane fluxes in Siberia: A meta-analysis, Environmental Research, 182, 109 096, https://doi.org/10.1016/j.envres.2019.109096, 2020.

Matthews, E. and Fung, I.: Methane emission from natural wetlands: Global distribution, area, and environmental characteristics of sources, Global biogeochemical cycles, 1, 61–86, 1987.

McCarthy, M., Boering, K., Rice, A., Tyler, S., Connell, P., and Atlas, E.: Carbon and hydrogen isotopic compositions of stratospheric methane: 2. Two-dimensional model results and implications for kinetic isotope effects, Journal of Geophysical Research: Atmospheres, 108, 2003.

McCarty, J. L., Smith, T. E., and Turetsky, M. R.: Arctic fires re-emerging, Nature Geoscience, 13, 658–660, 2020.

McCrystall, M. R., Stroeve, J., Serreze, M., Forbes, B. C., and Screen, J. A.: New climate models reveal faster and larger increases in Arctic precipitation than previously projected, Nature communications, 12, 1–12, 2021.

McGinnis, D. F., Greinert, J., Artemov, Y., Beaubien, S., and Wüest, A.: Fate of rising methane bubbles in stratified waters: How much methane reaches the atmosphere?, Journal of Geophysical Research: Oceans, 111, 2006.

McGuire, A. D., Lawrence, D. M., Koven, C., Clein, J. S., Burke, E., Chen, G., Jafarov, E., MacDougall, A. H., Marchenko, S., Nicolsky, D., et al.: Dependence of the evolution of carbon dynamics in the northern permafrost region on the trajectory of climate change, Proceedings of the National Academy of Sciences, 115, 3882–3887, 2018.

Membrive, O., Crevoisier, C., Sweeney, C., Danis, F., Hertzog, A., Engel, A., Bönisch, H., and Picon, L.: AirCore-HR: a high-resolution column sampling to enhance the vertical description of CH 4 and CO 2, Atmospheric Measurement Techniques, 10, 2163–2181, 2017.

Meredith, M., Sommerkorn, M., Cassotta, S., Derksen, C., Ekaykin, A., Hollowed, A., Kofinas, G., Mackintosh, A., Melbourne-Thomas, J., Muelbert, M., Ottersen, G., Pritchard, H., and Schuur, E.: Polar Regions. In: IPCC Special Report on the Ocean and Cryosphere in a Changing Climate [H.-O. Pörtner, D.C. Roberts, V. Masson-Delmotte, P. Zhai, M. Tignor, E. Poloczanska, K. Mintenbeck, A. Alegría, M. Nicolai, A. Okem, J. Petzold, B. Rama, N.M. Weyer, (eds.)]. In press., https://doi.org/10.1088/1748-9326/aab2b3, 2019.

Michalak, A., Hirsch, A., Bruhwiler, L., Gurney, K., Peters, W., and Tans, P.: Maximum likelihood estimation of covariance parameters for Bayesian atmospheric trace gas surface flux inversions, Journal of Geophysical Research: Atmospheres, 110, https://doi.org/10.1029/2005JD005970, 2005.

Milkov, A. V.: Molecular and stable isotope compositions of natural gas hydrates: A revised global dataset and basic interpretations in the context of geological settings, Organic geochemistry, 36, 681–702, 2005.

Miller, S. M., Commane, R., Melton, J. R., Andrews, A. E., Benmergui, J., Dlugokencky, E. J., Janssens-Maenhout, G., Michalak, A. M., Sweeney, C., and Worthy, D. E. J.: Evaluation of wetland methane emissions across North America using atmospheric data and inverse modeling, p. 11, 2016.

Mitchell, J. F., Senior, C., and Ingram, W.: C02 and climate: a missing feedback?, Nature, 341, 132–134, 1989.

Moon, T., Ahlstrøm, A., Goelzer, H., Lipscomb, W., and Nowicki, S.: Rising oceans guaranteed: Arctic land ice loss and sea level rise, Current climate change reports, 4, 211–222, 2018.

Morrison, A., Kay, J., Chepfer, H., Guzman, R., and Yettella, V.: Isolating the liquid cloud response to recent Arctic sea ice variability using spaceborne lidar observations, Journal of Geophysical Research: Atmospheres, 123, 473–490, 2018.

Murrell, J.: The aerobic methane oxidizing bacteria (methanotrophs), in: Handbook of hydrocarbon and lipid microbiology, 2010.

Myers-Smith, I. H., Kerby, J. T., Phoenix, G. K., Bjerke, J. W., Epstein, H. E., Assmann, J. J., John, C., Andreu-Hayles, L., Angers-Blondin, S., Beck, P. S., et al.: Complexity revealed in the greening of the Arctic, Nature Climate Change, 10, 106–117, 2020.

Myhre, G., Bréon, F.-M., and Granier, C.: Anthropogenic and Natural Radiative Forcing 2, Notes, 16, 2011.

Myhre, G., Myhre, C., Samset, B., and Storelvmo, T.: Aerosols and their relation to global climate and climate sensitivity, Nature Education Knowledge, 4, 7, 2013.

Nakicenovic, N., Alcamo, J., Davis, G., de Vries, B., Fenhann, J., Gaffin, S., Gregory, K., Grï, A., Jung, T. Y., Kram, T., et al.: IPCC: Special Report on Emissions Scenarios, 2000.

Narbaud, C., Paris, J.-D., Wittig, S., Berchet, A., Saunois, M., Nédelec, P., Belan, B. D., Arshinov, M. Y., Belan, S. B., Davydov, D., et al.: Disentangling methane and carbon dioxide sources and transport across the Russian Arctic from aircraft measurements, Atmospheric Chemistry and Physics Discussions, pp. 1–38, 2022.

Netz, L.: Arctic ocean methane emissions and sensitivity to upheavals in the ocean dynamic. Internship Report. Institut Mines-Télécom, Laboratoire des sciences du climat et de l'environnement., 2021.

Nisbet, E. G., Manning, M., Dlugokencky, E., Fisher, R., Lowry, D., Michel, S., Myhre, C. L., Platt, S. M., Allen, G., Bousquet, P., et al.: Very strong atmospheric methane growth in the 4 years 2014–2017: Implications for the Paris Agreement, Global Biogeochemical Cycles, 33, 318–342, 2019.

Oh, Y., Zhuang, Q., Liu, L., Welp, L. R., Lau, M. C., Onstott, T. C., Medvigy, D., Bruhwiler, L., Dlugokencky, E. J., Hugelius, G., et al.: Reduced net methane emissions due to microbial methane oxidation in a warmer Arctic, Nature Climate Change, 10, 317–321, 2020.

Overduin, P. P., Liebner, S., Knoblauch, C., Günther, F., Wetterich, S., Schirrmeister, L., Hubberten, H.-W., and Grigoriev, M. N.: Methane oxidation following submarine permafrost degradation: Measurements from a central Laptev Sea shelf borehole, Journal of Geophysical Research: Biogeosciences, 120, 965–978, 2015.

Overland, J. E. and Wang, M.: The 2020 Siberian heat wave, International Journal of Climatology, 41, E2341–E2346, 2021.

Pallandt, M. M. T. A., Kumar, J., Mauritz, M., Schuur, E. A. G., Virkkala, A.-M., Celis, G., Hoffman, F. M., and Göckede, M.: Model estimates of climate controls on pan-Arctic wetland methane emissions, p. 25, URL https://doi.org/10.5194/bg-19-559-2022, 2022.

Pankratova, N., Skorokhod, A., Belikov, I., Belousov, V., Muravya, V., and Flint, M.: Ship-Borne Observations of Atmospheric CH4 and δ^{13}C Isotope Signature in Methane over Arctic Seas in Summer and Autumn 2021, Atmosphere, 13, https://doi.org/10.3390/atmos13030458, 2022.

Panov, A., Prokushkin, A., Kübler, K. R., Korets, M., Urban, A., Bondar, M., and Heimann, M.: Continuous CO2 and CH4 Observations in the Coastal Arctic Atmosphere of the Western Taimyr Peninsula, Siberia: The First Results from a New Measurement Station in Dikson, Atmosphere, 12, 876, 2021.

Paris, J.-D., Ciais, P., Nédélec, P., Ramonet, M., Belan, B., Arshinov, M. Y., Golitsyn, G., Granberg, I., Stohl, A., Cayez, G., et al.: The YAK-AEROSIB transcontinental aircraft campaigns: new insights on the transport of CO2, CO and O3 across Siberia, Tellus B: Chemical and Physical Meteorology, 60, 551–568, 2008.

Paris, J.-D., Ciais, P., Nédélec, P., Stohl, A., Belan, B. D., Arshinov, M. Y., Carouge, C., Golitsyn, G. S., and Granberg, I. G.: New insights on the chemical composition of the Siberian air shed from the YAK-AEROSIB aircraft campaigns, Bulletin of the American Meteorological Society, 91, 625–642, 2010.

Parker, R. J., Webb, A., Boesch, H., Somkuti, P., Barrio Guillo, R., Di Noia, A., Kalaitzi, N., Anand, J. S., Bergamaschi, P., Chevallier, F., et al.: A decade of GOSAT Proxy satellite CH 4 observations, Earth System Science Data, 12, 3383–3412, 2020.

Patel, K.: Fires burn in Siberia, but Russian firefighting assets are in Ukraine, The Waschington Post, 2022.

Pegau, W. S. and Paulson, C. A.: The albedo of Arctic leads in summer, Annals of Glaciology, 33, 221–224, 2001.

Perovich, D., Meier, W., Tschudi, M., Hendricks, S., Petty, A., Divine, D., Farrell, S., Gerland, S., Haas, C., Kaleschke, L., Pavlova, O., Ricker, R., Tian-Kunze, X., Webster, M., and Wood, K.: Sea ice., In: Arctic Report Card, 2020.

Petrescu, A. M. R., van Beek, L. P. H., van Huissteden, J., Prigent, C., Sachs, T., Corradi, C. a. R., Parmentier, F. J. W., and Dolman, A. J.: Modeling regional to global CH4 emissions of boreal and arctic wetlands, Global Biogeochemical Cycles, 24, https://doi.org/10.1029/2009GB003610, 2010.

Peylin, P., Baker, D., Sarmiento, J., Ciais, P., and Bousquet, P.: Influence of transport uncertainty on annual mean and seasonal inversions of atmospheric CO2 data, Journal of Geophysical Research: Atmospheres, 107, ACH–5, 2002.

Phoenix, G. K. and Bjerke, J. W.: Arctic browning: extreme events and trends reversing arctic greening, Global change biology, 22, 2960–2962, 2016.

Pisso, I., Myhre, C. L., Platt, S. M., Eckhardt, S., Hermansen, O., Schmidbauer, N., Mienert, J., Vadakkepuliyambatta, S., Bauguitte, S., Pitt, J., Allen, G., Bower, K. N., O'Shea, S., Gallagher, M. W., Percival, C. J., Pyle, J., Cain, M., and Stohl, A.: Constraints on oceanic methane emissions west of Svalbard from atmospheric in situ measurements and Lagrangian transport modeling, Journal of Geophysical Research: Atmospheres, 121, 14,188–14,200, https://doi.org/https://doi.org/10.1002/2016JD025590, 2016.

Pisso, I., Sollum, E., Grythe, H., Kristiansen, N., Cassiani, M., Eckhardt, S., Arnold, D., Morton, D., Thompson, R. L., Groot Zwaaftink, C. D., Evangeliou, N., Sodemann, H., Haimberger, L., Henne, S., Brunner, D., Burkhart, J. F., Fouilloux, A., Brioude, J., Philipp, A., Seibert, P., and Stohl, A.: The Lagrangian particle dispersion model FLEXPART version 10.3, preprint, Atmospheric Sciences, https://doi.org/10.5194/gmd-2018-333, 2019a.

Pisso, I., Sollum, E., Grythe, H., Kristiansen, N. I., Cassiani, M., Eckhardt, S., Arnold, D., Morton, D., Thompson, R. L., Groot Zwaaftink, C. D., et al.: The Lagrangian particle dispersion model FLEXPART version 10.4, Geoscientific Model Development, 12, 4955–4997, 2019b.

Ponomarev, E., Yakimov, N., Ponomareva, T., Yakubailik, O., and Conard, S. G.: Current trend of carbon emissions from wildfires in Siberia, Atmosphere, 12, 559, 2021.

Potter, C. and Hugny, C.: Wildfire effects on permafrost and soil moisture in spruce forests of Interior Alaska., J. For. Res., 31, 553–563, URL https://doi.org/10.1007/s11676-018-0831-2, 2020.

Poulter, B., Bousquet, P., Canadell, J. G., Ciais, P., Peregon, A., Saunois, M., Arora, V. K., Beerling, D. J., Brovkin, V., Jones, C. D., Joos, F., Gedney, N., Ito, A., Kleinen, T., Koven, C. D., McDonald, K., Melton, J. R., Peng, C., Peng, S., Prigent, C., Schroeder, R., Riley, W. J., Saito, M., Spahni, R., Tian, H., Taylor, L., Viovy, N., Wilton, D., Wiltshire, A., Xu, X., Zhang, B., Zhang, Z., and Zhu, Q.: Global wetland contribution to 2000–2012 atmospheric methane growth rate dynamics, Environmental Research Letters, 12, 094 013, URL https://doi.org/10.1088/1748-9326/aa8391, 2017.

Prather, M. and Spivakovsky, C. M.: Tropospheric OH and the lifetimes of hydrochlorofluorocarbons, Journal of Geophysical Research: Atmospheres, 95, 18 723–18 729, 1990.

Prather, M. J., Holmes, C. D., and Hsu, J.: Reactive greenhouse gas scenarios: Systematic exploration of uncertainties and the role of atmospheric chemistry, Geophysical Research Letters, 39, https://doi.org/10.1029/2012GL051440, 2012.

Rajan, A., Mienert, J., Bünz, S., and Chand, S.: Potential serpentinization, degassing, and gas hydrate formation at a young (< 20 Ma) sedimented ocean crust of the Arctic Ocean ridge system, Journal of Geophysical Research: Solid Earth, 117, 2012.

Rajan, A., Bünz, S., Mienert, J., and Smith, A. J.: Gas hydrate systems in petroleum provinces of the SW-Barents Sea, Marine and Petroleum Geology, 46, 92–106, 2013.

RANDERSON, J., VAN DER WERF, G., GIGLIO, L., COLLATZ, G., and KASIBHATLA, P.: Global Fire Emissions Database, Version 4.1 (GFEDv4), p. 1925.7122549999906 MB, https://doi.org/10.3334/ORNLDAAC/1293, artwork Size: 1925.7122549999906 MB Publisher: ORNL Distributed Active Archive Center, 2017.

Rantanen, M., Karpechko, A. Y., Lipponen, A., Nordling, K., Hyvärinen, O., Ruosteenoja, K., Vihma, T., and Laaksonen, A.: The Arctic has warmed nearly four times faster than the globe since 1979, Commun Earth Environ, 3, 168 (2022), URL https://doi.org/10.1038/s43247-022-00498-3, 2022.

Reeburgh, W. S.: Oceanic methane biogeochemistry, Chemical reviews, 107, 486–513, 2007.

Rehder, G., Leifer, I., Brewer, P. G., Friederich, G., and Peltzer, E. T.: Controls on methane bubble dissolution inside and outside the hydrate stability field from open ocean field experiments and numerical modeling, Marine Chemistry, 114, 19–30, 2009.

Rein, G. and Huang, X.: Smouldering wildfires in peatlands, forests and the arctic: Challenges and perspectives, Current Opinion in Environmental Science & Health, 24, 100 296, 2021.

Revell, L. E., Stenke, A., Rozanov, E., Ball, W., Lossow, S., and Peter, T.: The role of methane in projections of 21st century stratospheric water vapour, Atmospheric Chemistry and Physics, 16, 13 067–13 080, 2016.

Rice, A., Tyler, S., McCarthy, M., Boering, K., and Atlas, E.: Carbon and hydrogen isotopic compositions of stratospheric methane: 1. High-precision observations from the NASA ER-2 aircraft, Journal of Geophysical Research: Atmospheres, 108, 2003.

Rice, A. L., Butenhoff, C. L., Teama, D. G., Röger, F. H., Khalil, M. A. K., and Rasmussen, R. A.: Atmospheric methane isotopic record favors fossil sources flat in 1980s and 1990s with recent increase, Proceedings of the National Academy of Sciences, 113, 10 791–10 796, 2016.

Ridgwell, A. J., Marshall, S. J., and Gregson, K.: Consumption of atmospheric methane by soils: A process-based model, Global Biogeochemical Cycles, 13, 59–70, 1999.

Riley, W., Subin, Z., Lawrence, D., Swenson, S., Torn, M., Meng, L., Mahowald, N., and Hess, P.: Barriers to predicting changes in global terrestrial methane fluxes: analyses using CLM4Me, a methane biogeochemistry model integrated in CESM, Biogeosciences, 8, 1925–1953, 2011.

Ringeval, B., Decharme, B., Piao, S., Ciais, P., Papa, F., de Noblet-Ducoudré, N., Prigent, C., Friedlingstein, P., Gouttevin, I., Koven, C., et al.: Modelling sub-grid wetland in the ORCHIDEE global land surface model: evaluation against river discharges and remotely sensed data, Geoscientific Model Development, 5, 941–962, 2012.

Rivkina, E. and Kraev, G.: Permafrost Degradation and Influx of Biogeogases into the Atmosphere, https://doi.org/10.13140/2.1.1797.0562, 2008.

Rodgers, C. D.: Inverse methods for atmospheric sounding, World Sci., URL https://www.worldscientific.com/physics/3171.html, 2000.

Ruppel, C. D.: Methane hydrates and contemporary climate change, Nature Eduction Knowledge, 2, 12, 2011.

Ryan, J. C., Hubbard, A., Stibal, M., Irvine-Fynn, T. D., Cook, J., Smith, L. C., Cameron, K., and Box, J.: Dark zone of the Greenland Ice Sheet controlled by distributed biologically-active impurities, Nature communications, 9, 1–10, 2018.

Rydsaa, J. H., Stordal, F., Bryn, A., and Tallaksen, L. M.: Effects of shrub and tree cover increase on the near-surface atmosphere in northern Fennoscandia, Biogeosciences, 14, 4209–4227, 2017.

Sæmundsson, Þ., Morino, C., Helgason, J. K., Conway, S. J., and Pétursson, H. G.: The triggering factors of the Móafellshyrna debris slide in northern Iceland: Intense precipitation, earthquake activity and thawing of mountain permafrost, Science of the total environment, 621, 1163–1175, 2018.

Salmon, E., Jégou, F., Guenet, B., Jourdain, L., Qiu, C., Guimbaud, C., Zhu, D., Ciais, P., Peylin, P., Gogo, S., Laggoun-Défarge, F., Aurela, M., Bret-Harte, M. S., Chen, J., Chu, H., Edgar, C. W., Euskirchen, E. S., Flanagan, L. B., Fortuniak, K., Holl, D., Klatt, J., Kolle, O., Kowalska, N., Kutzbach, L., Lohila, A., and Merbold, L.: Assessing methane emissions for northern peatlands in ORCHIDEE- PEAT revision 7020., p. 40, 2021.

Sasakawa, M., Shimoyama, K., Machida, T., Tsuda, N., Suto, H., Arshinov, M., Davydov, D., Fofonov, A., Krasnov, O., Saeki, T., Koyama, Y., and Maksyutov, S.: Continuous measurements of methane from a tower network over Siberia, Tellus B: Chemical and Physical Meteorology, 62, 403–416, https://doi.org/10.1111/j.1600-0889.2010.00494.x, 2010.

Saunois, M., Bousquet, P., Poulter, B., Peregon, A., Ciais, P., Canadell, J. G., Dlugokencky, E. J., Etiope, G., Bastviken, D., Houweling, S., Janssens-Maenhout, G., Tubiello, F. N., Castaldi, S., Jackson, R. B., Alexe, M., Arora, V. K., Beerling, D. J., Bergamaschi, P., Blake, D. R., Brailsford, G., Brovkin, V., Bruhwiler, L., Crevoisier, C., Crill, P., Covey, K., Curry, C., Frankenberg, C., Gedney, N., Höglund-Isaksson, L., Ishizawa, M., Ito, A., Joos, F., Kim, H.-S., Kleinen, T., Krummel, P., Lamarque, J.-F., Langenfelds, R., Locatelli, R., Machida, T., Maksyutov, S., McDonald, K. C., Marshall, J., Melton, J. R., Morino, I., Naik, V., O'Doherty, S., Parmentier, F.-J. W., Patra, P. K., Peng, C., Peng, S., Peters, G. P., Pison, I., Prigent, C., Prinn, R., Ramonet, M., Riley, W. J., Saito, M., Santini, M., Schroeder, R., Simpson, I. J., Spahni, R., Steele, P., Takizawa, A., Thornton, B. F., Tian, H., Tohjima, Y., Viovy, N., Voulgarakis, A., van Weele, M., van der Werf, G. R., Weiss, R., Wiedinmyer, C., Wilton, D. J., Wiltshire, A., Worthy, D., Wunch, D., Xu, X., Yoshida, Y., Zhang, B., Zhang, Z., and Zhu, Q.: The global methane budget 2000–2012, Earth System Science Data, 8, 697–751, https://doi.org/10.5194/essd-8-697-2016, 2016.

Saunois, M., Bousquet, P., Poulter, B., Peregon, A., Ciais, P., Canadell, J. G., Dlugokencky, E. J., Etiope, G., Bastviken, D., Houweling, S., Janssens-Maenhout, G., Tubiello, F. N., Castaldi, S., Jackson, R. B., Alexe, M., Arora, V. K., Beerling, D. J., Bergamaschi, P., Blake, D. R., Brailsford, G., Bruhwiler, L., Crevoisier, C., Crill, P., Covey, K., Frankenberg, C., Gedney, N., Höglund-Isaksson, L., Ishizawa, M., Ito, A., Joos, F., Kim, H.-S., Kleinen, T., Krummel, P., Lamarque, J.-F., Langenfelds, R., Locatelli, R., Machida, T., Maksyutov, S., Melton, J. R., Morino, I., Naik, V., O'Doherty, S., Parmentier, F.-J. W., Patra, P. K., Peng, C., Peng, S., Peters, G. P., Pison, I., Prinn, R., Ramonet, M., Riley, W. J., Saito, M., Santini, M., Schroeder, R., Simpson, I. J., Spahni, R., Takizawa, A., Thornton, B. F., Tian, H., Tohjima, Y., Viovy, N., Voulgarakis, A., Weiss, R., Wilton, D. J., Wiltshire, A., Worthy, D., Wunch, D., Xu, X., Yoshida, Y., Zhang, B., Zhang, Z., and Zhu, Q.: Variability and quasi-decadal changes in the methane budget over the period 2000–2012, Atmospheric Chemistry and Physics, 17, 11 135–11 161, https://doi.org/https://doi.org/10.5194/acp-17-11135-2017, 2017.

Saunois, M., Stavert, A. R., Poulter, B., Bousquet, P., Canadell, J. G., Jackson, R. B., Raymond, P. A., Dlugokencky, E. J., Houweling, S., Patra, P. K., Ciais, P., Arora, V. K., Bastviken, D., Bergamaschi, P., Blake, D. R., Brailsford, G., Bruhwiler, L., Carlson, K. M., Carrol, M., Castaldi, S., Chandra, N., Crevoisier, C., Crill, P. M., Covey, K., Curry, C. L., Etiope, G., Frankenberg, C., Gedney, N., Hegglin, M. I., Höglund-Isaksson, L., Hugelius, G., Ishizawa, M., Ito, A., Janssens-Maenhout, G., Jensen, K. M., Joos, F., Kleinen, T., Krummel, P. B., Langenfelds, R. L., Laruelle, G. G., Liu, L., Machida, T., Maksyutov, S., McDonald, K. C., McNorton, J., Miller, P. A., Melton, J. R., Morino, I., Müller, J., Murguia-Flores, F., Naik, V., Niwa, Y., Noce, S., O'Doherty, S., Parker, R. J., Peng, C., Peng, S., Peters, G. P., Prigent, C., Prinn, R., Ramonet, M., Regnier, P., Riley, W. J., Rosentreter, J. A., Segers, A., Simpson, I. J., Shi, H., Smith, S. J., Steele, L. P., Thornton, B. F., Tian, H., Tohjima, Y., Tubiello, F. N., Tsuruta, A., Viovy, N., Voulgarakis, A., Weber, T. S., van Weele, M., van der Werf, G. R., Weiss, R. F., Worthy, D., Wunch, D., Yin, Y., Yoshida, Y., Zhang, W., Zhang, Z., Zhao, Y., Zheng, B., Zhu, Q., Zhu, Q., and Zhuang, Q.: The Global Methane Budget 2000–2017, Earth System Science Data, 12, 1561–1623, https://doi.org/10.5194/essd-12-1561-2020, 2020.

Saxena, P., Srivastava, A., Tyagi, M., and Kaur, S.: Impact of tropospheric ozone on plant metabolism–a review, Pollut Res, 38, 175–180, 2019.

Schimel, J.: Playing scales in the methane cycle: from microbial ecology to the globe, Proceedings of the National Academy of Sciences, 101, 12 400–12 401, 2004.

Schneider von Deimling, T., Grosse, G., Strauss, J., Schirrmeister, L., Morgenstern, A., Schaphoff, S., Meinshausen, M., and Boike, J.: Observation-based modelling of permafrost carbon fluxes with accounting for deep carbon deposits and thermokarst activity, Biogeosciences, 12, 3469–3488, 2015.

Schuur, E., McGuire, A., Schädel, C., Grosse, G., Harden, J., Hayes, D., Hugelius, G., Koven, C., Kuhry, P., Lawrence, D., Natali, S., Olefeldt, D., Romanovsky, V., Schaefer, K., Turetsky, M., Treat, C., and Vonk, J.: Climate change and the permafrost carbon feedback. Nature 520, 171–179 (2015). https://doi.org/10.1038/nature14338, 2015.

Schuur, E. A., Abbott, B. W., Commane, R., Ernakovich, J., Euskirchen, E., Hugelius, G., Grosse, G., Jones, M., Koven, C., Leshyk, V., et al.: Permafrost and Climate Change: Carbon Cycle Feedbacks from the Warming Arctic, Annual Review of Environment and Resources, 47, 343–371, 2022.

Schuur, T.: Permafrost and the Global Carbon Cycle, NOAA Arctic Report Card 2019, 2019.

Screen, J. A. and Simmonds, I.: Increasing fall-winter energy loss from the Arctic Ocean and its role in Arctic temperature amplification, Geophysical Research Letters, 37, 2010.

Seibert, P. and Frank, A.: Source-receptor matrix calculation with a Lagrangian particle dispersion model in backward mode, Atmospheric Chemistry and Physics, 4, 51–63, https://doi.org/10.5194/acp-4-51-2004, 2004.

Serreze, M. C., Barrett, A. P., Stroeve, J. C., Kindig, D. N., and Holland, M. M.: The emergence of surface-based Arctic amplification, The Cryosphere, p. 9, 2009.

Shakhova, N., Alekseev, V., and Semiletov, I.: Predicted methane emission on the East Siberian shelf, in: Doklady Earth Sciences, vol. 430, p. 190, Springer Nature BV, 2010.

Shakhova, N., Semiletov, I., Sergienko, V., Lobkovsky, L., Yusupov, V., Salyuk, A., Salomatin, A., Chernykh, D., Kosmach, D., Panteleev, G., et al.: The East Siberian Arctic Shelf: towards further assessment of permafrost-related methane fluxes and role of sea ice, Philosophical Transactions of the Royal Society A: Mathematical, Physical and Engineering Sciences, 373, 20140 451, 2015.

Shakhova, N., Semiletov, I., and Chuvilin, E.: Understanding the permafrost–hydrate system and associated methane releases in the East Siberian Arctic shelf, Geosciences, 9, 251, 2019.

Sherwen, T., Schmidt, J. A., Evans, M. J., Carpenter, L. J., Großmann, K., Eastham, S. D., Jacob, D. J., Dix, B., Koenig, T. K., Sinreich, R., et al.: Global impacts of tropospheric halogens (Cl, Br, I) on oxidants and composition in GEOS-Chem, Atmospheric Chemistry and Physics, 16, 12 239–12 271, 2016.

Sherwood, O. A., Schwietzke, S., Arling, V. A., and Etiope, G.: Global inventory of gas geochemistry data from fossil fuel, microbial and burning sources, version 2017, Earth System Science Data, 9, 639–656, 2017.

Shupe, M. D. and Intrieri, J. M.: Cloud radiative forcing of the Arctic surface: The influence of cloud properties, surface albedo, and solar zenith angle, Journal of climate, 17, 616–628, 2004.

Singh, H. B., Kanakidou, M., Crutzen, P., and Jacob, D.: High concentrations and photochemical fate of oxygenated hydrocarbons in the global troposphere, Nature, 378, 50–54, 1995.

Skiles, S. M., Flanner, M., Cook, J. M., Dumont, M., and Painter, T. H.: Radiative forcing by light-absorbing particles in snow, Nature Climate Change, 8, 964–971, 2018.

Skorokhod, A. I., Berezina, E. V., Moiseenko, K. B., Elansky, N. F., and Belikov, I. B.: Benzene and toluene in the surface air of northern Eurasia from TROICA-12 campaign along the Trans-Siberian Railway, Atmospheric Chemistry and Physics, 17, 5501–5514, 2017.

Someya, Y., Yoshida, Y., and Maksyutov, S.: Large increase in atmospheric methane over West Siberian wetlands during summer detected from space, Scientific Online Letters on the Atmosphere (SOLA), pp. 3987–3998, https://doi.org/10.2151/sola.2020-027, 2020.

Spracklen, D. V., Bonn, B., and Carslaw, K. S.: Boreal forests, aerosols and the impacts on clouds and climate, Philosophical Transactions of the Royal Society A: Mathematical, Physical and Engineering Sciences, 366, 4613–4626, 2008.

Stein, A., Draxler, R. R., Rolph, G. D., Stunder, B. J., Cohen, M., and Ngan, F.: NOAA's HYSPLIT atmospheric transport and dispersion modeling system, Bulletin of the American Meteorological Society, 96, 2059–2077, 2015.

Stephens, G. L., O'Brien, D., Webster, P. J., Pilewski, P., Kato, S., and Li, J.-l.: The albedo of Earth, Reviews of geophysics, 53, 141–163, 2015.

Stohl, A., Wotawa, G., Seibert, P., and Kromp-Kolb, H.: Interpolation errors in wind fields as a function of spatial and temporal resolution and their impact on different types of kinematic trajectories, Journal of Applied Meteorology and Climatology, 34, 2149–2165, 1995.

Stohl, A., Hittenberger, M., and Wotawa, G.: Validation of the Lagrangian particle dispersion model FLEXPART against large-scale tracer experiment data, Atmospheric Environment, 32, 4245–4264, 1998.

Stohl, A., Forster, C., Frank, A., Seibert, P., and Wotawa, G.: Technical note: The Lagrangian particle dispersion model FLEXPART version 6.2, Atmos. Chem. Phys., p. 14, 2005.

Stone, R., Anderson, G., Shettle, E., Andrews, E., Loukachine, K., Dutton, E., Schaaf, C., and Roman III, M.: Radiative impact of boreal smoke in the Arctic: Observed and modeled, Journal of Geophysical Research: Atmospheres, 113, 2008.

Stroeve, J., Holland, M. M., Meier, W., Scambos, T., and Serreze, M.: Arctic sea ice decline: Faster than forecast, Geophysical Research Letters, 34, https://doi.org/10.1029/2007GL029703, 2007.

Ström, L., Mastepanov, M., and Christensen, T.: Species-specific Effects of Vascular Plants on Carbon Turnover and Methane Emissions from Wetlands., Biogeochemistry, 75, 65–82, URL https://doi.org/10.1007/s10533-004-6124-1, 2005.

Suto, H., Kataoka, F., Kikuchi, N., Knuteson, R. O., Butz, A., Haun, M., Buijs, H., Shiomi, K., Imai, H., and Kuze, A.: Thermal and near-infrared sensor for carbon observation Fourier transform spectrometer-2 (TANSO-FTS-2) on the Greenhouse gases Observing SATellite-2 (GOSAT-2) during its first year in orbit, Atmospheric Measurement Techniques, 14, 2013–2039, 2021.

Szénási, B., Berchet, A., Broquet, G., Segers, A., Denier van der Gon, H., Krol, M., Hullegie, J. J., Kiesow, A., Günther, D., Petrescu, A. M. R., et al.: A pragmatic protocol for characterising errors in atmospheric inversions of methane emissions over Europe, Tellus B: Chemical and Physical Meteorology, 73, 1–23, 2021.

Szopa, S., Naik, V., Adhikary, B., Artaxo, P., Berntsen, T., Collins, W., Fuzzi, S., Gallardo, L., Kiendler-Scharr, A., Klimont, Z., et al.: Short-lived climate forcers, in: AGU Fall Meeting Abstracts, vol. 2021, pp. U13B–06, 2021.

Tan, Z., Zhuang, Q., and Walter Anthony, K.: Modeling methane emissions from arctic lakes: Model development and site-level study, Journal of Advances in Modeling Earth Systems, 7, 459–483, 2015.

Tan, Z., Zhuang, Q., Henze, D. K., Frankenberg, C., Dlugokencky, E., Sweeney, C., Turner, A. J., Sasakawa, M., and Machida, T.: Inverse modeling of pan-Arctic methane emissions at high spatial resolution: what can we learn from assimilating satellite retrievals and using different process-based wetland and lake biogeochemical models?, Atmos. Chem. Phys., p. 18, 2016.

Tang, J., Zhuang, Q., Shannon, R. D., and White, J. R.: Quantifying wetland methane emissions with process-based models of different complexities, Biogeosciences, 7, 3817–3837, https://doi.org/10.5194/bg-7-3817-2010, 2010.

Tarantola, A.: Inverse problem theory and methods for model parameter estimation, SIAM, 2005.

Tarnocai, C., Canadell, J., Schuur, E., Kuhry, P., Mazhitova, G., and Zimov, S.: Soil organic carbon pools in the northern circumpolar permafrost region., Global Biogeochemical Cycles, 23:GB2023, https://doi.org/10.1029/2008GB003327, 2009.

Thanwerdas, J.: Estimation des émissions et puits de méthane par inversion atmosphérique multi-contraintes du transport et de la chimie atmosphérique à l'aide d'un ensemble d'observations. Océan, Atmosphère. Université Paris-Saclay, 2021. Français. NNT:2021UPASJ015. tel-03546754., 2021.

Thanwerdas, J., Saunois, M., Berchet, A., Pison, I., Vaughn, B. H., Michel, S. E., and Bousquet, P.: Variational inverse modelling within the Community Inversion Framework to assimilate δ$^{13}C(CH_4)$ and CH_4: a case study with model LMDz-SACS, Geoscientific Model Development Discussions, pp. 1–29, https://doi.org/10.5194/gmd-2021-106, publisher: Copernicus GmbH, 2021.

Thompson, R. L. and Stohl, A.: FLEXINVERT: an atmospheric Bayesian inversion framework for determining surface fluxes of trace species using an optimized grid, Geoscientific Model Development, 7, 2223–2242, https://doi.org/10.5194/gmd-7-2223-2014, 2014.

Thompson, R. L., Sasakawa, M., Machida, T., Aalto, T., Worthy, D., Lavric, J. V., Lund Myhre, C., and Stohl, A.: Methane fluxes in the high northern latitudes for 2005–2013 estimated using a Bayesian atmospheric inversion, Atmospheric Chemistry and Physics, 17, 3553–3572, https://doi.org/10.5194/acp-17-3553-2017, 2017.

Thompson, R. L., Nisbet, E., Pisso, I., Stohl, A., Blake, D., Dlugokencky, E., Helmig, D., and White, J.: Variability in atmospheric methane from fossil fuel and microbial sources over the last three decades, Geophysical Research Letters, 45, 11–499, 2018.

Thomson, D.: Criteria for the selection of stochastic models of particle trajectories in turbulent flows, Journal of fluid mechanics, 180, 529–556, 1987.

Thonat, T., Saunois, M., Bousquet, P., Pison, I., Tan, Z., Zhuang, Q., Crill, P. M., Thornton, B. F., Bastviken, D., Dlugokencky, E. J., Zimov, N., Laurila, T., Hatakka, J., Hermansen, O., and Worthy, D. E. J.: Detectability of Arctic methane sources at six sites performing continuous atmospheric measurements, Atmospheric Chemistry and Physics, 17, 8371–8394, https://doi.org/10.5194/acp-17-8371-2017, 2017.

Thonat, T., Saunois, M., Pison, I., Berchet, A., Hocking, T., Thornton, B. F., Crill, P. M., and Bousquet, P.: Assessment of the theoretical limit in instrumental detectability of northern high-latitude methane sources using δ 13 C CH4 atmospheric signals, Atmospheric Chemistry and Physics, 19, 12 141–12 161, 2019.

Thornton, B. F., Geibel, M. C., Crill, P. M., Humborg, C., and Mörth, C.-M.: Methane fluxes from the sea to the atmosphere across the Siberian shelf seas, Geophysical Research Letters, 43, 5869–5877, 2016.

Thornton, B. F., Prytherch, J., Andersson, K., Brooks, I. M., Salisbury, D., Tjernström, M., and Crill, P. M.: Shipborne eddy covariance observations of methane fluxes constrain Arctic sea emissions, Science Advances, 6, eaay7934, https://doi.org/10.1126/sciadv.aay7934, 2020.

Tiner, R. W., Lang, M. W., and Klemas, V. V.: Remote sensing of wetlands: applications and advances, 2015.

Tipka, A., Haimberger, L., and Seibert, P.: Flex_extract v7.1.2 – a software package to retrieve and prepare ECMWF data for use in FLEXPART, Geoscientific Model Development, 13, 5277–5310, https://doi.org/10.5194/gmd-13-5277-2020, publisher: Copernicus GmbH, 2020.

Tollefson, J.: Top climate scientists are sceptical that nations will rein in global warming, Nature, 599, 2021.

Treat, C., Natali, S., Ernakovich, J., Iversen, C., Lupascu, M., McGuire, A., Norby, R., Roy Chowdhury, T., Richter, A., Santruckova, H., Schädel, C., Schuur, E., Sloan, V., Turetsky, M., and Waldrop, M.: TA pan-Arctic synthesis of potential CH 4 and CO 2 production from anoxic soil incubations., Global Change Biology, 13:1922-1934, URL doi/10.1111/gcb.1287, 2015.

Tschudi, M. A., Meier, W. N., and Stewart, J. S.: An enhancement to sea ice motion and age products at the National Snow and Ice Data Center (NSIDC), The Cryosphere, 14, 1519–1536, 2020.

Tsuruta, A., Aalto, T., Backman, L., Krol, M. C., Peters, W., Lienert, S., Joos, F., Miller, P. A., Zhang, W., Laurila, T., Hatakka, J., Leskinen, A., Lehtinen, K. E. J., Peltola, O., Vesala, T., Levula, J., Dlugokencky, E., Heimann, M., Kozlova, E., Aurela, M., Lohila, A., Kauhaniemi, M., and Gomez-Pelaez, A. J.: Methane budget estimates in Finland from the CarbonTracker Europe-CH4 data assimilation system, Tellus B: Chemical and Physical Meteorology, 71, 1565 030, https://doi.org/10.1080/16000889.2018.1565030, 2019.

Turetsky, M., Wieder, R., Vitt, D., Evans, R., and Scott, K.: The disappearance of relict permafrost in boreal North America: Effects on peatland carbon storage and fluxes., Global Change Biology, 13:1922-1934, 2007.

Turetsky, M., Abbott, B., Jones, M., and et al.: Carbon release through abrupt permafrost thaw., Nat. Geosci., 13, 138–143, URL https://doi.org/10.1088/1748-9326/aab2b3, 2020.

Turner, A. J., Frankenberg, C., and Kort, E. A.: Interpreting contemporary trends in atmospheric methane, Proceedings of the National Academy of Sciences, 116, 2805–2813, 2019.

Umezawa, T., Machida, T., Aoki, S., and Nakazawa, T.: Contributions of natural and anthropogenic sources to atmospheric methane variations over western Siberia estimated from its carbon and hydrogen isotopes, Global Biogeochemical Cycles, 26, 2012.

USEPA: USEPA: Office of Atmospheric Programs (6207J), Methane and Nitrous Oxide Emissions From Natural Sources, U.S. Environ- mental Protection Agency, EPA 430-R-10-001, Washington, DC 20460, available at: http://nepis.epa.gov/, 2010.

Uttal, T., Makshtas, A., and Laurila, T.: Integrated Studies of Atmosphere-Surface Exchanges and Processes at the Tiksi Hydrometeorological Observatory in the Russian Far East, pp. EGU2013–11 819, URL https://ui.adsabs.harvard.edu/abs/2013EGUGA..1511819U, conference Name: EGU General Assembly Conference Abstracts ADS Bibcode: 2013EGUGA..1511819U, 2013.

Uttal, T., Starkweather, S., Drummond, J. R., Vihma, T., Makshtas, A. P., Darby, L. S., Burkhart, J. F., Cox, C. J., Schmeisser, L. N., Haiden, T., Maturilli, M., Shupe, M. D., Boer, G. D., Saha, A., Grachev, A. A., Crepinsek, S. M., Bruhwiler, L., Goodison, B., McArthur, B., Walden, V. P., Dlugokencky, E. J., Persson, P. O. G., Lesins, G., Laurila, T., Ogren, J. A., Stone, R., Long, C. N., Sharma, S., Massling, A., Turner, D. D., Stanitski, D. M., Asmi, E., Aurela, M., Skov, H., Eleftheriadis, K., Virkkula, A., Platt, A., Førland, E. J., Iijima, Y., Nielsen, I. E., Bergin, M. H., Candlish, L., Zimov, N. S., Zimov, S. A., O'Neill, N. T., Fogal, P. F., Kivi, R., Konopleva-Akish, E. A., Verlinde, J., Kustov, V. Y., Vasel, B., Ivakhov, V. M., Viisanen, Y., and Intrieri, J. M.: International Arctic Systems for Observing the

Atmosphere: An International Polar Year Legacy Consortium, Bulletin of the American Meteorological Society, 97, 1033–1056, https://doi.org/10.1175/BAMS-D-14-00145.1, publisher: American Meteorological Society Section: Bulletin of the American Meteorological Society, 2016.

van der Werf, G. R., Randerson, J. T., Giglio, L., van Leeuwen, T. T., Chen, Y., Rogers, B. M., Mu, M., van Marle, M. J. E., Morton, D. C., Collatz, G. J., Yokelson, R. J., and Kasibhatla, P. S.: Global fire emissions estimates during 1997–2016, Earth System Science Data, 9, 697–720, https://doi.org/10.5194/essd-9-697-2017, 2017.

Van Huissteden, J. and Dolman, A.: Soil carbon in the Arctic and the permafrost carbon feedback, Current Opinion in Environmental Sustainability, 4, 545–551, 2012.

Vihma, T., Screen, J., Tjernström, M., Newton, B., Zhang, X., Popova, V., Deser, C., Holland, M., and Prowse, T.: The atmospheric role in the Arctic water cycle: A review on processes, past and future changes, and their impacts, Journal of Geophysical Research: Biogeosciences, 121, 586–620, 2016.

Vojta, M., Plach, A., Thompson, R. L., and Stohl, A.: A comprehensive evaluation of the use of Lagrangian particle dispersion models for inverse modeling of greenhouse gas emissions, EGUsphere, pp. 1–39, 2022.

Vroom, R., van den Berg, M., Pangala, S., van der Scheer, O., and Sorrell, B.: Physiological processes affecting methane transport by wetland vegetation-a review, Aquatic Botany, p. 103547, 2022.

Wahba, G., Johnson, D., Gao, F., and Gong, J.: daptive tuning of numerical weather prediction models: Randomized GCV in three- and four-dimensional data assimilation, Mon. Wea. Rev., p. 12, https://doi.org/123,3358-3369, 1994.

Walker, X. J., Baltzer, J. L., Cumming, S. G., Day, N. J., Ebert, C., Goetz, S., Johnstone, J. F., Potter, S., Rogers, B. M., Schuur, E. A. G., Turetsky, M. R., and Mack, M. C.: Increasing wildfires threaten historic carbon sink of boreal forest soils, Nature, 572, 520–523, https://doi.org/10.1038/s41586-019-1474-y, 2019.

Walter Anthony, K., Schneider von Deimling, T., Nitze, I., Frolking, S., Emond, A., Daanen, R., Anthony, P., Lindgren, P., Jones, B., and Grosse, G.: 21st-century modeled permafrost carbon emissions accelerated by abrupt thaw beneath lakes, Nature communications, 9, 1–11, 2018.

Wang, X., Jacob, D. J., Eastham, S. D., Sulprizio, M. P., Zhu, L., Chen, Q., Alexander, B., Sherwen, T., Evans, M. J., Lee, B. H., et al.: The role of chlorine in global tropospheric chemistry, Atmospheric Chemistry and Physics, 19, 3981–4003, 2019.

Wang, X., Jacob, D. J., Downs, W., Zhai, S., Zhu, L., Shah, V., Holmes, C. D., Sherwen, T., Alexander, B., Evans, M. J., et al.: Global tropospheric halogen (Cl, Br, I) chemistry and its impact on oxidants, Atmospheric Chemistry and Physics, 21, 13 973–13 996, 2021.

Wania, R., Ross, I., and Prentice, I.: Implementation and evaluation of a new methane model within a dynamic global vegetation model: LPJ-WHyMe v1. 3.1, Geoscientific Model Development, 3, 565–584, 2010.

Webb, E., Loranty, M., and Lichstein, J.: Surface water, vegetation, and fire as drivers of the terrestrial Arctic-boreal albedo feedback, Environmental Research Letters, 16, 084 046, 2021.

Weber, T., Wiseman, N. A., and Kock, A.: Global ocean methane emissions dominated by shallow coastal waters, Nature communications, 10, 1–10, 2019.

West, J. and Plug, L. J.: Time-dependent morphology of thaw lakes and taliks in deep and shallow ground ice, Journal of Geophysical Research: Earth Surface, 113, 2008.

Whiteman, G., Hope, C., and Wadhams, P.: Vast costs of Arctic change, Nature, 499, 401–403, 2013.

Wild, B., Shakhova, N., Dudarev, O., Ruban, A., Kosmach, D., Tumskoy, V., Tesi, T., Joß, H., Alexanderson, H., Jakobsson, M., et al.: Organic matter across subsea permafrost thaw horizons on the East Siberian Arctic Shelf, The Cryosphere Discussions, pp. 1–26, 2018.

Wild, M., Folini, D., Hakuba, M. Z., Schär, C., Seneviratne, S. I., Kato, S., Rutan, D., Ammann, C., Wood, E. F., and König-Langlo, G.: The energy balance over land and oceans: an assessment based on direct observations and CMIP5 climate models, Climate Dynamics, 44, 3393–3429, 2015.

Willson, R. C. and Mordvinov, A. V.: Secular total solar irradiance trend during solar cycles 21–23, Geophysical Research Letters, 30, 2003.

Winderlich, J.: Setup of a CO2 and CH4 measurement system in Central Siberia and modeling of its results, p. 127, 2012.

Winiarek, V., Bocquet, M., Saunier, O., and Mathieu, A.: Estimation of errors in the inverse modeling of accidental release of atmospheric pollutant: Application to the reconstruction of the cesium-137 and iodine-131 source terms from the Fukushima Daiichi power plant, Journal of Geophysical Research: Atmospheres, 117, 2012.

Witze, A.: The Arctic is burning like never before–and that's bad news for climate change, Nature, 585, 336–338, 2020.

Wotawa, G., De Geer, L.-E., Denier, P., Kalinowski, M., Toivonen, H., D'Amours, R., Desiato, F., Issartel, J.-P., Langer, M., Seibert, P., et al.: Atmospheric transport modelling in support of CTBT verification—Overview and basic concepts, Atmospheric Environment, 37, 2529–2537, 2003.

Yu, J., Xie, Z., Sun, L., Kang, H., He, P., and Xing, G.: δ13C-CH4 reveals CH4 variations over oceans from mid-latitudes to the Arctic, Scientific reports, 5, 1–9, 2015.

Zhang, J., Wei, Y., and Fang, Z.: Ozone pollution: a major health hazard worldwide, Frontiers in immunology, 10, 2518, 2019.

Zhang, X., He, J., Zhang, J., Polyakov, I., Gerdes, R., Inoue, J., and Wu, P.: Enhanced poleward moisture transport and amplified northern high-latitude wetting trend, Nature Climate Change, 3, 47–51, 2013.

Zheng, B., Chevallier, F., Ciais, P., Yin, Y., Deeter, M. N., Worden, H. M., Wang, Y., Zhang, Q., and He, K.: Rapid decline in carbon monoxide emissions and export from East Asia between years 2005 and 2016, Environmental Research Letters, 13, 044 007, https://doi.org/10.1088/1748-9326/aab2b3, 2018.

Zhou, L. X., Kitzis, D., and Tans, P. P.: Report of the fourth WMO round-robin reference gas intercomparison, 2002-2007, in: Report of the 14th WMO Meeting of Experts on Carbon Dioxide Concentration and Related Tracer Measurement Techniques, WMO/GAW Rep, vol. 186, pp. 40–43, 2009.

Zolkos, S., Fiske, G., Windholz, T., Duran, G., Yang, Z., Olenchenko, V., Faguet, A., and Natali, S. M.: Detecting and Mapping Gas Emission Craters on the Yamal and Gydan Peninsulas, Western Siberia, Geosciences, 11, 21, 2021.

Zona, D., Gioli, B., Commane, R., Lindaas, J., Wofsy, S. C., Miller, C. E., Dinardo, S. J., Dengel, S., Sweeney, C., Karion, A., et al.: Cold season emissions dominate the Arctic tundra methane budget, Proceedings of the National Academy of Sciences, 113, 40–45, 2016.

Appendices

APPENDIX

A Acronyms and common notations

Table A.1: Acronyms and abbreviations used in this report

Acronym	Meaning
AVHRR	Advanced Very High Resolution Radiometer
CAFF	Conservation of Arctic Flora and Fauna
CASA	Carnegie-Ames-Stanford Approach
CCDAS	Carbon Cycle Data Assimilation Systems
CCM3	Community Climate Model
CRDS	Cavity Ring-Down Spectroscopy
ECCC	Environment and Climate Change Canada
ECMWF	European Centre for Medium-Range Weather Forecasts
EDGAR	Emissions Database for Global Atmospheric Research
ENVISAT	ENVIronment SATellite
ESA	European Space Agency
ESAS	East Siberian Arctic Shelf
FFDAS	Fossil-fuel Data Assimilation System
FMI	Finnish Meteorological Institute
FLEXPART	FLEXible PARTicle (model)
FLEXTRA	FLEXible TRAjectory (model)
GC-FID	Gas chromatography–flame ionization detection
GEC	gas emission craters
GFED	Global Fire Emission Database
GFS	Global Forecast System

GHGs	Greenhouse gases
GOSAT	Greenhouse gases Observing SATellite
GWP	Global warming potential
HYSPLIT	Hybrid Single-Particle Lagrangian Integrated Trajectory (model)
IFS	Integrated Forecast System
IPCC	Intergovernmental Panel on Climate Change
JRC	Joint Research Center
JR-STATIONS	Japan–Russia stations
LAI	Light-absorbing impurities
LPDM	Lagrangian particle dispersion models
MAGIC	Monitoring of Atmospheric composition and Greenhouse gases through multi-Instruments Campaigns
MODIS	Moderate Resolution Imaging Spectroradiometer
NAME	Numerical Atmospheric dispersion Modelling Environment (model)
NCAR	National Center for Atmospheric Research
NCEP	National Centers of Environmental Prediction
NDVI	Normalized difference vegetation index
NIES	National Institute for Environmental Studies
NOAA	National Ocean and Atmosphere Administration
NOAA-ESRL	National Oceanic and Atmospheric Administration Earth System Research Laboratories
RF	Radiative forcing
SD	Standard deviation
SOZ	Solar zenith angle
SRES	Special Report on Emissions Scenarios
SRM	Source-receptor matrix
STILT	Stochastic Time-Inverted Lagrangian Transport (model)
TROPOMI	TROPOspheric Monitoring Instrument
USGS	US Geological Survey
VOCs	Volatile organic compounds
e.g.	*exempli gratia* = for example
et al.	*et alii* = and contributors

Table A.2: Chemical & mathematical symbols and physical units

Symbols	**Meaning**
Ar	Argon
CH_3	Methyl radical
CH_3O_2	Methyl peroxy radical
CH_4	Methane
CH_2O	Formaldehyde
CH_3COOH	Acetic acid
Cl	Atomic chlorine
CO	Carbon monoxide
CO_2	Carbon dioxide
H_2	Molecular hydrogen
HCl	Hydrogen chloride
HCO_3^-	Bicarbonate
H_2O	Water vapour
HO_2	Hydroperoxyl radical
HS^-	Sulfide
N_2	Molecular nitrogen
NO	Nitrogen monoxide
NO_2	Nitrous oxide
NOx	Nitrogen oxide (NO & NO_2)
$O(^1D)$	Atomic oxygen, electronically excited
O_2	Molecular oxygen
O_3	Ozone
OH	Hydroxyl radical
SO_4^-	Sulfate
Pg	petagram
	$1\,\text{Pg} = 10^{15}\,\text{g}$
Tg	teragram
	$1\,\text{Tg} = 10^{12}\,\text{g}$
ppb	parts per billion
	$1\,\text{ppb} = 10^{-9}$
$\text{Tr}(\cdot)$	Trace operator

$(\cdot)^{\mathrm{T}}$	Transposed operator
$\mathbb{E}[\cdot]$	Expected value
$p(\mathbf{x}\|\mathbf{y})$	probability density of the variable $\mathbf{x}$ knowing $\mathbf{y}$
$\mathcal{H}$	Observation operator
$\mathbf{H}$	Jacobian matrix of the observation operator
$\mathbf{x}$	State vector
$\mathbf{x}^{\mathrm{b}}$	State vector (prior)
$\mathbf{x}^{\mathrm{t}}$	State vector (truth)
$\mathbf{x}^{\mathrm{a}}$	State vector (posterior)
$\boldsymbol{\epsilon}^{\mathrm{b}}$	Prior error
$\mathbf{B}$	Prior error covariance matrix
$\mathbf{P}$	Posterior error covariance matrix
$\mathbf{y}^{\mathrm{o}}$	Observation vector
$\boldsymbol{\epsilon}^{\mu}$	Measurement error
$\boldsymbol{\epsilon}^{\mathrm{m}}$	Modelling error
$\boldsymbol{\epsilon}^{\rho}$	Representation error
$\boldsymbol{\epsilon}^{\tau}$	Transport error
$\boldsymbol{\epsilon}^{\phi}$	Transported-emission
$\boldsymbol{\epsilon}^{\mathrm{o}}$	Observation error
$\mathbf{R}$	Observation error covariance matrix
$\mathbf{K}$	Kalman gain matrix

APPENDIX

B List of communications

Assessment of CH_4 sources in the Arctic using regional atmospheric measurements and their link to surface emissions

2020, *EGU General Assembly 2020, online* (poster)

Sophie Wittig[1], Antoine Berchet[1], Jean-Daniel Paris[1], Mishail Arshinov[2], Tochinobu Machida[3], Motoki Sasakawa[3], Douglas E. J. Worthy[4], and Isabelle Pison[1].

The Arctic is a critical area in terms of global warming. Not only are the rising temperatures already causing changes in the natural conditions of this region, but the high potential of increased methane CH_4 regional emissions are also likely to intensify global warming even stronger in the near term. This future effect consists in the thawing and destabilization of inland and sub-sea permafrost that enhance the release of methane into the atmosphere from extensive CH_4 and organic carbon pools which have so far been shielded by ice and frozen soil. Moreover, the high latitude regions are already playing a key role in the global CH_4-budget because of such large sources as wetlands and freshwater lakes in addition to human activities, predominantly the fossil fuel industry of the Arctic nations. However, the level of scientific understanding of the actual contribution of Arctic methane emissions to the global CH_4-budget is still relatively immature. Besides the difficulties in carrying out measurements in such remote areas, this is due to a high inhomogeneity in the spatial distribution of methane sources and sinks as well as to ongoing changes in hydrology, vegetation and carbon decomposition. Therefore, the aim of this work is to reduce the uncertainties about methane sources and sinks in the Arctic region during the most recent years by using an atmospheric approach, in order to improve the quality of the assessment of the local and global impacts. To do so, the data of atmospheric CH_4 concentrations measured at about 30 stations located in different Arctic nations have been analysed in regard to the trends, seasonal fluctuations and spatial patterns that they demonstrate as well as their link to regional emissions.

[1]Laboratoire des Sciences du Climat et de l'Environnement, CEA-CNRS-UVSQ, Gif-sur-Yvette, France
[2]V.E. Zuev Institute of Atmospheric Optics, Russian Academy of Sciences, Tomsk, Russia
[3]Center for Global Environmental Research, National Institute for Environmental Studies, Tsukuba, Japan
[4]Environment and Climate Change Canada, Climate Research Division, Toronto, Ontario, Canada.

Evaluating methane emissions between 2008 and 2019 in high northern latitudes by using inverse modeling

2022, *EGU General Assembly 2022, Vienna* (presentation)

2022, *Journées Nationales Méthane 2022, Paris* (presentation)

Sophie Wittig[1], Antoine Berchet[1], Jean-Daniel Paris[1], Marielle Saunois[1], Mishail Arshinov[2], Tochinobu Machida[3], Motoki Sasakawa[3], Douglas E. J. Worthy[4], and Isabelle Pison[1].

The Arctic is particularly sensitive to global warming and the effects of the increasing temperatures can already be detected in this region by occurring events such as thawing permafrost and decreasing Arctic sea ice area. One of the possible consequences is the risk of enhanced regional greenhouse gas emissions such as methane (CH_4) due to the exposure of large terrestrial carbon pools or subsea permafrost which have previously been shielded by ice and frozen soil. Various sources, both natural and anthropogenic, are presently emitting methane in the Arctic. Natural sources include wetlands and other freshwater biomes, as well as the ocean and biomass burning. Despite the relatively small population in this region, CH_4 emissions due to human activities are also significant. The main anthropogenic sources are the extraction and distribution of fossil fuels in the Arctic nations and, to a lesser extent, livestock activities and waste management. However, assessing the amount of CH_4 emissions in the Arctic and their contribution to the global budget still remains challenging due to the difficulties in carrying out accurate measurements in such remote areas. Besides, high variations in the spatial distribution of methane sources and a poor understanding of the effects of ongoing changes in carbon decomposition, vegetation and hydrology also complicate the assessment. Therefore, the aim of this work is to reduce uncertainties on methane emissions in high northern latitudes. In order to achieve that, an inverse modeling approach has been implemented by using observational data sets of CH_4 concentrations obtained at 42 surface stations located in different Arctic regions for the period from 2008 to 2019, the atmospheric transport model FLEXPART, as well as available bottom-up estimates of methane emissions provided by process-based surface models and CH_4 emission inventories. The results have been analysed with regards to seasonal and inter-annual fluctuations, spatial differences and trends over the period of study.

[1]Laboratoire des Sciences du Climat et de l'Environnement, CEA-CNRS-UVSQ, Gif-sur-Yvette, France
[2]V.E. Zuev Institute of Atmospheric Optics, Russian Academy of Sciences, Tomsk, Russia
[3]Center for Global Environmental Research, National Institute for Environmental Studies, Tsukuba, Japan
[4]Environment and Climate Change Canada, Climate Research Division, Toronto, Ontario, Canada.

APPENDIX

C List of scientific papers

Disentangling methane and carbon dioxide sources and transport across the Russian Arctic from aircraft measurements

Submitted to the journal *Atmospheric Chemistry and Physics* and accepted for final publication on January 26th, 2023.

Clément Narbaud[1], Jean-Daniel Paris[1,2], **Sophie Wittig**[1], Antoine Berchet[1], Marielle Saunois[1], Philippe Nédelec[3], Boris D. Belan[4], Mikhail Y. Arshinov[4], Sergei B. Belan[4], Denis Davydov[4], Alexander Fofonov[4], and Artem Kozlov[4].

A more accurate characterization of the sources and sinks of methane (CH_4) and carbon dioxide (CO_2) in the vulnerable Arctic environment is required to better predict climate change. A large-scale aircraft campaign took place in September 2020 focusing on the Siberian Arctic coast. CH_4 and CO_2 were measured in situ during the campaign and form the core of this study. Measured ozone (O_3) and carbon monoxide (CO) are used here as tracers. Median CH_4 mixing ratios are fairly higher than the monthly mean hemispheric reference (Mauna Loa, Hawaii, US) with 1890–1969 ppb vs 1887 ppb respectively, while CO_2 mixing ratios from all flights are lower (408.09–411.50 ppm vs 411.52 ppm). We also report on three case studies. Our analysis suggests that during the campaign the European part of Russia's Arctic and Western Siberia were subject to long-range transport of polluted air masses, while the East was mainly under the influence of local emissions of greenhouse gases. The relative contributions of the main anthropogenic and natural sources of CH_4 are simulated using the Lagrangian model FLEXPART in order to identify dominant sources in the boundary layer and in the free troposphere. In western terrestrial flights, air masses composition is influenced by emissions from wetlands and anthropogenic activities (waste management, fossil fuel industry and to a lesser extent the agricultural sector), while in the East, emissions are dominated by freshwaters, wetlands, and the oceans, with a likely contribution from anthropogenic sources related to fossil fuels. Our results highlight the importance of the contributions from freshwater and oceans emissions. Considering the large uncertainties associated to them, our study suggests that the emissions from these aquatic sources should receive more attention in Siberia.

[1]Laboratoire des Sciences du Climat et de l'Environnement, CEA-CNRS-UVSQ, Gif-sur-Yvette, France
[2]Climate and Atmosphere Research Centre (CARE-C), The Cyprus Institute, Nicosia, 2121, Cyprus
[3] Université de Toulouse, UT3, CNRS, IRD, Toulouse, France
[4]Independent researcher

Estimating Methane Emissions in the Arctic nations using surface observations from 2008 to 2019

Submitted to the journal *Atmospheric Chemistry and Physics*, November 14th, 2022 and currently under discussion.

Sophie Wittig[1], Antoine Berchet[1], Isabelle Pison[1], Marielle Saunois[1], Joël Thanwerdas[1], Adrien Martinez[1], Jean-Daniel Paris[1], Tochinobu Machida[2], Motoki Sasakawa[2], Douglas E. J. Worthy[3], Xin Lan[4], Rona L. Thompson[5], Espen Sollum[5], and Mishail Arshinov[6].

The Arctic is a critical region in terms of global warming. Environmental changes are already progressing steadily in high northern latitudes whereby, among other effects, a high potential of enhanced methane (CH_4) emissions is induced. With CH_4 being a potent greenhouse gas, additional emissions from Arctic regions may intensify global warming in the future by positive feedback. Various natural and anthropogenic sources are currently contributing to the Arctic's CH_4 budget; however the quantification of those emissions remains challenging. Assessing the amount of CH_4 emissions in the Arctic and their contribution to the global budget still remains challenging. This is on the one hand due to the difficulties in carrying out accurate measurements in such remote areas. Besides, high variations in the spatial distribution of methane sources and a poor understanding of the effects of ongoing changes in carbon decomposition, vegetation and hydrology also complicate the assessment. Therefore, the aim of this work is to reduce uncertainties on current bottom-up estimates of CH_4 emissions as well as soil oxidation by implementing an inverse modeling approach in order to better quantify CH_4 sources and sinks for the most recent years (2008 to 2019). More precisely, the objective is to detect occurring trends in the CH_4 emissions and potential changes in seasonal emission patterns. The implementation of the inversion included footprint simulations obtained with the atmospheric transport model FLEXPART, various emission estimates from inventories and land surface models as well as data of atmospheric CH_4 concentrations from 41 surface observation sites in the Arctic nations. The results of the inversion showed that the majority of the CH_4 sources currently present in high northern latitudes are poorly constrained by the existing observation network. Therefore, conclusions on trends and changes in the seasonal cycle could not be obtained for the corresponding CH_4 sectors. Only CH_4 fluxes from wetlands are adequately constrained, predominantly in North America. Within the period under study, wetland emissions show a slight negative trend in North America and a slight positive trend in East Eurasia. Overall, the estimated CH_4 emissions are lower compared to the bottom-up estimates but higher than similar results from global inversions.

[1]Laboratoire des Sciences du Climat et de l'Environnement, CEA-CNRS-UVSQ, Gif-sur-Yvette, France
[2]Center for Global Environmental Research, National Institute for Environmental Studies, Tsukuba, Japan
[3]Environment and Climate Change Canada, Climate Research Division, Toronto, Ontario, Canada.
[4]NOAA Global Monitoring Laboratory, Boulder, CO, USA
[5]Norsk Institutt for Luftforskning, NILU, Kjeller, Norway
[6]Independent researcher

APPENDIX

D

Supplements to Chapter VII

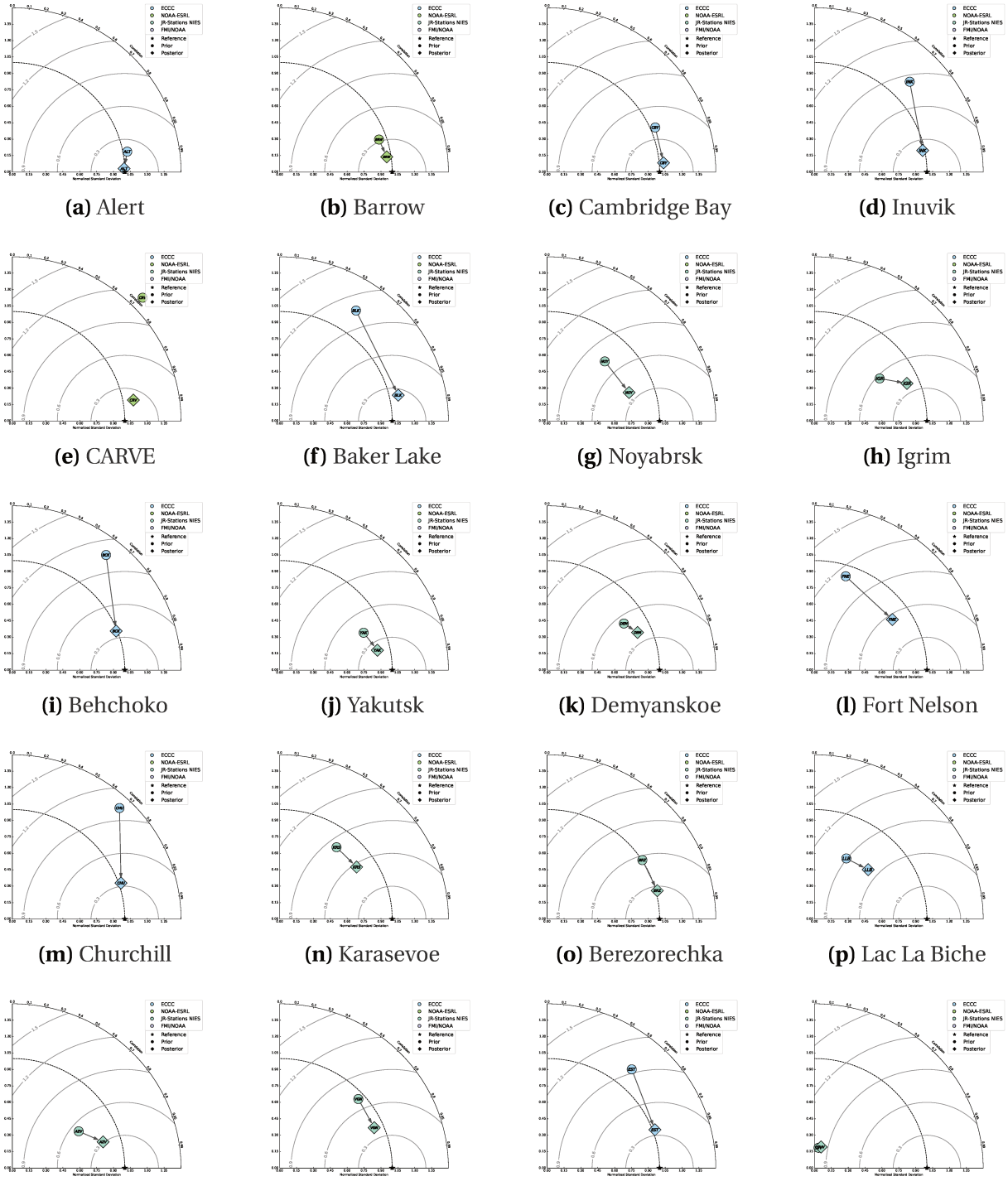

(a) Alert **(b)** Barrow **(c)** Cambridge Bay **(d)** Inuvik

(e) CARVE **(f)** Baker Lake **(g)** Noyabrsk **(h)** Igrim

(i) Behchoko **(j)** Yakutsk **(k)** Demyanskoe **(l)** Fort Nelson

(m) Churchill **(n)** Karasevoe **(o)** Berezorechka **(p)** Lac La Biche

(q) Azovo **(r)** Vaganovo **(s)** Esther **(t)** Savvushka

Figure D.1: Exemplary Taylor diagrams of different observation sites.

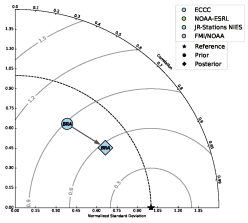

(a) Bratt's Lake

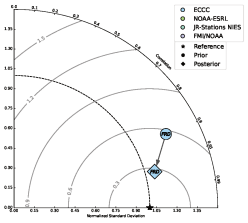

(b) Fraserdale

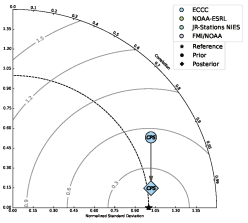

(c) Chapais

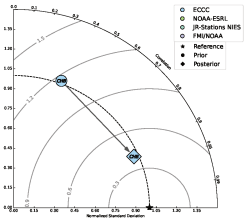

(d) Chibougamau

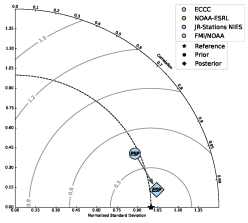

(e) Estevan Point

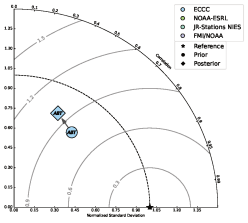

(f) Abbotsford

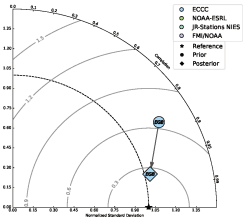

(g) Egbert

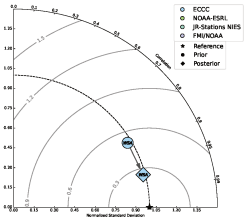

(h) Sable Island

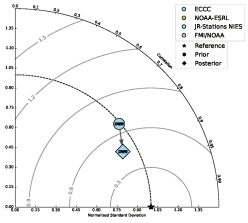

(i) Downsview

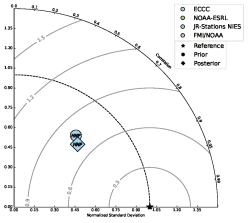

(j) Hanlan's Point

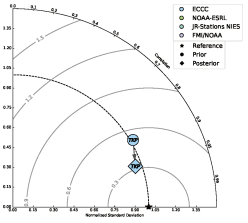

(k) Turkey Point

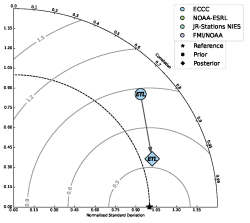

(l) East Trout Lake

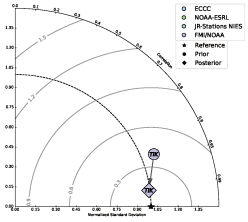

(m) Tiksi

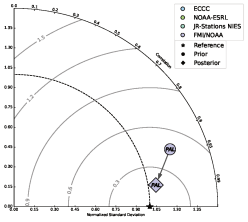

(n) Pallas

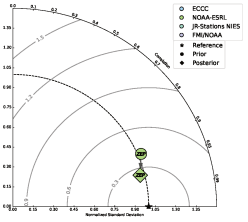

(o) Zeppelin

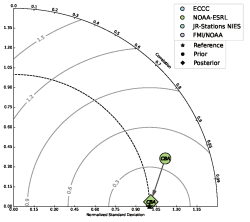

(p) Cold Bay

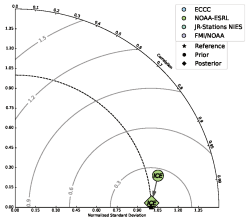

(q) Storhovdi Island

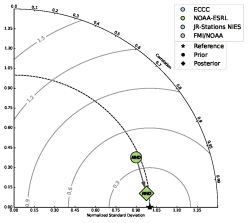

(r) Mace Head

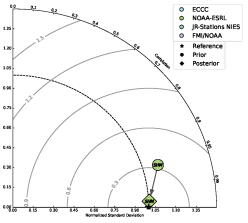

(s) Shemya Island

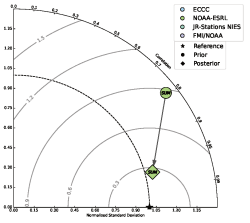

(t) Summit

Figure D.2: Exemplary Taylor diagrams of different observation sites.

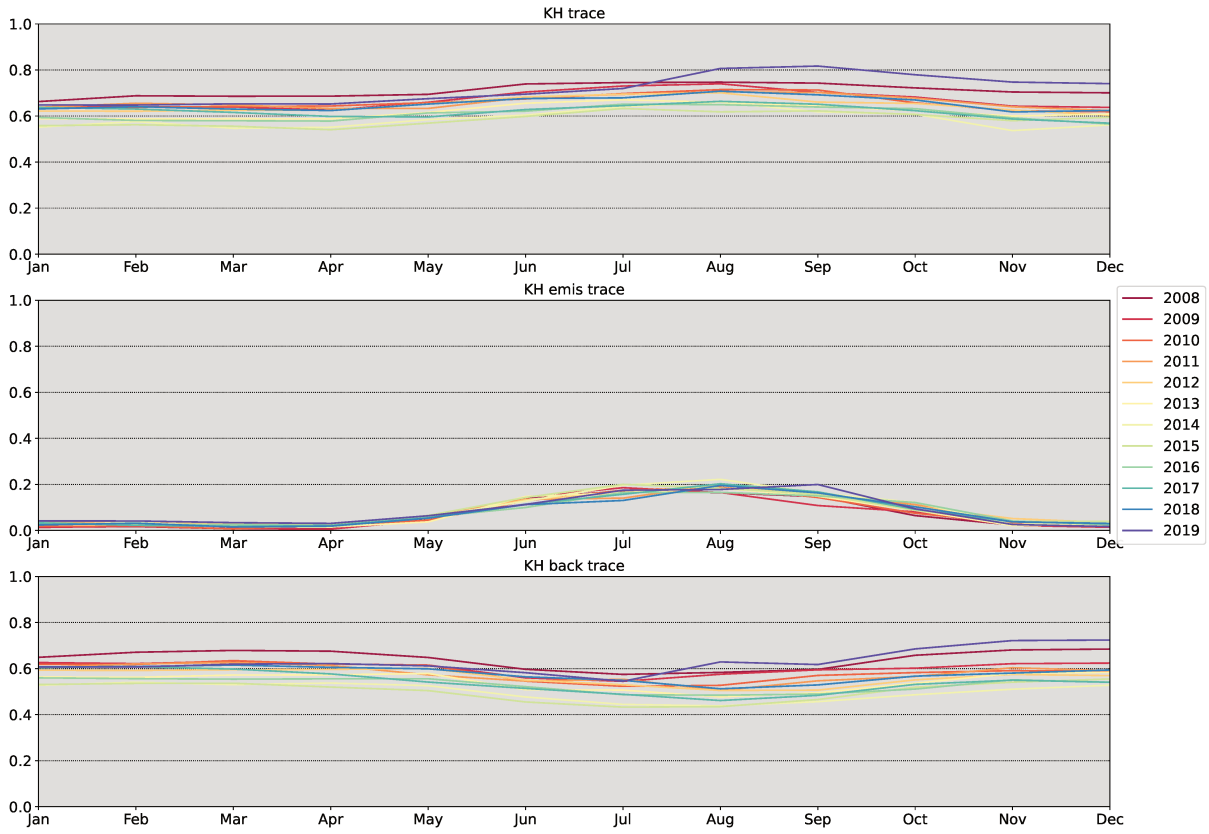

Figure D.3: Seasonal variation of $tr(\mathbf{KH})$ for all years from 2008 to 2019. The monthly traces are divided by the number of available observations for the corresponding month.

Table D.1: *Selected atmospheric observation sites for this study, by decreasing latitudes. "Environmental characteristics" gives a brief description of the surrounding of each station.*

ID	Site, country	Latitude	Longitude	Elevation (masl)/ Intake height (magl)	Time Period	Environmental characteristics
ALT	Alert, CAN	82.5 °N	62.5 °W	185/5	from 1988	snow covered cliffs, sparse polar desert vegetation
ZEP	Zeppelin, NOR	78.9 °N	11.9 °E	474/5	from 1994	mountains and glaciers, small village
SUM	Summit, GRL	72.6 °N	38.4 °E	3210/5	from 1997	year-round dry snow and ice
TIK	Tiksi, RUS	71.9 °N	128.9 °E	19/10	from 2010	Lena river delta
BRW	Barrow, USA	71.3 °N	156.6 °W	11/3	from 1986	thermokarst lakes
CBY	Cambridge Bay, CAN	69.1 °N	105.1 °W	35/12	from 2012	largest port of the Northwest Passage
INK	Inuvik, CAN	68.3 °N	133.5 °W	113/10	from 2012	Arctic Tundra, Mackenzie Delta channel
PAL	Pallas, FIN	68.0 °N	24.1 °E	565/5	from 2004	wetlands, lakes and patches of forest
CRV	CARVE, USA	65.0 °N	147.6 °W	611/32	2015 – 2016	evergreen forest, shrubland and woody wetlands
BLK	Baker Lake, CAN	64.3 °N	96.0 °W	95/10	from 2017	Arctic Tundra, small lakes
NOY	Noyabrsk, RUS	63.4 °N	75.8 °E	100/43	2005 – 2018	taiga forest, wetlands
ICE	Storhovdi Island, ISL	63.4 °N	20.2 °E	118/5	from 1992	grassy slopes and coastal cliffs
IGR	Igrim, RUS	63.2 °N	64.4 °E	25/47	2005 – 2013	10.000 inhabitant town, wetlands
BCK	Behchoko, CAN	62.8 °N	115.9 °W	160/60	from 2010	mixed forests, lakes and ponds
YAK	Yakutsk, RUS	62.1 °N	129.4 °E	130/70	2007 – 2013	taiga
DEM	Demyanskoe, RUS	59.8 °N	70.9 °E	75/63	2007 – 2013	taiga forest surrounded by wetlands
FNE	Fort Nelson, CAN	58.8 °N	122.6 °W	361/15	from 2014	boreal forest, southern fringe of permafrost region
CHU	Churchill, CAN	58.7 °N	93.8 °W	29/60	from 2011	Arctic Tundra, boreal wetlands
KRS	Karasevoe, RUS	58.3 °N	82.4 °E	50/67	2005 – 2018	taiga forest, wetlands
BRZ	Berezorechka, RUS	56.1 °N	112.5 °E	150/80	2008 – 2017	taiga, boreal forest
CBA	Cold Bay, USA	55.2 °N	162.7 ° E	21/4	from 1983	wet tundra

ID	Site, country	Latitude	Longitude	Elevation (masl)/ Sampling height (magl)	Time Period	Environmental characteristics
LLB	Lac La Biche, CAN	55.0 °N	112.5 °W	540/50	from 2007	peatlands and forest
AZV	Azovo, RUS	54.7 °N	73.0 °E	100/50	2009 – 2018	steppe, large city
VGN	Vaganovo, RUS	54.5 °N	62.3 °E	200/85	2008 – 2018	steppe, large city
ETL	East Trout Lake, CAN	54.3 °N	105.0 °W	500/105	from 2005	close to the southern edge of boreal forest
MHD	Mace Head, IRL	53.3 °N	9.9 °W	5/5	from 1991	boggy, small hills covered with grasses and sedges
SHM	Shemya Island, USA	52.7 °N	174.1 °W	23/3	from 1985	small remote island in Bering Sea
EST	Esther, CAN	51.7 °N	110.2 °W	707/50	from 2005	open prairie and cattle ranches
SVV	Savvushka, RUS	51.3 °N	82.1 °E	400/52	2014	steppe, small village
BRA	Bratt's Lake, CAN	50.2 °N	104.7 °W	595/35	from 2009	prairie, very flat topography
FRD	Fraserdale, CAN	49.9 °N	81.6 °W	210/40	from 1990	boreal forest, extensive wetland coverage
CPS	Chapais, CAN	49.8 °N	75.0 °W	391/40	from 2011	boreal forest, many lakes in surrounding area
CHB	Chibougamau, CAN	49.7 °N	74.3 °W	393/30	2007 – 2011	boreal forest, many lakes in surrounding area
ESP	Estevan Point, CAN	49.4 °N	126.5 °W	7/40	from 2009	surrounded by forests, Pacific Ocean to the west
ABT	Abbotsford, CAN	49.0 °N	122.3 °W	40/33	from 2014	close to Pacific Ocean, proximity to large cities
EGB	Egbert, CAN	44.2 °N	79.8 °W	251/25	from 2005	mixed woodland, small rural village
WSA	Sable Island, CAN	43.9 °N	60.0 °W	5/30	from 2003	remote island, grass and low-growing vegetation
DWN	Downsview, CAN	43.8 °N	79.5 °W	198/20	from 2003	urban site (Toronto)
HNP	Hanlan's Point, CAN	43.6 °N	79.4 °W	87/10	from 2014	urban site (Toronto Island, Lake Ontario)
TKP	Turkey Point, CAN	42.6 °N	80.6 °W	231/35	from 2012	mixed woodlands, close to Lake Erie

Table D.2: *Yearly traces of sensitivity and influence matrices.*

Year	$tr(\mathbf{HK})/tr(\mathbf{KH})$	$tr(\mathbf{KH_{emis}})$	$tr(\mathbf{KH_{back}})$	**Number of observations**
2008	154.29	15.31	139.00	217
2009	167.72	17.07	150.65	250
2010	196.27	21.66	174.61	298
2011	210.05	25.78	184.27	318
2012	216.00	27.32	188.68	334
2013	200.35	24.80	175.55	323
2014	212.31	31.33	180.98	362
2015	222.30	32.33	189.97	379
2016	229.98	29.69	200.29	378
2017	227.34	29.05	198.29	367
2018	250.87	28.87	222.00	384
2019	185.69	20.86	164.83	266

Table D.3: *Prior and Posterior emissions from different sectors in North America (NA), East Eurasia (EE), West Eurasia (WE) and the Arctic (AR). Note that the posterior results as well as the prior uncertainties only refer to one specific configuration of the ensemble of posterior states ($\mathbf{x}^{\mathbf{a}}_{\mathbf{max}}$).*

Sector	Prior				Posterior			
	NA	EE	WE	AR	NA	EE	WE	AR
Wetlands	30.4±26.1	13.8±11.9	3.3±2.9	13.2±11.4	18.8±13.0	12.2±9.5	3.2±2.7	9.8±7.9
Other natural	5.5±4.1	6.0±4.6	1.1±0.9	6.1±4.7	5.1±3.8	5.7±4.3	1.1±0.9	5.8±4.4
Anthropogenic	6.8±4.6	16.1±10.9	4.6±3.1	3.8±2.5	7.0±4.6	16.1±10.7	4.6±3.1	3.7±2.4
Total	42.6±34.8	35.9±27.3	9.0±6.8	23.1±18.5	30.8±21.4	34.1±24.6	8.9±6.6	19.4±14.8

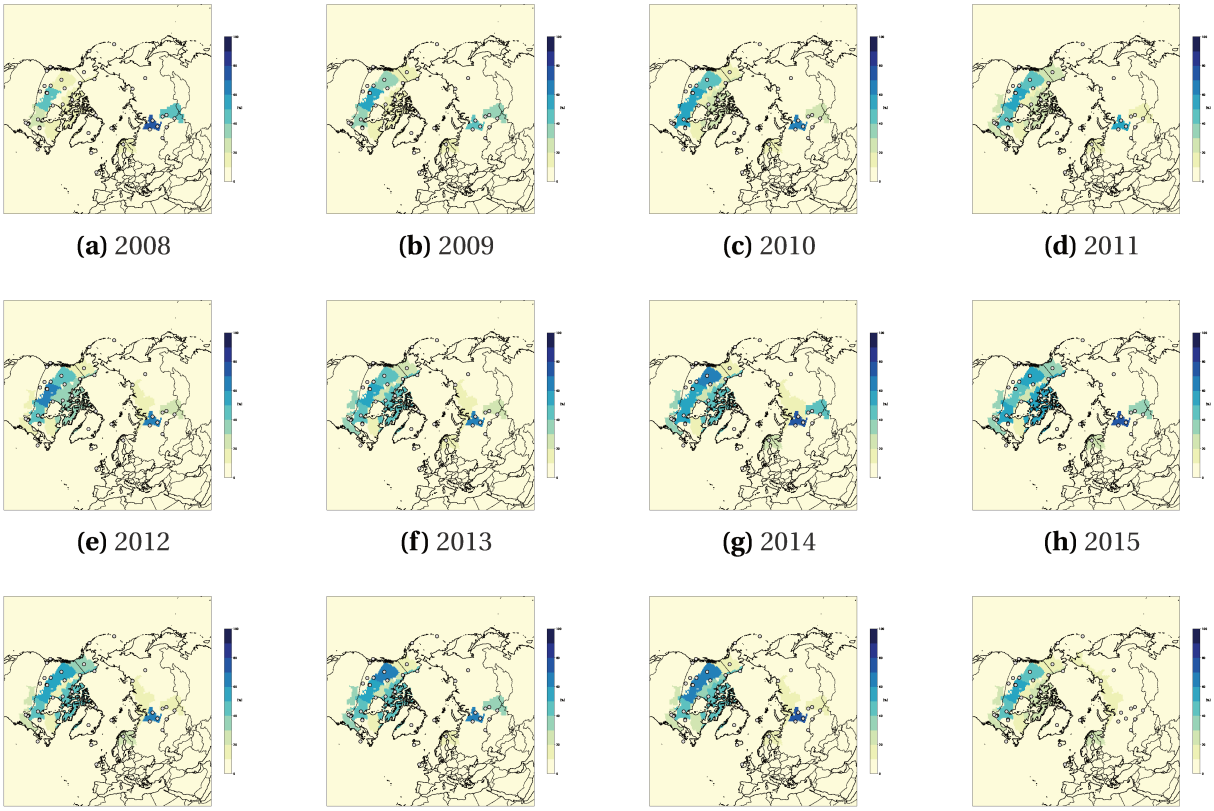

(a) 2008 **(b)** 2009 **(c)** 2010 **(d)** 2011

(e) 2012 **(f)** 2013 **(g)** 2014 **(h)** 2015

(i) 2016 **(j)** 2017 **(k)** 2018 **(l)** 2019

Figure D.4: Regional constraints on wetland emissions by year. Darker areas thereby indicate higher constraints. The percentages of the areas refer to the corresponding summed elements of $\mathbf{KH}$. The observation sites are marked as grey circles.

Table D.4: *Share of total modelled CH_4 mixing ratios from background and combined methane sources and sink. The values show the average over the whole period of monthly mixing ratios and, respectively, only over the summer and winter months.*

Station ID	Background							Source contribution						
	Total		SD	Summer		Winter		Total		SD	Summer		Winter	
	[ppb]	[%]	[ppb]	[ppb]	[%]	[ppb]	[%]	[ppb]	[%]	[ppb]	[ppb]	[%]	[ppb]	[%]
ALT	1907.1	99.7	16.6	1884.1	99.7	1922.8	99.6	6.0	0.3	2.8	5.1	0.3	8.2	0.4
ZEP	1912.3	99.9	18.9	1886.6	99.9	1931.3	99.8	2.8	0.1	1.3	2.1	0.1	4.1	0.2
SUM	1902.5	99.9	24.2	1880.2	99.9	1918.5	99.9	2.4	0.1	1.1	2.7	0.1	2.1	0.1
TIK	1916.5	98.4	20.7	1890.6	98.0	1938.5	98.6	30.6	1.6	10.4	39.3	2.0	26.9	1.4
BRW	1908.1	99.0	16.7	1885.7	98.8	1923.8	99.1	19.5	1.0	8.6	22.4	1.2	18.2	0.9
CBY	1908.6	99.4	16.0	1887.6	99.2	1924.5	99.5	12.0	0.6	9.4	15.3	0.8	8.9	0.5
INK	1905.6	98.6	14.7	1886.7	97.8	1918.3	99.1	28.1	1.4	20.7	42.0	2.2	17.3	0.9
PAL	1910.8	98.8	18.4	1887.5	98.8	1929.8	98.5	23.8	1.2	10.4	23.8	1.2	29.4	1.5
CRV	1897.5	99.3	16.1	1876.7	98.7	1907.6	99.7	13.2	0.7	10.2	24.6	1.3	6.3	0.3
BLK	1908.4	99.2	14.9	1889.6	98.9	1923.3	99.6	14.6	0.8	13.7	20.2	1.1	7.7	0.4
NOY	1925.3	95.1	26.5	1895.6	93.2	1957.3	95.5	99.4	4.9	39.2	139.3	6.8	93.1	4.5
ICE	1907.3	99.9	15.6	1885.8	99.9	1921.7	99.9	2.7	0.1	1.2	2.5	0.1	2.8	0.1
IGR	1923.7	97.8	26.5	1893.6	97.8	1955.0	97.1	43.4	2.2	17.7	43.4	2.2	58.8	2.9
BCK	1905.2	98.4	15.2	1887.4	97.3	1920.5	99.3	31.6	1.6	29.0	53.2	2.7	13.2	0.7
YAK	1918.1	98.9	22.1	1892.9	98.9	1943.7	98.5	22.2	1.1	8.2	22.0	1.1	29.7	1.5
DEM	1924.8	96.1	25.9	1896.9	94.3	1955.9	96.4	79.3	3.9	31.0	115.4	5.7	73.5	3.6
FNE	1893.2	98.6	16.6	1874.5	98.1	1904.2	98.9	26.3	1.4	15.1	36.5	1.9	20.3	1.1
CHU	1908.1	98.6	13.3	1892.4	97.5	1921.3	99.6	27.1	1.4	28.2	49.4	2.5	7.8	0.4
KRS	1926.3	97.1	25.2	1901.8	96.1	1956.7	96.9	58	2.9	20.3	77.8	3.9	63.1	3.1
BRZ	1925.4	97.4	23.9	1903.7	97.4	1954.1	96.7	50.6	2.6	15.0	50.8	2.6	67.3	3.3

Station ID	Background							Source contribution						
	Total		SD	Summer		Winter		Total		SD	Summer		Winter	
	[ppb]	[%]	[ppb]	[ppb]	[%]	[ppb]	[%]	[ppb]	[%]	[ppb]	[ppb]	[%]	[ppb]	[%]
CBA	1903.4	99.9	21.0	1873.2	99.9	1919.7	99.9	1.5	0.1	0.6	1.6	0.1	1.4	0.1
LLB	1894.7	97.8	15.5	1878.2	96.8	1905.5	98.1	43.0	2.2	20.4	62.2	3.2	37.5	1.9
AZV	1925.3	97.8	25.1	1901.1	97.7	1956.9	97.0	43.8	2.2	13.7	43.9	2.3	60.0	3.0
VGN	1920.6	98.1	22.7	1896.1	98.5	1947.5	97.2	37.3	1.9	13.7	29.4	1.5	55.6	2.8
ETL	1901.6	97.8	14.2	1886.3	96.2	1915.1	98.7	43.2	2.2	27.0	74.0	3.8	25.6	1.3
MHD	1904.5	99.9	14.7	1884.5	99.9	1916.7	99.9	2.4	0.1	1.0	2.4	0.1	2.1	0.1
SHM	1906.1	99.9	22.7	1873.2	99.9	1924.2	99.9	1.6	0.1	0.6	1.4	0.1	1.8	0.1
EST	1893.9	99.1	14.9	1875.4	97.9	1907.1	99.8	17.9	0.9	20.2	40.6	2.1	4.5	0.2
SVV	1918.8	97.6	19.7	1903.0	96.2	1941.4	97.6	48.2	2.4	23.1	74.7	3.8	47.3	2.4
BRA	1897.4	99.1	14.8	1880.2	98.0	1911.5	99.8	17.5	0.9	17.5	37.9	2.0	4.0	0.2
FRD	1901.8	99.4	17.6	1892.4	98.9	1916.4	99.8	11.9	0.6	11.6	21.6	1.1	3.4	0.2
CPS	1908.1	99.3	11.3	1898.8	98.8	1917.9	99.8	12.6	0.7	12.8	22.8	1.2	3.2	0.2
CHB	1907.9	99.3	11.2	1898.7	98.8	1917.6	99.8	12.6	0.7	12.8	23.0	1.2	3.2	0.2
ESP	1887.1	99.4	15.2	1864.7	98.7	1895.9	99.7	11.4	0.6	10.3	25.5	1.3	6.0	0.3
ABT	1884.8	98.8	14.8	1863.0	97.9	1894.5	99.4	22.6	1.2	16.3	40.8	2.1	11.8	0.6
EGB	1906.2	98.6	11.2	1898.3	97.3	1915.5	99.7	26.5	1.4	24.8	53.0	2.7	6.5	0.3
WSA	1901.7	99.0	11.7	1889.3	98.4	1911.0	99.4	18.9	1.0	11.2	30.6	1.6	11.6	0.6
DWN	1905.8	96.9	11.4	1897.4	96.0	1915.3	97.4	60.8	3.1	20.2	79.1	4.0	51.7	2.6
HNP	1905.5	96.9	11.5	1896.9	96.0	1915.1	97.3	61.7	3.1	19.7	79.2	4.0	53.1	2.7
TKP	1904.6	97.4	11.5	1895.5	96.6	1914.5	97.7	51.3	2.6	16.3	66.8	3.4	44.6	2.3

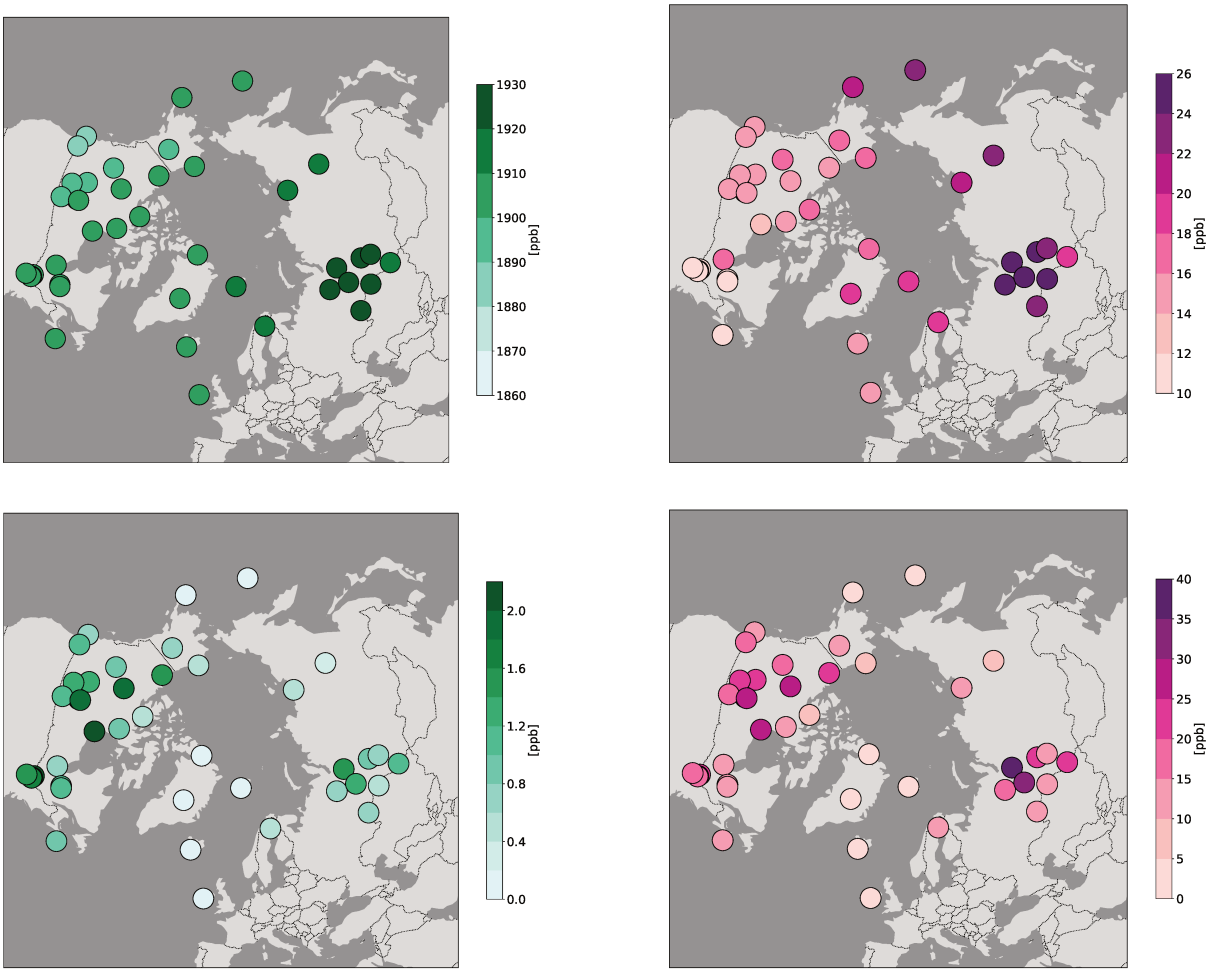

Figure D.5: Contributions to the total simulated mixing ratio signals at each observation site. Left panels show average contributions, right panels the standard deviations of the contributions for the background (top) and regional emissions (bottom) respectively.

Summary

1 English

The Arctic is an especially critical region with regard to global climate change. With temperatures in high northern latitudes increasing around three times faster than the global average, changes in environmental characteristics such as declining sea ice extent or thawing permafrost soils are proceeding rapidly. As a consequence, positive climatic feedbacks are triggered in this region, whereby the Arctic warming is accelerated even further. One important impact is the high risk of increased methane (CH_4) emissions. CH_4 is a potent greenhouse gas whose global average concentration in the atmosphere has increased by about 160 % since pre-industrial times, a trend that is also reflected in the Arctic. Currently, various CH_4 sources, both natural and anthropogenic, are contributing to CH_4 emissions from the Arctic region. Anthropogenic emissions are predominantly caused by the extraction and distribution of fossil fuels by the Arctic nations. The dominant natural source of CH_4 are high northern latitude wetlands; however, other freshwater systems, wildfire events, geological fluxes and oceanic emissions of different origins also contribute to the Arctic CH_4 budget. Furthermore, the thawing and destabilization of terrestrial and sub-sea permafrost will potentially increase CH_4 emissions in the near future, for instance by the exposure of degradable soil organic matter. However, assessing the amount of CH_4 emissions in the Arctic and their contribution to the global budget still remains challenging. This is on the one hand due to the difficulties in carrying out accurate measurements in such remote areas. Besides, high variations in the spatial distribution of methane sources and a poor understanding of the effects of ongoing changes in carbon decomposition, vegetation and hydrology also complicate the assessment. Therefore, the aim of this work is to reduce uncertainties on current bottom-up estimates of CH_4 emissions as well as soil oxidation by implementing an inverse modeling approach in order to better quantify CH_4 sources and sinks for the most recent years (2008 to 2019). More precisely, the objective is to detect occurring trends in the CH_4 emissions and potential changes in seasonal emission patterns as well as to analyze the capability of the current stationary observation network in the Arctic to constrain the different CH_4 sectors and to detect possible future trends caused by a potential “methane bomb”. The implementation of the inversion included hereby footprint simulations obtained with the atmospheric transport model FLEXPART, various emission estimates from inventories and land surface models as well as data of atmospheric CH_4 concentrations from 41 surface observation sites in the Arctic nations. The results of the inversion showed that the majority of the CH_4 sources currently present in high northern latitudes are poorly constrained by the existing observation

network. Therefore, conclusions on trends and changes in the seasonal cycle could not be obtained for the corresponding CH_4 sectors. Only CH_4 fluxes from wetlands are adequately constrained, predominantly in North America. Within the period under study, wetland emissions show a slight negative trend in North America and a slight positive trend in East Eurasia. Overall, the estimated CH_4 emissions are lower compared to the bottom-up estimates but higher than similar results from global inversions. The insufficient constraint by the observation network is also shown by a hypothetical scenario simulating future increases in CH_4 emissions. Thereby, the applied trends are not only incorrectly detected in the regions they are assigned to, but elevated CH_4 emissions are also attributed to areas where no trend is given by the scenario. A hypothetical expanded observation network of stationary sites show hereby only minor improvements.

2 Français

L'Arctique est une région critique pour le changement climatique. Les températures aux hautes latitudes Nord augmentent environ trois fois plus vite que la moyenne mondiale: les changements environnementaux tels que la diminution de l'étendue de la banquise ou le dégel du pergélisol progressent donc rapidement. En conséquence, des rétroactions climatiques positives sont déclenchées dans cette région, ce qui accélère encore son réchauffement. L'un de ces changements est la possible augmentation des émissions de méthane (CH_4). Le CH_4 est un puissant gaz à effet de serre dont la concentration moyenne mondiale dans l'atmosphère a augmenté d'environ 160 % depuis l'ère préindustrielle, une tendance qui se retrouve en Arctique. Actuellement, diverses sources de CH_4, naturelles et anthropiques, contribuent aux émissions en Arctique. Les émissions anthropiques sont principalement dues à l'extraction et à la distribution de combustibles fossiles par les nations arctiques. La principale source naturelle de CH_4 est constituée par les zones humides situées aux hautes latitudes Nord, mais d'autres systèmes d'eau douce, les feux de forêt, des flux géologiques et des émissions océaniques de différentes origines contribuent également au bilan de CH_4 de l'Arctique. En outre, le dégel et la déstabilisation du pergélisol terrestre et sous-marin pourraient augmenter les émissions de CH_4 dans un avenir proche, par exemple en raison de l'exposition de la matière organique du sol. Cependant, l'évaluation des émissions de CH_4 en Arctique et de leur contribution au budget mondial reste difficile. Cela est dû, d'une part, aux difficultés à effectuer des mesures dans des zones aussi difficiles d'accès. D'autre part, de fortes variations dans la distribution spatiale des sources de méthane et une mauvaise compréhension des effets des changements en cours sur la décomposition du carbone, la végétation et l'hydrologie compliquent l'évaluation. Le but de ce travail est donc de réduire les incertitudes sur les estimations actuelles des émissions de CH_4 grâce à une approche de modélisation inverse pour mieux quantifier les sources et les puits de CH_4 pour les années récentes (2008 à 2019). Plus précisément, il s'agit de détecter les tendances des émissions de CH_4 et les changements éventuels dans les cycles saisonniers et d'analyser la capacité du réseau d'observation in-situ actuel à caractériser les différents secteurs et les tendances futures potentiellement causées par une «bombe à méthane». La mise en œuvre de l'inversion comprend des simulations par le modèle de transport atmosphérique FLEXPART, des émissions provenant d'inventaires et de modèles biogéochimiques et des données de concentrations atmosphériques de CH_4 en 41 sites d'observation dans différentes nations arctiques. Les résultats de l'inversion montrent que la majorité des sources de CH_4 actuellement présentes aux hautes latitudes sont peu contraintes par le réseau d'observation existant. On ne peut donc tirer des conclusions sur les tendances et les changements dans le cycle saisonnier pour les secteurs correspondants. Seuls les flux de CH_4 des zones humides sont suffisamment contraints, principalement en Amérique du Nord. Au cours de la période étudiée, les émissions des zones humides ont une légère tendance négative en Amérique du

Nord et une légère tendance positive en Eurasie orientale. Dans l'ensemble, les émissions de CH_4 obtenues sont inférieures aux estimations ascendantes mais supérieures aux résultats des inversions globales. La contrainte insuffisante du réseau d'observation se retrouve dans un scénario simulant des augmentations futures des émissions de CH_4. Les tendances appliquées ont non seulement été détectées de manière incorrecte dans les régions où elles étaient prescrites mais encore, des émissions élevées de CH_4 ont été attribuées à des zones où aucune tendance n'était présente. Un hypothétique réseau d'observation étendu ne montre que des améliorations mineures.